

**Investigation of Isospin Symmetry Breaking in the $f_{7/2}$
Region, Studied through One-nucleon Knockout and
Lifetime Measurements**

Scott Alexander Milne

Ph.D

University of York

Physics

September 2016

Abstract

In this thesis, the results of two experiments are presented. The first experiment was performed at the National Superconducting Cyclotron Laboratory (NSCL) at Michigan State University (MSU), USA, while the second experiment was performed at the Gesellschaft für SchwerIonenforschung (GSI) facility near Darmstadt, Germany.

For the experiment performed at MSU, γ -ray spectroscopy has been performed for both the mirror $T_z = \pm 3/2$ pair ^{53}Ni and ^{53}Mn , produced via mirrored one-nucleon knockout, and the $T_z = -1$ nuclide ^{52}Co , produced via one-neutron knockout. Several new transitions have been identified in both ^{53}Ni and ^{52}Co , from which new level schemes have been constructed. The presence of a high-spin isomeric state ($J^\pi = 19/2^-$) in the ^{53}Co beam facilitated the study of high-spin states up to and including the 11^+ band termination state in ^{52}Co , where this work also represents the first use of this new technique (isomer knockout) to study high-spin states in exotic nuclei. Relative cross sections for knockout have been analysed and compared with reaction model calculations, where a high level of agreement is observed, especially for states in ^{52}Co . Mirror Energy Differences (MED) between Isobaric Analogue States (IAS) have been measured, compared to large scale shell-model calculations and interpreted in terms of INC effects for both the $T_z = \pm 1$, $A = 52$ and $T_z = \pm 3/2$, $A = 53$ mirror pairs. The analysis presented here demonstrates the importance of including a full set of J -dependent INC terms to explain the experimental observations. Finally, lifetimes for the long-lived $J^\pi = 5/2^-$ analogue states in both ^{53}Mn and ^{53}Ni have been extracted through lineshape analysis, giving half-lives of $T_{\frac{1}{2}} = 120(14)$ ps and $T_{\frac{1}{2}} = 198(12)$ ps, respectively.

In the experiment performed at GSI, Coulex and lifetime measurements (using a novel “stretched gold target” technique) were performed for the analogue $2_{T=1}^+ \rightarrow 0_{T=1}^+$ transition across the $A = 46$, $T = 1$ isobaric triplet $^{46}\text{Cr}(T_z=-1)$, $^{46}\text{V}(T_z=0)$ and $^{46}\text{Ti}(T_z=+1)$. Preliminary Coulex cross sections have been obtained and a “proof-of-principle” test has been performed for the new lifetime method.

Contents

Abstract	3
Contents	5
List of figures	9
List of tables	24
Acknowledgements	27
Declaration	29
1 Introduction	31
1.1 Thesis Overview	33
2 Theory	35
2.1 Isospin	35
2.1.1 Mirror Energy Differences	36
2.1.2 Pairing and Isospin Mixing	36
2.2 The Independent Particle Shell Model	38
2.3 Shell Model Calculations	41
2.3.1 Residual Interactions	44
2.3.2 MED Calculations	45
2.3.2.1 The Coulomb Multipole Term	45
2.3.2.2 The Radial Monopole Term	46
2.3.2.3 Single-Particle Monopole Term	46
2.3.2.4 Nuclear Charge Symmetry Breaking Term	47
2.4 Knockout Reaction Calculations	49

2.4.1	Knockout	49
2.4.2	One-nucleon Knockout Calculations	49
2.5	Reduced Transition Probabilities and Coulomb Excitation	51
2.5.1	Coulomb Excitation	51
2.5.2	Reduced Transition Strengths	54
3	Investigation of One-Nucleon Knockout Reactions	55
3.1	Experimental Considerations	56
3.2	Experimental set up	58
3.2.1	Primary Beam Production	58
3.2.2	Secondary Beam Production and the A1900 Separator	59
3.2.3	The S800 Analysis Line and Spectrograph	62
3.2.3.1	The S800 Analysis Line	63
3.2.3.2	The S800 Spectrograph	64
3.2.3.3	Cathode Readout Drift Counters	64
3.2.3.4	Ionisation Chamber	66
3.2.3.5	Scintillation Detectors	67
3.2.3.6	Aberration Correction	68
3.2.4	The SeGA array	69
3.3	S800 Calibrations & Corrections and Particle Identification	73
3.3.1	CRDC Calibrations	74
3.3.1.1	CRDC Pad Amplitude Calibrations	74
3.3.1.2	CRDC Mask Calibrations	75
3.3.2	Particle Corrections at the Target Position	76
3.3.3	Ion Chamber Calibrations and Corrections	77
3.3.4	Scintillator Corrections	78
3.3.5	Particle Identification	80
3.4	SeGA and γ -ray Calibrations	84
3.4.1	Energy and Efficiency Calibrations of SeGA	84
3.4.2	Doppler reconstruction of γ rays	87
3.4.3	Production of Clean γ -ray Spectra	89
3.4.3.1	SeGA Timing Condition	92
3.4.4	Energy and Lifetime Simulations	93
3.4.5	Analysis Techniques	96

3.4.5.1	γ - γ Coincidence Analysis	96
3.4.5.2	Doppler Correction Analysis	97
3.4.5.3	Mirror Symmetry Arguments and Spectral Comparison . .	100
4	Results from One-nucleon Knockout Reactions	101
4.1	Population of states in the $A = 53, T_z = \pm\frac{3}{2}$ mirror pair	102
4.1.1	Spectroscopy of ^{53}Mn	102
4.1.2	Spectroscopy of ^{53}Ni	108
4.1.3	Population of the Observed States	113
4.1.4	Spin Assignment of the $(\frac{5}{2})^+$ State	116
4.1.5	Mirror Lifetime Measurements	117
4.2	Population of States in ^{52}Co ($T_z = -1$)	123
4.2.1	Spectroscopy of ^{52}Co	123
4.2.2	Population of High-spin States in ^{52}Co	125
4.2.2.1	The Longer-lived (11^+) State	128
4.2.2.2	Summary of the Observation High-spin States in ^{52}Co . . .	129
4.2.3	Population of Low-spin States in ^{52}Co	129
4.2.3.1	Establishing the (5^+) State	131
4.2.3.2	Establishing the (4^+) State	131
4.2.3.3	Establishing the ($3^+, 4^+$) State	133
4.2.3.4	Summary of the Observed States in ^{52}Co	134
4.2.3.5	Mass Measurement of ^{52}Co	134
4.3	Shell Model and Cross Section Calculations	138
4.4	The $A = 53, T_z = \pm\frac{3}{2}$ mirror pair	138
4.4.1	Relative Cross Sections Analysis	138
4.4.2	MED Analysis	144
4.5	The $A = 52, T_z = \pm 1$ mirror pair	146
4.5.1	Relative Cross Section Analysis	146
4.5.2	MED Analysis	148
4.6	Discussion	149
4.6.1	Mirrored Knockout Process	149
4.6.2	One-nucleon Knockout from Isomeric States	151
4.6.3	Significance of the MED Results	151
4.7	Summary	152

5 Lifetime and Coulex Measurements Across the $T = 1$ $A = 46$ Triplet of Nuclei	155
5.1 Previous Information	156
5.2 Experimental Considerations	157
5.2.1 Stretched Gold Target (SGT) Lifetime Simulations	159
5.3 Experimental Set-up	164
5.3.1 Primary Beam Production	164
5.3.2 Secondary Beam Production and the GSI Fragment Separator . . .	165
5.3.3 FRS Auxiliary Detectors	167
5.3.3.1 Time Projection Chambers	167
5.3.3.2 FRS Scintillator Detectors	169
5.3.3.3 Multiple Sampling Ionisation Chambers	169
5.3.4 The LYCCA Detector Array	170
5.3.4.1 Double-Sided Silicon Strip Detectors (DSSSDs)	171
5.3.4.2 Caesium Iodide (CsI) Scintillators	172
5.3.4.3 LYCCA Plastic Scintillator Detectors	173
5.3.5 Stretched Gold Target (SGT) and Coulex Target	174
5.3.6 AGATA	174
5.3.6.1 The AGATA Array	175
5.3.6.2 Determination of the γ -ray Interaction Position	177
5.3.6.3 Principles of γ -ray Tracking	178
5.4 FRS Calibrations/Corrections and Incoming Particle Identification	180
5.4.1 Central Beam Trajectory Correction	182
5.4.2 TPC Calibrations	182
5.4.3 FRS Scintillator Calibrations	182
5.4.3.1 ToF Calibrations	182
5.4.3.2 Position Calibrations	184
5.4.4 MUSIC Calibrations and Corrections	185
5.4.5 Incoming Particle Identification	185
5.5 LYCCA Calibrations/Corrections and Outgoing Particle Identification . . .	187
5.5.1 DSSSD Calibrations and Corrections	187
5.5.2 CsI Scintillator Calibrations	189
5.5.3 Plastic Scintillator Corrections	189

5.5.4	Outgoing Particle Identification	190
5.6	AGATA and γ -ray Calibrations	191
5.6.1	Doppler reconstruction of γ rays	191
5.6.2	AGATA Timing Condition	193
5.6.3	Multiplicity Gate	193
5.6.4	Optimising Peak Resolution	194
5.6.4.1	LYCCA β Corrections	194
5.6.4.2	LYCCA Target DSSSD XY-Corrections	195
6	Results for Lifetime and Coulex Measurements across the $T = 1$ $A = 46$	
	Triplet of Nuclei	197
6.1	Scope of this Thesis	197
6.2	Results for the $^{46}\text{Ti}/^{46}\text{Cr}$ Coulex Analysis	199
6.3	Results for the $^{46}\text{Ti}/^{46}\text{V}$ Lifetime Analysis	206
6.4	Summary	214
6.5	Future Work	215
7	Summary	217
	Abbreviations	219
	Bibliography	221

List of Figures

2.1	Schematic diagram of the two possible types of pairing in nuclei. (a) Shows like-nucleon pairing, where nucleons are coupled to $J = 0, T = 1$ (isovector). (b) Shows neutron-proton coupling to $T = 0$ (isoscalar), where the PEP allows only non-zero components of angular momentum ($J > 0$). Taken from Ref. [14].	37
2.2	Shows the allowed and forbidden isospin, T , states for a nucleus with a total isospin projection, T_z , in accordance with Equation 2.8. In general, higher T states are also much higher in energy and thus for most nuclei the ground state has an isospin $T = T_z$. The one exception to this is in odd-odd $N = Z$ nuclei, where $T = 1$ are typically much lower in energy, and in some case, so low in energy they even become the ground state, see text for more details [15].	38
2.3	Energy difference between the first $T = 1$ and $T = 0$ state as a function of atomic mass number, A , for $N = Z$ odd-odd nuclei. Adapted from Ref. [16].	39
2.4	Comparison between a typical Wood-Saxon and Harmonic Oscillator potential. Taken from Ref. [19].	40
2.5	The single-particle energy levels for a simple harmonic oscillator (left), a modified harmonic oscillator including the l^2 term (centre), and a realistic shell model potential, including the l^2 and spin orbit ($\hat{\mathbf{I}} \cdot \hat{\mathbf{s}}$) terms. Note the experimentally observed magic numbers are only reproduced following the inclusion of both terms. Taken from Ref. [20].	42
2.6	Probability distribution for the radial separation between two like-nucleons in the $f_{7/2}$ shell, coupled to different angular momenta. The centre of each plot represents zero separation. Adapted from Ref. [9], calculation performed in Ref. [38].	46

2.7	Comparison between the experimental and predicted MED for four mirror pairs in the $f_{\frac{7}{2}}$ region. The dashed line shows the predicted MED with no CSB V_B term, while the solid line shows the predicted MED including the best-fit V_B^J term. Taken from Ref. [10].	48
2.8	Plot of equivalent photon number (proportional to cross section) against beam energy, for the Coulomb excitation of the 2^+ state in ^{40}S , using a gold target and assuming a minimum impact parameter of 16 fm. Taken from Ref. [54].	53
3.1	A schematic of the ion source, K500 and K1200 coupled cyclotrons and the A1900 fragment separator, taken from Ref. [71].	59
3.2	Particle identification plot of the secondary beam constituents observed during the A1900 setting optimised for the proton-rich ^{54}Ni secondary beam. The axes, xfp-E1 time and obj-E1 time represent the particle time of flight between the XFP and OBJ scintillators, and the E1 scintillator, respectively.	61
3.3	Schematic of the S800 analysis line and Spectrograph, taken from [74] . . .	63
3.4	Schematic of the S800 focal plane detectors, taken from [75]	65
3.5	The SeGA array shown in the classic SeGA configuration, with two rings of detectors at 37° and 90° with respect to the beam axis. The Germanium crystals are shown in red and yellow, in addition to their segmentation. The target is shown by a blue circle at the centre of the array. Taken from Ref. [79].	69
3.6	A schematic diagram of a SeGA crystal, where the radial and lateral segmentation as well as the dimensions of the central contact (dotted line) are shown. The SeGA crystal is labelled using the standard labelling convention. Taken from Ref. [78]	70
3.7	A flow chart which shows the process used to determine the most probable first interaction point of a γ -ray interaction within a SeGA Germanium crystal. In the case that two segments are hit, the distance between the segments and the target is considered. If this distance is the same, i.e. if the γ ray Compton scatters into an adjacent segment, the energy of the γ ray is considered. This is due to the energy of the first and second interaction varying, as a function of the initial γ -ray energy, as shown in Fig. 3.8. . . .	72

3.8	Shows the ratio of the energy deposited in a Compton scattering event ($E1$) with that of the outgoing γ -ray energy ($E2$), as a function of the initial γ -ray energy (E_γ), for a scattering angle of 90°	73
3.9	CRDC pad number vs pad max amplitude (pad max) spectra gated on outgoing ^{51}Fe recoils, where (a) shows the amplitudes before calibration and (b) shows the amplitudes after calibration, which have been aligned to an arbitrary pad max value.	75
3.10	The CRDC mask calibration spectrum of CRDC1 using either (a) uncalibrated positions or (b) calibrated positions.	75
3.11	Spectra of ion chamber energy loss (dE) vs x_0 position measured in CRDC1, before (a) and after (b) the ion chamber energy loss position correction has been applied, see text for more details.	78
3.12	CRDC spectra of dispersive angle a_{fp} (a,b) and dispersive position x_{fp} (c,d) against OBJ scintillator time for the outgoing recoils. The spectra are shown before (a,c) and after (b,d) corrections have been applied, see text for more details.	79
3.13	The effect of S800 focal plane detector corrections to the outgoing PID, where (a) shows the PID with no corrections, (b) shows the PID with ion chamber corrections, (c) shows the PID with scintillator corrections and (d) shows the PID with all corrections. All spectra were produced with an incoming gate on ^{52}Fe and with both the CRDC and ion chamber calibrations optimised.	81
3.14	The PID showing recoils from reactions at the secondary target in coincidence with the ^{54}Ni secondary beam. ^{54}Ni and the main nuclide of interest, ^{53}Ni , have been labelled. Vertical and horizontal lines of total isospin, T_z , and atomic number, Z , respectively, are also shown for recoil identification.	82
3.15	The PID showing recoils from reactions at the secondary target in coincidence with the ^{54}Fe beam. ^{54}Fe and the main nuclide of interest, ^{53}Mn , have been labelled.	83
3.16	The PID showing recoils from reactions at the secondary target in coincidence with the ^{53}Co beam. ^{53}Co and the main nuclide of interest, ^{52}Co , have been labelled.	83

- 3.17 The efficiency curve for the 37° (forward) ring of SeGA, where data points were collected using a combination of ^{56}Co , ^{152}Eu and ^{226}Ra radioactive sources. The line was fit using the function described in Equation 3.9. . . . 86
- 3.18 2D histogram of β vs γ -ray energy, for the combined 37° and 90° ring energy spectra of SeGA. Each energy spectrum is Doppler corrected using the corresponding β -value along the y-axis. The histogram was produced in coincidence with incoming and outgoing ^{52}Fe beam particles, where excited states were populated from inelastic scattering with the ^9Be reaction target. 89
- 3.19 The Doppler corrected energy spectrum for γ rays in coincidence with incoming and outgoing ^{52}Fe beam particles. The spectrum has been produced using an average $\beta=\frac{v}{c}$ value of 0.35. The main features in the energy spectrum have been labelled, including sources of background contamination and the main γ -ray transitions observed, using information from Ref. [65]. . 90
- 3.20 Timing signals from the SeGA Ge crystals measured relative to signals from the the OBJ scintillator. The red dashed lines represent the cut used to reduce the Bremsstrahlung background. 92
- 3.21 The Doppler corrected energy spectrum for γ rays in coincidence with incoming and outgoing ^{52}Fe beam particles, with (black line) and without (red line) a time gate. The spectrum has been produced using a $\beta=\frac{v}{c}$ value of 0.35. 93
- 3.22 Experimental particle spectra for ^{53}Ni recoils (black markers) fitted with their simulated equivalents (red line), after parameter optimisation in the lifetime code. The dispersive (a_{ta}) and non-dispersive (b_{ta}) beam angular distributions at the target position are shown in panels (a) and (b), respectively. The Y-position (y_{ta}) and the relative energy spread of the beam particles (d_{ta}) at the target position are shown in panels (c) and (d), respectively. 95
- 3.23 A 2D histogram of γ -ray energy vs γ -ray energy for multiplicity >1 γ -ray events, gated on incoming ^{53}Co beam and outgoing ^{52}Co recoil. 96

- 3.24 2D histogram of β vs γ -ray energy, for the combined 37° and 90° ring energy spectra of SeGA. Each energy spectrum is Doppler corrected using the corresponding β -value along the y-axis. The histogram was produced in coincidence with incoming ^{52}Fe beam particles and outgoing ^{50}Mn recoils. The approximate ion velocities at the centre ($\beta = 0.360$) and back ($\beta = 0.335$) of the target are also shown by dashed lines, data for labels taken from Ref [85]. 98
- 4.1 (a) Doppler corrected energy spectrum for γ rays in coincidence with ^{53}Mn fragments, populated via one-proton knockout reactions from ^{54}Fe . (b) γ - γ total projection, showing all γ rays with multiplicity >1 . (c-d) Background subtracted γ - γ coincidence spectra for γ rays in coincidence with (c) the 377.88 keV transition and (d) the 912.0 keV transition. All spectra have been produced using an average $\beta = \frac{v}{c}$ value of 0.411. Peaks labeled in parentheses are tentatively observed and transition energy labels for ^{53}Mn are shown from more accurate previous measurements [64]. 103
- 4.2 The partial energy-level scheme for ^{53}Mn as observed in this work, where information on the ordering of the γ -rays was used from Ref. [64]. Tentatively observed transitions and states are indicated by dashed lines and tentatively assigned spins are shown in brackets, see text for more details. Branching ratios for the $\frac{3}{2}_1^-$ level are indicated in red with square brackets and the energy, spin and parity labels used for ^{53}Mn come from more accurate previous measurements [64]. The widths of the arrows are proportional to the relative γ -ray intensities observed. 104
- 4.3 The Doppler corrected spectrum for high-energy γ rays (detected in the 90° SeGA ring) in coincidence with ^{53}Mn fragments. The spectrum has been produced using an average $\beta = \frac{v}{c}$ value of 0.411. 105
- 4.4 The Doppler corrected spectra for γ rays in coincidence with (a) ^{53}Mn and (b) ^{53}Ni fragments, where the spectra have been produced using average $\beta = \frac{v}{c}$ values of 0.411 and 0.383, respectively. The dashed lines indicate the proposed analogue transitions in the mirror nuclei. Transition energy labels for ^{53}Mn are shown from more accurate previous measurements [64]. Tentatively observed γ -ray transitions are indicated in parentheses. 108

- 4.5 (a) γ - γ total projection spectra for ^{53}Ni , showing all γ -rays with multiplicity >1 . (b-d) Background subtracted γ - γ coincidence spectra for ^{53}Ni , showing γ -rays in coincidence with (b) the 320(3) keV transition, (c) the 972(2) keV transition and (d) the 1550(2) keV transition. All spectra have been produced using an average $\beta=\frac{v}{c}$ value of 0.383. 110
- 4.6 The energy level schemes for ^{53}Ni and ^{53}Mn as observed in this work. The spins and parities are in parentheses for ^{53}Ni as the assignments are made on mirror-symmetry arguments. Tentative transitions are indicated by dashed lines. Branching ratios for the $\frac{3}{2}_1^-$ level are indicated in red with square brackets and the energy labels used for ^{53}Mn come from more accurate previous measurements [64]. The widths of the arrows are proportional to the relative γ -ray intensities observed. 112
- 4.7 An energy level scheme of ^{53}Mn showing the states strongly populated in one-proton knockout from the ^{54}Fe 10^+ spin-trap isomer. The population of each state is predicted from cross section calculations using the method described in Section 2.4.2, with spectroscopic factors calculated using the ANTOINE code [24] in the full fp valence space using the KB3G interaction [25]. Information on the state energies and branching ratios were used from previous experimental studies on ^{53}Mn [64]. 115
- 4.8 The γ -ray spectrum for γ rays in coincidence with ^{53}Mn fragments, showing the shift in the 377.9-keV transition due to its 117(6)ps half-life [96]. The spectrum has been produced using an average $\beta=\frac{v}{c}$ value of 0.411. 117
- 4.9 Plot of $\chi^2 - \chi_{min}^2$ for simulated spectra (varying either energy or half-life) fitted to the ^{53}Ni experimental spectra for the $J^\pi:(\frac{5}{2}_1^-) \rightarrow (\frac{7}{2}_{g.s.}^-)$ transition in (a) the 37° SeGA ring and (b) the 90° SeGA ring. (c) The combined $\chi^2 - \chi_{min}^2$ plot of (a) and (b) where the measured half-life and energy are shown by an asterisk at 320.5 keV and 198 ps. Statistical errors in (c) are shown by ellipses, whereby the $\pm 1\sigma$, $\pm 2\sigma$ and $\pm 3\sigma$ errors are represented by a solid line, a dashed line and a dash-dot line respectively. See text for more details. 119

- 4.10 Plot of $\chi^2 - \chi_{min}^2$ for simulated spectra (varying either energy or half-life) fitted to the ^{53}Mn experimental spectra for the $J^\pi: (\frac{5}{2}_1^-) \rightarrow (\frac{7}{2}_{g.s.}^-)$ transition in (a) the 37° SeGA ring and (b) the 90° SeGA ring. Measured transition energies (half-lives) of 378.2 keV (134 ps) and 377.1 keV (111 ps) were obtained for the (a) the 37° SeGA ring and (b) the 90° SeGA ring data, respectively, see text for more details. 120
- 4.11 The best-fit simulated line-shapes (red line) to the experimental data (black points), as determined using a reduced χ^2 , for (a,c) the 37° SeGA ring data and (b,d) the 90° SeGA ring data for the $J^\pi: \frac{5}{2}_1^- \rightarrow \frac{7}{2}_{g.s.}^-$ transition in ^{53}Ni (320 keV) and ^{53}Mn (377.9 keV). 121
- 4.12 The Doppler corrected γ -ray spectra for γ rays in coincidence with ^{52}Co fragments populated via one-neutron knockout from ^{53}Co . The spectrum has been produced using an average $\beta = \frac{v}{c}$ value of 0.370. 123
- 4.13 The Doppler corrected γ -ray spectra for γ rays in coincidence with ^{52}Co fragments populated either via $1n1p$ removal from ^{54}Ni . The spectrum has been produced using an average $\beta = \frac{v}{c}$ value of 0.362. 124
- 4.14 The Doppler corrected γ - γ coincidence spectra for γ rays in coincidence with the (a) 911(2) keV, (b) 1022(3) keV and (c) 1421(2) keV transitions observed in ^{52}Co , populated via one-neutron knockout from ^{53}Co . All spectra have been produced using an average $\beta = \frac{v}{c}$ value of 0.370. 126
- 4.15 The deduced energy-level scheme for the high-spin states ($J \geq 7$) in ^{52}Co , as observed in this work, shown next to a partial level scheme of ^{52}Mn , using information from Ref. [65]. The spins and parities for ^{52}Co are shown in parentheses as the assignments are made on the basis of mirror symmetry arguments. The widths of the arrows (for the ^{52}Co level scheme) are proportional to the observed relative γ -ray intensities. Branching ratios are shown in red with square brackets. 127
- 4.16 A comparison between the ^{52}Co Doppler corrected (a) γ -ray spectrum and (b) γ - γ total projection spectrum. The $\beta = \frac{v}{c}$ value used was chosen in order to optimise the γ -ray spectra to give the best resolution for the observed transitions. 130

4.17 The deduced energy-level scheme for ^{52}Co , as observed in this work, shown beside a partial level scheme of ^{52}Mn , using information from Ref. [65]. The spins and parities for ^{52}Co are in parentheses as the assignments are made on the basis of mirror-symmetry arguments. Tentatively assigned transitions are indicated by dashed lines. A number of state energies are tentative as indicated by dashed lines with energies in parentheses due to the uncertainty in the energy of the (2^+) state, see text for more details. The widths of the arrows (for the ^{52}Co level scheme) are proportional to the relative γ -ray intensities observed. State branching ratios for both ^{52}Co and ^{52}Mn are shown in red with square brackets. Two previously observed transitions in ^{52}Co , as reported in Ref. [99], are also included for comparison purposes and shown as hollow arrows. 135

4.18 Calculated momentum distributions for the removal of either an $f_{7/2}$ (black), $d_{5/2}$ (red) or an $s_{1/2}$ (blue) proton from ^{54}Fe [67]. 139

4.19 Calculated and experimental relative cross sections for states in ^{53}Ni and ^{53}Mn , populated via one-neutron and one-proton knockout, respectively. The calculations for ^{53}Ni and ^{53}Mn (panels (a) and (c)) were obtained using spectroscopic factors calculated in the shell-model, while spectroscopic factors for the positive parity states were taken from experimental data for ^{53}Mn and assumed to be the same for ^{53}Ni . The predicted relative cross sections and energies of both yrast states (black filled) and non-yrast states (red unfilled) are shown. Panels (b) and (d) show the measured relative cross sections to states in ^{53}Ni and ^{53}Mn , respectively, where statistical errors are also shown. States coloured in green (unfilled) can be compared with the calculated cross sections, while states coloured in blue (filled) can not be populated in direct knockout reactions from the ground state of the projectiles. 142

- 4.20 (a) A comparison between the experimental MED and the shell-model calculations. The dotted line shows the shell-model calculations including the V_B term for $J = 2$ only, the solid line shows inclusion of the fitted parameters for V_B , and the dashed line shows the calculations with no V_B term included, see text for more details. (b) The four isospin-breaking components of the shell-model calculations (described in Section 2.3.2), the sum of which yields the solid line in (a). For the V_B term, the fitted parameters have been used, see text for details. In (a) and (b) theoretical and experimental data points for yrast states and non-yrast states are coloured blue and red, respectively, where the lines only connect the yrast states. 145
- 4.21 (a) Calculated relative cross sections for states in ^{52}Co populated either via one-neutron knock-out from the ^{53}Co ground state ($J^\pi = \frac{7}{2}^-$) [no fill], the high-spin isomeric state ($J^\pi = \frac{19}{2}^-$) [blue filled] or both [red/white diagonal lines]. A fractional population of the isomer of 22% has been assumed, see text for more details. The cross sections were calculated using a knockout reaction model using spectroscopic factor inputs from a shell-model calculation performed in the full fp valence space. (b) The experimentally measured relative cross sections for states in ^{52}Co 147
- 4.22 (a) A comparison between the experimental MED and the shell-model calculations. The three lines correspond to three different methods for determining the INC term, V_B . The dashed line determines V_B using a single +100 keV INC matrix element for $f_{\frac{7}{2}}$ protons coupled to $J = 2$, as in previous work (i.e. see Ref. [9]). The solid line uses four INC matrix elements (-72, +32, +8, -12 keV for $J = 0, 2, 4, 6$ extracted from a fit across the $f_{\frac{7}{2}}$ shell) to calculate the V_B term. The dotted line also uses four fitted matrix elements, but where the data for ^{52}Co has been excluded from the fit. (b) The four isospin-breaking components of the shell-model calculations (described in Section 2.3.2), the sum of which yields the solid line. 149
- 5.1 (a) The first excited $2_{T=1}^+$ states in the $T = 1$ $A = 46$ triplet of nuclei. (b) Matrix elements for the $T = 1 \rightarrow 1$, $J^\pi : 2^+ \rightarrow 0^+$ transitions in the $T = 1$ $A = 46$ triplet of nuclei. Data for both plots is taken from Refs. [120–123]. . 157
- 5.2 Comparison of shell model predicted and experimentally observed energies for $T = 0$ and $T = 1$ states in ^{46}V , taken from Ref. [124] 158

5.3 (a) Illustration of the Stretched Gold Target (SGT), where each gold foil acts as both a Coulex target and as a degrader, resulting in the observation of a triple peak distribution, due to differences in the ion emitter velocity after each target. (b) Simulated triple peak distribution for the stretched target device, where the Doppler correction has been optimised for the second peak. 159

5.4 (a) Simulated number of total excited ions produced through Coulomb excitation reactions with a gold target of different thicknesses, where the number of ions decaying both inside and outside the target is calculated, see text for more details. (b) Calculated energy loss for a 170MeV/u ^{46}Ti ion beam passing through a gold foil. 161

5.5 Schematic diagram of the Stretched Gold Target (SGT) target, showing the target measurements from both the side and front. 163

5.6 Photographs of the Stretched Gold Target (SGT), showing the target from both (a) the side and (b) the front. The target consists of three gold foils, each with a thickness of 0.375, 0.25 and 0.25 mm from front to back, where each gold foil is separated by a distance of 1.0 mm. 164

5.7 Schematic of the experimental set-up used at GSI during the 2014 AGATA-PreSPEC campaign, showing from left to right, the SIS, the FRS, AGATA and LYCCA. Taken from Ref. [131]. 165

5.8 Schematic diagram of the TPC detectors used to track particle positions through the FRS, shown beside a picture of the mounted detector [133]. . . 168

5.9 Schematic layout of the various LYCCA detectors (shown in black) used at GSI [136]. The LYCCA ToF target detector was not available during the experiment, see text for more details. 170

5.10 Hit pattern of the LYCCA wall DSSSD modules used at GSI, where the standard labelling convention for the LYCCA modules used in this experiment is also shown. The white lines observed in this plot represent either the gaps between the modules, or in some cases, faulty strips in the DSSSD detector modules. 171

5.11 Schematic drawing of a LYCCA wall module, taken from Ref. [137]. 172

5.12 Photograph of the LYCCA ToF Start/Stop scintillator, see text for details, photos taken from Ref. [138]. 173

5.13	Photographs of (a) the mounted 0.25 mm thick gold Coulex target and (b) the mounted SGT (Section 5.2.1), at the centre of the reaction target chamber.	174
5.14	Configuration (hit pattern) of AGATA during the 2014 PreSPEC-AGATA campaign at GSI, showing the six triple cryostats (with two missing outer crystals) and three double cryostats.	175
5.15	(a) The standard labelling scheme for a 36-fold segmented HPGe AGATA crystal, where the six ring along the longitudinal axis, labelled 1-6, are each subdivided into six segments labelled a-f. (b) Schematic drawing of the three different shaped crystal in a standard AGATA triple cryostat, where the dimensions of each crystal are displayed in mm. Adapted from Ref. [140].	176
5.16	An example of the signals produced in both the core and six segments of a 6-fold segmented detector following the full absorption of a γ ray in segment 4. Due to the interactions closer proximity to segment 3, the amplitude of the signal recorded here is slightly larger than in segment 5. Taken from Ref [141].	177
5.17	Simulation of a 1.33 MeV, multiplicity=30 γ -rays interaction positions in a 4π Ge shell, where γ -ray events have been reconstructed using a cluster tracking algorithm. Correctly and incorrectly identified clusters are shown inside pink circles or green rectangles, respectively. Taken from Ref. [141]. .	180
5.18	(a) Calibrated position spectrum of TPC ₂₁ using an active scintillator grid and (b) the corresponding x-position spectrum.	183
5.19	Calibrated FRS PID for the ⁴⁶ Ti FRS beam setting (Coulex data), using x-positions measured either by (a) the TPCs or (b) the scintillators. Due to issues regarding the recorded signals from the left FRS scintillator PMTs a repeated ID is also observed, while the high beam rate also resulted in pile up in the MUSIC detectors, see text for more details. The nuclide of interest, ⁴⁶ Ti, has been labelled in both PID.	186
5.20	Calibrated FRS PID for the ⁴⁶ Cr FRS beam setting, using x-positions measured either by (a) the TPCs or (b) the scintillators. The nuclide of interest, ⁴⁶ Cr, has been labelled in both PID.	187

5.21	Calibrated FRS PID for the ^{46}Ti FRS beam setting (Coulex data), where x-positions were measured using the scintillators. The PID are shown with (a) correctly determined positions and (b) incorrectly determined positions, where differences in position measurements arose due to issues regarding the signals from the left PMTs of the FRS scintillators, SC_{21} and SC_{41} , see text for more details.	188
5.22	Recorded energy loss in the LYCCA wall DSSSD module 13, both (a) before and (b) after calibrating the energy loss recorded in the strips on both the n-side and p-side of the detector.	188
5.23	Calibrated LYCCA PID for outgoing fragments after the reaction target, produced in the ^{46}Ti FRS setting. The unique identification of different isobars of nuclei can be observed by the horizontal stripes.	190
5.24	(a) Time-Energy histogram for ^{46}Ti , showing the applied time gate (45 ns wide). (b) Doppler corrected energy spectrum for ^{46}Ti , with (black) and without (red) an applied time gate.	192
5.25	Doppler corrected energy spectrum for ^{46}Ti , showing the effects of different multiplicity gates on the Coulex peak.	193
5.26	(a) LYCCA ToF offset scanner for γ rays in coincidence with ^{46}Ti . Each energy spectrum is Doppler corrected using the LYCCA β , derived from the modified event-by-event average LYCCA ToF, between the ToF start and ToF stop scintillators. (b) Plot of FWHM for the ^{46}Ti Coulex peak against ToF offset, where the minimum represents the optimal offset.	195
5.27	Doppler corrected energy spectrum for ^{46}Ti , showing the effects of the peak resolution both before (red) and after (black) XY-position corrections have been applied to the target DSSSD.	196
6.1	Incoming gates applied to the FRS PID for (a) the ^{46}Ti beam setting and (b) the ^{46}Cr beam setting. Both PID were produced with a condition on trigger 10, see text for more details.	199
6.2	Outgoing gates applied to the LYCCA PID for (a) the ^{46}Ti beam setting and (b) the ^{46}Cr beam setting. Both PID were produced with an incoming FRS gate on the nuclei of interest.	200
6.3	Doppler corrected γ -ray spectra for (a) ^{46}Ti and (b) ^{46}Cr , using the optimised event-by-event LYCCA β	201

- 6.4 (a) Measured scattering angle for ^{46}Ti ions, using positions measured in the TPCs at S4, the target DSSSD and the wall DSSSDs. (b) Simulated scattering angle distributions for ^{46}Ti ions, using a number of experimentally extracted parameters such as XY-positions and the resolutions of the various position-sensitive detectors, see text for details. 202
- 6.5 Doppler corrected γ -ray spectra for (a) ^{46}Ti and (b) ^{46}Cr , using the optimised event-by-event LYCCA β . A cut on the LYCCA scattering angle has been applied to the data to ensure only “safe” Coulex events are considered, see text for more details. 203
- 6.6 (a) MBS dead time as a function of time, during a ^{46}Ti beam run, where the dead time was calculated by comparing two scaler signals, 10kHz and 10kHz-veto-dT, see text for more details. (b) AGAVA status as a function of event number, for trigger 9 events (FRS+AGATA+LYCCA), shown during a ^{46}Ti beam run. Events in y-bin 1 refer to validated (accepted) events and events in y-bin 5 refer to rejected events. 204
- 6.7 Doppler corrected γ -ray spectra for (a) ^{46}Ti and (b) ^{46}V , using the event-by-event LYCCA β . The Doppler correction is only approximately optimised for the first peak in the triplet distributions. 206
- 6.8 Simulated Doppler corrected energy, as a function of γ -ray angle, for the same energy transition emitted at three different velocities, where the Doppler correction was performed for only one of these velocities. In this case, the predicted velocities of ^{46}Ti after each gold target, using LISE [73] calculations, have been used. 208
- 6.9 (a) Distribution of γ -ray events observed at different γ -ray angles of emission, where the angle cut of $30\pm 5^\circ$ used during this analysis is also shown. (b) The observed Doppler corrected ^{46}Ti triple peak spectrum following the application of an angle cut at $30\pm 5^\circ$ 208
- 6.10 Doppler corrected γ -ray spectra, with Doppler correction optimised for (a-c) each peak of the triplet distribution in ^{46}Ti and (d-f) each peak of the triplet distribution in ^{46}V , using the event-by-event LYCCA β . The Doppler correction of each peak was guided by simulations performed using LISE, where both the LISE β and optimised LYCCA β for each peak are shown. . 210

6.11 (a) Simulated ratio of counts in peak1/(peak2+peak3), as a function of half-life. See Section 5.2.1 for more details. (b) Doppler corrected γ -ray spectrum for ^{46}Ti , fitted with a triple Gaussian function plus linear background to extract the number of counts in each peak. 211

6.12 Doppler corrected γ -ray spectra for (a) ^{46}Ti and (b) ^{46}V , using the event-by-event LYCCA β . Both spectra have been produced with a γ -ray angle cut of $39(5)^\circ$ 212

6.13 Doppler corrected γ -ray spectrum for (a) ^{46}Ti and (b) ^{46}V , using the event-by-event LYCCA β , fitted with a triple Gaussian function plus linear background to extract the number of counts in each peak. Both spectra have been produced with a γ -ray angle cut of $39(5)^\circ$ 212

6.14 Doppler corrected γ -ray spectrum for ^{46}Ti , using the event-by-event LYCCA β , fitted with a triple Gaussian function plus linear background to extract the number of counts in each peak. The spectrum has been produced with a γ -ray angle cut of $39(5)^\circ$. The FWHM of the Gaussian fit to the second peak has been fixed to a similar width as the other two peaks ($\sim 1.4\%$), see text for more details. 213

List of Tables

3.1	The main constituents of the ^{54}Ni and ^{54}Fe A1900 settings delivered to the reaction target, measured using the ToF between the XFP and OBJ scintillators. Secondary beam rates for the individual beam constituents are also shown.	62
4.1	Details of the excited states in ^{53}Mn which were observed in this experiment. All values, except the relative γ -ray intensities ($I_{\gamma(\text{rel})}$) are taken from Ref. [64]. Unobserved transitions from states which are observed to be populated in this analysis are also shown for completeness, with an $I_{\gamma(\text{rel})}$ of X.	107
4.2	Ground state of ^{54}Fe , calculated using the ANTOINE code [24], in the full fp valence space using the KB3G interaction [25]. All ground state admixtures greater than 1% are shown.	113
4.3	Details of the new excited states observed in ^{53}Ni and the relevant isobaric analogue states observed in ^{53}Mn . Ground state and excited state half-lives for ^{53}Ni and ^{53}Mn , with the exception of the measured half-life for the $\frac{5}{2}_1^-$ state in ^{53}Ni and the upper limit set for the $(\frac{5}{2})_1^+$ state in ^{53}Mn , are taken from Ref. [64]. State and transition energies for ^{53}Mn are taken from more accurate previous measurements [64].	122
4.4	Three candidate analogue transitions in ^{52}Mn to the 459(1) keV transition observed in ^{52}Co , using information from Ref. [65].	133

4.5	Details of the new excited states and transitions observed in ^{52}Co . Two previously observed transitions in ^{52}Co , as reported in Ref. [99], have also been included for completeness (with $I_{\gamma(\text{rel})}$ of X). Excited state half-lives in ^{52}Co have been estimated using a Doppler correction analysis in conjunction with energy loss calculations performed using LISE [73], see text for more details. Tentative state energies and assigned transitions are shown in parentheses, see text for more details. The ground state half-life for ^{52}Co is taken from Ref. [65].	136
4.6	Details of the proposed IAS and mirror transitions in ^{52}Mn to those observed in ^{52}Co , using data from Ref. [65].	137
5.1	Summary of the different degrader material used during each FRS setting.	167
5.2	Summary of the four ^{58}Ni FRS calibration (effective matter) runs performed during the experiment at GSI. The FRS ToF and $\beta = \frac{v}{c}$, between the SC ₂₁ and SC ₄₁ scintillators, were extracted from LISE simulations [73].	181
6.1	Summary of the FRS settings and experimental details for the four sub experiments performed during the experiment at GSI. The S2 and S4 Beam rates are extracted from the average scalar rates, per spill length, during each FRS setting. Secondary beam energies, before the reaction target, were calculated for the nuclei of interest through the use of LISE [73].	198
6.2	Summary of the experimental data and the resulting Coulex cross section, for both ^{46}Ti and ^{46}Cr , obtained using Equation. 6.1. The dead time for the MBS DAQ was calculated by comparing two scaler signals, 10kHz and 10kHz-veto-dT, while the dead time for NARVAL DAQ was calculated by comparing the validated and rejected AGAVA status events, with a trigger 9 condition (FRS+AGATA+LYCCA), see text for more details. The AGATA efficiency used here (after accounting for the Lorentz boost) was taken from Ref. [157].	205

Acknowledgements

First and foremost, I would like to say a big thank you to my supervisor Prof. Mike Bentley for his fantastic support and guidance throughout my Ph.D. It has been a pleasure to work with Mike who has played a key role in my development during the last four years and also helped make my time as a Ph.D student a thoroughly enjoyable experience. I would also like to thank all other members of the Nuclear Physics Group at York for their assistance throughout my Ph.D, particularly Dr. Paul Davies for his help regarding any coding related issues, Dr. Tom Henry for helping me get started with the MSU data analysis, Dr. Lianne Scruton for her help with any LYCCA related issues and finally Dr. Adam Nichols for helping me get started with the Lifetime simulations. Furthermore, I'd also like to say a big thanks to Ed Simpson for kindly performing knockout calculations for this analysis.

I would also like to say a big thank you to my collaborator Alberto Boso for his continued assistance and cooperation throughout the AGATA analysis. In addition, I would also like to thank everyone involved in the AGATA-PreSPEC 2014 campaign.

Last but not least, I would like to thank my parents and my family for their continued support throughout the last four years of my Ph.D, and would like to dedicate this work to them.

Declaration

I declare that the work presented in this thesis, except where otherwise stated, is based on my own research and has not been previously submitted for any other degree or qualification. All of the work presented in this thesis was performed under the supervision of Prof. M. A. Bentley. Some parts of this thesis have however been previously published in journals

Publications:

- S. A. Milne, M. A. Bentley, E. C. Simpson *et al.*, “Mirrored One-nucleon Knockout Reactions to the $T_z = \pm \frac{3}{2}$ $A = 53$ Mirror Nuclei”, *Phys. Rev. C* **93**, 024318 (2016).
- S. A. Milne, M. A. Bentley, E. C. Simpson *et al.*, “Isospin Symmetry at High Spin Studied via Nucleon Knockout from Isomeric States”, *Phys. Rev. Lett.* **117**, 082502 (2016).

Chapter 1

Introduction

The near identical nature of the strong nuclear interaction between neutron-neutron (nn), proton-proton (pp) and neutron-proton (np) [1] pairs, means that the nuclear force can be assumed to be both charge symmetric and charge independent, which therefore gives rise to the concept of isospin symmetry. Based on this assumption, one would expect, in absence of the electromagnetic interaction, for isobaric multiplets to be degenerate in energy, and for all bound nuclear states to have a definite and pure isospin [2]. Of course, as previously alluded to, some small differences do exist between the nucleon-nucleon interactions, and thus the nuclear force is neither charge symmetric nor charge independent. However, the symmetry breaking effects arising due these differences are small compared with the absolute values and thus in the shell model calculations, the nuclear interaction is treated as being charge symmetric. Charge Symmetry Breaking (CSB) effects instead, arise due to the Coulomb interaction. Despite our good understanding of the Coulomb interaction however, Nolen and Schiffer found calculated Mirror Displacement Energies (MDE), i.e. the displacement energy between the ground states of mirror nuclei, to be surprisingly inaccurate [3]. In fact, calculations were found to underestimate MDE by around $\sim 7\%$ [3]. Due to the unknown origin of this discrepancy, this effect has since become known as the “Nolen-Schiffer anomaly”.

One way in which nuclear structure can be probed and Isospin-Non-Conserving (INC) effects in nuclei can be quantified is through the study of Mirror Energy Differences (MED), i.e. energy differences between analogue states in mirror nuclei. In an early MED study by Cameron *et al.* [4] the MED for the $T_z = \pm\frac{1}{2}$ mirror pair ^{49}Mn and ^{49}Cr was plotted as a function of spin where at larger spins a larger MED was observed. This was interpreted in terms of particle alignment, where it was proposed that the pp spatial separation increased

with increasing alignment of nucleon angular momentum vectors. These effects in MED calculations could not be properly reproduced however until the introduction of Coulomb Matrix Elements (CME) to large scale shell model calculations. Such CME can either be derived theoretically, from a Harmonic Oscillator (HO) basis [5], or empirically, from fits to experimental data. In the case of the $f_{7/2}$ shell region, these CME are obtained from fits to $A = 42$ data [6], i.e. nuclei with 2 $f_{7/2}$ nucleons above a closed ^{40}Ca core. However, CME extracted in this way will also include contributions from other INC effects. Therefore, in order to account for these additional INC effects, matrix elements were introduced, following the work of Zuker *et al.* [7] and Williams *et al.* [6]. Furthermore, through the study of the $A = 42$ and $A = 54$ mirror pairs, i.e two particle and two hole states in the $f_{7/2}$, it became clear that an additional isovector term for $f_{7/2}$ protons coupled to $J = 2$ was required in the calculations [7,8]. This was included by adding a single repulsive interaction of 100 keV (in addition to the Coulomb interaction) to the two-body matrix elements for $f_{7/2}$ protons coupled to $J = 2$. The origin of this isovector effect is still currently unknown, and thus it is commonly referred to as the “ $J = 2$ anomaly”

A detailed description of these INC terms is given in Ref. [9], where two additional monopole terms, accounting for radial and single-particle effects, are also included. Furthermore, in a very recent study by Bentley *et al.* [10], a full set of spin-dependent effective isovector ($pp-nn$) matrix elements were extracted in the $f_{7/2}$ shell, by fitting the shell model to all experimental MED data so far obtained in the shell. This yielded matrix elements of $V_B = -72, +32, +8, -12$ keV for $J = 0, 2, 4, 6$ couplings, whereby the inclusion of these matrix elements to the shell-model calculations resulted in a further improvement in theoretical fit to the experimental data [10]. Thus, a detailed shell-model prescription has now been developed for the study of mirror nuclei. To test the validity of this prescription however, requires more data to be collected in the shell and for more studies to be performed for mirror nuclei at larger differences in isospin, since a number of the INC terms in this shell-model prescription have a strong dependence on T_z .

In this thesis, the results of two experiments will be presented. In the analysis for the experiment performed at MSU, the use of one-nucleon knockout reactions, to populate excited states in nuclei along the $N \approx Z$ line, will be discussed. This analysis consists of two main parts, (a) mirrored one-nucleon knockout, where states in the $T_z = \pm\frac{3}{2}$ mirror pair ^{53}Ni and ^{53}Mn were populated and (b) one-nucleon knockout from a high-spin isomeric state, where high-spin states in $T_z = -1$ nuclide ^{52}Co were populated with

sizeable cross sections. In both cases, the methods employed are novel, whereby no similar work has been previously performed. Furthermore, for both of these analyses, a detailed MED study and relative cross section analysis have also been performed, where it will be shown, through the use of reaction cross-section calculations, that states populated either via mirrored one-nucleon knockout or isomeric knockout, can be predicted with a high degree of confidence. Therefore, the work performed in this thesis serves to demonstrate the effectiveness of these new methods in investigating isospin symmetry, as well as to present a new method for the study high-spin states in exotic nuclei. The work performed for both of these analyses is published in Refs. [11,12].

In regards to the analysis performed for the experiment at GSI, a few important points need to first be made, (a) the experiment occurred during the latter stages of my PhD and (b) the experiment/analysis was performed in collaboration with Alberto Boso from the Univerità Degli Studi di Padova. The original aim of the experiment at GSI was to investigate isospin mixing between the $2_{T=0}^+$ and $2_{T=1}^+$ states in ^{46}V , where this was to be achieved by performing precise B(E2) measurements for the analogue $2_{T=1}^+ \rightarrow 0_{T=1}^+$ transition, across the $A = 46$, $T = 1$ isobaric triplet $^{46}\text{Cr}(T_z=-1)$, $^{46}\text{V}(T_z=0)$ and $^{46}\text{Ti}(T_z=+1)$. Since these B(E2) measurements were performed using both Coulex and lifetime measurements (using a novel “stretched gold target” technique), the analysis for this experiment was therefore divided, whereby Alberto’s main focus was on the Coulex analysis and my focus was predominantly on the lifetime analysis. Therefore, due late occurrence of this experiment during my PhD, the main focus of this analysis was to perform a “proof-of-principle” test for the new “stretched Gold target” lifetime method, whereby this analysis has been completed, with positive results. A full simulated spectral analysis however, is out of the scope of this thesis and will instead be performed at a later date by Marc Labiche at Daresbury. For interest, a preliminary Coulex cross section analysis has also been performed, whereby this analysis was performed independently and later confirmed with Alberto. A complete Coulex cross section analysis however is out of the scope of this thesis and will instead be performed by Alberto.

1.1 Thesis Overview

In Chapter 2, an overview of the theory of isospin and the shell model are given. This is then followed by details on both the shell model calculations and knockout calculations. Lastly, a brief description on the reaction mechanisms investigated in this thesis are also

given.

In Chapter 3, experimental details for the experiment performed at MSU are given, where all of the calibration procedures for the various detectors are also discussed. This is then followed by Chapter 4, where the analysis of the experimental data from the experiment at MSU is discussed in detail. In addition, in this chapter, comparisons between experimental and theoretical shell model and knockout calculations are also discussed. Finally, the results of this analysis are summarised at the end of the chapter.

In Chapter 5, experimental details are given for the experiment performed at GSI, where all of the detector calibration procedures are also discussed. Following this, in Chapter 6, the preliminary analysis of the experimental data from the experiment performed at GSI is presented and discussed. Finally, the results of this preliminary analysis are then summarised at the end of the chapter.

Lastly, in Chapter 7, a brief summary of the main results from both analyses is given.

Chapter 2

Theory

2.1 Isospin

In the absence of the electromagnetic interaction, the proton and neutron can be considered as two quantum states of the same particle, the nucleon. In order to distinguish between these like particles, they are assigned an isospin quantum number $t = \frac{1}{2}$ with a projection t_z along an isospin quantization axis. In this construct, the proton is assigned a projection $t_z = -\frac{1}{2}$ and the neutron $t_z = +\frac{1}{2}$, whereby the total isospin projection of the nucleus is given by the sum of the individual isospin projections [13],

$$T_z = \sum^A t_z = \frac{N - Z}{2}. \quad (2.1)$$

This concept also depends upon the strong nuclear force being both charge symmetric,

$$V_{pp} = V_{nn} \quad (2.2)$$

and charge independent,

$$V_{np} = \frac{V_{pp} + V_{nn}}{2} \quad (2.3)$$

where previous experimental data has indeed shown the nucleon-nucleon interaction to be approximately equal for neutron-neutron, proton-proton and neutron-proton pairs [1]. In the absence of Isospin Non-Conserving (INC) interactions, one would expect degeneracy between analogue states in nuclei of the same mass number, also known as Isobaric Analogue States (IAS). However, this degeneracy is broken, particularly due to the Coulomb interaction, which acts as a long-range repulsive force, felt only by protons. Therefore, differences in excitation energies between IAS (normalised to the ground state), can be attributed to INC interactions resulting from either the electromagnetic interaction or any

charge dependence of the nucleon-nucleon interaction, where these INC interactions can be categorised either as isovector effects, $V_{isovector}$, or as isotensor effects, $V_{isotensor}$,

$$V_{isovector} = V_{pp} - V_{nn} \quad (2.4)$$

$$V_{isotensor} = V_{pp} + V_{nn} - 2V_{np}. \quad (2.5)$$

The study of mirror nuclei therefore, i.e. nuclei in which the number of protons and neutrons have been interchanged, allows for isovector effects in bulk nuclear systems to be investigated, since in these nuclei, the number of np pairs is the same. However, the study of $T = 1$ isobaric triplets, i.e. triplets of nuclei centred on the $N = Z$ line which all have the same atomic mass number, allows for isotensor effects in bulk nuclear systems to be investigated.

2.1.1 Mirror Energy Differences

In this thesis (Chapters 3 and 4), isovector effects in mirror nuclei were investigated through the study of Mirror Energy Differences (MED), i.e. differences in excitation energies between IAS (normalised to the ground state) in mirror nuclei, which are calculated by,

$$MED_J = E_{J,T,-T_z}^* - E_{J,T,T_z}^* \quad (2.6)$$

where E_{J,T,T_z}^* represents the excitation energy of a state of spin, J , isospin, T and isospin projection, T_z . Since these excitation energies are measured relative to the ground state, effects relating to Mirror Displacement Energies (MDE), i.e. displacement energies between the ground states of mirror nuclei, are eliminated. Thus, only the spin-dependent contributions to the excitation energies of analogue states are considered. As the electromagnetic interaction is well understood, a detailed comparison between experimentally deduced and theoretical MED values, extracted using state-of-the-art shell-model calculations, as will be discussed in Section. 2.3, allows for Charge Symmetry Breaking (CSB) of the strong nuclear force in bulk nuclear systems to be investigated.

2.1.2 Pairing and Isospin Mixing

In most known nuclei, particularly those with $N > Z$, like nucleon pairing dominates, where pairs of neutrons (nn) and protons (pp) are coupled in time-reversed orbits to $J = 0$, $T = 1$ (isovector), in accordance with the Pauli Exclusion Principle (PEP). However, in nuclei which lie along the $N \approx Z$ line, np pairing may also occur, as here, neutrons and protons

occupy the same orbitals and therefore have the maximum spatial overlap. Since neutrons and protons are not identical particles, the restrictions of the PEP no longer apply and np pairs can therefore couple to either $J = 0, T = 1$ (isovector) or $J > 0, T = 0$ (isoscalar). These two types of pairing, isovector and isoscalar, are illustrated in Fig. 2.1 [14].

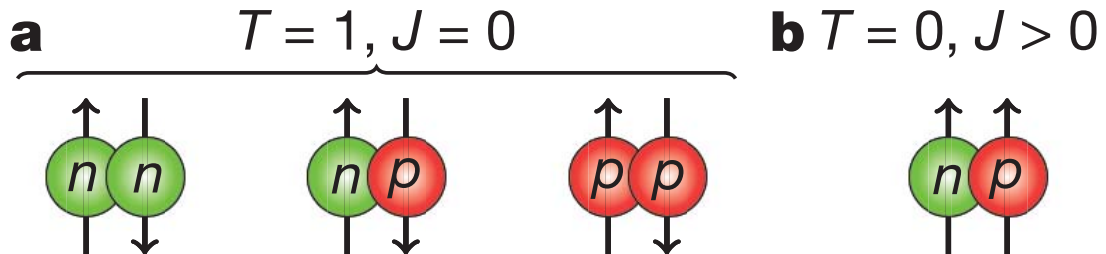


Figure 2.1: Schematic diagram of the two possible types of pairing in nuclei. (a) Shows like-nucleon pairing, where nucleons are coupled to $J = 0, T = 1$ (isovector). (b) Shows neutron-proton coupling to $T = 0$ (isoscalar), where the PEP allows only non-zero components of angular momentum ($J > 0$). Taken from Ref. [14].

In nuclei, the total isospin, T , of a state is given by the vector sum of all the individual isospin vectors,

$$\mathbf{T} = \sum_{i=1}^A \mathbf{t}_i \quad (2.7)$$

where the range of isospin states which can be formed in a particular nucleus is given by,

$$\frac{N - Z}{2} \leq T \leq \frac{N + Z}{2}. \quad (2.8)$$

This is illustrated in Fig. 2.2, where the allowed and forbidden isospin states for nuclei with different total isospin projections, T_z , are shown. In general (with the exception of most nuclei which lie along the $N = Z$ line), yrast states, i.e. the lowest energy states for a given spin, will also have the lowest possible value of isospin (i.e. $T = T_z$), while those with higher T , will normally be much higher in energy. In the case of odd-odd $N = Z$ nuclei however, some nuclei are observed to have $T = 0$ ground states, while others are observed to have $T = 1$ ground states. This is demonstrated in Fig. 2.3, where the energy difference between the lowest energy $J = 0, T = 1$ and $J > 0, T = 0$ states in odd-odd $N = Z$ nuclei is shown, for nuclei between $A = 6$ and $A = 62$ [16]. Here, it can be observed for nuclei below $A = 42$, with the exception of ^{34}Cl , that isoscalar correlations dominate and therefore nuclei here have $T = 0$ ground states [16]. However, for odd-odd $N = Z$ nuclei with $42 \leq A \leq 54$ (i.e. nuclei in the $f_{7/2}$ region), isovector correlations dominate,

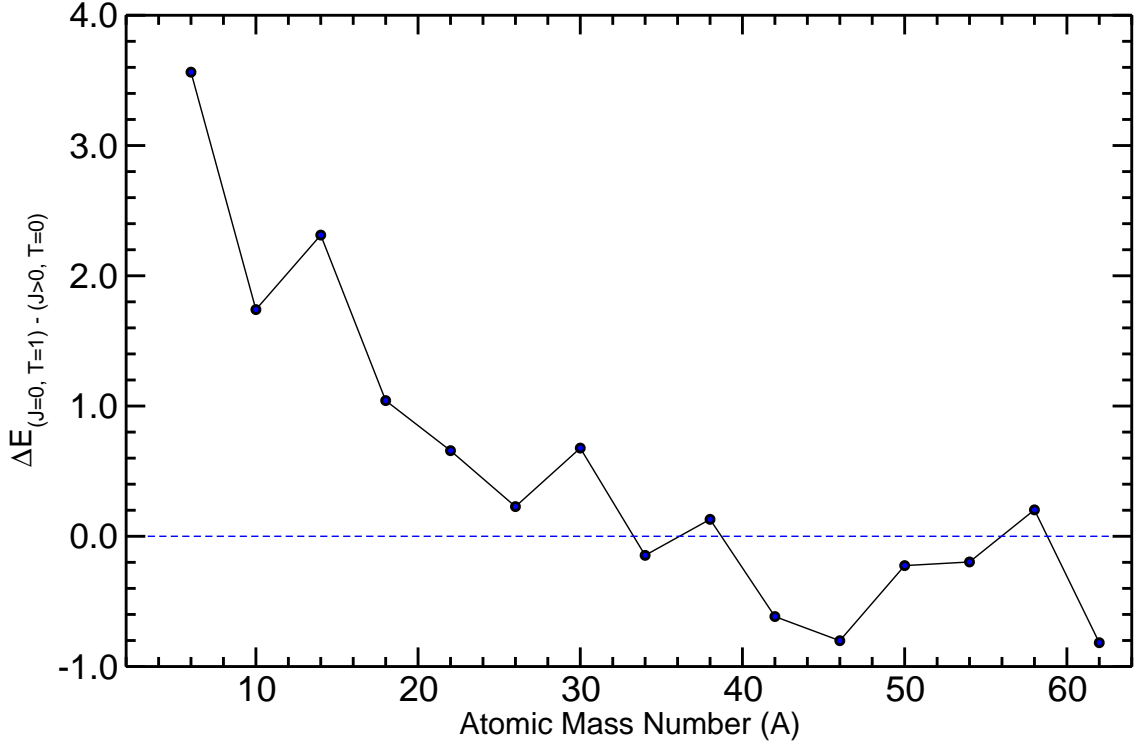


Figure 2.3: Energy difference between the first $T = 1$ and $T = 0$ state as a function of atomic mass number, A , for $N = Z$ odd-odd nuclei. Adapted from Ref. [16].

Nobel Prize in Physics for their contributions to the model [17]. The shell-like structure of the nucleus, analogous to that of the atomic shell structure, was first proposed by Maria Goeppert-Mayer, following her work compiling lists of isotopic abundances, where she discovered nuclei with 2, 8, 20, 28, 50, 82, or 126 protons and/or neutrons to be especially stable [17]. These so-called “magic number” of nucleons were later found to correspond with specific nuclear shell closures.

In contrast to the atomic shell model, the nuclear shell model does not have a well-defined central potential. Instead, the central potential is created by the individual nucleons themselves. By considering only two-body interactions, the nuclear Hamiltonian can be written as the sum of the kinetic energy, T , and potential energy, V [18],

$$H = T + V = \sum_{i=1}^A \frac{\hat{\mathbf{p}}_i^2}{2m_i} + \sum_{j>i}^A V_{i,j}(\hat{\mathbf{r}}_i, \hat{\mathbf{r}}_j). \quad (2.9)$$

This expression can be further simplified by introducing a mean field interaction, $V_i(\hat{\mathbf{r}})$, which depends only upon the radial distance, $\hat{\mathbf{r}}$, of each nucleon,

$$H = \sum_{i=1}^A \left[\frac{\hat{\mathbf{p}}_i^2}{2m_i} + V_i(\hat{\mathbf{r}}) \right] + \left[\sum_{j>i}^A V_{i,j}(\hat{\mathbf{r}}_i, \hat{\mathbf{r}}_j) - \sum_{i=1}^A V_i(\hat{\mathbf{r}}) \right] = H_0 + H_{res}. \quad (2.10)$$

In this expression, H_0 , denotes the shell-model Hamiltonian, which includes only the mean field interaction, $V_i(\hat{\mathbf{r}})$, while, H_{res} , denotes the residual interactions, which includes the two-body nucleon-nucleon interactions that are not accounted for by the mean field interaction.

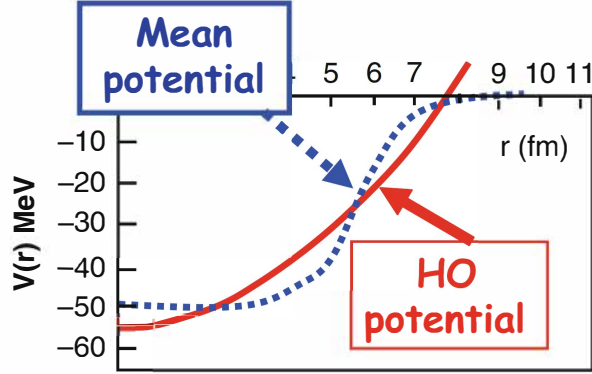


Figure 2.4: Comparison between a typical Wood-Saxon and Harmonic Oscillator potential. Taken from Ref. [19].

If a suitable mean field is chosen, the residual interaction (H_{res}) will be small and therefore the shell-model Hamiltonian (H_0) will represent a good approximation for the exact expression of the Hamiltonian (H). In general, either a Woods-Saxon potential or Harmonic Oscillator (HO) potential is chosen to represent the nuclear potential. The Woods-Saxon potential is given by,

$$V(\hat{\mathbf{r}}) = \frac{V_0}{1 + \exp(\frac{\hat{\mathbf{r}}-R}{a})} \quad (2.11)$$

where, V_0 , is the depth of the potential well, R is the mean radius of the potential and a is the surface diffuseness term. Meanwhile, the HO potential is given by,

$$V(\hat{\mathbf{r}}) = \frac{1}{2}mw^2\hat{\mathbf{r}}^2 \quad (2.12)$$

where, m is the mass of the nucleon, w is the oscillator angular frequency and $\hat{\mathbf{r}}$ is the radius. A comparison between the two potentials is presented in Fig. 2.4. In general, due to the HO potential being simpler to solve in the Schrödinger equation, it is usually the preferred choice for the nuclear potential.

In order to replicate the experimentally observed magic numbers, see Fig. 2.5 two additional contributions to the HO potential need to be included. The first of these contributions results from an attractive term, which is proportional to the square of the

orbital angular momentum, l . This $\hat{\mathbf{I}} \cdot \hat{\mathbf{I}}$ term acts to increase the binding energy for nucleons with a larger orbital angular momentum, which results in a flattening of the potential well. The second contribution results from the interaction between the spin and orbital angular momentum of a nucleon, also known as the spin-orbit interaction. This $\hat{\mathbf{I}} \cdot \hat{\mathbf{s}}$ term is of nuclear origin and acts to split the degeneracy of levels with the same n and l . Since parallel alignments are favoured, this results in a lowering in energy of $j = l + s$ levels, while raising those with $j = l - s$. Following the inclusion of these two additional terms, the potential is given by,

$$V(\hat{\mathbf{r}}) = V_{HO}(\hat{\mathbf{r}}) + V_{\hat{\mathbf{I}}\hat{\mathbf{I}}} + V_{\hat{\mathbf{I}}\hat{\mathbf{s}}}(\hat{\mathbf{r}}) \quad (2.13)$$

where

$$V_{\hat{\mathbf{I}}\hat{\mathbf{I}}} = V_{ll} \hat{\mathbf{I}} \cdot \hat{\mathbf{I}} \quad (2.14)$$

and

$$V_{\hat{\mathbf{I}}\hat{\mathbf{s}}} = -V_{ls} \frac{\partial V_{HO}(\hat{\mathbf{r}})}{\partial r} \hat{\mathbf{I}} \cdot \hat{\mathbf{s}}, \quad (2.15)$$

where, V_{ll} and V_{ls} represent strength constants.

2.3 Shell Model Calculations

In shell-model calculations, the nucleon single-particle energy levels are firstly calculated by solving the Schrödinger equation for the shell-model Hamiltonian (H_0). Following this, basis states are then constructed by considering all of possible configurations of nucleons in the single-particle levels.

The wavefunction of a state, $\Psi_\alpha(r_1, r_2, \dots, r_A)$, in a nucleus with A nucleons, can be expressed as a linear sum of the complete orthonormal set of basis states [21],

$$\Psi_\alpha(r_1, r_2, \dots, r_A) = \sum_{k=1} C_k^\alpha \Phi_k(r_1, r_2, \dots, r_A) \quad (2.16)$$

where r_i represents all of the independent variables of the system related to nucleon i and C_k^α denotes the expansion coefficients for the α^{th} eigenfunction. The square of these expansion coefficients can be interpreted as the probability of finding the nucleus with quantum numbers associated with Φ_k , if it is in a state described by Ψ_α . Since we are dealing with system consisting of fermions, the PEP dictates that the wavefunction must be antisymmetric for the exchange of coordinates of two nucleons. This is satisfied by

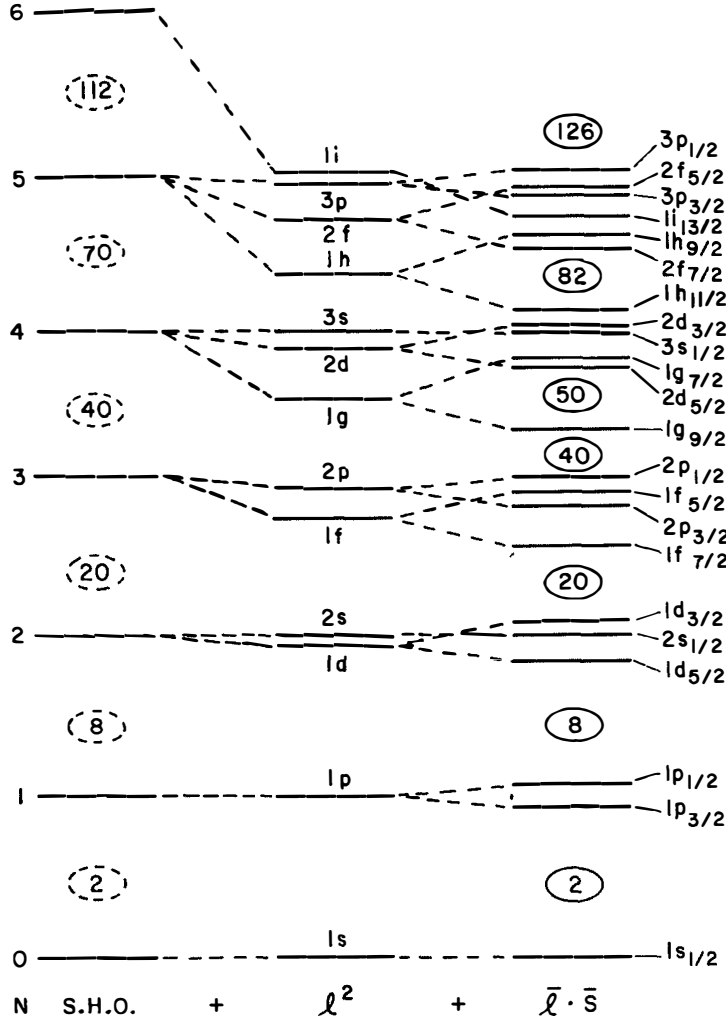


Figure 2.5: The single-particle energy levels for a simple harmonic oscillator (left), a modified harmonic oscillator including the l^2 term (centre), and a realistic shell model potential, including the l^2 and spin orbit ($\hat{\mathbf{l}} \cdot \hat{\mathbf{s}}$) terms. Note the experimentally observed magic numbers are only reproduced following the inclusion of both terms. Taken from Ref. [20].

expressing the basis states in the form of a Slater determinant [21],

$$\Phi_k(r_1, r_2, \dots, r_A) = \frac{1}{\sqrt{A!}} \det \begin{vmatrix} \phi_1(r_1) & \phi_2(r_1) & \cdots & \phi_A(r_1) \\ \phi_1(r_2) & \phi_2(r_2) & \cdots & \phi_A(r_2) \\ \vdots & \vdots & \ddots & \vdots \\ \phi_1(r_A) & \phi_2(r_A) & \cdots & \phi_A(r_A) \end{vmatrix} \quad (2.17)$$

where $\phi_i(r_i)$ denotes the single-particle wavefunctions. To find the eigenvalues of a wave-

function, one must first solve the Schrödinger equation for the full Hamiltonian,

$$H\Psi_\alpha(r_1, r_2, \dots, r_A) = E_\alpha\Psi_\alpha(r_1, r_2, \dots, r_A) \quad (2.18)$$

which, after expanding for Equation 2.16, can also be written as,

$$H \sum_{k=1} C_k^\alpha \Phi_k(r_1, r_2, \dots, r_A) = E_\alpha \sum_{k=1} C_k^\alpha \Phi_k(r_1, r_2, \dots, r_A). \quad (2.19)$$

After multiplying both sides on the left by Ψ_j^* (the conjugate of the basis state Ψ_k), and integrating over all independent variables, this expression can be reduced to [21],

$$\sum_{k=1} H_{jk} C_k^\alpha = E_\alpha C_j^\alpha. \quad (2.20)$$

where, H_{jk} denotes the Hamiltonian matrix elements between basis states Φ_j and Φ_k ,

$$H_{jk} \equiv \langle \Phi_j(r_1, r_2, \dots, r_A) | H | \Phi_k(r_1, r_2, \dots, r_A) \rangle. \quad (2.21)$$

In matrix form, Equation 2.20 can be expressed as [21],

$$\begin{pmatrix} H_{11} & H_{12} & \cdots \\ H_{21} & H_{22} & \cdots \\ \vdots & \vdots & \ddots \end{pmatrix} \begin{pmatrix} C_1^\alpha \\ C_2^\alpha \\ \vdots \end{pmatrix} = E_\alpha \begin{pmatrix} C_1^\alpha \\ C_2^\alpha \\ \vdots \end{pmatrix} \quad (2.22)$$

In order to obtain the corresponding eigenvalues for the wavefunction of a particular state, the Hamiltonian matrix must be diagonalised, which is performed in the shell-model calculations. Following this, the wavefunctions are then modified in the calculations until the minimum energy is found for a given spin-parity state.

Calculations using this approach however, also referred to as “no-core” shell-model calculations, are too computationally intensive and therefore are limited to very light nuclei ($A \leq 12$) [22, 23]. For heavier nuclei, calculations must instead be restricted to the valence nucleons which significantly contribute to the states of interest and effective residual interactions must be employed. To achieve this, one must first define an appropriate shell-model space for the calculation. This starts by assuming an inert core, i.e. a core of nucleons which do not contribute to the states of interest, where these nucleons are also fixed in their respective single-particle levels and are not considered by the residual interaction. Secondly, one must consider a truncation of the shell-model space, i.e. a restriction on the shell-model single particle levels which the valence nucleons can occupy in the calculation, sometimes referred to as a vertical truncation. Following these two considerations, a valence space is then defined, in which the valence nucleons can freely move.

The states of interest therefore, are defined by the different configurations of these valence nucleons, where only the residual interactions between these nucleons are considered in the calculations. In some cases however, despite this truncation, the calculations can still be too computationally intensive. As a result, the valence space for these calculations needs to be further truncated, i.e. by limiting the number of allowed nucleon excitations across a particular shell within the valence space. If the truncation is too severe however, the states calculated will have unrealistic wavefunctions and higher binding energies. This issue can be overcome by slowly reducing the truncation until the calculated state of interest is at its lowest binding energy. If any further decreases in the truncation do not result in a further lowering of this binding energy, the result is said to be converged. While shell-model calculations as a whole produce fairly reasonable results, they can be particularly limited in the case of some nuclear regions, either due to poor shell closure or the nuclei studied being heavily deformed. The shell-model calculations discussed in this thesis were performed using the shell-model code ANTOINE [24].

2.3.1 Residual Interactions

The residual interaction, H_{res} , accounts for the additional interactions which are not accounted for by the mean field interaction. This includes the nucleon-nucleon interactions between the nucleons occupying the single-particle energy levels, which are accounted for by the inclusion of a set of Two-Body Matrix Elements (TBME) in the residual interactions. These TBME can be evaluated in three main ways [18]:

- Empirical interactions - extracted from experimental data, such as by investigating binding energies of nuclei at or near shell closure. Single-particle energies can also be obtained by employing a χ^2 -fitting method to experimental binding and excitation energies of excited states [26,27].
- Schematic interactions - obtained from interactions such as Skyrme [28] and Gogny forces [29].
- Realistic interactions - inferred from effective nucleon-nucleon potentials fitted to experimental nucleon-nucleon scattering data [30,31].

It is important to note that any effective residual interaction is only reliable in the model space in which it was derived. In the shell-model region of interest for the experiments

discussed in this thesis (the fp region), there are a number of different residual interactions to choose from. The two most commonly used are the KB3G [25] and GXPF1 [32] interactions.

- KB3G - matrix elements firstly derived from the Hamada-Johnston nucleon-nucleon potential by Kuo and Brown [33–35]. The interaction was later improved by extracting single-particle energies from fits to experimental data [25, 36].
- GXPF1 - matrix elements originally derived from nucleon-nucleon interactions by Hjorth-Jensen *et al.* [37], after which, the single-particle energies and matrix elements were fitted to reproduce experimental data, including 669 energy levels from 87 nuclei between $A = 47$ and $A = 66$.

For the work discussed in this thesis, all shell model calculations were performed using the KB3G interaction [25].

2.3.2 MED Calculations

The four main INC terms considered in the shell-model calculations are the Coulomb multipole term (V_{CM}), the radial monopole term (V_{Cr}), the single-particle monopole term (V_{ll} and V_{ls}) and finally the nuclear Charge Symmetry Breaking term (V_B). In the following sections, each of these terms will be briefly described, where a more in depth discussion on these terms can be found in Refs. [7, 9].

2.3.2.1 The Coulomb Multipole Term

One way in which excited states can be generated in nuclei is from the recoupling of the angular momentum vectors of a pair of nucleons. For example, in the $f_{7/2}$ shell, a pair of protons (or neutrons) can couple to $J = 0, 2, 4, 6$. This recoupling to higher J however, is also predicted, due to the Pauli Exclusion Principle (PEP), to result in an increase in the spatial separation between the pair of nucleons. This effect is illustrated in Fig. 2.6, which shows the calculated probability distribution for the separation of a pair of protons coupled to different angular momenta in the $f_{7/2}$ shell, as calculated in Ref. [38]. In the case of pp couplings therefore, this increase in spatial separation results in a decrease in the Coulomb repulsion between the pair, while in the case of nn couplings, no corresponding change in the Coulomb repulsion will occur. As a result, one would expect to observe a negative MED for states in mirror nuclei generated by pure $f_{7/2}$ recouplings. In order to

account for this effect in the framework of the shell-model calculations, Coulomb Matrix Elements (CME) are added to the effective two-body interaction for protons.

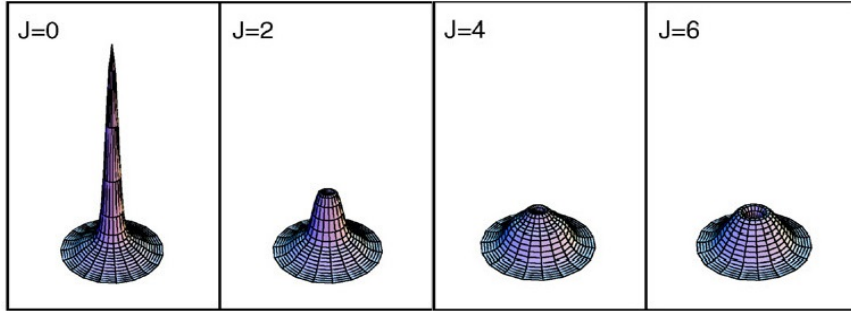


Figure 2.6: Probability distribution for the radial separation between two like-nucleons in the $f_{7/2}$ shell, coupled to different angular momenta. The centre of each plot represents zero separation. Adapted from Ref. [9], calculation performed in Ref. [38].

2.3.2.2 The Radial Monopole Term

The radial term (V_{Cr}) is a monopole term which accounts for the Coulomb energy associated with changes in mean nuclear radius or deformation as a function of spin, in accordance with [39]. Such changes in the mean nuclear radius arise due to changes in the occupation of different orbitals, where orbitals with different angular momentum, l , have different mean radii. In the shell-model calculations performed for nuclei in the $f_{7/2}$ region, changes in the occupancy of the $p_{3/2}$ orbital is tracked, as this orbital is expected to have a larger mean radius. The V_{Cr} term is calculated by [40],

$$V_{Cr} = 2T\alpha_r \left(\frac{m_\pi(g.s.) + m_v(g.s.)}{2} - \frac{m_\pi(J) + m_v(J)}{2} \right) \quad (2.23)$$

where T is the isospin of the state, α_r (200 keV) is a constant deduced from $A = 41$ data [40], and m_π & m_v are the proton and neutron occupancies of the ground (g.s.) and nuclear state of interest (J), respectively.

2.3.2.3 Single-Particle Monopole Term

The single-particle monopole term includes two effects, V_{ll} and V_{ls} , which account for the Coulomb [39] and ElectroMagnetic Spin-Orbit (EMSO) shifts [41] of the single-particle levels, respectively. Here, the V_{ll} effect relates to the Coulomb energy stored in the single-particle orbitals for protons, due to their overlap with the core. This effect strongly

depends upon the orbital angular momentum, l , and is accounted for in the calculations by [42],

$$E_{ll} = \frac{-4.5Z_{cs}^{13/12}[2l(l+1) - n(n+3)]}{A^{1/3}(n + \frac{3}{2})} \quad (2.24)$$

where Z_{cs} is the proton number of the core and n is the principal quantum number.

The second effect, V_{ls} , relates to shifts in the single-particle levels for protons, due to interactions between the spin moment of the nucleon and the Coulomb field of the nucleus [3]. Following the assumption that the Coulomb potential, V_C is given by a uniform sphere with radius, R_C , Nolen and Schiffer [3] derived an expression which gives a rough estimate of the energy shift resulting from the EMSO effect,

$$E_{ls} \simeq (g_s - g_l) \frac{1}{2m_N^2 c^2} \left(-\frac{Ze^2}{R_C^3} \right) \langle \vec{l} \cdot \vec{s} \rangle. \quad (2.25)$$

Here, g_s & g_l represent the free values of the gyromagnetic factors for protons (5.586 & 1) and neutrons (-3.828 & 0), and m_N is the nucleon mass. From the gyromagnetic factors alone, it can be observed that the energy shift will have opposite signs for protons and neutrons. Furthermore, the sign also depends upon the spin-orbit coupling, were $\langle \vec{l} \cdot \vec{s} \rangle$, is given by $l/2$ for $j = l + s$ and $-(l + 1)/2$ for $j = l - s$.

In combination, V_{ll} and V_{ls} effects can result in differences of around 100-200 keV between the single-particles levels for neutrons and protons.

2.3.2.4 Nuclear Charge Symmetry Breaking Term

Despite the electromagnetic interaction being well understood, the inclusion of the three aforementioned INC terms in shell-model calculations was found in a large number of cases to be insufficient to reproduce the experimental MED data in the $f_{7/2}$ region [43]. It was therefore proposed by A. P Zuker *et. al.* that an additional isovector INC term should be included in the MED calculations [7]. In this case, it was found, that the inclusion of an additional isovector term for the $J = 2$ channel, included in the calculation by adding a single repulsive interaction of 100 keV (in addition to the Coulomb interaction) to the two-body matrix elements for $f_{7/2}$ protons coupled to $J = 2$, was necessary to achieve a more reasonable agreement with the experimental data [9, 39]. This value was found empirically by investigating the anomalous MED behaviour for the $A = 42$ and $A = 54$ $T_z = \pm 1$ mirror pairs, where an unexpected sharp rise (or decrease in the case of $A = 54$) in the MED of ~ 100 keV, for $J = 2$ $f_{7/2}$ couplings, was observed [7, 8]. The origin of

this phenomenon however, also commonly referred to as the “ $J = 2$ anomaly”, remains unclear.

In a very recent study by Bentley *et al.* [10], a full set of spin-dependent effective isovector ($pp - nn$) matrix elements were extracted in the $f_{7/2}$ shell, by fitting the shell model to all experimental MED data so far obtained in the shell. This yielded matrix elements of $V_B = -72, +32, +8, -12$ keV for $J = 0, 2, 4, 6$ couplings, respectively, where a clear rise of ~ 100 keV is still evident between $J = 0$ and $J = 2$ couplings, in agreement with previous work. In fig 2.7, a comparison between the experimental and predicted MEDs for four mirror pairs, including (solid line) or excluding (dashed line) the fitted V_B term, are presented. As can be seen, a significant improvement in the theoretical fit to the experimental data is achieved through the inclusion of these effective isovector ($pp - nn$) matrix elements, both in terms of the magnitude and the general trend. The origin of these additional spin-dependent effective isovector ($pp - nn$) matrix elements still remains unclear, though their strong J -dependence, magnitude and sign suggests they most likely arise due to some other electromagnetic contribution that is currently missing in the model [10].

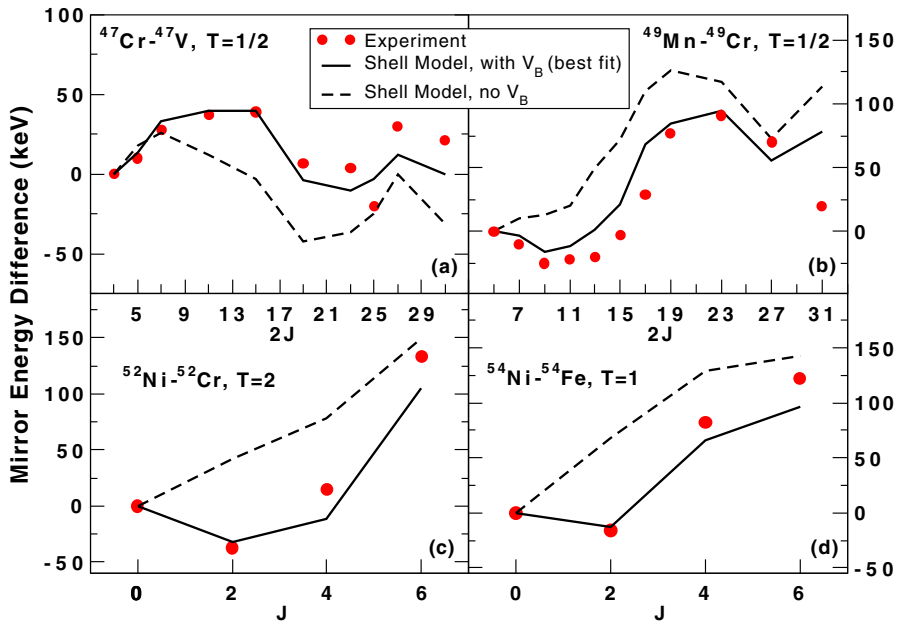


Figure 2.7: Comparison between the experimental and predicted MED for four mirror pairs in the $f_{7/2}$ region. The dashed line shows the predicted MED with no CSB V_B term, while the solid line shows the predicted MED including the best-fit V_B^J term. Taken from Ref. [10].

2.4 Knockout Reaction Calculations

In the first experiment discussed in this thesis (Chapters 3 and 4), excited states in the $T_z = \pm\frac{3}{2}$ mirror nuclei ^{53}Ni and ^{53}Mn , and $T_z = -1$ nuclide ^{52}Co were studied through the use of the highly selective one-nucleon knockout reaction mechanism. In the following sections, a basic description of the knockout reaction process, as well as the knockout calculations performed during this analysis, will be given.

2.4.1 Knockout

Knockout is a direct process in which one or two nucleons are removed from a projectile nucleus, following peripheral, grazing collisions with a target nucleus [44]. In general, experiments utilising this reaction mechanism are performed using high-energy beams, typically >70 MeV/u, produced using projectile fragmentation and in-flight separation techniques. These beams are usually impinged upon light, thin targets, most commonly composed of ^9Be . Due to the high beam energies involved in these experiments, a number of other reaction processes may also occur, depending upon the impact parameter of the reaction. For example, at low impact parameters, fragmentation reactions may occur, where many nucleons are removed from the projectile nucleus. Furthermore, at these low impact parameters, spallation reactions may also occur where the target nucleus is broken up. Providing an experimental set up exists where incoming and outgoing projectile nuclei can be uniquely identified however, other such reaction mechanisms can be excluded from the analysis. For the work discussed in this thesis, proton-rich nuclei were studied through the use of the one-nucleon knockout reaction mechanism.

2.4.2 One-nucleon Knockout Calculations

A number of different reaction processes contribute to one-nucleon knockout. These processes include, “stripping” (inelastic breakup), “diffraction” (elastic breakup) and Coulomb dissociation [44]. In stripping reactions, the removed nucleon is scattered at large angles and the target is left in an excited state, while in diffraction reactions, the removed nucleon is emitted in a forward direction and the target is left in its ground state. Finally, in Coulomb dissociation, the projectile is broken up, due to electromagnetic interactions with the target. Since contributions from Coulomb dissociation are normally very small however, especially for experiments in which a light (i.e. low atomic number,

Z) target has been used, this process is normally neglected [44]. Thus, for the processes considered here, the single-particle cross section, (σ_{sp}), is given by,

$$\sigma_{sp} = \sigma_{sp}^{str} + \sigma_{sp}^{dif} \quad (2.26)$$

where σ_{sp}^{str} and σ_{sp}^{dif} represent the single-particle stripping and diffraction cross sections, respectively. In general, at high beam energies, the single-particle cross section for one-nucleon knockout is dominated by stripping reactions, while at lower energies, 50-60 MeV/nucleon, the contributions from stripping and diffraction are similar [44, 45].

In the work presented here, the single-nucleon removal cross sections were calculated under the ‘‘spectator-core’’ approximation, assuming eikonal reaction dynamics [46, 47]. The two single-particle contributions were computed separately, by integrating over the projectile’s centre of mass impact parameter, \mathbf{b} , using (see Refs. [48, 49], for more details),

$$\sigma_{sp}^{str} = \frac{1}{2J+1} \int d\mathbf{b} \sum_m \langle \Phi_{JM}^c | (1 - |\mathbf{S}_n|^2) |\mathbf{S}_c|^2 | \Phi_{JM}^c \rangle, \quad (2.27)$$

$$\begin{aligned} \sigma_{sp}^{dif} = \frac{1}{2J+1} \int d\mathbf{b} & \left[\sum_M \langle \Phi_{JM}^c | (1 - \mathbf{S}_c \mathbf{S}_n)^2 | \Phi_{JM}^c \rangle \right. \\ & \left. - \sum_{M, M'} |\langle \Phi_{JM'}^c | (1 - \mathbf{S}_c \mathbf{S}_n) | \Phi_{JM}^c \rangle|^2 \right], \end{aligned} \quad (2.28)$$

where Φ_{JM}^c is the wavefunction of the projectile, with total angular momentum, J , and projection, M . \mathbf{S}_c and \mathbf{S}_n are the scattering matrices for the interaction of the core and the valence nucleon, respectively, with the target. In Equation 2.27, $|\mathbf{S}_c|^2$ represents the probability that the core survives the reaction, while $1-|\mathbf{S}_n|^2$ represents the probability that the nucleon is absorbed [44, 48].

In order to compare calculated single-particle cross sections, σ_{sp} , with experimental ones however, they first must be normalised by the spectroscopic factor, C^2S , associated with the change in the subshell occupation, between the initial and final state [44]. By summing over the normalised single-particle cross sections for each subshell considered, the theoretical cross section, σ_{th} , for populating a specific residue state with spin-parity J^π can be found by [48],

$$\sigma_{th}(J^\pi) = \sum_{n\ell j} \left(\frac{A}{A-1} \right)^N C^2S \sigma_{sp}(n\ell j, S_N + E_x) \quad (2.29)$$

where $n\ell j$ denotes the quantum numbers of the nucleon removed. The mass dependent term is the required centre-of-mass correction to the shell-model spectroscopic factors,

with $N = 3$ for the fp -shell [50]. The single-nucleon wave functions were calculated in a Woods-Saxon potential (central plus spin-orbit), with diffuseness $a = 0.6$ fm and spin-orbit strength $V_{so} = 6$ MeV. The radius parameters r_0 of the binding potentials were constrained to reproduce the rms radii and binding energies of SkX interaction [51] Skyrme Hartree-Fock calculations. The depth of the central potential was then adjusted to give states at the appropriate effective separation energy $S_N + E_x$, where S_N is the projectile ground-state to residue ground-state nucleon separation energy and E_x the residue excitation. Densities, from the same Hartree-Fock calculations, were used in calculating the core-target S -matrices in the $t\rho\rho$ approximation (see, e.g., [52]).

In these calculations, spectroscopic factors represent a measurement of the overlap between the initial and final state configurations, while the single-particle cross sections, σ_{sp} , describe the condition in which exactly one nucleon is removed from a specified state. Therefore, spectroscopic factors can be understood to contain all of the nuclear structure information, while the single-particle cross sections, σ_{sp} , can be understood to contain information related the reaction mechanism. For the work discussed in this thesis, spectroscopic factors were calculated using the ANTOINE code [24], using the KB3G [25] interaction in the full fp -shell space.

2.5 Reduced Transition Probabilities and Coulomb Excitation

In the second experiment discussed in this thesis (Chapters 5 and 6), reduced $B(E2 : 2^+_{T=1} \rightarrow 0^+_{T=1})$ transition strengths across the $T = 1$, $A = 46$ triplet of nuclei (^{46}Cr , ^{46}V and ^{46}Ti) were studied through lifetime and Coulex cross section measurements, utilising intermediate-energy Coulomb excitation. In the following sections, a brief description of the Coulomb excitation reaction mechanism, as well as the relationship between the Coulex cross section/partial γ -ray lifetime and the reduced $B(E2)$ transition strength, will be given.

2.5.1 Coulomb Excitation

Coulomb excitation is an inelastic process in which a nucleus is excited through the electromagnetic interaction with another nucleus, via the exchange of virtual photons [53,54]. In general, experiments utilising this reaction mechanism are usually performed in inverse

kinematics, using either low-energy stable/near-stable beams (5 MeV/u), or intermediate-energy radioactive beams (30-300 MeV/u) [54, 55]. Due to the Coulomb interactions strong dependence on Z , these beams are usually impinged upon a target with a high atomic number, such as gold or lead.

The main advantage of using low-energy Coulomb excitation is that it ensures that nuclear processes do not contribute to the excitation cross section of the states of interest, due to the beam energies being below the Coulomb barrier. Furthermore, at these low beam energies, the excitation probability between the projectile and target is also greater, which allows for multi-step excitations to occur, therefore facilitating the study of high-lying states in collective bands. However, in order to correctly measure the Coulex cross section of low-lying states here, any feeding between states, particularly between those which form collective bands, must be accounted for. The main disadvantage of low-energy Coulomb excitation is the experimental limitation on the range of nuclei which can be studied using this approach, i.e. nuclei which are either stable or which have relatively long half-lives. In contrast, the use of intermediate-energy Coulomb excitation, using relativistic beams of exotic nuclei produced utilising projectile fragmentation and in-flight separation techniques, allows for Coulomb excitation in much more exotic nuclei to be investigated. Due to the short interaction time between the target and projectile nucleus in intermediate-energy Coulomb excitation, multi-step excitations are highly hindered, which therefore results in a much simpler spectral analysis for low-lying states. The two main disadvantages of intermediate-energy Coulomb excitation however, are the reduced Coulex cross sections, due to the Coulomb interactions $\sim 1/E$ dependence (e.g. see Fig. 2.8), and the increase in the number of nuclear contributions, due to the beam energy being much larger than the Coulomb barrier. These two issues can be addressed however, through the use of much thicker targets (i.e. 100-1000 times thicker than in low-energy Coulex [55]) to increase the Coulex cross section, and by only considering reactions with a very forward (“safe”) scattering angle, such that the impact parameter is large enough for nuclear contributions to be considered negligible. Such “safe” scattering angles can be deduced by considering Cline’s “safe Coulex” criterion [56], which states that the distance between nuclear surfaces must be greater than 5 fm for the nuclear interaction to be considered negligible (i.e. $<0.1\%$). Under this criterion, the minimum impact parameter, d_{min} , is given by,

$$d_{min} = 1.25 \cdot (A_p^{1/3} + A_t^{1/3}) + 5.0 [fm] \quad (2.30)$$

and the “safe” (center of mass) scattering angle, θ_{CoM} , by,

$$\theta_{CoM} = 2 \cdot \sin^{-1} \left(\frac{0.72}{E_{lab}} \cdot \frac{Z_p Z_t}{d_{min}} \cdot \frac{(A_p + A_t)}{A_t} - 1 \right) \quad (2.31)$$

where, A_p/Z_p and A_t/Z_t denote the atomic mass/atomic number of the projectile and target, respectively, and E_{lab} denotes the lab frame energy of the projectile.

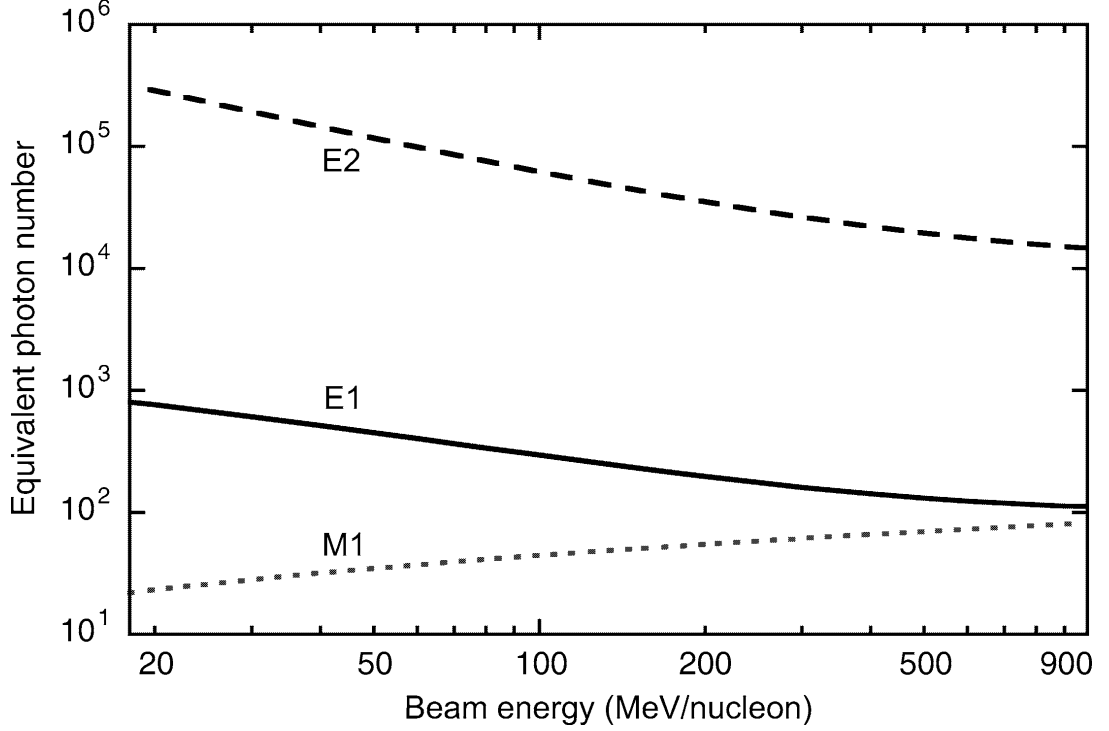


Figure 2.8: Plot of equivalent photon number (proportional to cross section) against beam energy, for the Coulomb excitation of the 2^+ state in ^{40}S , using a gold target and assuming a minimum impact parameter of 16 fm. Taken from Ref. [54].

At intermediate energies, the Coulex cross section can be calculated by taking a semi-classical approach, as discussed in detail in Refs. [54,57], where this cross section is directly related to both the electromagnetic transition matrix element $B(\sigma L)$ and the minimum impact parameter, d_{min} . The approximate Coulex cross section for an electric quadrupole (E2) excitation is given by [54]

$$\sigma_{E2} \approx \left(\frac{Ze^2}{\hbar c} \right)^2 \frac{B(E2, 0 \rightarrow 2)}{e^2 d_{min}^2}. \quad (2.32)$$

More accurate measurements of electromagnetic transition matrix elements can be achieved however, through the use of semi-classical Coulomb excitation codes, such as GOSIA [58] or DWEIKO [59].

2.5.2 Reduced Transition Strengths

In nuclear structure physics, reduced transition strengths represent an important measurement, as they allow for direct information on the structure of states, between which a γ -ray transition occurs, to be obtained. For example, the study of transition strengths to the first 2^+ state across isotopic chains allows for important information on shell structure to be obtained [60–62].

Starting from Fermi's Golden rule, a general expression for the transition probability, $\lambda(\sigma L)$, of an electromagnetic transition of character σ (electric or magnetic) and multipolarity, L , can be derived (see Ref. [63] for more details),

$$\lambda(\sigma L) = \frac{2(L+1)}{\hbar\epsilon_0 L [(2L+1)!!]^2} \left(\frac{E_\gamma}{\hbar c} \right)^{2L+1} B(\sigma L). \quad (2.33)$$

In this expression, \hbar is the reduced Planck's constant (1.054×10^{-34} Js), ϵ_0 is the vacuum permittivity (8.854×10^{-12} Fm $^{-1}$) and c is the speed of light. Since the transition probability is also given by the inverse of the partial lifetime of a transition, τ_γ ,

$$\lambda = \frac{1}{\tau_\gamma} \quad (2.34)$$

an expression can be deduced relating the reduced B(E2) transition strength, of a transition between two states with initial and final angular momenta J_i and J_f , to the energy, E_γ , and partial lifetime of the transition,

$$B(E2, J_i \rightarrow J_f) = \frac{1}{1.22 \times 10^9 E_\gamma^5 \times \tau_\gamma}. \quad (2.35)$$

This therefore allows for reduced B(E2) transition strengths to be measured directly, by performing experiments in which both the half-life and energy of a γ -ray transition are measured. Furthermore, these transition strengths are also directly related to the transition matrix elements, m_{if} , by the following expression [63]

$$m_{if}(\sigma L) = [(2J_i + 1) \times B(\sigma L, J_i \rightarrow J_f)]^{1/2}, \quad (2.36)$$

where matrix elements represent a measurement of the overlap between the initial and final wavefunctions of two states, connected by a transition σL .

Chapter 3

Investigation of One-Nucleon Knockout Reactions

The study of mirror nuclei along the $N \approx Z$ line has been of increasing interest among nuclear physicists in recent times, particularly in the $f_{\frac{7}{2}}$ and upper fp shell regions of the nuclear chart. The advancements in radioactive beam technology and facilities has meant that previously inaccessible nuclei can now be populated with the intensities required to perform in-beam γ -ray spectroscopy experiments. This has also presented the opportunity to perform MED studies for previously unstudied nuclei, at large differences in isospin, which lie far from the line of stability. For lighter nuclei, below the $f_{\frac{7}{2}}$ region ($N = Z = 20$), the line of stability follows the $N \approx Z$ line, while for heavier nuclei, this line gradually shifts towards nuclei with $N > Z$. Due to this, the proton-rich mirrors of the $A \approx 50$ nuclei studied in this thesis lie very close to the proton drip line and decay predominantly via β^+ decay, with typical half-lives of the order of 20 to 300 ms.

The present investigation looks at the $A = 53$, $T = \pm\frac{3}{2}$ mirror nuclei ^{53}Ni and ^{53}Mn , populated via mirrored (i.e. isospin-symmetric) one-nucleon knockout reactions from ^{54}Ni and ^{54}Fe , respectively, and the $A = 52$, $T = -1$ nuclide ^{52}Co populated via one-neutron knockout from ^{53}Co . For the two proton-rich nuclei investigated here, ^{53}Ni and ^{52}Co , very few excited states have been previously observed [64, 65]. This therefore presented the opportunity to both greatly expand upon the known energy-level scheme of these nuclei as well as to extend upon previous MED studies in $f_{\frac{7}{2}}$ region. Furthermore, the study of these nuclei, in addition to ^{53}Mn , through the use of the highly selective one-nucleon knockout reaction mechanism, also allowed for detailed cross section calculations to be performed which could then be compared with the observed population of states in these

nuclei.

The presence of high-spin isomeric states in the ion beams used during the experiment also presented the opportunity to study, for the first time, one-nucleon knockout from isomeric states. Due to the high spin of these isomeric states, compared to that of the ground states of the parent nuclei, this allowed for the population of much higher spin states in the daughter nuclei. Furthermore, due to the well-known spin-parity and energy of these isomeric states, this also presented the opportunity to perform detailed cross section calculation for one-nucleon knockout from these isomeric states, whereby the results of these calculations could be compared with the observed population of high-spin states in the daughter nuclei, particularly in the case of ^{52}Co .

The following Chapter is divided into several sections. In the first section (Section 5.2), a number of experimental considerations are presented, which is then followed by an outline of the experiment performed, in Section 3.2. Following this, two sections (Sections 3.3 and 3.4) are presented which give details on the calibration procedures performed during the analysis, in order to be able to both select the reaction channels of interest and produce clean γ -ray spectra.

3.1 Experimental Considerations

The primary objective of the experiment was to populate the nuclei of interest, ^{53}Ni , ^{53}Mn and ^{52}Co , with the required levels of intensity to perform γ -ray spectroscopy. Since the aim of the experiment was to study these nuclei through the use of one-nucleon knockout reactions, it meant that high-energy ion beams of ^{54}Ni , ^{54}Fe and ^{53}Co needed to be produced, from which these reactions could occur. While ^{54}Fe is stable, ^{54}Ni and ^{53}Co are both unstable, with half-lives of 104(7) ms and 240(9) ms [64, 66], respectively, and therefore the production of these Radioactive Ion Beams (RIBs) required the use of a radioactive beam facility which could both produce and deliver these RIBs to the experimental area in a very short time.

In general, RIBs can be produced using one of two methods, Isotope Separation On-Line (ISOL) or projectile fragmentation. The first method involves impinging highly accelerated light ion beams, with typical beam energies of ~ 0.1 -1 GeV, upon thick targets, with a high atomic mass, in order to produce the reaction products of interest. These reaction products are then ionised and separated from any unwanted contaminants, before then being re-accelerated to a desired beam energy and delivered to the experimental area.

The second method, projectile fragmentation, generally involves the acceleration of heavier ion beams to energies of the order of 0.1-1 GeV/nucleon, which then impinge upon a thick target, typically composed of ^9Be . The resulting fragments are then separated in-flight, primarily through the use of electric and magnetic fields, before then being transferred to the experimental area. While the ISOL technique offers the production of a high quality beam with a high purity, a small beam spot and a more selective beam energy, the process also has a number of limitations, including the difficulty in extracting certain isotopes from the target, the slow beam production time (typically 100 ms or greater) and the very low beam intensity for more exotic nuclides. Projectile fragmentation however, while offering a poorer quality beam in terms of its purity, beam spot size and momentum spread, does allow for the fast production and delivery of ion beams to the experimental area, typically in less than 500 ns, as well as the production of high-intensity beams for more exotic nuclides. Furthermore, due to the nature of the in-flight fragment separation technique utilised in projectile fragmentation, it also leads to the production of ion cocktail beams which contain the ion beam of interest as well as a number of different isotones (same N , different Z). Therefore, the projectile fragmentation technique was chosen for the production of the the ion beams used in this experiment, due to the high beam intensities required, the fast beam production/delivery times required (due to the short-lived RIBs used) and finally due to availability of the $N = 26$ isotones, ^{54}Ni and ^{53}Co , in the same ion cocktail beam.

At RIB facilities, primary beams can only be produced from the acceleration of stable nuclei extracted from ion sources. The closest stable nuclide to the ion beams of interest, which could also be fragmented to produce these ion beams, was ^{58}Ni , which was therefore chosen as the primary beam for the experiment. In order to maximise both the production and transmission of the beam fragments of interest, a thick production target of 802 mg/cm^2 ^9Be was chosen as well as a high primary beam energy of 160 MeV/nucleon.

A commonly used target material in experiments investigating knockout reactions is ^9Be , due to its high purity, low charge, low mass and low γ -ray background. In addition, the target used in such experiments must also be sufficiently thick to ensure a good reaction rate, while the beam energy must also be sufficiently high to ensure that the beam particles are still transmitted and not stopped in the target, since the outgoing particles need to be identified downstream of the target. An additional consideration which must also be made when choosing the reaction target thickness is the background radiation resulting

from Bremsstrahlung, which arises due to the slowing of charged beam particles in the target, as this will be greater for thicker targets. Therefore, a $188\text{mg}/\text{cm}^2$ ^9Be reaction target was chosen for the study of knockout reaction in this experiment, where the high beam energies of ~ 87 MeV/nucleon at the reaction target position were sufficiently high to ensure that particles were not stopped in the reaction target. This gave predicted knockout cross sections (from the ground state of the parent nuclei) of $\sim 80\text{mb}$, $\sim 69\text{mb}$ and $\sim 41\text{mb}$ for the $^{53}\text{Mn}(^{54}\text{Fe}-1\text{p})$, $^{53}\text{Ni}(^{54}\text{Ni}-1\text{n})$ and $^{52}\text{Co}(^{53}\text{Co}-1\text{n})$ reactions [67], respectively.

The final experimental requirements included the need for a γ -ray detector system with a good energy resolution and ideally a high efficiency, in order to perform γ -ray spectroscopy for the exotic proton-rich nuclei studied in the experiment. Furthermore, a good system of particle tracking, energy loss and timing detectors was also required to ensure the unique identification of incoming and outgoing particles in order to study only the reaction channels of interest, free from contamination from other reaction channels. All of these requirements were met by the experimental set up discussed in the following sections.

3.2 Experimental set up

In order to extend upon previous MED studies in the $f_{7/2}$ region, projectile fragmentation experiments were performed at the National Superconducting Cyclotron Laboratory (NSCL) at Michigan State University (MSU). Proton-rich nuclei in the $f_{7/2}$ region, in addition to their neutron-rich mirror partners, were populated via knockout and fragmentation reactions from either proton-rich (^{54}Ni , ^{53}Co , etc.) or neutron-rich (^{54}Fe , ^{53}Mn , etc.) secondary cocktail beams (Section 3.2.2), respectively. The resulting reaction products were identified with the S800 spectrograph (Section 3.2.3) and γ rays were detected using SeGA (Section 3.2.4).

3.2.1 Primary Beam Production

Primary beams for experiments performed at NSCL are provided by the Coupled Cyclotron Facility (CCF) [69], as shown in Fig. 3.1, which consists of an Electron Cyclotron Resonance (ECR) ion source [SuSI (Superconducting Source for Ions) [70]], a K500 cyclotron and a K1200 cyclotron. The first stage of primary beam production begins with the ECR ion source, which provides stable beams of positive ions and injects them into

the central region of the K500 cyclotron, after which they are accelerated up to energies of around 8-12 MeV/u. Following this, the ions are extracted from the K500 cyclotron and injected radially into the K1200 cyclotron, where they are stripped of their electrons by a Carbon foil and further accelerated up to energies generally in the region of 100-160 MeV/u. The use of this facility allows for the production of a wide range of primary beams, from Oxygen to Uranium, which facilitates the study of a wide range of nuclei, right across the nuclear chart.

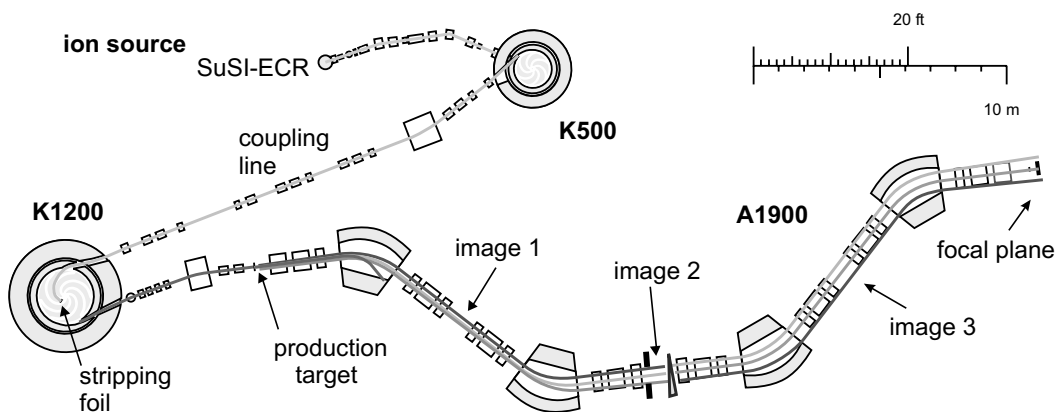


Figure 3.1: A schematic of the ion source, K500 and K1200 coupled cyclotrons and the A1900 fragment separator, taken from Ref. [71].

3.2.2 Secondary Beam Production and the A1900 Separator

The secondary beams of interest, ^{54}Ni ($T_z = -1$) and ^{54}Fe ($T_z = +1$), in addition to ^{53}Co ($T_z = -\frac{1}{2}$), an isotonic contaminant in the proton-rich ^{54}Ni secondary beam, were produced via the fragmentation of a ^{58}Ni secondary beam provided by the Coupled Cyclotron Facility (CCF). These secondary beams, which also represent a mirror pair ($T_z = \pm 1$), were chosen in order to facilitate the study of mirror nuclei (at large differences in isospin) through direct, isospin-symmetric, one-nucleon knockout reactions. In particular, for the analysis discussed in this thesis, the study of excited states in the $T_z = \pm\frac{3}{2}$ mirror nuclei ^{53}Ni and ^{53}Mn , populated via one-neutron and one-proton knockout, respectively, from the ^{54}Ni and ^{54}Fe secondary beams.

To produce the secondary beams of interest, a 160 MeV/nucleon ^{58}Ni primary beam impinged upon a 802 mg/cm^2 ^9Be production target, positioned at the target position of the A1900 separator, see Fig. 3.1. This resulted in the production of many beam-like

fragments with $A < 58$, produced either via knockout or fragmentation reactions, which are dominant at these beam energies. These fragments ($A < 58$), in addition to any unreacted ^{58}Ni primary beam, were then separated using the A1900 [71, 72], a high acceptance projectile fragment separator, located immediately after the production target. This separation was achieved, in the A1900, through the use of four 45° bend superconducting dipole magnets (each with a maximum magnetic rigidity of 6 Tm), and 24 large diameter superconducting quadrupole magnets, whereby 16 of these quadrupole magnets also had a coaxial set of superconducting hexapole and octupole coils, used for aberration corrections. In general, the quadrupole magnets are used to focus the beam while the 45° bend dipole magnets are used to provide an A/Q dispersion of the beam. Therefore, the magnetic rigidity, $B\rho$, of these dipole magnets can be set such that only the nuclei of interest (or those with a similar mass-to-charge ratio) make it through the separator, in accordance with Equation 3.1, which describes the motion of a charged particle in the presence of a magnetic field, at relativistic velocities.

$$B\rho = \frac{Mc}{Ze}\beta\gamma \approx \frac{Am_u c}{Ze}\beta\gamma \quad (3.1)$$

Here, B is the strength of the magnetic field, ρ is the bending radius of the dipole magnet (or alternatively the bending radius of the particle trajectory), $M (\approx Am_u)$ and Z are the mass and charge of the particle, e is the electronic charge, and $\beta = v/c$ and $\gamma = (1/\beta^2)^{-\frac{1}{2}}$ are the relativistic factors.

The initial filtering of the beam occurs along a dispersive beam line, which consists of a pair of 45° bend superconducting dipole magnets and a variable aperture, which are used in conjunction to select a beam with a single magnetic rigidity, $B\rho$. This is then followed by a set of variable slits, located at image 2 (see Fig. 3.1), which can be adjusted in order to restrict both the nuclei that are accepted and the momentum spread of the beam. Following this, isotopic selection is achieved through the use of an achromatic Al wedge which acts to degrade the beam from a single magnetic rigidity, $B\rho$, thus leaving the exiting ions with different momenta, depending upon their atomic number, Z . Furthermore, the use of this wedge as well as the A1900 in achromatic mode, as opposed to monochromatic mode (selection of ions by energy), also results in an increase in the positional separation between the different beam fragments, allowing for an improvement in the selectivity of the outgoing beam. Further isotopic selection of the secondary beam is then finally achieved

by passing the beam through a second dispersive line consisting of a further two 45° dipole magnets and a variable aperture, after which the final secondary cocktail beam of interest is obtained at the A1900 focal point. This secondary cocktail beam is then transferred through a transfer hall and along an analysis line before then being focused upon a reaction target, located at the target position of the S800 spectrograph (see Section 3.2.3).

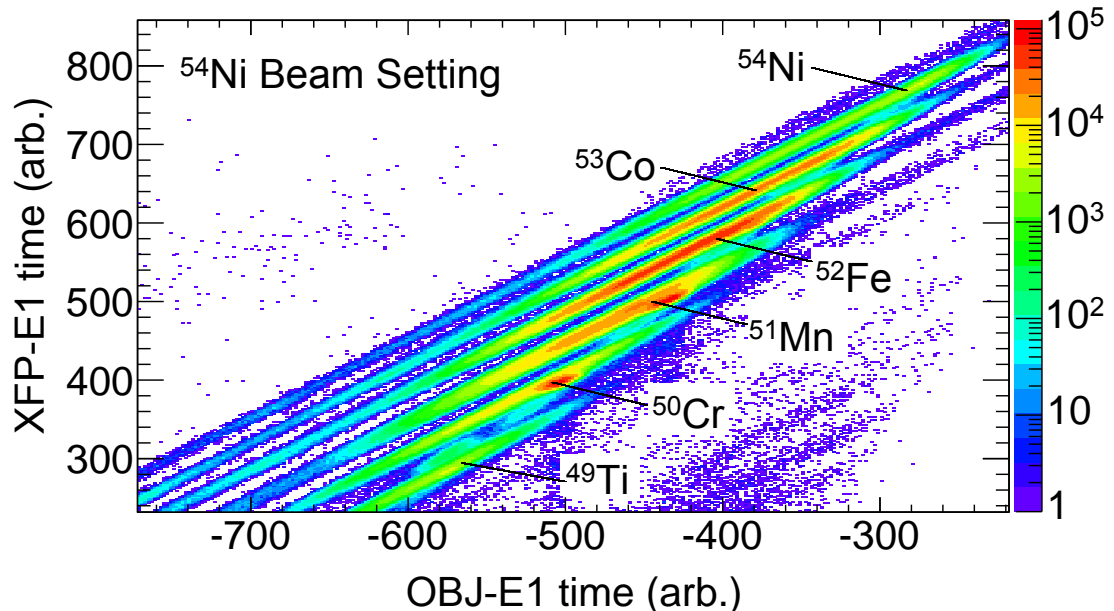


Figure 3.2: Particle identification plot of the secondary beam constituents observed during the A1900 setting optimised for the proton-rich ^{54}Ni secondary beam. The axes, xfp-E1 time and obj-E1 time represent the particle time of flight between the XFP and OBJ scintillators, and the E1 scintillator, respectively.

In the experiment performed for this analysis, two A1900 settings were chosen (as guided by simulations using LISE [73]), where magnetic rigidity ($B\rho$) settings, slit widths and the wedge/degrader thickness were optimised in order to obtain the highest achievable rates of ^{54}Fe and ^{54}Ni (in addition to their $N = 28$ and $N = 26$ isotones, respectively), without exceeding the rates which could be handled by the various detector systems of the A1900 and S800. Following this, the constituents of the secondary cocktail beams were then uniquely identified, on an event-by-event basis, from their Time-of-Flight (ToF) between two plastic scintillators, the first of which was positioned at the extended focal plane of the A1900 (the XFP scintillator), and the second of which was positioned at the object position of the S800 (the OBJ scintillator), approximately 30 m further downstream. This unique identification of secondary beam constituents (as shown for the ^{54}Ni A1900

beam setting in Fig. 3.2), could then be used to select the desired incoming beam at the reaction target, through the use of software gates. The individual constituents of both the ^{54}Ni and ^{54}Fe A1900 settings are detailed in Table 3.1, whereby the measured secondary beam rate of each constituent is also shown.

Table 3.1: The main constituents of the ^{54}Ni and ^{54}Fe A1900 settings delivered to the reaction target, measured using the ToF between the XFP and OBJ scintillators. Secondary beam rates for the individual beam constituents are also shown.

Beam Constituent	Fraction of Total Beam Transmitted (%)	Rate
^{54}Ni A1900 Setting		
^{54}Ni	7.34(8)	~ 5 kHz
^{53}Co	30.99(20)	~ 21 kHz
^{52}Fe	36.90(22)	~ 25 kHz
^{51}Mn	21.10(15)	~ 14.5 kHz
^{50}Cr	2.91(5)	~ 2 kHz
^{49}V	0.75(4)	~ 0.5 kHz
^{54}Fe A1900 Setting		
^{55}Co	0.35(4)	~ 250 Hz
^{54}Fe	71.86(56)	~ 45.5 kHz
^{53}Mn	27.09(36)	~ 17 kHz
^{52}Cr	0.71(6)	~ 0.5 kHz

3.2.3 The S800 Analysis Line and Spectrograph

The S800 is a high-resolution, large acceptance magnetic spectrometer designed to identify and analyse reaction products on an event-by-event basis in fast, radioactive beam experiments [74, 75]. The S800 system, as shown in Fig 3.3, is comprised of two main sections, an analysis line, used for the identification of incoming secondary beam particles, and a spectrograph, used for the identification of outgoing particles after the reaction target position.

In the experiment performed for this analysis, $\sim 87\text{MeV/nucleon}$ secondary cocktail

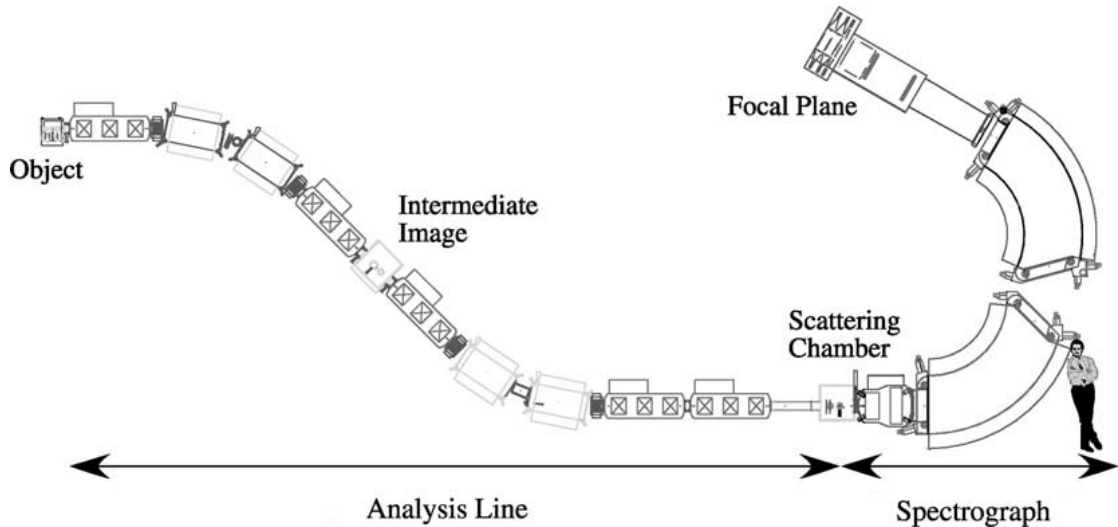


Figure 3.3: Schematic of the S800 analysis line and Spectrograph, taken from [74]

beams of either ^{54}Fe or ^{54}Ni (in addition to their respective $N=28$ and $N=26$ isotones) were transferred along the S800 analysis line and impinged upon a $188\text{mg}/\text{cm}^2$ ^9Be reaction target, placed at the target position of the S800 spectrograph, from which knockout and fragmentation reactions occurred. In-flight γ decays from excited states populated in the nuclei of interest, ^{53}Ni ($T_z = -\frac{3}{2}$), ^{53}Mn ($T_z = +\frac{3}{2}$) and ^{52}Co ($T_z = -1$), through one-nucleon knockout reactions, were then detected using SeGA (see Section 3.2.4). Outgoing recoils were then uniquely identified on an event-by-event basis by measuring their energy loss in the S800 ionisation chamber and their ToF through the S800 spectrograph. In the following sections, a summary will be given of the operation of the S800 and its various detector systems.

3.2.3.1 The S800 Analysis Line

The S800 analysis line is comprised of four superconducting magnetic dipoles and five superconducting magnetic quadrupole triplets which are used in conjunction to focus and guide the secondary beam particles produced in the A1900 (Section 3.2.2) to the reaction target position of the S800, see Fig. 3.3. Depending upon the purpose of the experiment, the S800 analysis line can be operated in two different main modes, i.e. “dispersion-matched mode”, where the highest possible position resolution is required at the focal plane, for example in momentum distribution measurements, or “focus mode”, where the highest possible position resolution is required at the target position, for example in γ -ray

spectroscopy [74]. In the experiment performed for this analysis, the S800 analysis line was operated in “focus mode”, whereby the beam was focused into a spot on the reaction target.

3.2.3.2 The S800 Spectrograph

The S800 spectrograph consists of a large magnetic quadrupole doublet, two 75° bend superconducting dipole magnets (with a maximum magnetic rigidity, $B\rho$, of 4 Tm) and a selection of tracking, energy loss and timing detectors located at the S800 focal plane, as shown in Fig. 3.3. The quadrupole doublet, located just after the target chamber, serves the purpose of focusing the outgoing ions after the reaction target, firstly in the non-dispersive (y) plane and then in the dispersive (x) plane, in order to maximise the acceptance of the spectrograph. Furthermore, at the end of the second quadrupole, a high-order sextuple magnet is also used for additional aberration corrections, which reduces the broadening of the beam at the focal plane. Following this, two 75° bend superconducting dipole magnets are used to both deliver and disperse the reaction products at the focal plane, filtering out any unwanted unreacted secondary beam through the use of a beam blocker. This is particularly necessary when the secondary beam has a similar magnetic rigidity ($B\rho$) to that of the reaction products of interest, and when the rate at the focal plane is too high for the focal plane detectors. The focal plane detectors of the S800, as shown in Fig 3.4, consist of two position sensitive Cathode-Readout-Drift-Counters (CRDCs), followed by a multi-segmented ionisation chamber and a stack of three plastic scintillators.

3.2.3.3 Cathode Readout Drift Counters

Cathode-Readout-Drift-Counters (CRDC) are position sensitive detectors, used to measure the XY-positions of charged particles which pass through them. At the beginning of the S800 focal plane, two position sensitive CRDC detectors are used for this purpose, whereby each detector has an active area of 59 cm (in the dispersive plane) \times 30 cm (in the non-dispersive plane), and an active thicknesses of 1.5 cm. The volume of each CRDC is filled with a gas mixture of 80% CF_4 (freon-14) and 20% C_4H_{10} (isobutane) at a typical pressure of around 140 Torr, where this gas has a number of advantages, including, low aging characteristics, a high drift velocity and a low avalanche spread due to photon mediation [75]. The detectors function by incident charged beam particles ionising the

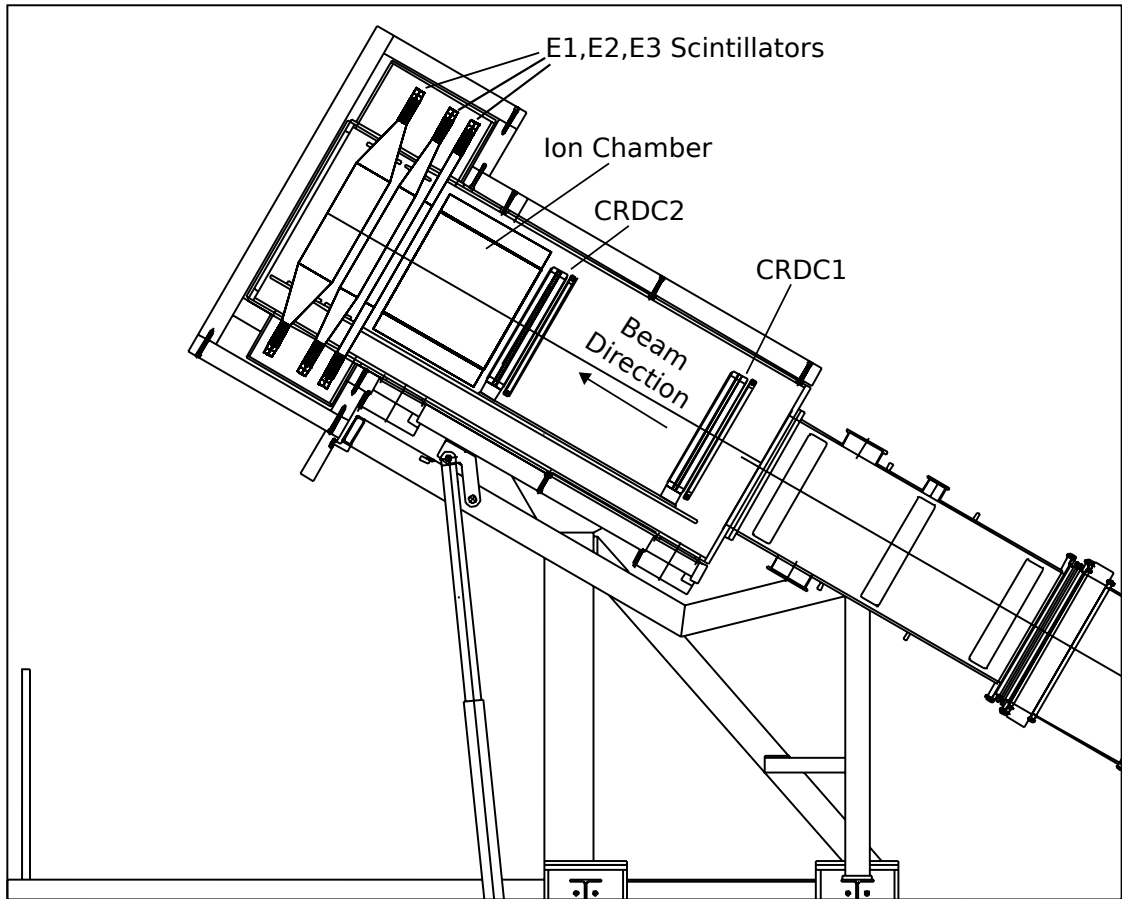


Figure 3.4: Schematic of the S800 focal plane detectors, taken from [75]

gas mixture, resulting in the production of electrons, which, in the presence of an applied uniform electric field, drift uniformly towards an anode wire. This additionally leads to a Townsend avalanche effect, whereby the moving energetic electrons act to ionise more gas particles, multiplying the number of drifting electrons and thus resulting in a larger current. Located both in front and behind the anode wire are 224 cathode pads, each with a pitch of 2.54 mm, whereby the collection of charge on the anode wire induces a positive charge on the cathode pads. In order to determine the position in the dispersive plane (x), a Gaussian function can be fitted to the charge distribution on the cathode pads, or alternatively the centre of gravity of the induced charge distribution can be determined. However, in order to determine the position in the non-dispersive plane (y), the drift time of the electrons to the anode wire, relative to a timing signal from the E1 scintillator, is used. Since the typical drift times of these electrons to the anode wire are of the order of 0 to 20 μs , this limits the CRDC detectors to a maximum rate of around 5 kHz, which can be processed effectively. Through the performance of a commissioning experiment involv-

ing the use of a 80 MeV/u ^{22}Ne beam passed through the entire S800 spectrometer, each CRDC detector was found to have a position resolution better than 0.51 mm FWHM [75].

Through the use of XY-position information provided by the two CRDC detectors (separated by a distance, d , of ~ 1073 mm), particle trajectories through the focal plane can be reconstructed, which also allows for the determination of incident angles. For example, the dispersive angle at the focal plane (a_{fp}) can be calculated by,

$$a_{fp} = \tan^{-1}\left(\frac{x_2 - x_1}{d}\right) \quad (3.2)$$

where x_1 and x_2 are the dispersive (x) positions measured in CRDC1 and CRDC2, respectively. The determination of particle positions and angles at the focal plane is particularly important because particles which take different paths, take different times to traverse the spectrograph. If corrections to the ToF are not included (see Section 5.5.3), the ability to clearly resolve between nuclei with a different mass-to-charge ratio (A/Q) is reduced.

3.2.3.4 Ionisation Chamber

The S800 ionisation chamber is located downstream of the two CRDC detectors and is used for energy loss (dE) measurements of particles at the focal plane. The ion chamber used is a standard Frisch-gridded ion chamber which is 41 cm deep and divided into sixteen 1 inch anode segments which run perpendicular to the direction of the beam particles. The gas fill of the chamber is a mixture of 90% Ar and 10% CH_4 (methane), more commonly known as P10, at a typical pressure of around 300 Torr. Incident charged beam particles which traverse the ion chamber lose energy by ionising gas molecules along their trajectory, whereby the resulting positive ions and electrons drift towards their nearest anode-cathode pair. The resulting signals in the sixteen anode segments are then summed to provide the total energy loss (dE) signal for a given particle event. The advantage of summing the energy loss signals in this way, from sixteen smaller anode segments (as apposed to using just one large anode), is that the electronic noise is proportional to the capacitance, which, for the smaller segments, is much lower. Furthermore, since the noise from the individual anode segments are not correlated, they will sum in quadrature, which results in a lower total noise for the ion chamber.

Since the energy loss of a charged particle travelling through matter is proportional to Z^2 , in accordance with the Bethe-Bloch formula (Equation 3.3), the atomic number, Z , of

a charged particle can be determined. The use of the S800 ionisation chamber allows for elements up to $Z = 50$ to be uniquely identified.

$$-\left\langle \frac{dE}{dx} \right\rangle = \frac{4\pi n Z^2}{m_e c^2 \beta^2} \left(\frac{e^2}{4\pi \epsilon_o} \right)^2 \left[\ln \left(\frac{2m_e c^2 \beta^2}{I(1 - \beta^2)} \right) - \beta^2 \right] \quad (3.3)$$

Here, n is the electron density of the material, m_e and e are electron mass and charge, respectively, c , is the speed of light in a vacuum, ϵ_o , is the vacuum permittivity, $\beta = \frac{v}{c}$ is the velocity of the particle, and I is the average excitation potential of the material. Similarly to the ToF correction discussed previously, a similar correction also needs to be applied for the energy loss measurements in the ion chamber, since particles taking different paths through the ion chamber deposit different amounts of energy. Thus, in order to obtain the best possible Z resolution, energy loss corrections need to be applied (see Section 5.5.1).

3.2.3.5 Scintillation Detectors

Immediately following the ion chamber is a large stack of three plastic scintillators (E1, E2 and E3) each with a thickness of 5, 10 and 20 cm, respectively, and each with an area covering the active area of the CRDC detectors. The scintillator detectors function by charged beam particles traversing the detector material and generating light (through scintillation), which is then collected by PhotoMultiplier Tubes (PMTs), connected to both the top and bottom of each plastic scintillator, and converted into an electrical signal. The timing signal of each scintillator is then calculated by the average time signal from each PMT. Although the scintillator detectors are primarily used for timing information, since all charged particles are additionally stopped in the scintillator material, energy loss and total energy loss measurements can also be performed.

The E1 scintillator is used to define a valid trigger in the S800. In addition, all scintillator time signals, as well as the drift times in the two CRDCs, are measured relative to the timing signal from the E1 scintillator. In order to uniquely identify reaction products by their mass-to-charge (A/Q) ratios at the focal plane, on an event-by-event basis, the ToF between the OBJ scintillator, located at the object point of the S800, and the E1 scintillator, located at the end of the focal plane, is used. The plastic scintillators can

handle rates up to 1 MHz, however at higher rates, the timing resolutions worsens. Furthermore, the time resolution can also be worsened due to the different path lengths of the nuclei traversing the focal plane, though this effect can be corrected for through the use of position and angle information provided by the CRDC detectors (see Section 5.5.3).

3.2.3.6 Aberration Correction

The large acceptance of the S800 spectrograph makes it more susceptible to aberrations in the magnetic field, which can greatly effect the resolution of the spectrometer. Usually, in smaller acceptance spectrometers, aberrations and higher-order field effects are corrected by the use of higher-order magnets. However, these corrections become considerably more complex with a much larger acceptance. Therefore, in order to achieve both a high acceptance and a high resolution, particle trajectory reconstruction techniques are used, where precise magnetic field maps are recorded during the experiment and used with the ion optical code COSY Infinity [76] to generate an inverse map for each recoil [77]. This map relates the dispersive and non-dispersive positions (x_{fp}, y_{fp}) and angles (a_{fp}, b_{fp}) of a particle at the focal plane to the relative energy spread ($d_{ta} = \delta E/E$), dispersive and non-dispersive angles (a_{ta}, b_{ta}) and non-dispersive position (y_{ta}) of the particle at the target position, as shown in Equation 3.4,

$$\begin{pmatrix} a_{ta} \\ y_{ta} \\ b_{ta} \\ d_{ta} \end{pmatrix} = S^{-1} \begin{pmatrix} x_{fp} \\ a_{fp} \\ y_{fp} \\ b_{fp} \end{pmatrix}, \quad (3.4)$$

where S^{-1} denotes the inverse map. In order to reduce the number of variables introduced when reconstructing the particle trajectories, the dispersive (x) position at the target is assumed to be zero, whereby the uncertainty in this variable is folded into the energy resolution of the spectrometer. Since the particle information determined at the target position, through the use of these inverse maps (for each nuclide), also depends upon the position and angle measurements at the S800 focal plane, these measurements must be accurately calibrated (see Section 3.3).

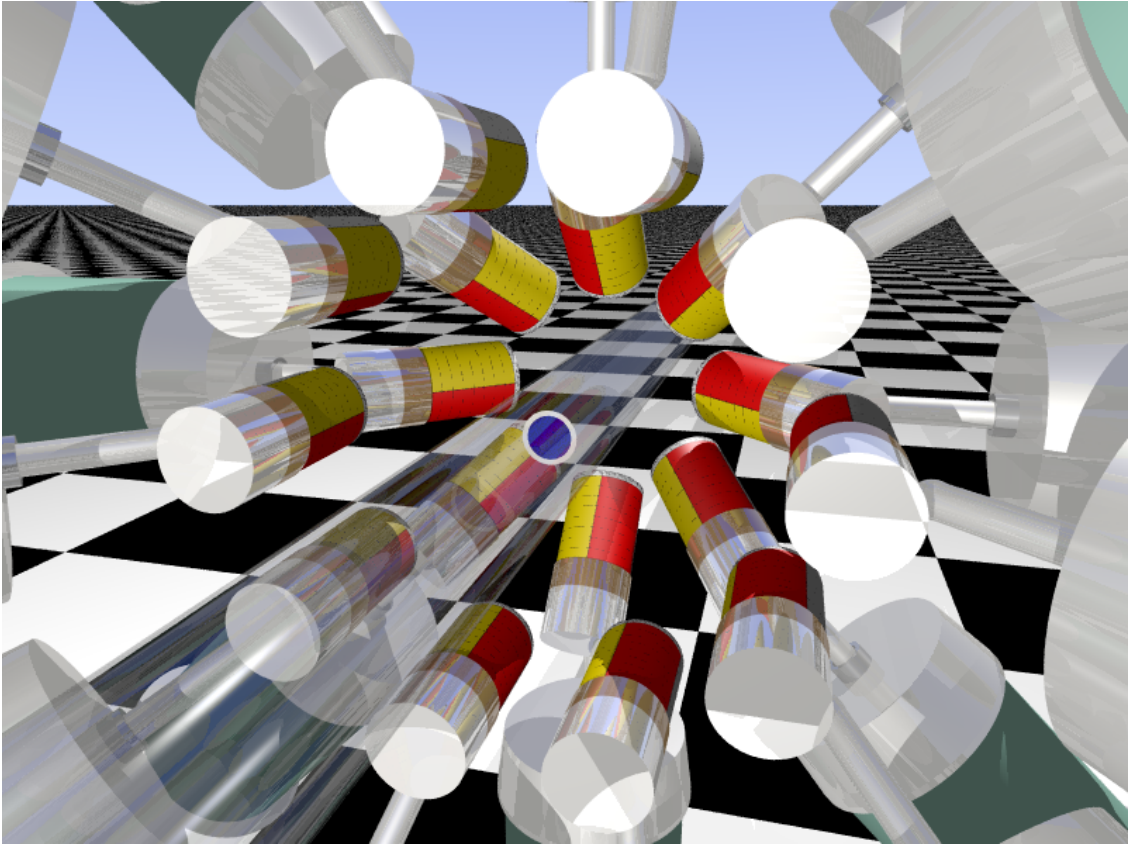


Figure 3.5: The SeGA array shown in the classic SeGA configuration, with two rings of detectors at 37° and 90° with respect to the beam axis. The Germanium crystals are shown in red and yellow, in addition to their segmentation. The target is shown by a blue circle at the centre of the array. Taken from Ref. [79].

3.2.4 The SeGA array

Surrounding the secondary target position of the S800 was the Segmented Germanium Array (SeGA) [78], which consists of a maximum of 18 electronically segmented (32-fold) High-Purity Germanium (HPGe) detectors, which are used to detect in-flight γ rays from decaying excited states in nuclei, populated after the secondary target. Depending upon the type of experiment performed, i.e. high velocity, low velocity, stopped beam, etc., the array can be arranged into several different configurations, each with their own individual benefits and limitations. For example, in experiments where the angular dependence of γ radiation is investigated, the array can be set-up using the delta SeGA configuration, which consists of 18 detectors at 9 different angle groups. For the experiment performed for this analysis, the array was set-up using the classic SeGA configuration, as shown in Fig. 3.5, which consisted of 17 detectors (due to space limitations), arranged into two

rings at 37° (forward) and 90° , with respect to the beam axis. In this configuration, the forward ring contained 7 detectors and the 90° contained 10 detectors, whereby each detector was located 24.2 cm from the central target position. This particular configuration of SeGA detectors is optimised for γ -ray efficiency in high-velocity experiments ($>0.3c$) where Doppler boosted γ rays are more forwards focused.

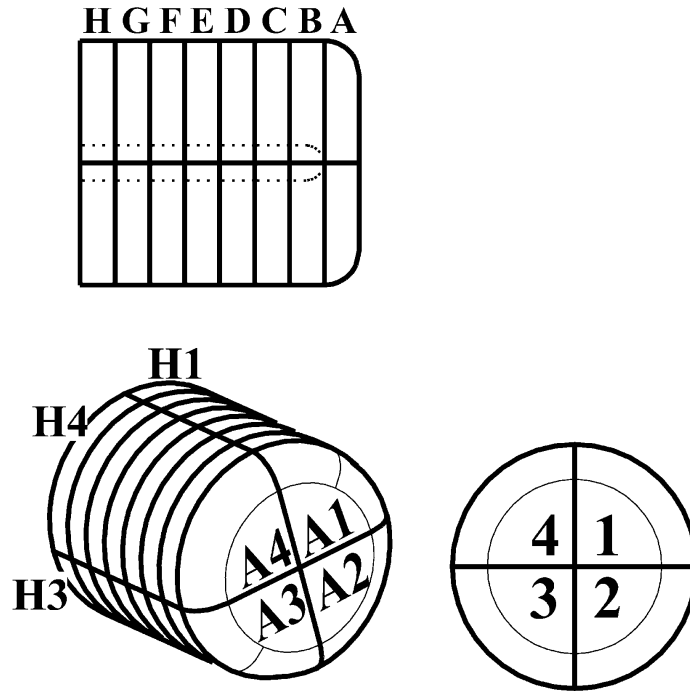


Figure 3.6: A schematic diagram of a SeGA crystal, where the radial and lateral segmentation as well as the dimensions of the central contact (dotted line) are shown. The SeGA crystal is labelled using the standard labelling convention. Taken from Ref. [78]

Each SeGA detector is comprised of a cylindrically-symmetric n-type coaxial germanium crystal, with an external diameter of 70 mm and length of 80 mm. Each crystal is electronically segmented into eight 10 mm wide disks in the lateral direction, which are quartered in the radial direction to give a total of 32 segments, as shown in Fig. 3.6, where the standard labelling convention for the individual segments is also shown. The detectors are orientated such that the 8-fold segmented length of the crystal is facing the target position, as shown in Fig. 3.5, therefore providing a high position resolution for the first interaction point. This therefore reduces the uncertainty in the azimuthal angle of emission ($\Delta\theta$) for a γ -ray event, which therefore improves the energy resolution of the

detector. However, for the outer disk segments, which are not directly facing the target position, the radial segmentation becomes increasingly important. This is because an interaction near the front or rear of these disk segments will correspond to a different angle of emission for the γ -ray.

Running through the centre of each Ge crystal is a central contact which records the total energy deposited in the crystal during a γ -ray interaction. Since a γ -ray may interact with multiple segments, particularly through Compton scattering events, the segment readouts are used primarily to identify which segments were hit during the interaction and how much energy was deposited in each segment. This information can then be used to help with the Doppler reconstruction of a γ -ray event by identifying the most likely initial point of interaction in the Ge crystal (and therefore the angle of emission for the γ -ray), through the use of an algorithm, illustrated by the flow chart in Fig. 3.7 (also see Fig. 3.8 for more details). Since this method also relies upon the energy recorded in each segment, they must be accurately calibrated in order to obtain the best possible Doppler correction (see Section 3.4.1).

The maximum total rate each SeGA detector/crystal can safely process is 3 kHz (for γ rays with $E > 100$ keV), which roughly corresponds to a total secondary beam rate of around 0.5 MHz. However, as was previously shown in Table 3.1, for the experiments performed for this analysis, the total secondary beam rates were well below this value.

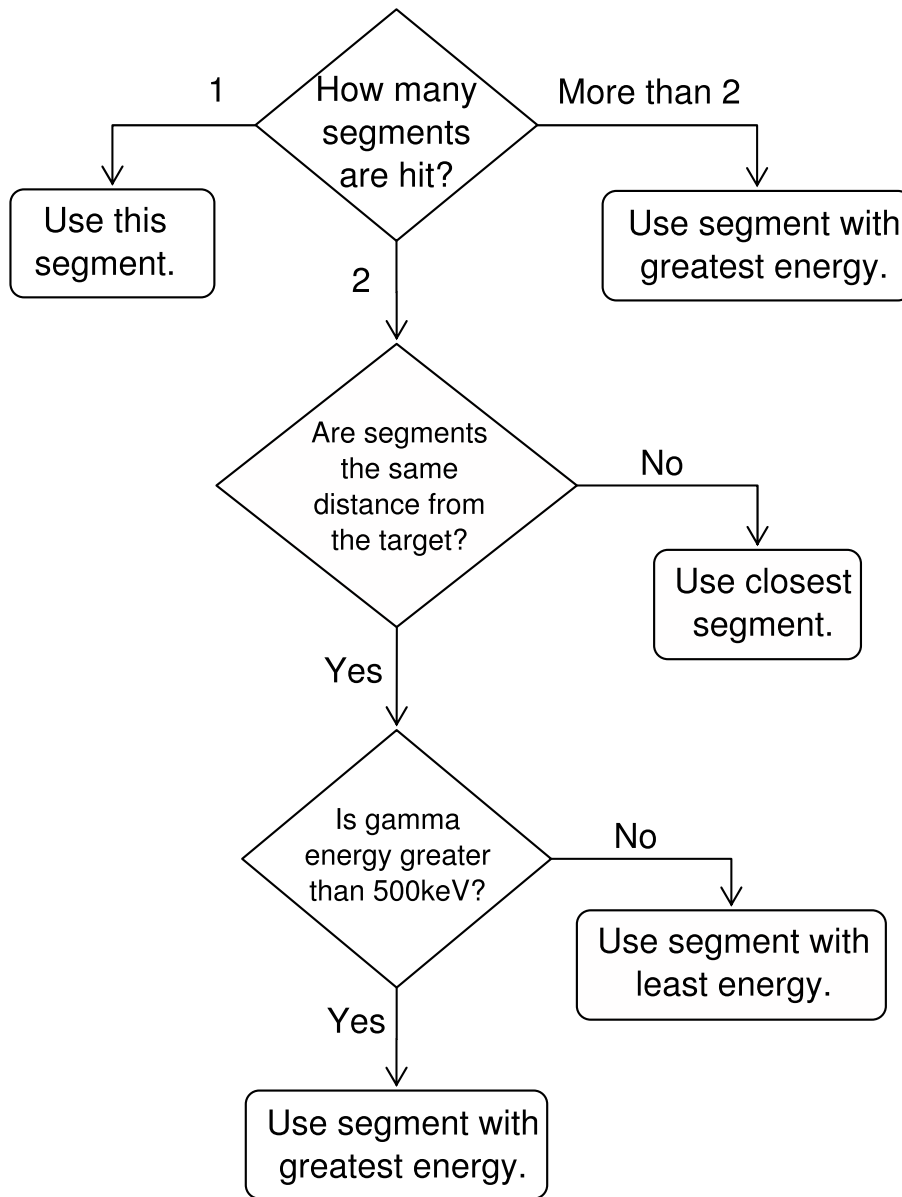


Figure 3.7: A flow chart which shows the process used to determine the most probable first interaction point of a γ -ray interaction within a SeGA Germanium crystal. In the case that two segments are hit, the distance between the segments and the target is considered. If this distance is the same, i.e. if the γ ray Compton scatters into an adjacent segment, the energy of the γ ray is considered. This is due to the energy of the first and second interaction varying, as a function of the initial γ -ray energy, as shown in Fig. 3.8.

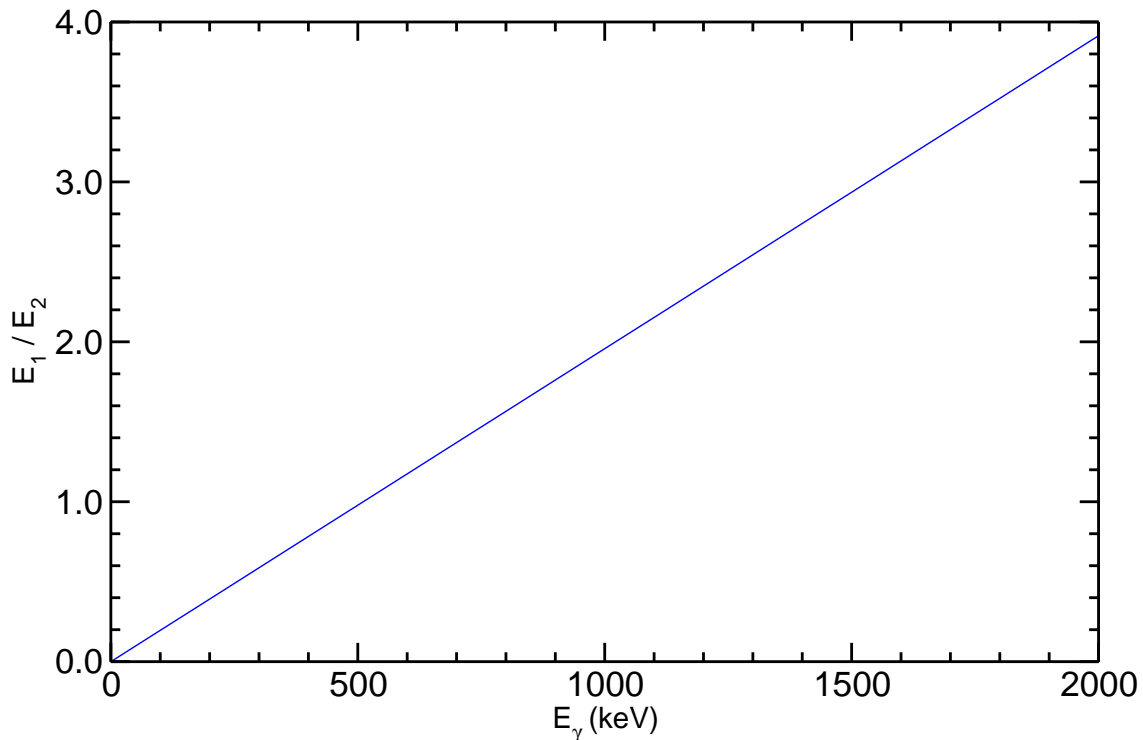


Figure 3.8: Shows the ratio of the energy deposited in a Compton scattering event (E_1) with that of the outgoing γ -ray energy (E_2), as a function of the initial γ -ray energy (E_γ), for a scattering angle of 90° .

3.3 S800 Calibrations & Corrections and Particle Identification

Following the selection of an incoming secondary beam, as described in Section 3.2.2, in order to be able to select the outgoing recoil of interest, a number of calibrations and corrections need to be applied to the various focal plane detectors used by the S800. In this section, a summary of these calibrations is given, whereby all of these calibrations were originally performed by Dr Paul Davies, though later in the analysis a number of these calibrations were further optimised, particularly regarding the CRDCs, in order to investigate momentum distributions. Unfortunately, due to both low statistics and momentum cuts offs at the focal plane, due to the beam blocker (with the S800 analysis line being ran in “focus mode”), this type of analysis could not be performed. However, since the particle information at the target position ($a_{ta}, y_{ta}, b_{ta}, d_{ta}$) is determined through the use of inverse maps and particle information measured at the focal plane (x_{fp}, a_{fp}, y_{fp} ,

b_{fp}), the optimisation of these CRDC calibrations was still essential. Furthermore, since all subsequent focal plane detector calibrations depend upon the CRDC calibrations, these were also updated. All of the spectra shown in the following sections were produced using these updated calibrations, whereby the resulting Particle IDentification (PID) spectra for the reaction channels of interest are shown in Section 5.5.4.

3.3.1 CRDC Calibrations

The CRDC calibrations consisted of two stages, firstly the CRDC pad amplitudes were calibrated through a gain-matching procedure to obtain calibrated dispersive (x) position information, then secondly, mask calibrations were performed to obtain calibrated non-dispersive (y) position information. This calibrated XY-position information, in both CRDC detectors, could then be used to track the trajectories taken by different nuclei traversing the focal plane, on an event-by-event basis.

3.3.1.1 CRDC Pad Amplitude Calibrations

The beam particles dispersive (x) positions at the focal plane are determined from the induced charge distributions on the cathode pads of the CRDCs detectors, which run vertically along the side of each CRDC, both in front and behind the anode wire. Since the cathode pad positions are fixed, each with a pitch of 2.54 mm, the positions of these pads can be directly translated into their respective dispersive (x) positions. However, the signal responses from the individual pads can greatly vary and therefore they need to be calibrated relative to each other, which can be achieved by following an iterative gain-matching procedure. This procedure involves applying rough software gates to a number of outgoing nuclei, which ideally spread the whole range of the CRDC detectors, then running a pre-written program (PadCal) which, on an event-by-event basis, fills “CRDCpad” (max pad) histograms with the value of the CRDC pad with the maximum amplitude, while also filling “CRDCpad0” (pad max) histograms with this value and the amplitude of the two neighbouring pads. The offset and gains for all pads are then determined by the program through a gain-matching procedure, whereby since there is no absolute calibration, all pads are calibrated to some arbitrary channel. The readouts of the individual CRDC pads before and after this calibration are shown in Fig. 3.9.

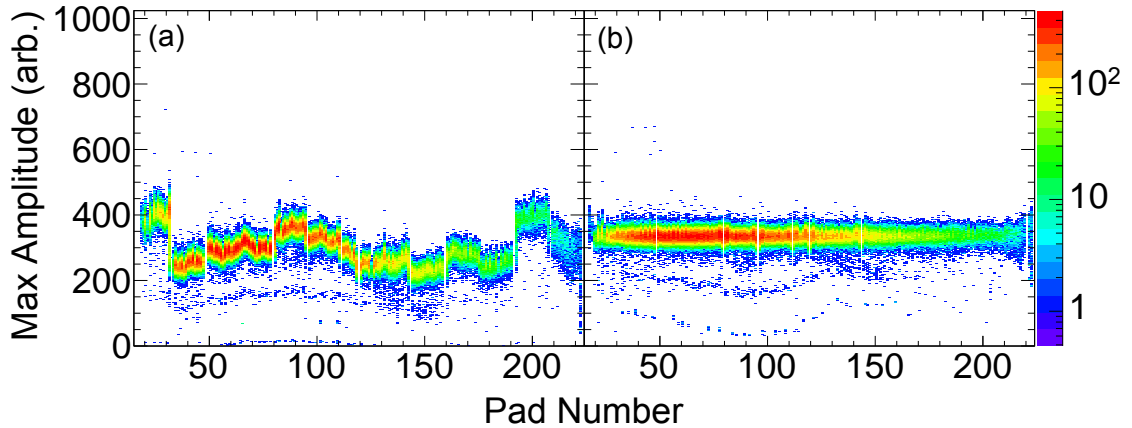


Figure 3.9: CRDC pad number vs pad max amplitude (pad max) spectra gated on outgoing ^{51}Fe recoils, where (a) shows the amplitudes before calibration and (b) shows the amplitudes after calibration, which have been aligned to an arbitrary pad max value.

3.3.1.2 CRDC Mask Calibrations

During the experiment, a number of CRDC mask calibration runs were performed, in which a tungsten mask was placed either in front of either CRDC1 or CRDC2. This mask consisted of a pattern of holes and slits, at known locations and separations, whereby only the particles passing through these holes/slits were detected by the CRDC detectors. This resulted in the observation of hit patterns in the CRDC position spectra, an example for which is shown in Fig. 3.10(a).

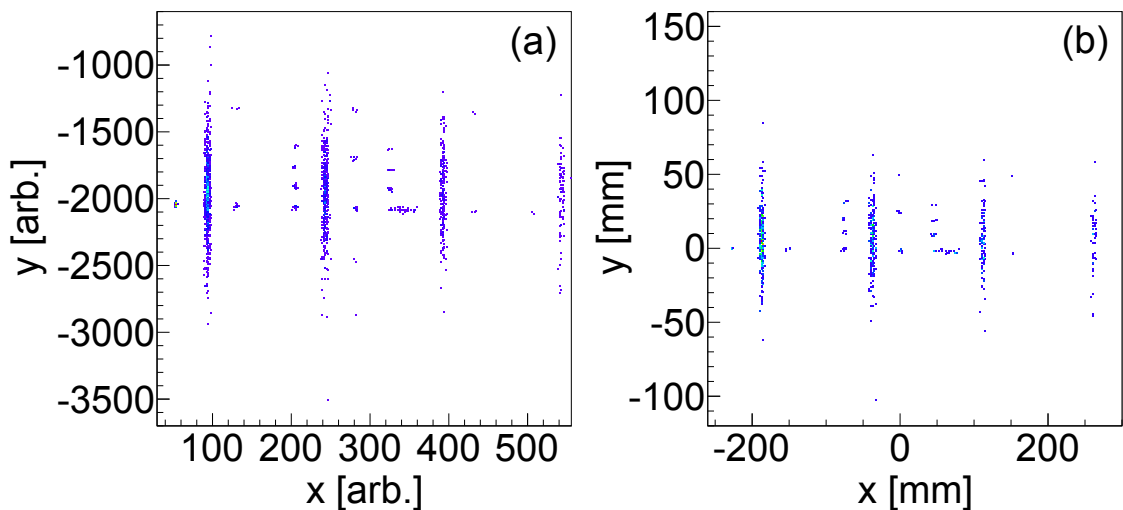


Figure 3.10: The CRDC mask calibration spectrum of CRDC1 using either (a) uncalibrated positions or (b) calibrated positions.

As discussed previously, the dispersive (x) position calibration is fixed by the pad pitch (2.54 mm). However, the non-dispersive (y) position calibration is determined by the drift time of the electrons in the ionised gas. Therefore, calibrating each CRDC, such that the positions of the observed hit pattern match those of the mask positions (i.e. see Fig. 3.10(b)), allows for the raw time signals from the CRDCs to be converted from channels to distance in mm, thus calibrating the electron drift times such that they correspond to real spatial non-dispersive (y) positions. For this analysis, the calibration was performed by hand, whereby a number of uncalibrated hole positions in each CRDC detector were measured and plotted against the correct positions of the mask (in mm). The gain and offset coefficients to align these positions in both CRDC detectors were then extracted from linear fits to these plots. Performing these calibrations for both CRDCs then allows for accurate XY-position information to be obtained on an event-by-event basis, which can then be used to calculate the different trajectories and incident angles of nuclei at the focal plane. Since small changes in the gas composition of the CRDCs can have large effects on the electron drift times and therefore the non-dispersive (y) position measurements, mask calibrations were performed at both the start and towards the end of the ^{54}Ni experimental beam runs. Comparing these two sets of CRDC mask calibration runs (using the calibrations parameters derived for the first set) showed only very minor shifts in the measured non-dispersive (y) positions, suggesting the XY-position information provided by the CRDC detectors throughout the experimental beam runs should be reliable.

3.3.2 Particle Corrections at the Target Position

The particle information at the target position ($a_{ta}, y_{ta}, b_{ta}, d_{ta}$) is determined through the use of inverse maps and particle information measured at the focal plane ($x_{fp}, a_{fp}, y_{fp}, b_{fp}$), using the CRDC detectors. This information is then used to create a_{ta}, y_{ta}, b_{ta} and d_{ta} spectra for each recoil at the target position. A further correction which needs to be applied after the creation of these spectra is the centring of the dispersive and non-dispersive angle spectra at the target (a_{ta}, b_{ta}) to 0. Since the distributions in these spectra are Gaussian shaped or near-Gaussian shaped, their centroids can be easily extracted and the spectra can be centred by simple additive corrections in the sort code.

3.3.3 Ion Chamber Calibrations and Corrections

The calibration/correction procedure for the ionisation chamber requires that both the energy loss (dE) measurements of the sixteen 1 inch anode segments are corrected for dependencies on the particle trajectory through the ion chamber (determined using position measurements in the CRDCs), and that each of the segments are calibrated, such that they record the same energy loss for a given event. Firstly, the energy loss (dE) of each anode segment is corrected for by the following equation

$$E_{cor} = E \cdot \exp(p \cdot (x - x_0)) \quad \text{for } x < x_0, \quad (3.5)$$

where E_{cor} is the corrected energy, E is the uncorrected energy, x_0 is the position measured in CRDC1 and p is a correction parameter. The calibration is performed by firstly creating software gates for both an incoming secondary beam and a few of the outgoing recoils, then running a pre-written program (corrections) which performs a fitting procedure to obtain the correction parameters. The procedure consists of the inverse of Equation 3.5 being fitted to the profile of a histogram of energy loss (dE) in the ion chamber vs x_0 gated on the outgoing recoils (i.e. the mean energy loss measured in the ion chamber for a given value of x_0), whereby the resulting correction parameters are then used to plot a corrected version of this histogram. The results of this correction procedure are such that, for a given event, the distribution of ion chamber energy loss measurements are all aligned to a constant arbitrary value, for all values of x , as shown in Fig. 3.11.

The ion chamber is calibrated by aligning the energy loss measurements in each of the sixteen anode segments, such that they all correspond to the same energy loss for a given event. This calibration is performed by firstly creating software gates for both an incoming secondary beam and two or more outgoing recoils (a rough cut can also be applied for a range of outgoing recoils but it must cover nuclei of the same atomic number, Z , i.e. provide a constant energy deposition for the gain-matching procedure). Following this, a pre-written program (ICCal) is ran which fits the energy loss distribution measured in each anode segment with a Gaussian function to determine the centroid. This information is then used to obtain the calibration parameters to align the energy loss distributions measured in each segment to that of an arbitrary segment, since there is no absolute

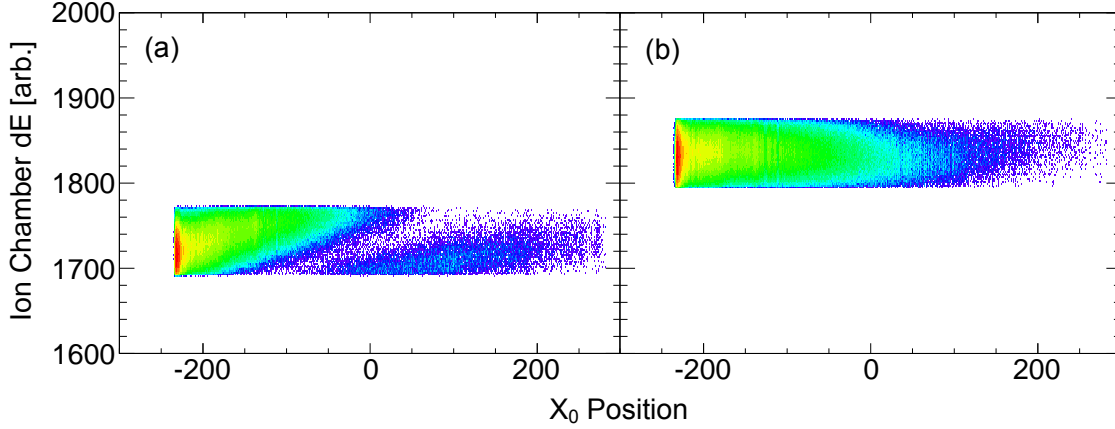


Figure 3.11: Spectra of ion chamber energy loss (dE) vs x_0 position measured in CRDC1, before (a) and after (b) the ion chamber energy loss position correction has been applied, see text for more details.

calibration value. The total energy loss (dE) of a particle traversing the ion chamber is then found by the sum of the sixteen anode segments. Since the energy loss of a particle traversing a material is proportional to Z^2 in accordance with the Bethe-Bloch formula (see Equation 3.3), the unique isotopic selection of outgoing recoils can finally be achieved following this calibration.

3.3.4 Scintillator Corrections

Secondary beam particles are uniquely identified using a ToF-ToF method, which uses the ToF measured between the XFP scintillator, at the extended focal plane of the A1900, and the OBJ scintillator, at the object point of the S800. Outgoing recoils however, are uniquely identified using a dE-ToF method, which uses the ToF measured between the OBJ scintillator and the E1 scintillator at the S800 focal plane. As previously discussed in Section 3.2.2 and Section 3.2.3, only beam particles with the correct magnetic rigidity ($B\rho$) will be transmitted through the A1900 and S800 in accordance with Equation 3.6,

$$B\rho \approx \frac{Am_u v}{Ze} \gamma \quad (3.6)$$

where v is the velocity of the beam particle. From this equation it can be seen that a range of particles with both a lower A/Q but higher velocity, or conversely, a higher A/Q but lower velocity will also be transmitted, with the same (or similar) magnetic rigidity ($B\rho$).

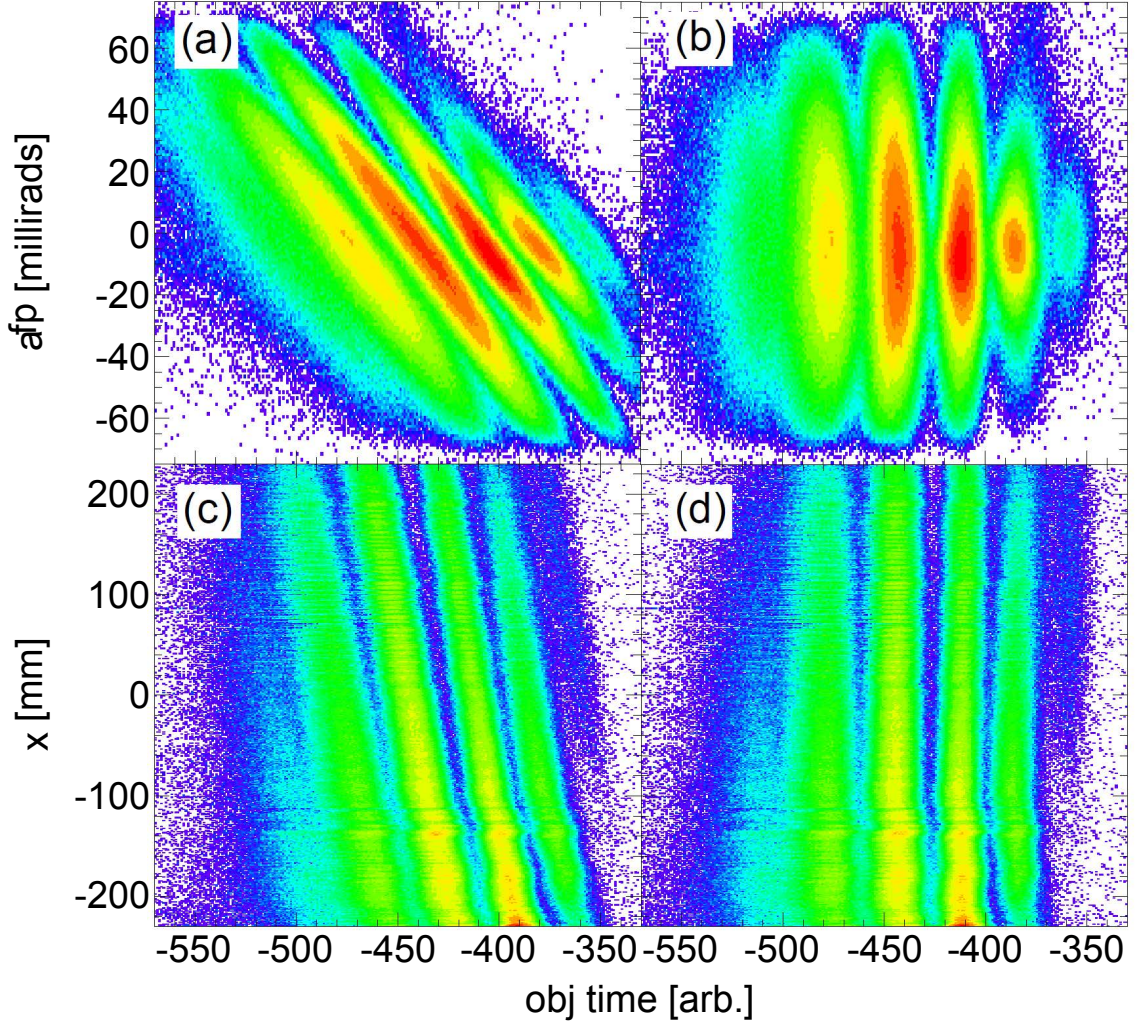


Figure 3.12: CRDC spectra of dispersive angle a_{fp} (a,b) and dispersive position x_{fp} (c,d) against OBJ scintillator time for the outgoing recoils. The spectra are shown before (a,c) and after (b,d) corrections have been applied, see text for more details.

Furthermore, particles of the same atomic number (Z) and mass number (A), but with slightly different momenta ($m_u v$), will also be transmitted but follow slightly different trajectories and therefore arrive at different positions and angles at the focal plane, whereby this is particularly important when identifying recoils through the S800 spectrograph due to its larger momentum acceptance. Therefore, in order to identify outgoing recoils correctly it is important to account for the small differences in the ToF of each particle due to small differences in momentum (and therefore path length travelled through the S800 spectrograph). This is achieved by tracking a particle's position through the focal plane using the CRDC detectors, whereby this information can be used to determine both the

particle’s trajectory and its incident angles at the focal plane. Corrections are applied to the experimental data through the use of a pre-written program (corrections), which acts to align the S800 dispersive angle (a_{fp}) and dispersive position (x_{fp}) of a specific recoil to a common scintillator time in the OBJ scintillator. This is achieved with the program by projecting the a_{fp}/x_{fp} vs OBJ time two-dimensional histograms onto the time axis, then iteratively adjusting a “tilting parameter” until the widths of the resulting distributions are minimised. The results for this calibration are shown in Fig. 3.12.

3.3.5 Particle Identification

Recoils are identified at the focal plane using a dE-ToF method, whereby the total energy loss (dE) information is provided by the ionisation chamber and the ToF timing information is provided by the OBJ and E1 scintillators. Following the calibrations and corrections outlined in the previous section, outgoing recoils could be uniquely identified on an event-by-event basis. In particular, the corrections applied to the ion chamber and OBJ scintillator, to account for the differences in particle trajectories and incident angles at the focal plane, due to variations in particle momenta, were particularly important. The effects of the various corrections discussed in the previous sections are shown in Fig. 3.13, where in 3.13(a) the PID with no corrections is shown, then in 3.13(b) the PID with ion chamber corrections is shown, then in 3.13(c) the PID with scintillator corrections is shown, then finally in 3.13(d) the PID with all corrections is shown. All of the PID shown in this figure were additionally produced in coincidence with incoming ^{52}Fe beam particles, through the use of software gates as discussed in Section 3.2.2, in order to avoid any contamination from other reactions channels. Through the application of software gates to the ‘blobs’ shown in Fig. 3.13(d), outgoing recoils could be uniquely selected, with negligible contamination.

In Figs. 3.14, 3.15 and 3.16, the PIDs for all recoils in coincidence with ^{54}Ni , ^{54}Fe and ^{53}Co secondary beam particles, respectively, are shown, where the nuclei of interest for this thesis, ^{53}Ni , ^{53}Mn and ^{52}Co , are clearly identified. In Fig. 3.14, the identification of outgoing recoils is shown by vertical and horizontal lines of total isospin, T_z , and atomic number, Z , respectively.

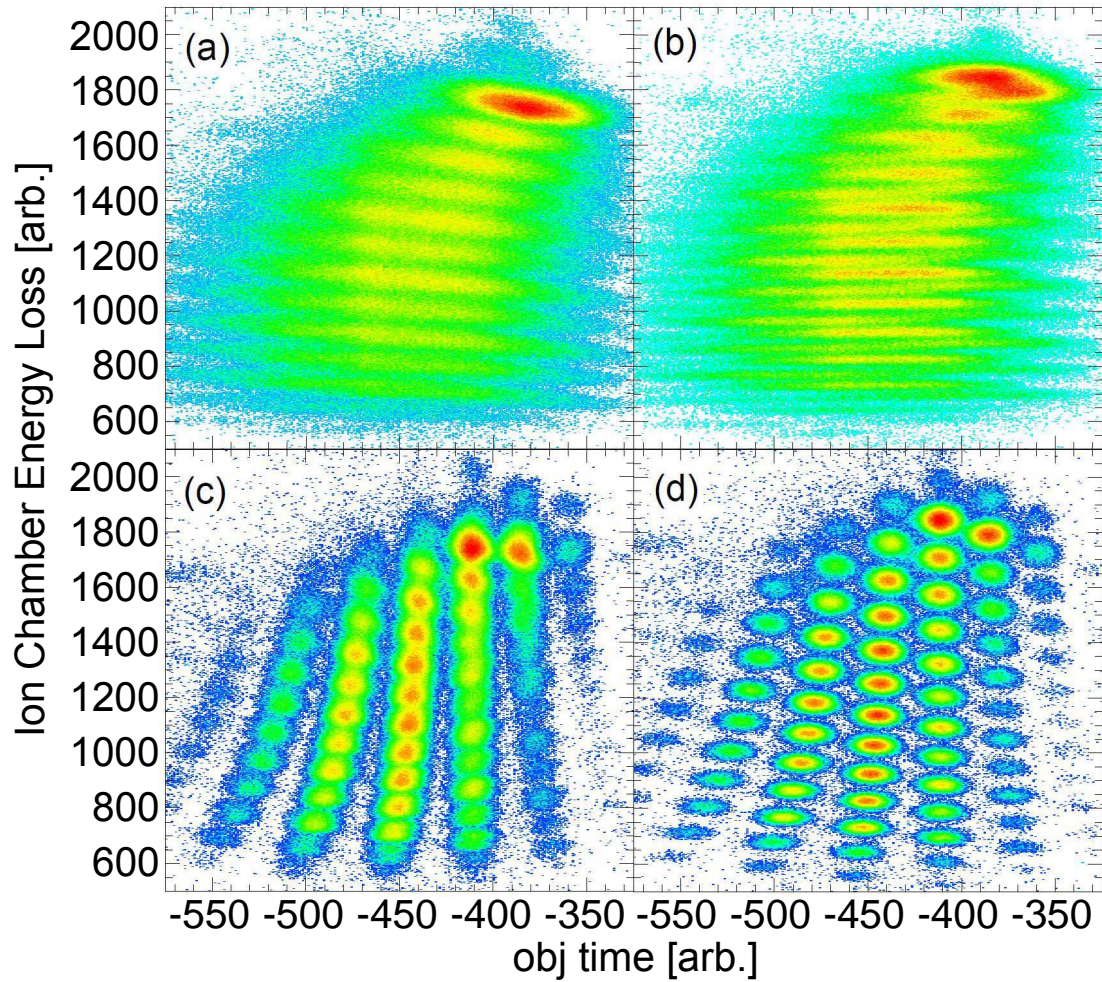


Figure 3.13: The effect of S800 focal plane detector corrections to the outgoing PID, where (a) shows the PID with no corrections, (b) shows the PID with ion chamber corrections, (c) shows the PID with scintillator corrections and (d) shows the PID with all corrections. All spectra were produced with an incoming gate on ^{52}Fe and with both the CRDC and ion chamber calibrations optimised.

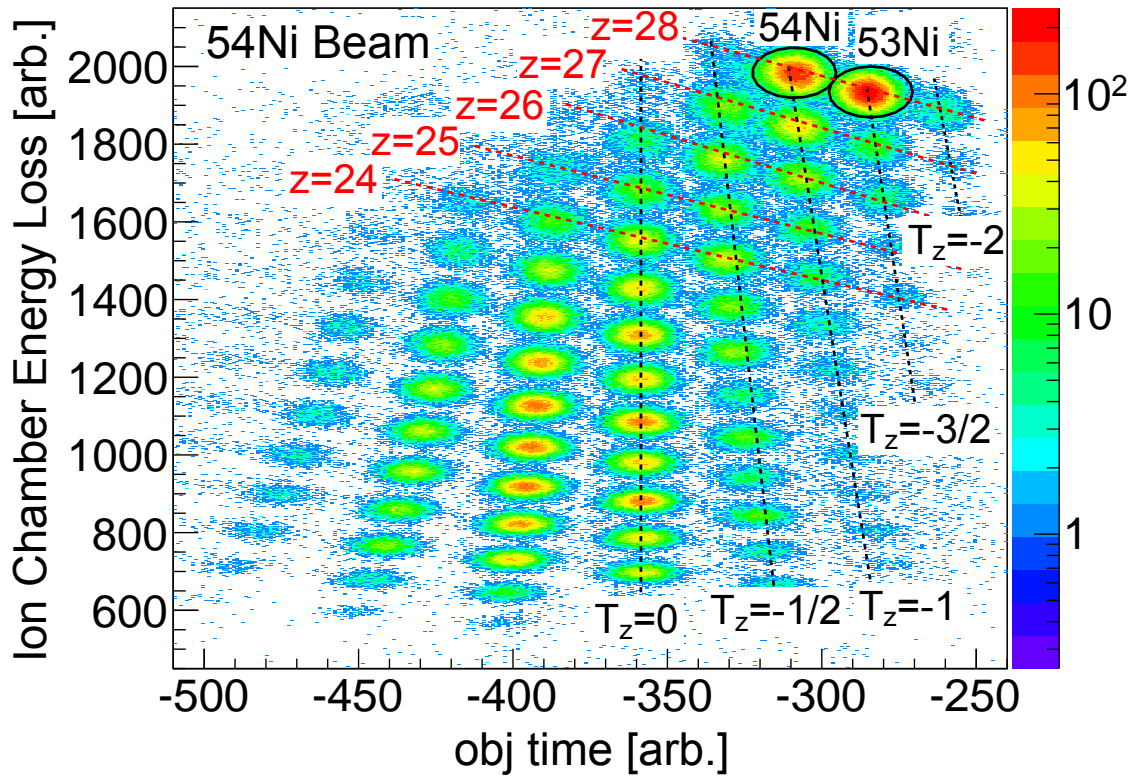


Figure 3.14: The PID showing recoils from reactions at the secondary target in coincidence with the ^{54}Ni secondary beam. ^{54}Ni and the main nuclide of interest, ^{53}Ni , have been labelled. Vertical and horizontal lines of total isospin, T_z , and atomic number, Z , respectively, are also shown for recoil identification.

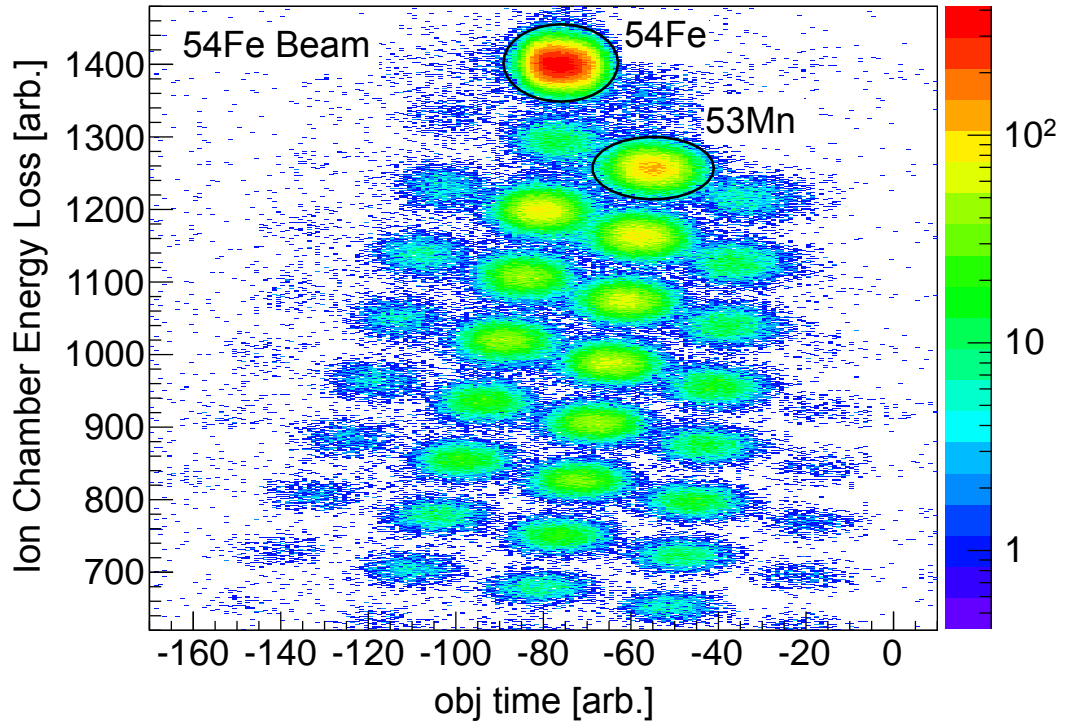


Figure 3.15: The PID showing recoils from reactions at the secondary target in coincidence with the ^{54}Fe beam. ^{54}Fe and the main nuclide of interest, ^{53}Mn , have been labelled.

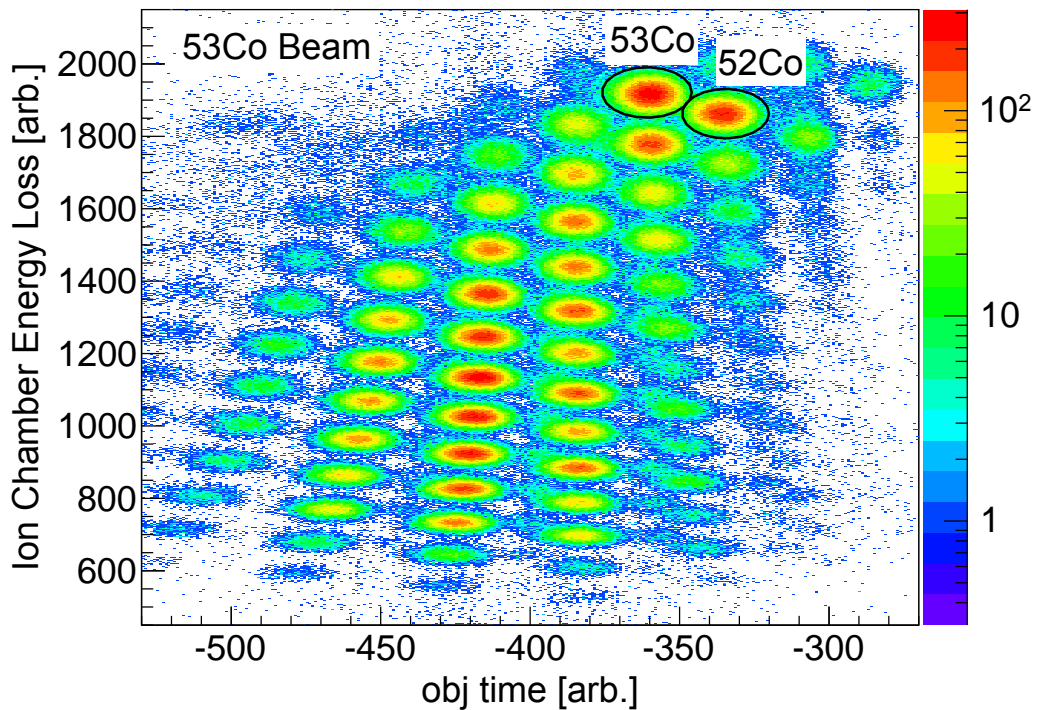


Figure 3.16: The PID showing recoils from reactions at the secondary target in coincidence with the ^{53}Co beam. ^{53}Co and the main nuclide of interest, ^{52}Co , have been labelled.

3.4 SeGA and γ -ray Calibrations

The unique identification and selection of different reaction channels, through the application of software gates to both incoming and outgoing Particle Identification (PID) spectra, then allows for the creation of γ -ray spectra, showing only the γ -ray detected in coincidence with the chosen reaction channel. However, in order to be able to observe a clean γ -ray spectrum, with a reduced background and sharp peaks at the correct energy, a number of additional calibrations and procedures need to first be followed, as will be discussed in the following sections. All of the calibrations and procedures discussed in the following sections were performed by myself, with the exception of the SeGA energy calibrations, for both the central contact (core) and the individual segments of each SeGA detector, which were performed by Dr Paul Davies.

3.4.1 Energy and Efficiency Calibrations of SeGA

During the experiment a number of source calibration runs were performed, both before and after the experimental beam runs, using the standard ^{56}Co , ^{133}Ba , ^{152}Eu and ^{226}Ra sources provided at NSCL. These calibration runs involve a source, of a known strength/activity (at the time of production), being placed at the centre of the target chamber, whereby γ rays from excited states populated in daughter nuclei (following the decay of the source), are detected by the SeGA detector array. Energy calibrations for the SeGA detectors were performed during the experiment, where γ rays with well-known energies, observed during these source runs, were fitted with a Gaussian function to obtain their centroids. Following this, calibrations were performed to the raw signals from the central contact of each SeGA detector in order to convert channels into energy, in units of keV, whereby this transformation had a linear relationship. These calibrations were additionally checked following the experiment, which showed that the observed γ -ray energies were still well calibrated. The second energy calibration to be performed involved calibrating the energy recorded in each SeGA detector segment. As discussed previously in Section 3.2.4, the algorithm used to identify the most probable first interaction point of a γ -ray event in SeGA, relies upon the energy recorded in each segment. Since the correct Doppler reconstruction of a γ -ray event relies upon this positional information, it means that each segment, of the 17 SeGA detectors used in the experiment, needs to be correctly calibrated. To perform this calibration, the energy recorded in a segment, for a fold one γ -ray event (i.e. where a photons deposits its entire energy into only one

segment), is compared with that of the energy recorded by the calibrated central contact, which should be the same. Parameters are then determined from this calibration which corrects the energies recorded in the 32 individual segments to that of the energy recorded by the central contact (in fold one events) for each SeGA detector. In addition, similar calibrations are also performed for fold two events, i.e. where a photon deposits its entire energy into two segments (such as in a Compton scattering event), though this requires significantly more calibration parameters in order to also account for all the different possible pairings of segments. Higher fold events than this are neglected in the calibration procedure due to the very large number of calibration parameters required. However, fold one and two events typically account for 40-70% of all γ -ray events in the usual energy region of interest.

The final calibration performed for SeGA was to measure the γ -ray efficiency of the detectors. Since the array was configured into two rings, with 7 detectors at 37° (forward) and 10 detectors at 90° , with respect to the beam axis, efficiency calibrations were performed for each ring grouping separately. These calibrations were performed using the ^{56}Co , ^{152}Eu and ^{226}Ra source runs, whereby the strength/activity of these sources were precisely measured at the time they were produced. The activity of these sources, during the calibration runs, could therefore be deduced using Equation 3.7, which describes the activity of unstable nuclei which have undergone radioactive decay.

$$A(t) = A_0 \cdot \exp\left(-\frac{t}{\tau}\right) \quad (3.7)$$

Here, $A(t)$ describes the activity (in Bq) of the source after time t (in seconds), after the source was produced, where A_0 describes the initial activity (in Bq) of the source and τ describes the mean lifetime of the source.

The calibration sources used for measuring the efficiency of SeGA are well studied, whereby the energy and intensity of γ -ray transitions observed from these sources is well documented [80–82]. Therefore, efficiency calibrations could be performed by fitting strongly observed transitions with a Gaussian function plus background, to measure their intensities. The absolute photopeak efficiency, $\epsilon(E)$, could then be found by

$$\epsilon(E) = \frac{\text{PeakArea}}{I \times A(t) \times t \times t_{live}}, \quad (3.8)$$

where *Peak Area* is the measured number of counts in a γ -ray transition, I is the previously established intensity per radioactive decay of a particular γ -ray transition, $A(t)$ is the activity of the source at the time of the calibration run, t is the duration of the source run (in seconds) and t_{live} is the live time of the SeGA detectors during the source run.

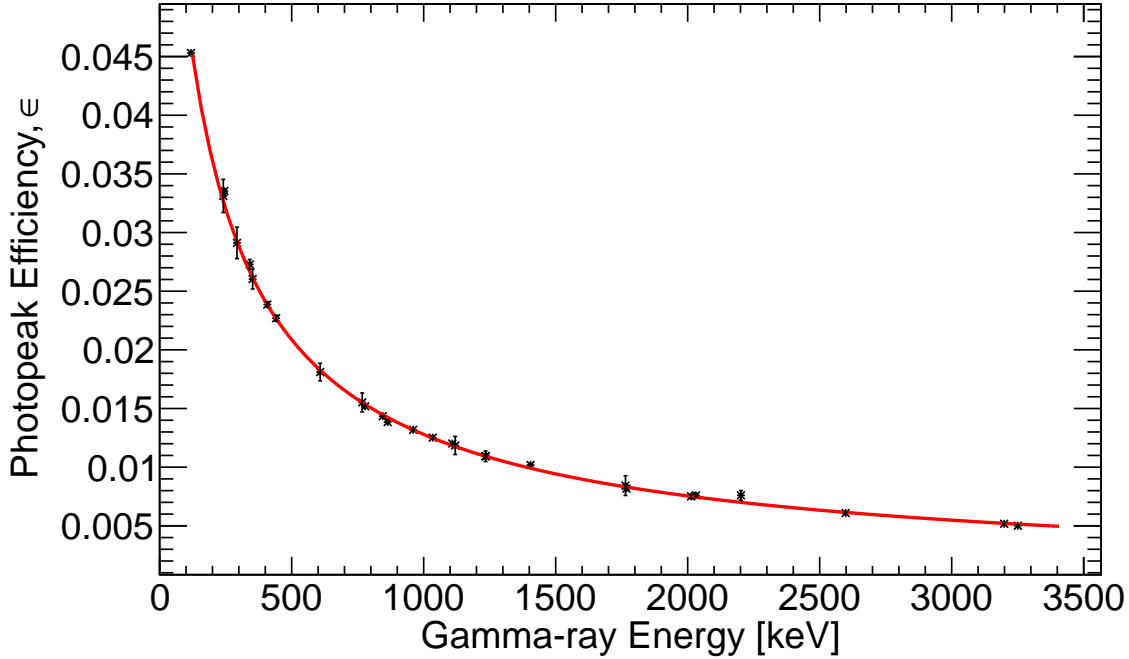


Figure 3.17: The efficiency curve for the 37° (forward) ring of SeGA, where data points were collected using a combination of ^{56}Co , ^{152}Eu and ^{226}Ra radioactive sources. The line was fit using the function described in Equation 3.9.

After fitting a large number of strongly observed transitions in the ^{56}Co , ^{152}Eu and ^{226}Ra source runs, the data was then used to plot absolute photopeak efficiency against γ -ray energy, for both the 37° and 90° SeGA rings. The data was then fitted by the following function,

$$\epsilon(E) = A \cdot (E_{\gamma(lab)} - C)^{-B}, \quad (3.9)$$

where $E_{\gamma(lab)}$ is the measured energy of the γ -ray transition in the lab frame, and A, B and C are coefficients extracted by the fit. During the experimental beam runs however, γ rays are emitted from ions moving at high velocities, rather than emitted at rest, such as during the source runs. This has two effects on the analysis, firstly, γ rays detected by the SeGA detectors (in the lab frame) are heavily Doppler shifted, meaning that they

are detected at energies where the SeGA efficiency is lower, and secondly, the emission of γ rays is more forward focused, resulting in a higher efficiency for detectors at smaller angles and a lower efficiency for detectors at larger angles. The first effect is accounted for in the efficiency correction of γ rays by using the SeGA efficiency at the non-Doppler corrected γ -ray energy, while the second effect, also known as the Lorentz boost, is accounted for through the introduction of a Lorentz boost factor. The boosted efficiency, $\epsilon(E)_{boost}$, therefore, is given by

$$\epsilon(E)_{boost} = \epsilon(E) \cdot \frac{1 - \beta^2}{(1 - \beta \cos \theta)^2}, \quad (3.10)$$

where θ is the angle between the ion and γ -ray trajectories.

The highest energy γ -ray transition (corrected for efficiency) observed in this analysis was a 2331 keV transition, emitted from an ion with a velocity of $\sim 0.375c$, which corresponds to a lab frame energy of ~ 3.0 MeV and ~ 2.2 MeV in the 37° and 90° SeGA rings, respectively. Therefore, data points were collected for the SeGA efficiency beyond 3 MeV to ensure a reliable measurement of efficiency for such high-energy γ -ray transitions, as shown in Fig 3.17, which shows the measured efficiency of the 37° SeGA ring. Furthermore, it should additionally be noted that due to the energy of γ rays in the 90° ring being less Doppler shifted than those in the 37° ring, that the effective efficiency for higher energy γ rays is greater, often leading to high energy γ rays only being detected in the 90° ring.

3.4.2 Doppler reconstruction of γ rays

The high velocity of the recoils populated at the secondary target in this experiment, typically with velocities of ~ 0.36 - $0.42c$, meant that the γ rays emitted from these nuclei were heavily Doppler shifted in the lab frame, in which the SeGA detectors detected them. In order to obtain the correct γ -ray energy of these transitions, in the nuclear rest frame, $E_{\gamma(res)}$, the observed γ rays in the lab frame, $E_{\gamma(lab)}$, needed to be reconstructed by,

$$E_{\gamma(res)} = \frac{E_{\gamma(lab)}(1 - \beta \cos \theta)}{\sqrt{1 - \beta^2}} \quad (3.11)$$

where $\beta = \frac{v}{c}$ is the velocity of the recoil and θ is the angle between the γ -ray and the ion trajectory (i.e. the beam direction), which is calculated using positional information

from the SeGA detector segments, as described in Section 3.2.4, and the target position. However, whilst the SeGA segment positions were fixed during the experiment, the target was placed approximately at the centre of the target chamber by hand, creating an additional uncertainty in θ (in addition to the opening angle of the detector). Therefore, the ‘effective’ target position, Z , along the beam axis, needed to be determined analytically in order to correct for this uncertainty in the target position and to therefore ensure that γ -ray events were reconstructed correctly, especially for the observation of new γ -ray transitions. This was achieved by producing a γ -ray spectrum of a well-studied nuclide and Doppler correcting a γ ray from a very short-lived state ($T_{1/2} < 0.5$ ps), which ideally was populated directly, with small feeding. The Doppler correction process performed involved finding the β value at a given Z value which aligned the transition in both the 37° and 90° ring spectra. However, there is an infinite number of possible solutions of β and Z which will align a transition, but there is only one solution of β and Z which will align this transition at the correct γ -ray energy. Therefore, the correct solution was found using a pre-written code (FindBeta.C), which, after inputting the measured centroid energies of a transition in both rings for a given β value, then iteratively scanned through a range of β values to find the β value, in accordance with Equation 3.11, which would align the transition in both rings. However, it was often necessary to repeat the procedure of fitting the peak in both rings and running this code a number of times to ensure the correct β for alignment was found, especially if the initial β value significantly differed to the one generated by the code. Following this, the code could then be used to estimate the energy of the γ -ray transition for a range of Z values, based on Equation 3.11, by calculating the change in the ‘effective’ θ angles for the two rings as a function of Z position, in the target chamber. This could then be finally used to find the Z position, after some additional minor adjustments in β , which aligned the γ -ray transition in both rings and at the correct energy. This analysis yielded Z values of -0.3 and 3.5 mm for the ^{54}Ni and ^{54}Fe beam experiments, respectively.

It should be noted that the Z values calculated here are only correct for prompt γ -ray transition from short-lived states ($T_{1/2} < 1$ ps), since they decay, on average, at the centre of the target. Transitions from longer-lived states however, have an average decay points further downstream. For example, recoils with a typical velocity of $\sim 0.36\text{-}0.42c$, travel a distance of around 0.11-0.13 mm/ps. Therefore, at these high velocities, it only takes approximately 9 ps for a beam particle to traverse the 188mg/cm^2 ^9Be reaction target, with

a thickness of 1.0 mm. Furthermore, since the outgoing recoils are produced on average at the centre of the target, states with a half-life of ~ 4.5 ps or greater have an average decay point downstream of the reaction target. This therefore leads to an additional uncertainty in the measured energy of γ rays from such states, since they are Doppler corrected assuming they decay at the centre of the target. However, γ -ray transitions with longer half-lives can easily be identified, as will be discussed in Section 3.4.5, from the β values required for their Doppler correction. For γ -ray transitions from states with much longer half-lives, of the order of ~ 50 ps or greater, this thesis work shows that both their energy and half-life can be determined through the use of simulations, due to their asymmetrical line shapes, as will be discussed in Section 3.4.4.

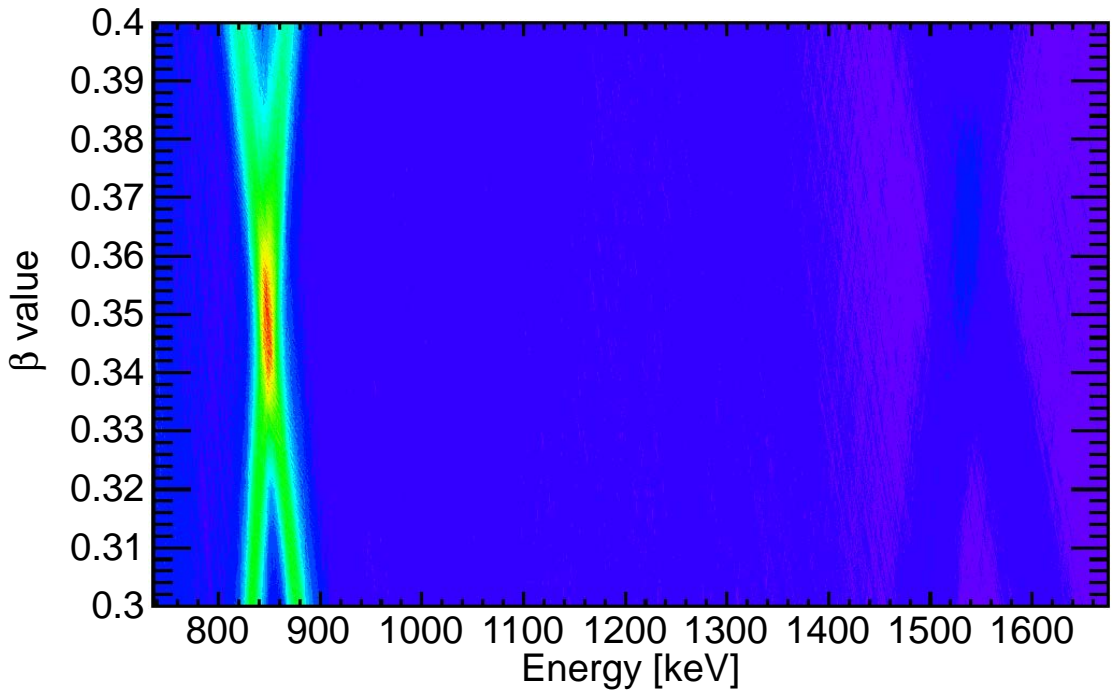


Figure 3.18: 2D histogram of β vs γ -ray energy, for the combined 37° and 90° ring energy spectra of SeGA. Each energy spectrum is Doppler corrected using the corresponding β -value along the y-axis. The histogram was produced in coincidence with incoming and outgoing ^{52}Fe beam particles, where excited states were populated from inelastic scattering with the ^9Be reaction target.

3.4.3 Production of Clean γ -ray Spectra

Following the calibration of SeGA and the use of software gates applied to calibrated PID spectra for incoming secondary beam particles and outgoing recoils, γ -ray spectra for

the reaction channels of interest can be produced. These spectra however, still contain significant sources of background which must be corrected for in order to produce clean γ -ray spectra. Firstly, the γ -ray spectra must be produced using a suitable approximate β value for the Doppler correction, which can simply be found by producing a 2D histogram of β vs γ -ray energy (37° and 90° SeGA ring energy spectra combined) for the reaction channel of interest, as shown in Fig. 3.18. In this example, the reaction under investigation is the inelastic scattering of ^{52}Fe beam particles with the ^9Be reaction target.

The stripes observed in this 2D histogram represent the Doppler corrected energy of γ -ray transitions in either the 37° or the 90° ring energy spectrum, for a given value of β , whereby the exact β value which aligns each transition in both rings, lies somewhere in the centre of where the stripes cross. Therefore, a suitable approximate β value of 0.35 was chosen for the Doppler correction of the ^{52}Fe energy spectrum, as shown in Fig. 3.19.

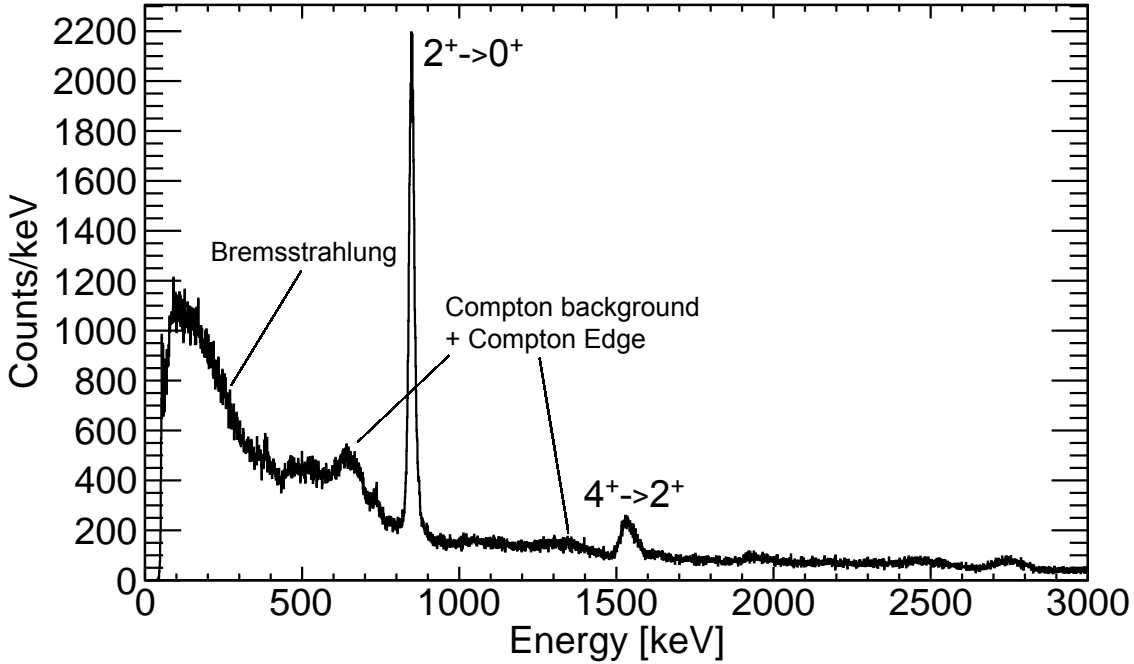


Figure 3.19: The Doppler corrected energy spectrum for γ rays in coincidence with incoming and outgoing ^{52}Fe beam particles. The spectrum has been produced using an average $\beta = \frac{v}{c}$ value of 0.35. The main features in the energy spectrum have been labelled, including sources of background contamination and the main γ -ray transitions observed, using information from Ref. [65].

A number of sources of background contamination can be observed in this spectrum, including a Compton continuum, due to the lack of Compton shielding around the SeGA

detectors, and Bremsstrahlung radiation. The Compton continuum results from γ rays scattering in the detector, depositing only a portion of their energy, before escaping the detector volume. The energy deposited in the detector therefore, is only a fraction of the energy of the γ ray, resulting in a continuum of background on the lower energy side of the γ -ray transition. The energy of the escaping γ ray, E_f , is related to both the initial energy of the γ ray, E_i , and the scattering angle between their trajectories, θ , by the following Compton scattering formula,

$$E_f = \frac{E_i}{1 + (1 - \cos\theta)E/(m_e c^2)} \quad (3.12)$$

where m_e is the mass of the electron and c is the speed of light. Since the total energy, E_T , deposited in the detector is given by $E_T = E_i - E_f$, it can be observed by Equation 3.13, that the maximum energy deposition will occur when the γ -ray fully back scatters (i.e. when $\theta = 180^\circ$). This results in a sharp rise on the lower energy side of a γ -ray transition known as the Compton Edge, which can be calculated by the following formula.

$$E_T(\text{max}) = E_i \left(1 - \frac{1}{1 + \frac{2E}{m_e c^2}} \right) \quad (3.13)$$

At smaller angles than $\theta = 180^\circ$, lower energies will be deposited in the detector, resulting in the observation of a Compton continuum. For γ rays with an energy greater than two times the rest mass of the electron (1.022 MeV), pair production may also occur within the detector volume, whereby the resulting positron annihilates with a surrounding electron, resulting in the production of two γ rays, each with an energy of 511 keV. Due to the finite size of the detector volume, there is a probability that either one or both of these γ rays will escape undetected, resulting in the observation of single escape and double escape peaks in the γ -ray spectrum, with energies of $E_\gamma - 511$ keV and $E_\gamma - 1022$ keV, respectively.

The second main source of background, Bremsstrahlung radiation, results from the deceleration of charged beam particles due to their interactions with the target electrons and nuclei. Due to the conservation of energy, charged particles which decelerate must lose this energy in the form of electromagnetic radiation. As the change in energy of the decelerating beam particle increases, the radiation emitted shifts towards higher frequencies. Therefore, due to the high velocity of the beam particles in this experiment, this meant that the radiation was emitted in the form of a γ -ray continuum.

3.4.3.1 SeGA Timing Condition

One way in which the background of γ -ray spectra can be reduced is through the application of timing conditions to the detected γ rays. In this analysis, this was achieved by using the measured time signals from the SeGA Ge crystals, relative to that of the time signals from the OBJ scintillator, as shown in Fig. 3.20. By applying a time gate to this spectrum, γ rays not associated with the recoils of interest, mostly in the form of Bremsstrahlung radiation, could be removed from the γ -ray spectra. This is particularly evident in Fig. 3.21, where a large reduction in the lower energy background radiation is observed following the application of this time gate, though the effects are less noticeable at higher energies. The peaks in this γ -ray spectrum however, remain mostly unaffected

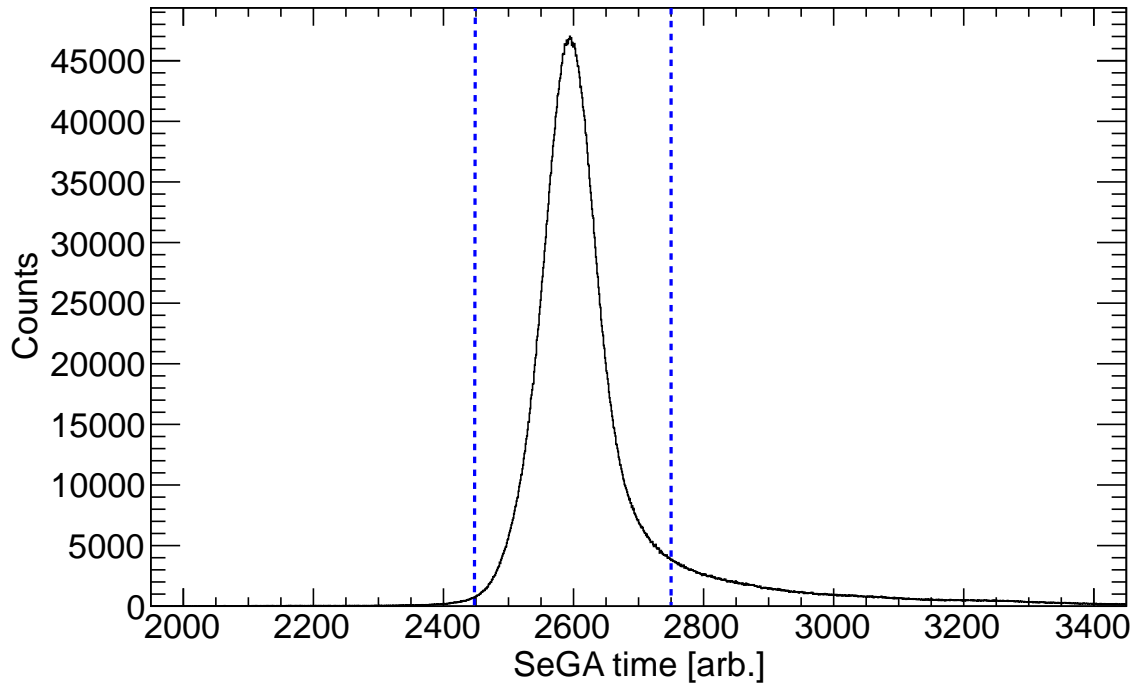


Figure 3.20: Timing signals from the SeGA Ge crystals measured relative to signals from the the OBJ scintillator. The red dashed lines represent the cut used to reduce the Bremsstrahlung background.

by the application of this time gate, though for lower energies (≤ 300 keV), the timing response of SeGA is poor, which can lead to the reduction in the size of peaks around this energy if the timing conditions applied are too stringent. Therefore, this must be taken into consideration whenever dealing with transitions at very low energies, especially whenever the measured intensity of these transitions is important, such as when performing cross

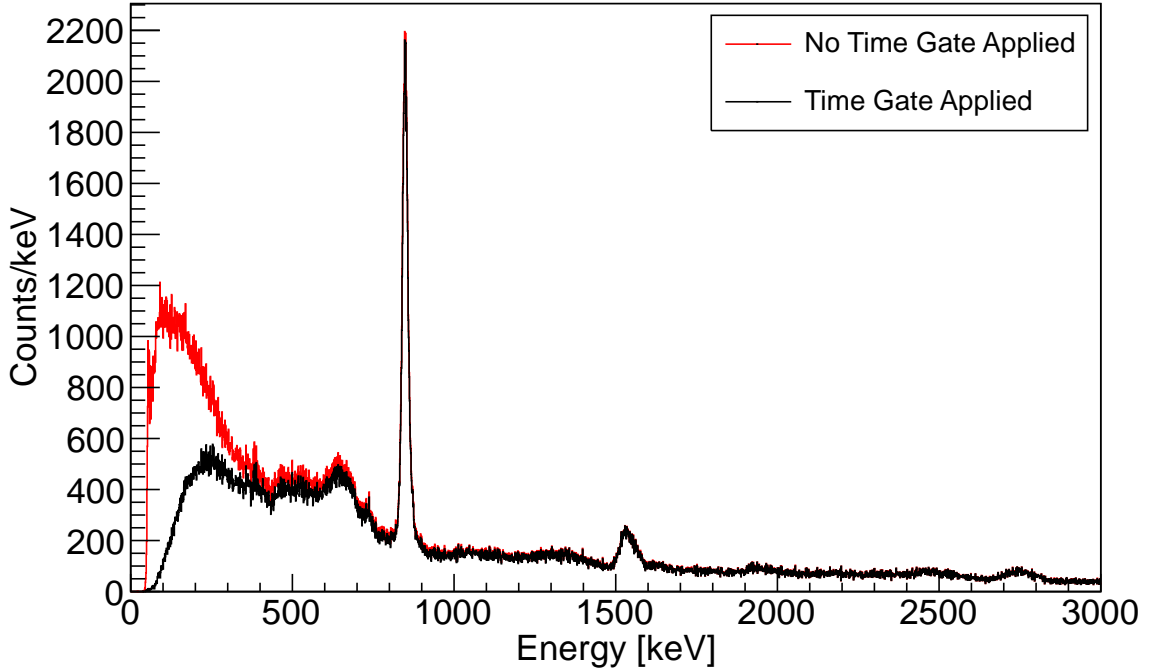


Figure 3.21: The Doppler corrected energy spectrum for γ rays in coincidence with incoming and outgoing ^{52}Fe beam particles, with (black line) and without (red line) a time gate. The spectrum has been produced using a $\beta = \frac{v}{c}$ value of 0.35.

section analysis or when constructing energy-level schemes.

3.4.4 Energy and Lifetime Simulations

The half-life results, discussed later in Section 4.1.5, were extracted through the comparison of experimental γ -ray spectra with simulated γ -ray spectra, which were generated using a dedicated lifetime code developed at NSCL [97] utilising the GEANT4 framework [98]. The simulation code used is capable of accurately replicating a number of the experimental characteristics, including those of the incoming beam, the outgoing recoil, the geometry of the detector system, the reaction kinematics and those of the reaction target used. The simulations are performed using macro files which contain a number of different adjustable parameters which all need to be corrected and optimised in order to accurately replicate the experiment that was performed. These parameters are extracted in the simulation by fitting simulated particle spectra to their experimental equivalent, gated on either the incoming secondary beam or the outgoing recoil, whereby these parameters are adjusted until the best agreement is observed. The main experimental particle spectra compared with their simulated equivalents are:

- The a_{ta} and b_{ta} spectra, which show the distribution of dispersive and non-dispersive beam angles, respectively, at the target position.
- The y_{ta} spectrum, which shows the distribution of non-dispersive (y) positions of beam particles at the target position.
- The d_{ta} spectrum, which shows the relative energy spread ($\delta E/E$) of beam particles at the target position.
- The β spectrum, which is closely related to the d_{ta} spectrum, but shows the spread of beam particle velocities at the target position.

The first experimental characteristic which needs to be optimised in the simulations is the incoming secondary beam energy, $KE_{u(in)}$. This is achieved through the comparison of simulated (empty target) particle spectra (a_{ta} , b_{ta} and y_{ta}) with the experimental equivalents observed in unreacted beam runs, with no target. Following the replication of these incoming beam characteristics, using an outgoing beam energy, $KE_{u(out)}$, as determined from the S800 $B\rho$ setting during the unreacted beam run, the $KE_{u(in)}$ and dpFWHM parameters are adjusted until the simulated and experimental β spectra both align at the same value, with the same velocity spread. These two parameters then remain unchanged for the rest of the simulations performed. The next step of the simulation involves a very minor correction to the target scale density, which essentially accounts for the difference in the stopping tables used in LISE and GEANT. However, due to the lack of any unreacted beam runs being performed with a target during the experiment, this effect could not be corrected for, though the effect should be small (the scale density parameter in the code is typically in the range of 0.95 to 1.05). The final stage of the simulation involves creating a recoil simulation which replicates the reaction mechanism under investigation. The procedure followed is very similar to that used for calculating the incoming secondary beam energy, except the simulated and experimental particle spectra (a_{ta} , b_{ta} and y_{ta}) which are compared are those of the outgoing recoil. Following the replication of these experimental particle spectra in the simulations, the β spectra of the simulation and outgoing recoil are compared, whereby very minor adjustments are made to a dpfrac parameter, to account for any momentum loss of the projectile in the reaction that is not accurately accounted for by GEANT. An additional feature in these particle simulations is the option to include cut off points, which can be accurately set to replicate those observed in the experiment

due to the beam blocker. Furthermore, small adjustments can also be made to $KE_{u(out)}$, to align the simulated d_{ta} spectra of the recoil with the experimental equivalent.

Following the creation of recoil simulations which accurately replicate all of the various experimental characteristics, as shown in Fig. 3.22 for ^{53}Ni , the simulations can then be used to simulate γ -ray transitions. In these simulations, the energy and the half-life of the transition can be chosen, as well as whether or not to include feeding from other transitions.

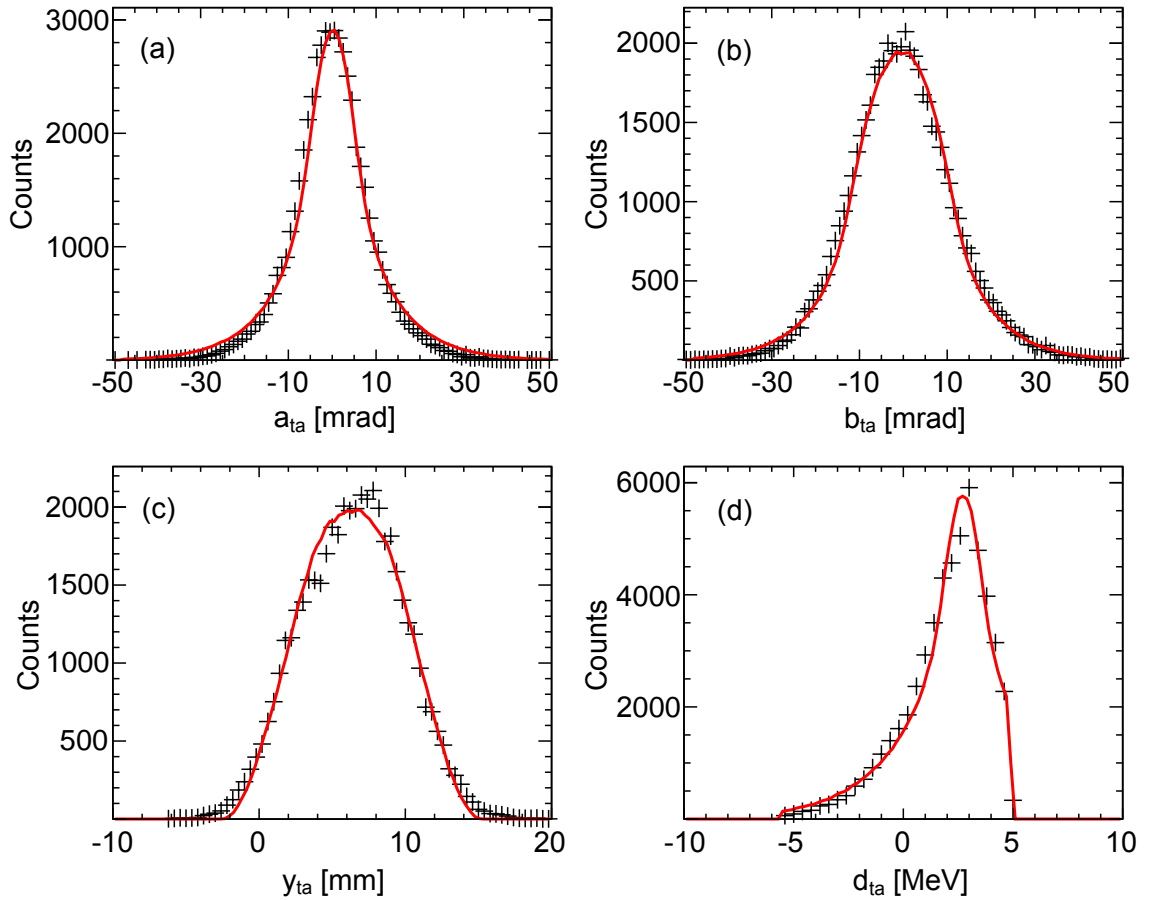


Figure 3.22: Experimental particle spectra for ^{53}Ni recoils (black markers) fitted with their simulated equivalents (red line), after parameter optimisation in the lifetime code. The dispersive (a_{ta}) and non-dispersive (b_{ta}) beam angular distributions at the target position are shown in panels (a) and (b), respectively. The Y-position (y_{ta}) and the relative energy spread of the beam particles (d_{ta}) at the target position are shown in panels (c) and (d), respectively.

3.4.5 Analysis Techniques

Throughout this analysis, various analytical techniques were employed to help analyse and extract as much information as possible about the γ -ray transitions observed in this work. This was in order to help determine their positions in energy-level schemes in order to facilitate the study of mirror symmetry. The main techniques used are briefly summarised in the following sections.

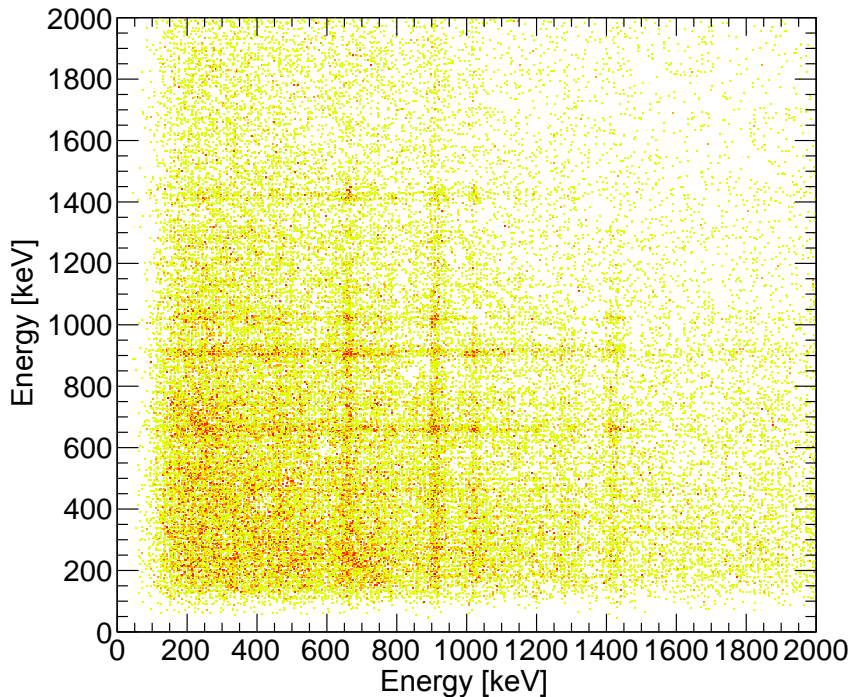


Figure 3.23: A 2D histogram of γ -ray energy vs γ -ray energy for multiplicity > 1 γ -ray events, gated on incoming ^{53}Co beam and outgoing ^{52}Co recoil.

3.4.5.1 γ - γ Coincidence Analysis

This type of analysis is used primarily to identify transitions which are in coincidence, i.e. transitions which form part of the same cascade. Such γ -ray events are identified in coincidence if they are detected within the same coincidence time window of the detector system, whereby the number of γ rays detected in coincidence within the same coincidence window defines the multiplicity of a γ -ray event. This technique however, also leads to the possibility of “accidental coincidences”, which result from uncorrelated background events, such as Bremsstrahlung radiation, also being detected in coincidence, which needs to be corrected for. In general, due to the low geometric efficiency of SeGA this type

of analysis can only be used for higher statistics data. The analysis involves filling a 2D histogram of γ -ray energy vs γ -ray energy, with γ -ray events with multiplicity >1 , as shown in Fig. 3.23, where each event (dot) represents a coincidence between two γ -ray energies and the histogram produced is completely symmetric across the diagonal.

Therefore, the total projection of this histogram onto either the x or y-axis can simply be considered as the energy spectrum of the recoil, with a multiplicity >1 gate, which, when compared with the γ -ray spectrum, can be used to identify transitions with many or few γ -ray coincidences, by comparing the relative strengths of transitions in both spectra. In order to produce γ - γ coincidence spectra for individual transitions, the 2D histogram can simply be projected only between the bin range of the transition of interest, identified using the total-projection spectrum. However, in order to reduce the number of uncorrelated background events in this spectrum, a background subtraction must be performed, which ideally involves subtracting a spectrum which is representative of the background around the energy of the transition. This is typically achieved by subtracting the average of two background spectra, produced by projecting on either side of the transition, with the same bin width as that of the transition.

3.4.5.2 Doppler Correction Analysis

As discussed previously in Section 3.4.2, the Doppler correction performed for transitions in this analysis assumes that all excited states which are populated are short-lived ($T_{1/2} \leq 1$ ps) and therefore decay, on average, at the centre of the target. However, states with half-lives of just ~ 4.5 ps or greater, decay on average, downstream of the target. Therefore, decays from such longer-lived states need to be identified, especially those which decay much further downstream ($T_{1/2} > 50$ ps), since for these transitions, the measured centroid energy will be significantly shifted (towards a lower energy). Fortunately, a Doppler correction technique can be employed to identify such transitions and potentially in some cases be used to estimate the approximate half-life of relatively short-lived states ($T_{1/2} \leq 9$ ps). This Doppler correction involves finding the required β value to align the energies of transitions in both the 37° and 90° SeGA rings, whereby safe uncertainties in this β -value can be determined by finding the corresponding upper and lower β values in which the transition energies in the two rings do not align, within error. Providing the spectrum has at least one transition from a very short-lived state ($T_{1/2} \leq 0.5$ ps), ideally which has been populated directly in the reaction investigated, the β value required to

align this transition gives us an insight into the approximate ion velocity of a given recoil at the centre of the target position. Since beam particles and recoils lose energy as they traverse the reaction target, this results in noticeable changes in the average emitter velocity for states with slightly longer half-lives, as can be seen in Fig. 3.24.

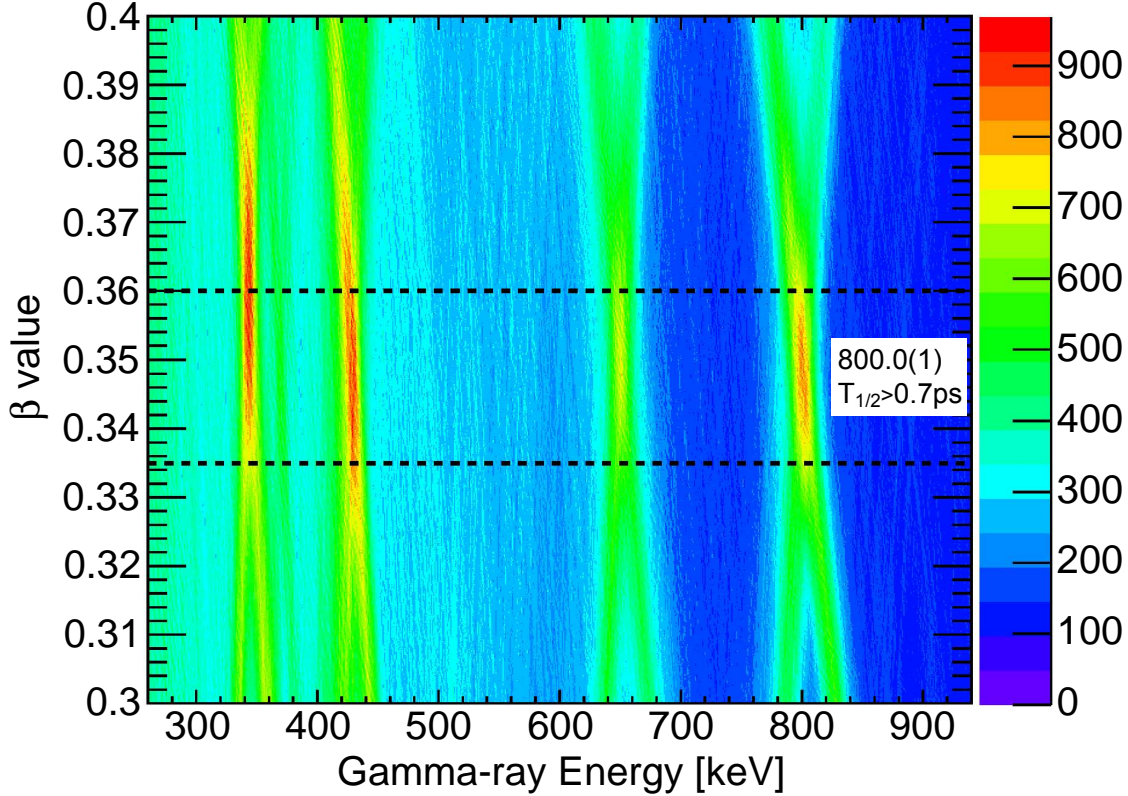


Figure 3.24: 2D histogram of β vs γ -ray energy, for the combined 37° and 90° ring energy spectra of SeGA. Each energy spectrum is Doppler corrected using the corresponding β -value along the y-axis. The histogram was produced in coincidence with incoming ^{52}Fe beam particles and outgoing ^{50}Mn recoils. The approximate ion velocities at the centre ($\beta = 0.360$) and back ($\beta = 0.335$) of the target are also shown by dashed lines, data for labels taken from Ref [85].

Once an approximate velocity at the centre of the target has been determined, the approximate energy spread from the centre to back of the reaction target can be determined through the use of energy loss calculations, using LISE [73]. Following this, the β values required to Doppler correct each transition can be used, in conjunction with these energy loss calculations, to determine whether they decay on average within the target volume or further downstream. For transitions from short-lived states, their Doppler correction β values can be used to estimate their approximate half-lives or to set conservative up-

per/lower limits. For example, if we consider that the average β value, β_{av} , required to align a given transition, is composed of a portion of the decays, a_1 , occurring inside the target volume with the average centre of the target velocity, β_{ta} , and a portion of the decays, a_2 , occurring outside the target volume with the average back of target velocity, β_{ou} ,

$$a_1 \cdot \beta_{ta} + a_2 \cdot \beta_{ou} = \beta_{av} \quad (3.14)$$

where

$$a_1 + a_2 = 1 \quad (3.15)$$

then the portion of decays occurring inside the target, can be found by,

$$a_1 = \frac{\beta_{av} - \beta_{ou}}{\beta_{ta} - \beta_{ou}} = 1 - \frac{N(t)}{N_0}, \quad (3.16)$$

where, $N(t)/N_0$ is the portion of decays which occur on average downstream of the target.

Finally, combining this with the equation for radioactive decay,

$$\frac{N(t)}{N_0} = \exp\left(-\frac{t}{\tau}\right) \quad (3.17)$$

gives an expression relating the half-life of a state to the portion of decays which occur within the target volume,

$$T_{1/2} = \frac{-t_{av} \times \ln(2)}{\ln(1 - a_1)} \quad (3.18)$$

where $t_{av}(= x/(2 \cdot \beta_{ta}))$ is the average time a recoil spends inside a target of thickness, x . This method of extracting half-lives is very sensitive to the measurement of recoil velocity at the centre of the target, since this value is additionally used to calculate the back of the target velocity as well, through the use of energy loss calculations. Therefore, only the β value used to align transitions from very short-lived states (or states predicted to be short-lived based on mirror symmetry), which are also believed to be populated directly

with small feeding, should be used to determine this velocity. Furthermore, the method should also be mostly restricted to short lived states ($T_{1/2} \leq 9$ ps) whereby the large majority of the decays will occur within a small distance travelled by the recoils. Testing this method for the 849.43(10) keV $J^\pi:2^+ \rightarrow 0^+$ transition in ^{52}Fe , populated either via one-proton knockout from ^{53}Co or inelastic scattering of a ^{52}Fe ion beam, gave half-life measurements of 7.3(21) and 7.0(19) ps, respectively, which both compare favourably with the previous measurement of 7.8(10) ps [65].

3.4.5.3 Mirror Symmetry Arguments and Spectral Comparison

The use of mirror symmetry arguments in this analysis refers to the comparison of transition and state properties, measured in proton-rich nuclei, with those previously measured in their more well-studied mirror partners, in order to make tentative assignments of spin and parity. The properties which are typically compared are transition energies, state energies, half-lives, and branching ratios. Since, in general, these properties are very similar for analogue states in mirror nuclei, they can therefore be used to help identify potential analogue transitions and states, as well as allow us to make tentative assignments of state spin and parity.

The second analysis technique related to mirror symmetry in this analysis is the use of direct isospin-symmetric reactions to populate mirror nuclei, such as mirrored one-nucleon knockout reactions. Due to the near symmetrical wavefunctions of mirror nuclei, in the absence of any significant differences in deformation, direct one-nucleon knockout reactions should populate the same set of analogue states in both nuclei with similar intensities. Therefore, the resulting γ -ray spectra, produced under identical conditions, can be used to tentatively identify mirror transitions through ‘spectral comparison’, providing the analogue states populated in both nuclei are particle bound. This new approach to MED studies has already shown great potential in previous work studying proton-rich nuclei in this region, as discussed in Refs. [86–88].

Chapter 4

Results from One-nucleon Knockout Reactions

A large range of isotopes were populated in the experiment performed at MSU, as previously shown in Figs. 3.14, 3.15 and 3.16, whereby experimental runs were performed for two separate A1900 settings, with S800 magnetic rigidity settings centred on either the $T_z = -2$ or the $T_z = +2$ reaction products. The two settings were ran for approximately ~ 86 hours and ~ 1.5 hours for the proton-rich and neutron-rich isotopes respectively, whereby the large run time difference was mainly due to the much lower production cross section of the more proton-rich isotopes, but also due to the cyclotrons breaking during the ^{54}Fe A1900 setting. Due to the nature of the in-flight fragment separation process using the A1900 fragment separator, secondary cocktail beams were produced containing a range of different isotones (i.e. ^{54}Ni , ^{53}Co , ^{52}Fe , ^{51}Mn in the case of the ^{54}Ni A1900 beam setting), which resulted in a large number of different reaction channels to investigate. In the following sections, both the analysis of the $A = 53$, $T_z = \pm 3/2$ mirror pair, ^{53}Mn and ^{53}Ni , populated via mirrored one-nucleon knockout, and the $A = 52$, $T_z = -1$ nuclide, ^{52}Co , populated via one-neutron knockout, will be discussed, whereby the work presented here has also been published in Refs. [11, 12].

The γ -ray spectra presented in this chapter for the nuclei of interest were all produced following the calibrations and corrections as discussed in Sections 3.3 and 3.4, in addition to the application of gating conditions as described in Section 3.4.3. Coincidence gates were applied to both incoming and outgoing nuclei in order to ensure the γ rays observed were both associated with correct nuclei and reaction channel under investigation.

4.1 Population of states in the $A = 53$, $T_z = \pm\frac{3}{2}$ mirror pair

The mirror nuclei ^{53}Mn ($T_z = +3/2$) and ^{53}Ni ($T_z = -3/2$) were populated via mirrored one-nucleon knockout reactions from the ^{54}Fe ($T_z = +1$) and ^{54}Ni ($T_z = -1$) secondary beams, respectively. In this section it will be discussed how the use of direct, isospin symmetric, one-nucleon knockout reactions can be used to assign γ -ray transitions and states in exotic proton-rich nuclei with a high level of confidence. Furthermore, the unexpected observation of high-spin states, most notably in ^{53}Mn , will be discussed in the context of one-nucleon knockout from a high-spin isomeric state, present in both secondary beams.

4.1.1 Spectroscopy of ^{53}Mn

The Doppler corrected γ -ray spectrum for the more neutron-rich ^{53}Mn is shown in Fig. 4.1(a), where γ -ray transitions up to an energy of 1717.5 keV were confidently observed, all of which could be identified with known γ rays [64]. Sufficient statistics were not obtained to perform a complete γ - γ coincidence analysis, though a partial analysis could be performed, as shown in Fig. 4.1(b-d), in order to partially confirm the ordering of the excited states.

In Fig. 4.1(b), the γ - γ coincidence spectrum for all γ rays in coincidence with another γ ray is shown, where the majority of the transitions observed in the γ -ray spectrum in Fig. 4.1(a) can also be observed. Interestingly, a number of weakly observed transitions in the γ -ray spectrum appear strongly in Fig. 4.1(b), such as the proposed 1117.5/1121.7 keV doublet and the 1230.3 and 1252.1 keV transitions. This suggests that these transitions must either have strong transitions in coincidence and/or form part of a high-multiplicity cascade with numerous transitions in coincidence. Indeed, as will be discussed later, in Section 4.1.3, a number of these transitions are believed to form part of a high-spin cascade, whereby the high-spin states from which they decay are populated via one-proton knockout from a high-spin isomeric state, present in the ^{54}Fe secondary beam. In Figs. 4.1(c) and 4.1(d) the background subtracted γ - γ coincidence spectra for transitions in coincidence with the 377.9 keV and 912.0 keV transitions are shown, respectively. This analysis shows that these transitions are both in coincidence with each other, though due to low statistics it was not possible to observe any other transition in coincidence, or to perform γ - γ coincidence analysis for any of the other transitions observed in this analysis.

A partial level scheme for ^{53}Mn , showing only the γ rays observed in this analysis, is presented in Fig. 4.2, where tentatively observed transitions and states are indicated by

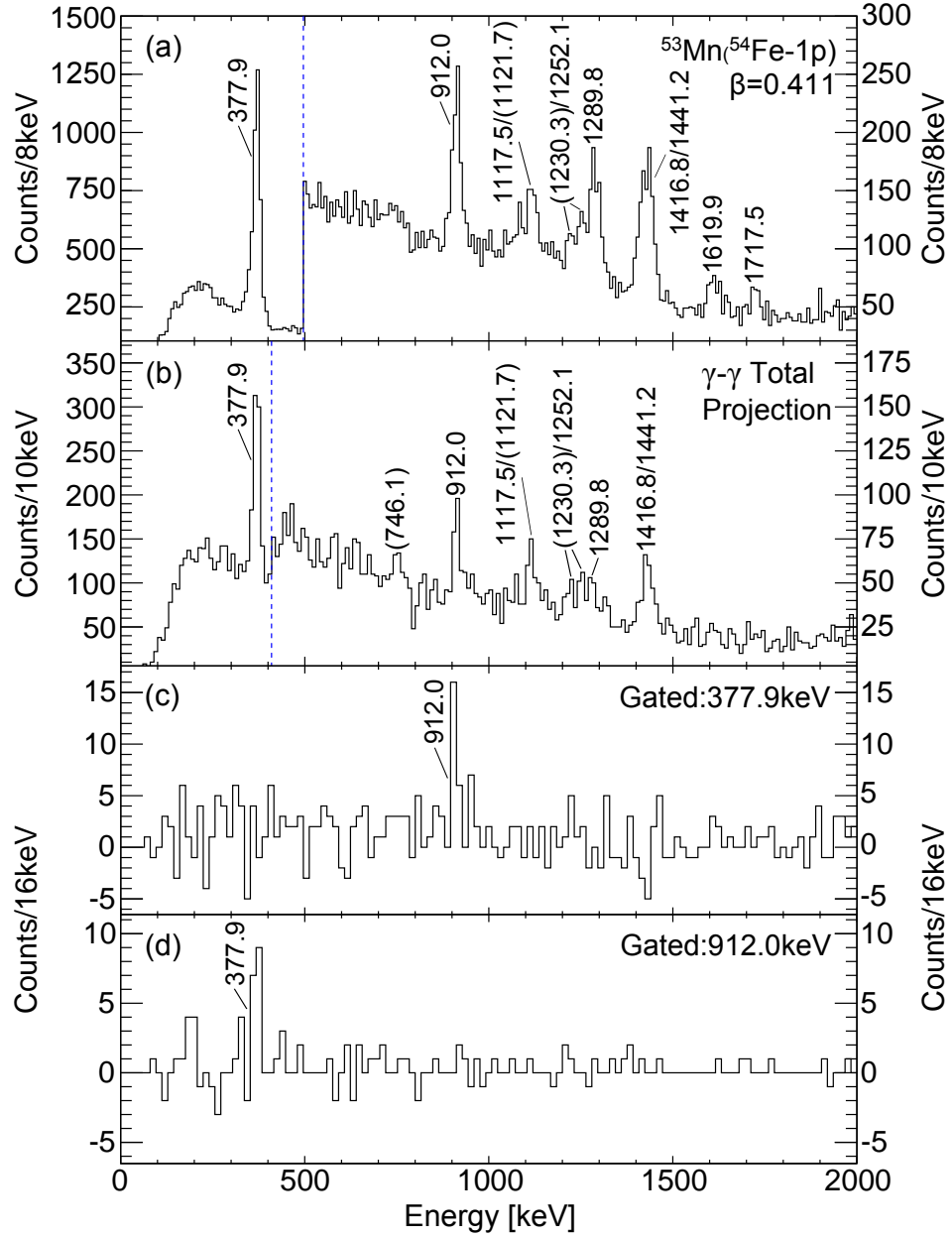


Figure 4.1: (a) Doppler corrected energy spectrum for γ rays in coincidence with ^{53}Mn fragments, populated via one-proton knockout reactions from ^{54}Fe . (b) $\gamma\text{-}\gamma$ total projection, showing all γ rays with multiplicity >1 . (c-d) Background subtracted $\gamma\text{-}\gamma$ coincidence spectra for γ rays in coincidence with (c) the 377.88 keV transition and (d) the 912.0 keV transition. All spectra have been produced using an average $\beta = \frac{v}{c}$ value of 0.411. Peaks labeled in parentheses are tentatively observed and transition energy labels for ^{53}Mn are shown from more accurate previous measurements [64].

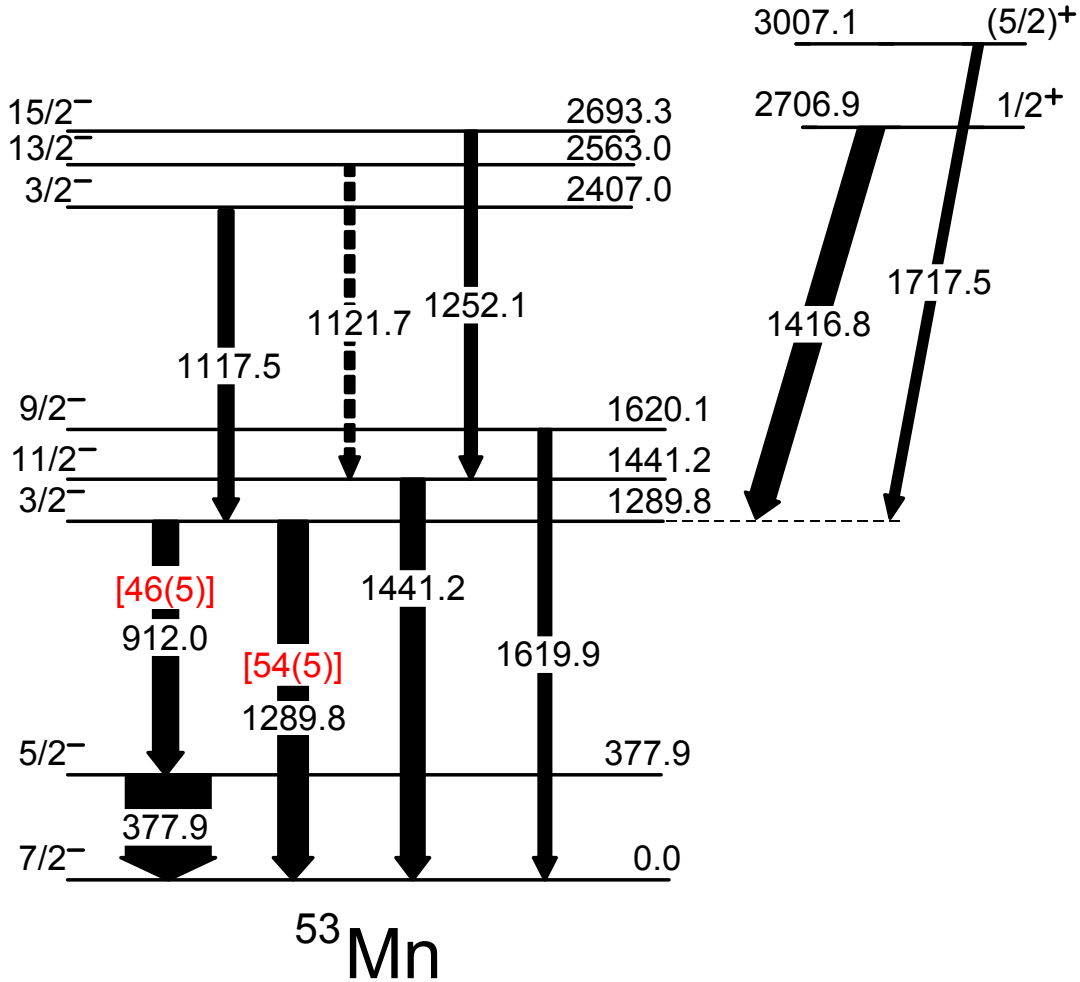


Figure 4.2: The partial energy-level scheme for ^{53}Mn as observed in this work, where information on the ordering of the γ -rays was used from Ref. [64]. Tentatively observed transitions and states are indicated by dashed lines and tentatively assigned spins are shown in brackets, see text for more details. Branching ratios for the $3/2^-$ level are indicated in red with square brackets and the energy, spin and parity labels used for ^{53}Mn come from more accurate previous measurements [64]. The widths of the arrows are proportional to the relative γ -ray intensities observed.

dashed lines. One of the states in question is the known $\frac{13}{2}^-$ state, which is only said to be tentatively observed. This is because the transition observed has a measured energy of 1118(4) keV and is therefore likely to correspond to the 1117.5 keV transition from the $(\frac{3}{2}^-)$ state, with a possible contribution from the 1121.7 keV transition from the $\frac{13}{2}^-$ state. In addition, another (weak) transition is tentatively observed, which is believed to correspond to the 1230.3(5) keV transition from the $(\frac{19}{2}^-)$ state. It will be shown later in Section 4.1.3 that the same mechanism (isomer knockout) that is believed to have populated the $\frac{15}{2}^-$ state (which is observed) is also expected to populate both the $\frac{13}{2}^-$ and $(\frac{19}{2}^-)$ states. Furthermore, as will be shown in Section 4.1.2, the observed transition at 1118(4) keV has a significantly larger relative intensity than the mirror transition in ^{53}Ni and therefore may correspond to a 1117.5/1121.7 keV doublet. Finally, the last state in question in ^{53}Mn is the $(\frac{5}{2})^+$ state, where the spin assignment of this state is considered to be tentative. More details on this assignment will be discussed later in Section 4.1.4.

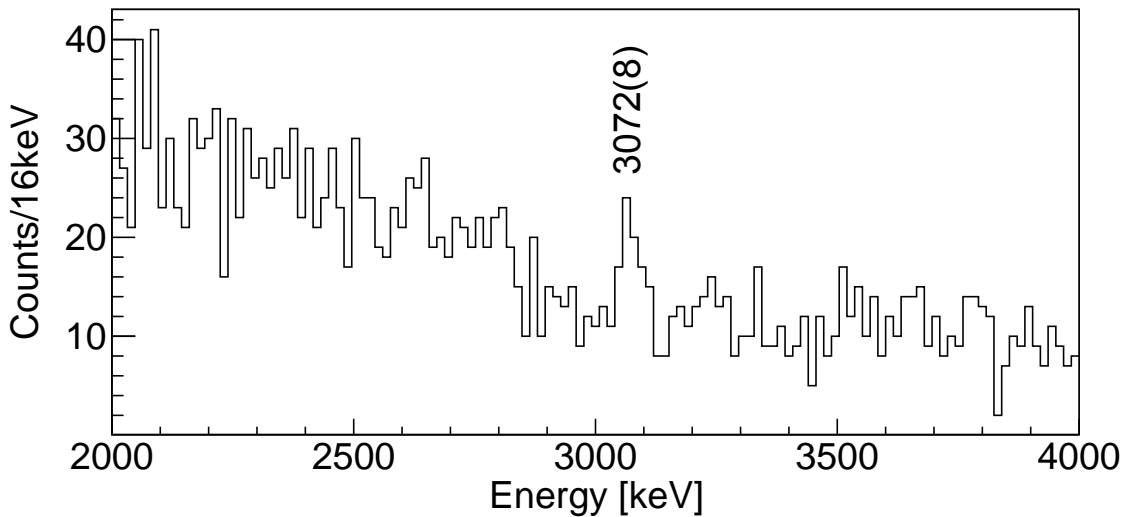


Figure 4.3: The Doppler corrected spectrum for high-energy γ rays (detected in the 90° SeGA ring) in coincidence with ^{53}Mn fragments. The spectrum has been produced using an average $\beta = \frac{v}{c}$ value of 0.411.

Only one (tentatively) observed γ -ray transition in ^{53}Mn , with a measured transition energy of 3072(8) keV (which could only be clearly observed in the 90° SeGA ring spectrum, see Fig. 4.3), could not have its position established in the level scheme shown in Fig. 4.2. This was due to there being an insufficient level of statistics to perform γ - γ coincidence analysis for this transition and due to there being a number of known transitions in ^{53}Mn with a similar transition energy. However, in cross section calculations discussed

later in Section. 4.4, a number of high-lying $7/2^-$ states are predicted, with sizeable cross sections. This transition may therefore correspond to the decay of one of these states, and may also explain the unexpected population of the $9/2^-$ state, which most likely is populated due to the decay of such a high-lying $7/2^-$ state.

The relative γ -ray intensities, $I_{\gamma(rel)}$, of the observed γ rays in ^{53}Mn were measured by fitting peaks in both the 37° and 90° SeGA rings and dividing the measured intensities by the respective detector efficiencies (calculated using Equation 3.10) of each ring, at the lab-frame energies at which the γ -rays were detected. The efficiency corrected intensities of transitions in both rings were then summed and normalised to the measured intensity of the 377.88-keV transition. The relative γ -ray intensity results are tabulated in Table 4.1.

Table 4.1: Details of the excited states in ^{53}Mn which were observed in this experiment. All values, except the relative γ -ray intensities ($I_{\gamma(\text{rel})}$) are taken from Ref. [64]. Unobserved transitions from states which are observed to be populated in this analysis are also shown for completeness, with an $I_{\gamma(\text{rel})}$ of X.

		Initial State			Final State	
E_x (keV)	J^π	$t_{1/2}$	E_γ	$I_{\gamma(\text{rel})}$	E_x (keV)	J^π
0.0	$\frac{7}{2}^-$	$3.74(4) \times 10^6$ y				
377.89(7)	$\frac{5}{2}^-$	117(6) ps	377.88(9)	100.0(35)	0.0	$\frac{7}{2}^-$
1289.83(11)	$\frac{3}{2}^-$	0.55(4) ps	912.0(3)	29.2(25)	377.89(7)	$\frac{5}{2}^-$
			1289.8(4)	33.7(29)	0.0	$\frac{7}{2}^-$
1441.15(10)	$\frac{11}{2}^-$	0.60(8) ps	1441.2(1)	26.3(30)	0.0	$\frac{7}{2}^-$
1620.12(10)	$\frac{9}{2}^-$	0.48(6) ps	1241.7(10)	X	377.89(7)	$\frac{5}{2}^-$
			1619.9(1)	14.2(21)	0.0	$\frac{7}{2}^-$
2407.03(14)	$\frac{3}{2}^-$	0.11(4) ps	1117.5	16.3(23) ¹	1289.83(11)	$\frac{3}{2}^-$
			2029.4	X	377.89(7)	$\frac{5}{2}^-$
			2406.8	X	0.0	$\frac{7}{2}^-$
2562.99(13)	$\frac{13}{2}^-$	10.7(13) ps	1121.7(1)	¹	1441.15(10)	$\frac{11}{2}^-$
2693.29(20)	$\frac{15}{2}^-$	2.7(4) ps	130.1(4)	X	2562.99(13)	$\frac{13}{2}^-$
			1252.1(2)	12.5(30)	1441.15(10)	$\frac{11}{2}^-$
2706.92(22)	$\frac{1}{2}^+$	0.8(3) ps	1416.8	29.1(32)	1289.83(11)	$\frac{3}{2}^-$
3007.13(18)	$(\frac{5}{2})^+$	>0.84 ps	1717.5	9.5(18)	1289.83(11)	$\frac{3}{2}^-$
			2629.3	X	377.89(7)	$\frac{5}{2}^-$
			3007.3	X	0.0	$\frac{7}{2}^-$

¹Proposed in this work to correspond to a 1117.5/1121.7 keV doublet, but has been fitted as a single peak here, with the intensity assigned to the 1117.5 keV transition.

4.1.2 Spectroscopy of ^{53}Ni

The Doppler corrected γ -ray spectra for both ^{53}Mn and the exotic proton-rich ^{53}Ni are presented in Fig. 4.4(a) and 4.4(b), respectively, where γ -rays up to 1718(3) keV were confidently observed in ^{53}Ni .

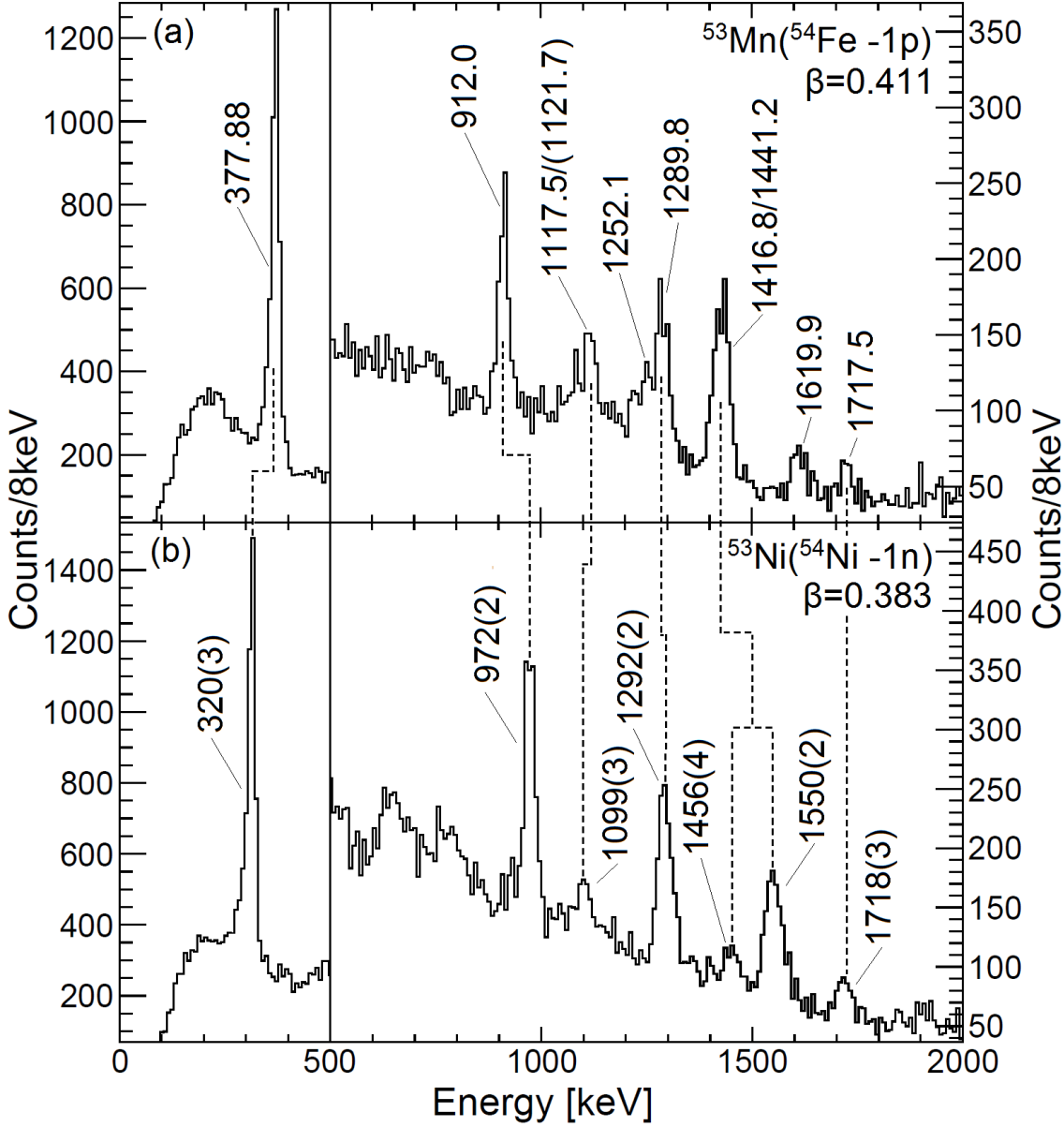


Figure 4.4: The Doppler corrected spectra for γ rays in coincidence with (a) ^{53}Mn and (b) ^{53}Ni fragments, where the spectra have been produced using average $\beta = \frac{v}{c}$ values of 0.411 and 0.383, respectively. The dashed lines indicate the proposed analogue transitions in the mirror nuclei. Transition energy labels for ^{53}Mn are shown from more accurate previous measurements [64]. Tentatively observed γ -ray transitions are indicated in parentheses.

Only two γ -ray transitions, at energies of 320(5) keV and 1453(6) keV, have been previously observed in ^{53}Ni (populated via the fragmentation of a ^{56}Ni beam), as reported by Brown *et al.* [87], where these transitions were assigned as decays from the yrast ($\frac{5}{2}^-$) and ($\frac{11}{2}^-$) states, respectively. The analysis performed here, for ^{53}Ni , confirms the observation of these two transitions, in addition to several new γ -ray transitions. A comparison of the spectra in Fig. 4.4(a) and 4.4(b) demonstrates a clear one-to-one correspondence between the the strongest γ -ray peaks observed, allowing for the identification of the proposed analogue γ -ray transitions in the mirror nuclei. However, for some of the weaker transitions, the correspondence is less clear, but some suggestions for this are discussed later in Section 4.1.3. The assignment of most of the stronger transitions in ^{53}Ni , to their analogues in ^{53}Mn , was further supported by γ - γ coincidence analysis, as shown in Fig. 4.5.

In Fig. 4.5(a), the γ - γ coincidence spectrum for all γ -rays in coincidence with other γ -rays is shown, where all of the strongly observed transitions in the γ -ray spectrum shown in 4.4(b) could be clearly identified, in addition to two weakly observed transitions at ~ 630 and ~ 930 keV. The very weak observation of the 1099 keV transition in Fig. 4.5(a), when compared to that of the proposed mirror transition, previously shown in Fig. 4.1(b), also further supports the earlier proposal made that the 1118(4) keV transition observed in ^{53}Mn in fact corresponds to a 1117.5/1121.7 keV doublet. This is because the strong appearance of this transition in Fig. 4.1(b) likely results from the 1121.7 keV transition, which is believed to form part of a high-spin cascade connected to the strongly observed 1441.2 keV transition. In order to help establish a new level scheme for ^{53}Ni , γ - γ coincidence analysis was performed for the three strongest transitions observed in Fig. 4.5(a), which were the 320(3), 972(2) and 1550(2) keV transitions. In Fig. 4.5(b), the background subtracted γ - γ coincidence spectrum, gated on the 320(3) keV transition, is shown, where six transitions were detected in coincidence. This included three previously observed transitions in the γ -ray spectrum at energies of 972(2), 1550(2) and 1718(3) keV and three previously unobserved transitions at energies of ~ 200 , ~ 280 and ~ 3666 keV. It is possible that the first two unobserved transitions could correspond to some residual background not fully subtracted, while the ~ 3666 keV transition most likely corresponds to the decay of some high-lying state populated in the one-neutron knockout reaction. In Fig. 4.5(c), the background subtracted γ - γ coincidence spectrum for transitions in coincidence with the 972(2) keV transition is shown, where three transitions were detected in coincidence, at energies of 972(2), 1550(2) and 1718(3) keV. While in Fig. 4.5(d), the background

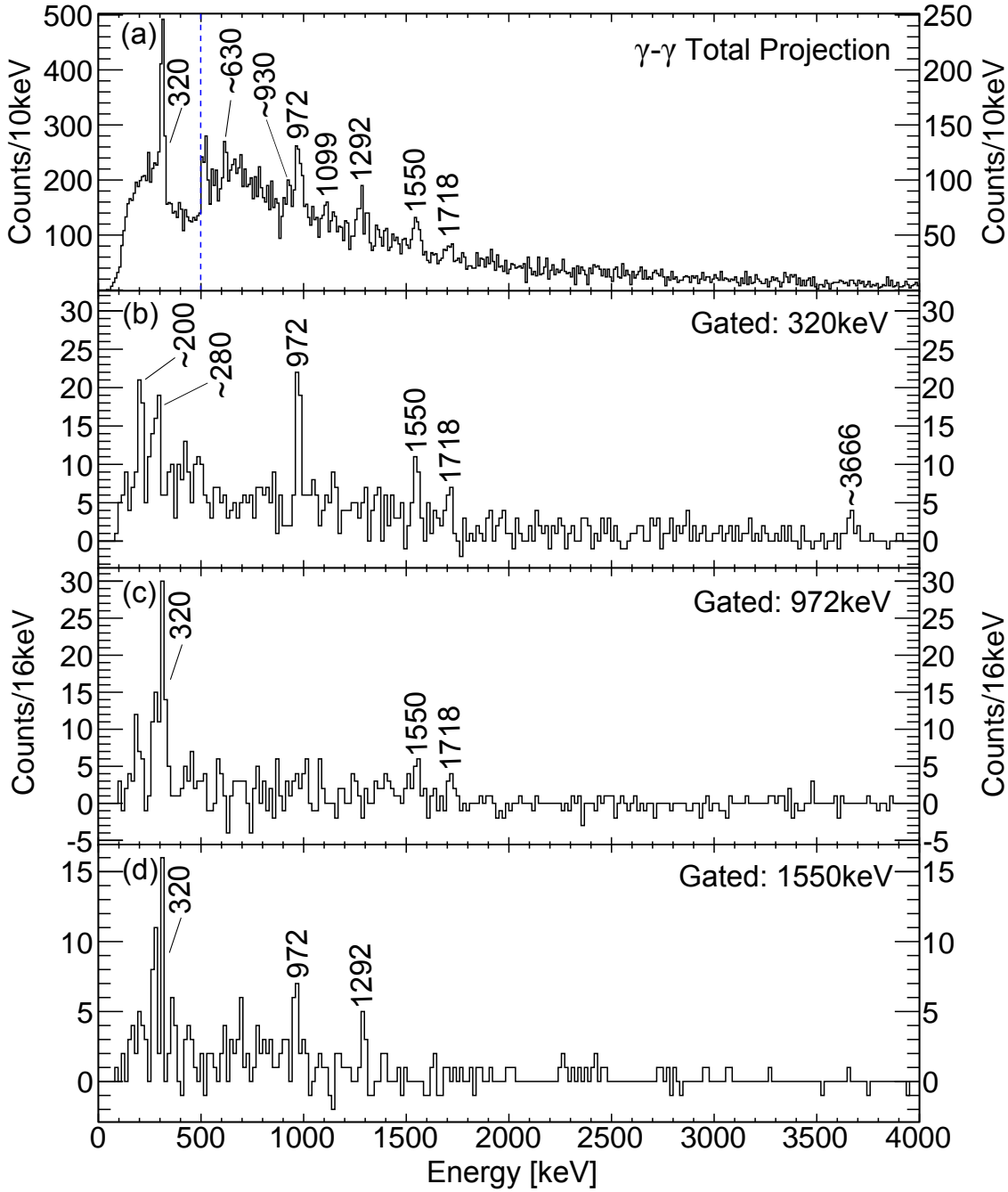


Figure 4.5: (a) γ - γ total projection spectra for ^{53}Ni , showing all γ -rays with multiplicity >1 . (b-d) Background subtracted γ - γ coincidence spectra for ^{53}Ni , showing γ -rays in coincidence with (b) the 320(3) keV transition, (c) the 972(2) keV transition and (d) the 1550(2) keV transition. All spectra have been produced using an average $\beta = \frac{v}{c}$ value of 0.383.

subtracted γ - γ coincidence spectrum for transitions in coincidence with the 1550(2) transition is shown, where three transitions were also detected in coincidence, at energies of

320(3), 972(2) and 1292(2) keV. Therefore, using a combination of γ - γ coincidence analysis, spectral comparison and transition intensity arguments a new level scheme for ^{53}Ni was deduced, as shown in Fig. 4.6, where the spins and parities are assigned on the basis of mirror symmetry arguments. Whilst the direct, mirrored, reaction process does give confidence in the spin/parity assignments presented here, since they have not been formally measured they are presented in parentheses. Furthermore, in previous work performed for ^{53}Ni [87] it was not possible to accurately measure the energy of the γ -ray emission from the $(\frac{5}{2}_1^-)$ state, due to its long half-life. However, this has now been established as 320(3) keV due to the energy difference between the 972(2) keV and 1292(2) keV prompt γ -ray transitions observed in this analysis.

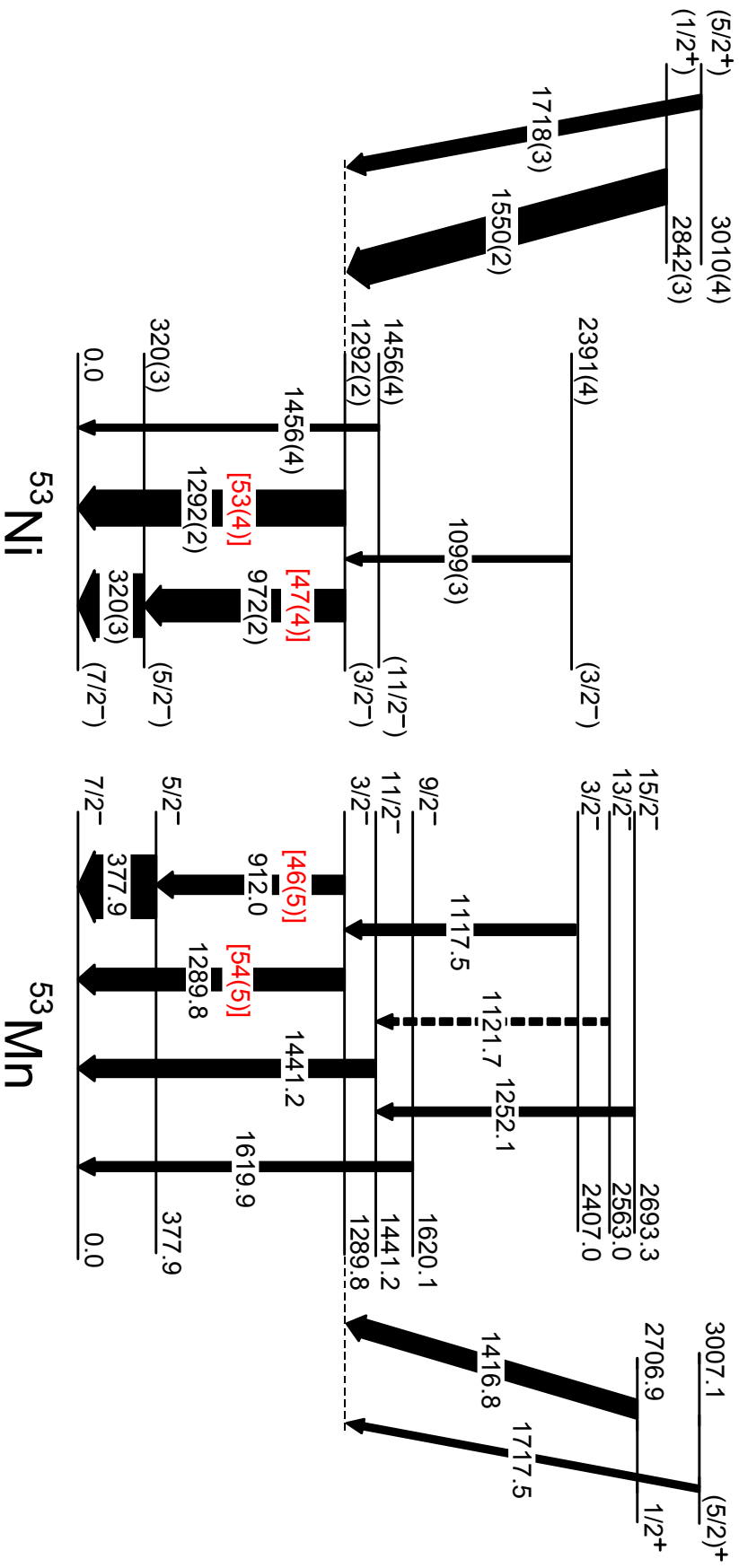


Figure 4.6: The energy level schemes for ^{53}Ni and ^{53}Mn as observed in this work. The spins and parities are in parentheses for ^{53}Ni as the assignments are made on mirror-symmetry arguments. Tentative transitions are indicated by dashed lines. Branching ratios for the $\frac{3}{2}_1^-$ level are indicated in red with square brackets and the energy labels used for ^{53}Mn come from more accurate previous measurements [64]. The widths of the arrows are proportional to the relative γ -ray intensities observed.

4.1.3 Population of the Observed States

The population of most of the states observed in this work for ^{53}Mn and ^{53}Ni can be well understood by simply considering the reaction mechanism used to populate these nuclei. For example, one-nucleon knockout reactions from ^{54}Ni (^{54}Fe), with a ground state of 0^+ (wavefunction shown in Table 4.2), are expected to populate a range of negative-parity states with $J^\pi = \frac{7}{2}^-$, $\frac{3}{2}^-$, $\frac{5}{2}^-$ and $\frac{1}{2}^-$ through the removal of $f_{\frac{7}{2}}$, $p_{\frac{3}{2}}$, $f_{\frac{5}{2}}$ and $p_{\frac{1}{2}}$ neutrons (protons) near the Fermi level. Furthermore, since both parent nuclei are also below the doubly magic ^{56}Ni , with a fully closed $f_{\frac{7}{2}}$ shell of protons and neutrons, the spectroscopic strength to these $\frac{1}{2}^-$, $\frac{3}{2}^-$ and $\frac{5}{2}^-$ states is expected to be weak. This is additionally supported by measured spectroscopic factors for proton removal from ^{54}Fe to ^{53}Mn [110], which indicates that the bulk of the $f_{\frac{7}{2}}$ spectroscopic strength lies in the $J^\pi = \frac{7}{2}^-$ ground state. Thus, the direct population of all the negative parity excited states in ^{53}Ni and ^{53}Mn is expected to be weak. This is verified in Fig. 4.6, where it is seen that a significant amount of the intensity observed, proceeding through the excited states in these mirror nuclei, comes from the direct population of positive-parity states with $J^\pi = (\frac{5}{2})^+$ and $\frac{1}{2}^+$, through the removal of $d_{(\frac{5}{2})}$ and $s_{\frac{1}{2}}$ neutrons(protons) from ^{54}Ni (^{54}Fe).

Table 4.2: Ground state of ^{54}Fe , calculated using the ANTOINE code [24], in the full fp valence space using the KB3G interaction [25]. All ground state admixtures greater than 1% are shown.

^{54}Fe	Proton Occupation				Neutron Occupation			
Probability	$1f_{\frac{7}{2}}$	$2p_{\frac{3}{2}}$	$1f_{\frac{5}{2}}$	$2p_{\frac{1}{2}}$	$1f_{\frac{7}{2}}$	$2p_{\frac{3}{2}}$	$1f_{\frac{5}{2}}$	$2p_{\frac{1}{2}}$
0.5418	6	0	0	0	8	0	0	0
0.02590	6	0	0	0	7	0	1	0
0.02610	6	0	0	0	7	1	0	0
0.02230	6	0	0	0	6	2	0	0
0.05728	6	0	0	0	6	0	2	0
0.04359	5	0	1	0	7	0	1	0
0.01833	5	1	0	0	7	1	0	0
0.01594	4	2	0	0	8	0	0	0
0.06222	4	0	2	0	8	0	0	0

The observation of high-spin states in the daughter nuclei however, particularly in the case of ^{53}Mn , is most likely due to the presence of an isomeric state in both of the secondary beams. This is because, as discussed previously, the maximum spin-parity state that can be populated in the direct, one-nucleon removal from ^{54}Fe or ^{54}Ni , with a ground state of 0^+ , is $\frac{7}{2}^-$. Indeed, a 10^+ spin-trap isomer has been previously observed in both ^{54}Fe and ^{54}Ni , with measured half-lives of 364(7) ns and 152(4) ns, respectively [90, 91]. Both of these isomers are sufficiently long-lived to still be present in the secondary beam at the secondary target position, after their initial population at the production target, since the ToF between these two targets is ~ 300 ns.

One-nucleon knockout from these isomers could, in principle, populate a range of high-spin states from $\frac{13}{2}^-$ to $\frac{27}{2}^-$ in the daughter nuclei, and could explain in particular the observation of the $\frac{15}{2}^-$ and $\frac{13}{2}^-$ states in ^{53}Mn . Additional support for this argument comes from cross section calculations performed (using the same approach as described in Section 2.4.2) but assuming direct proton knockout from this isomer in ^{54}Fe to ^{53}Mn . Fig. 4.7 shows a theoretically-produced decay scheme, using experimental energies and branching ratios, assuming that these states are populated with the theoretically calculated cross sections. These calculations suggest that the entirety of the intensity from the strongly populated states will feed through the $\frac{15}{2}^-$ and $\frac{13}{2}^-$ states and collect in the $\frac{11}{2}^-$ state. This may explain the strong γ -ray transition observed from this state, particularly in ^{53}Mn . This population of high-spin states does not appear to be mirrored in both daughter nuclei but instead appears to be much stronger in ^{53}Mn , as can be seen in Fig. 4.6. This could be due to different initial isomeric ratios in the secondary beams, but will also be due, in part, to the shorter half-life of the ^{54}Ni 10^+ isomer, compared with that of ^{54}Fe . This will therefore result in a smaller residual population of the isomer at the secondary target for knockout from ^{54}Ni to ^{53}Ni .

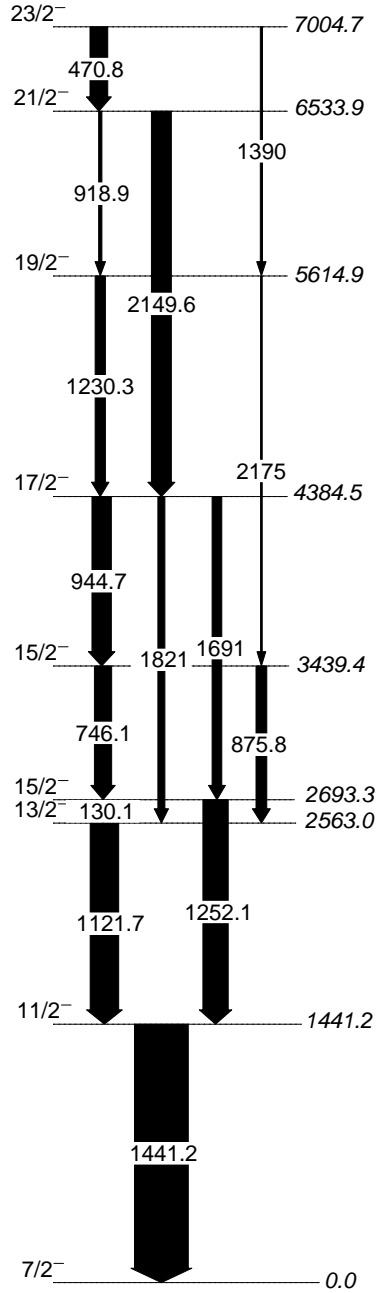


Figure 4.7: An energy level scheme of ^{53}Mn showing the states strongly populated in one-proton knockout from the ^{54}Fe 10^+ spin-trap isomer. The population of each state is predicted from cross section calculations using the method described in Section 2.4.2, with spectroscopic factors calculated using the ANTOINE code [24] in the full fp valence space using the KB3G interaction [25]. Information on the state energies and branching ratios were used from previous experimental studies on ^{53}Mn [64].

4.1.4 Spin Assignment of the $(\frac{5}{2})^+$ State

The spin assignment of the 3007.1-keV [64] positive-parity state in ^{53}Mn , $J^\pi = (\frac{5}{2})^+$ in Fig. 4.6, is uncertain. Its first observation in a proton-stripping reaction was shown to correspond to $l = 2$ [92]. From this, it was assumed to correspond to removal of a $d_{\frac{3}{2}}$ proton from ^{54}Fe , and thus the state would have an assignment of $\frac{3}{2}^+$. Subsequent papers have since used this assignment. However, the current evaluated nuclear data compilation [64] has this state as a tentative $\frac{5}{2}^+$, based on the observed direct decay to the ground state, assumed to be a dipole transition. Earlier work [93] has demonstrated, through energy centroid shift methods, that this state has a half-life lower limit of 0.84 ps. In order to gain some further information on this half-life, and to help resolve this assignment, a Doppler correction analysis was performed, whereby the optimum β -value to align a γ -ray peak, in both the 37° and 90° SeGA rings, is determined. This analysis has shown that a β -value of ~ 0.41 is required for the other fast transitions in ^{53}Mn with half-lives ~ 1 ps. These transitions are emitted with the largest value of β as they are emitted from within the target volume. It takes around 8 ps for the beam to traverse the target thickness and therefore for states with half-lives of the order of 10 ps and greater, the majority of decays take place downstream of the target, where the emitter velocity has been reduced due to energy loss in the target. For example, we find a β -value of 0.390 is required to align the γ rays associated with the decay of the long-lived $J^\pi = \frac{5}{2}_1^-$ state, which is known to decay downstream of the target. These numbers are consistent with LISE++ [73] calculations that predict a change in β from the center (i.e. the average interaction point) to the back of the target from 0.409 to 0.394. Our analysis for the 1717.5-keV transition yielded a β -value of 0.416(6), where the error comes from our estimate of the uncertainty in aligning the transition energies in the two detector rings. Thus, our experimental data clearly point to the average point of decay being inside the target volume, and so we can put a safe upper limit on the half-life of ~ 4 ps. The state in question is known to decay to the $\frac{7}{2}^-$ ground state with a 14% branch [94] and depending on whether it has a spin of $\frac{3}{2}$ or $\frac{5}{2}$ will determine whether it decays via an M2 or E1 transition. Typical transition strengths for M2 transitions in the $A=45-90$ region have been observed in the range of $0.02 \rightarrow 0.2$ W.u. whilst E1 transitions have typically been observed in the range of $(10^{-6} \rightarrow 10^{-4})$ W.u. [95]. With a maximum 4 ps half-life for the 3007.1-keV state, the M2 and E1 transition strengths would be a minimum of 0.3 W.u. and 6×10^{-7} W.u., respectively. This lower-limit M2 transition strength is above the typical range, but nevertheless below the recommended

upper limit of 1 W.u. proposed in reference [95]. Thus, it is not possible to make a definitive assignment here, although the systematics suggest that the current assignment of $\frac{5}{2}^+$ is most likely.

4.1.5 Mirror Lifetime Measurements

Due to the long half-life (117(6) ps [96]) of the $\frac{5}{2}_1^-$ state in ^{53}Mn (and presumably of that in ^{53}Ni), decays from this state occur up to a few cm downstream of the target. This has the effect of smearing the effective angle for the SeGA detectors which in turn yields a broad, asymmetrical lineshape, with a centroid below the correct energy, as shown in Fig. 4.8.

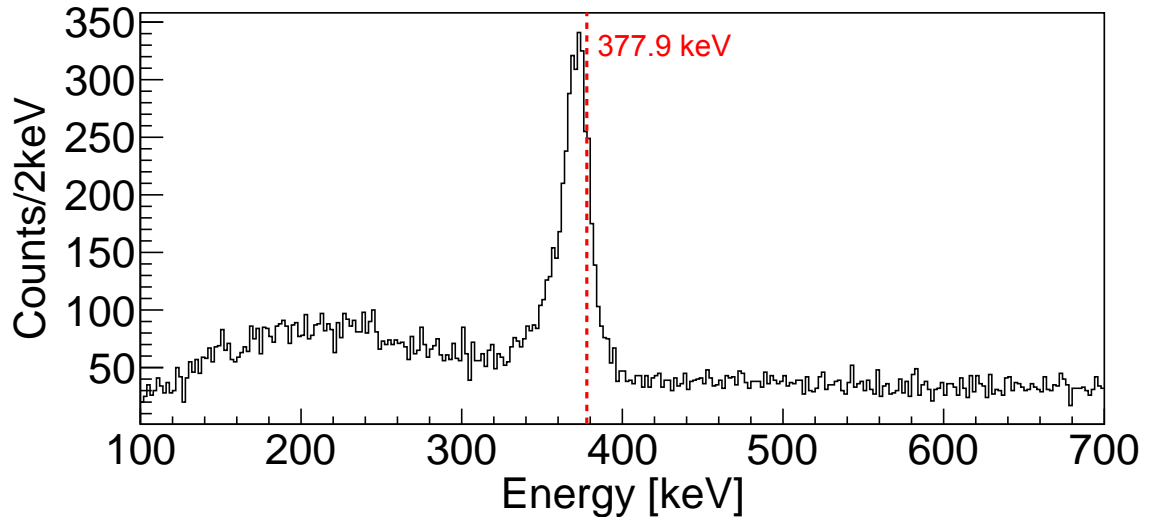


Figure 4.8: The γ -ray spectrum for γ rays in coincidence with ^{53}Mn fragments, showing the shift in the 377.9-keV transition due to its 117(6)ps half-life [96]. The spectrum has been produced using an average $\beta = \frac{v}{c}$ value of 0.411.

This presented the opportunity for measurement of lifetimes, through a lineshape analysis, for the analogue transitions in this mirror pair. Half-lives were extracted through comparison of experimental γ -ray spectra with simulations generated using a dedicated lifetime code developed at NSCL [97] utilising the GEANT4 framework [98], as discussed in Section 3.4.4. Although the simulation package also allows for the addition of feeding states, each of which have their own independent lifetimes and intensities, the lifetimes of the observed states feeding the $\frac{5}{2}_1^-$ state in ^{53}Mn are known to be small (< 1 ps), and therefore were not included. It was assumed through mirror symmetry arguments that these states were also short lived enough to be neglected for ^{53}Ni . A second-order polynomial

background, which accurately replicated the experimental backgrounds in either the 37° and 90° SeGA rings, was added to the simulations over the region of lifetime sensitivity.

The simulations were produced for both the 37° and 90° SeGA rings and fitted to the experimental spectra using a χ^2 minimisation method. By fitting a range of simulated γ -ray spectra, varying either the half-life of the state (at a fixed transition energy) or the energy of the transition (at a fixed state half-life), to the experimental γ -ray spectra, a half-life and energy could both be measured for the $\frac{5}{2}_1^-$ state in both ^{53}Ni and ^{53}Mn . The resulting $\chi^2 - \chi_{min}^2$ plots for ^{53}Ni are shown in Fig. 4.9, where Fig. 4.9(a) shows the results for the simulated fits to the 37° experimental ring and Fig. 4.9(b) shows the results for the simulated fits to the 90° experimental ring. Since the results of the simulated fits in each SeGA detector ring were consistent with one another it was possible to combine these results into a single $\chi^2 - \chi_{min}^2$ plot, see Fig. 4.9(c), from which an energy of 320.5(2) keV and a half-life of 198(8) ps could be determined, where errors only contain the statistical component, derived from $\chi_{min}^2 + 1$ (corresponding to $\pm 1\sigma$) as shown by the solid line ellipse. Since both the energy and half-life were allowed to vary independently, a more complete analysis could be performed for evaluating the statistical error component. In order to determine the systematic error contribution, the same prescription as described in Ref [97] was adopted, in which lifetime measurements were performed for states with a similar half-life and decay energy to those investigated in this work. A number of systematic error contributions were identified in this study, including uncertainties due to ambiguities in the geometry of the setup (3%), γ -ray anisotropy effects (1.5%), assumptions in the background (3%) and finally effects due to feeding (1%), which in this case would include feeding of the $\frac{5}{2}_1^-$ state from short-lived states. Adding these uncertainties in quadrature results in an overall systematic error of 4.6%. Taking into account both the systematic and statistical error contributions, a half-life of 198(12) ps was determined for the ($\frac{5}{2}_1^-$) state in ^{53}Ni .

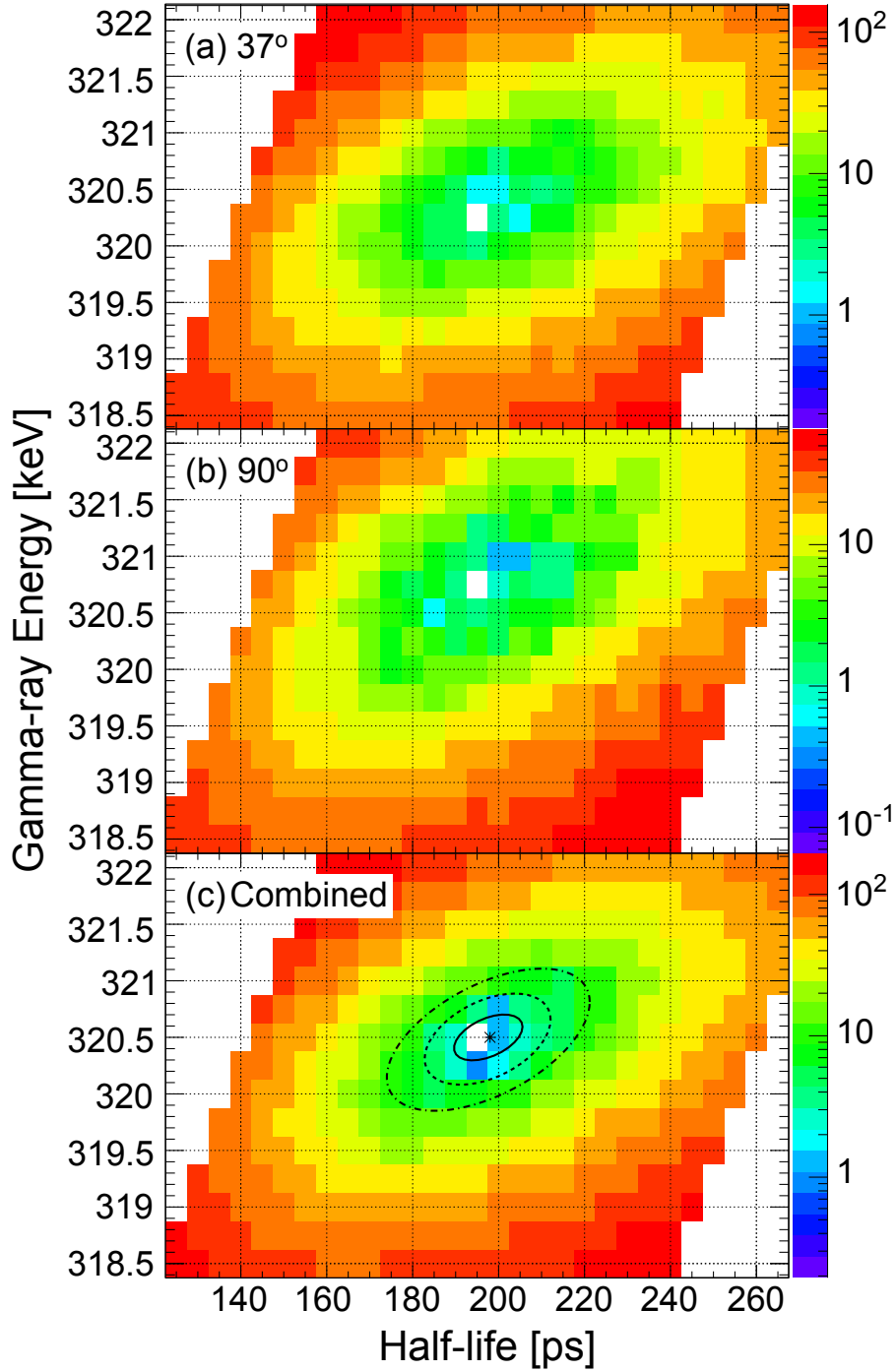


Figure 4.9: Plot of $\chi^2 - \chi_{min}^2$ for simulated spectra (varying either energy or half-life) fitted to the ^{53}Ni experimental spectra for the $J^\pi: (\frac{5}{2}_1^-) \rightarrow (\frac{7}{2}_{g.s.}^-)$ transition in (a) the 37° SeGA ring and (b) the 90° SeGA ring. (c) The combined $\chi^2 - \chi_{min}^2$ plot of (a) and (b) where the measured half-life and energy are shown by an asterisk at 320.5 keV and 198 ps. Statistical errors in (c) are shown by ellipses, whereby the $\pm 1\sigma$, $\pm 2\sigma$ and $\pm 3\sigma$ errors are represented by a solid line, a dashed line and a dash-dot line respectively. See text for more details.

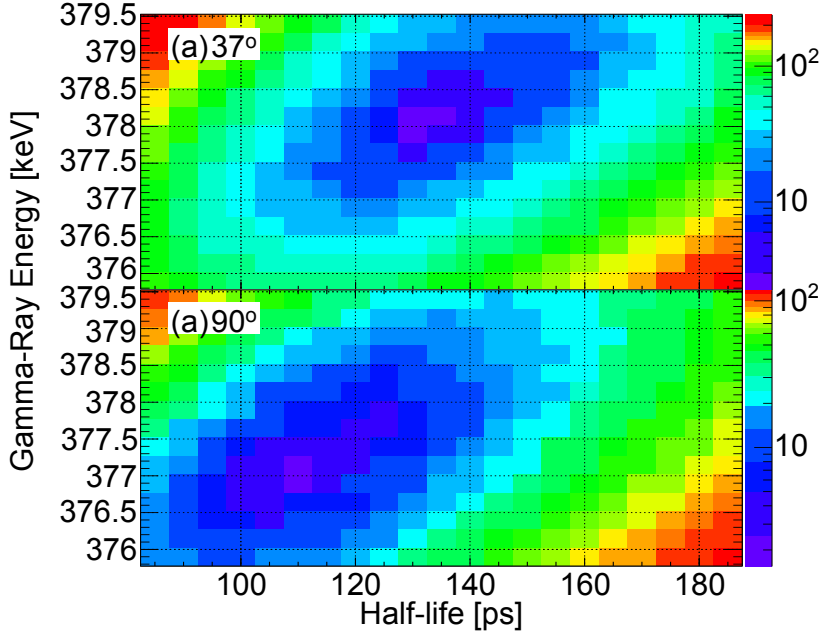


Figure 4.10: Plot of $\chi^2 - \chi_{min}^2$ for simulated spectra (varying either energy or half-life) fitted to the ^{53}Mn experimental spectra for the $J^\pi: (\frac{5}{2}^-) \rightarrow (\frac{7}{2}^-_{g.s.})$ transition in (a) the 37° SeGA ring and (b) the 90° SeGA ring. Measured transition energies (half-lives) of 378.2 keV (134 ps) and 377.1 keV (111 ps) were obtained for the (a) the 37° SeGA ring and (b) the 90° SeGA ring data, respectively, see text for more details.

An identical approach was followed for the $\frac{5}{2}^-$ state in ^{53}Mn , as a test of the method. However, in this case, the results for the simulated fits to the individual 37° and 90° SeGA rings were only consistent at the $\sim 2\text{-}\sigma$ level, whereby half-life measurements of 134(10) ps and 111(8) ps were made for the 37° and 90° data, respectively, as shown in Fig. 4.10(a) and 4.10(b). The discrepancy in these half-life measurements may have resulted due to uncertainties in the target position, which was calculated to be $\sim 3.5\text{mm}$ downstream of the centre of the target chamber. In order to conservatively account for this, an additional systematic error of half the difference between the two independent half-life results was included in the final error analysis for the weighted average result. This resulted in a weighted average half-life of 120(14) ps for the $\frac{5}{2}^-$ state in ^{53}Mn , which compares very favorably with the previous measurement of 117(6) ps [96]. Furthermore, the lowest χ^2 fits to both the 37° and 90° SeGA ring data for ^{53}Ni and ^{53}Mn are also shown in Fig. 4.11.

The relative intensities (normalised to the 320(3) keV transition) for the observed γ -rays in ^{53}Ni are tabulated in Table 4.3, where the relevant transitions observed in ^{53}Mn are also shown, in addition to the results for the lifetime measurements performed for

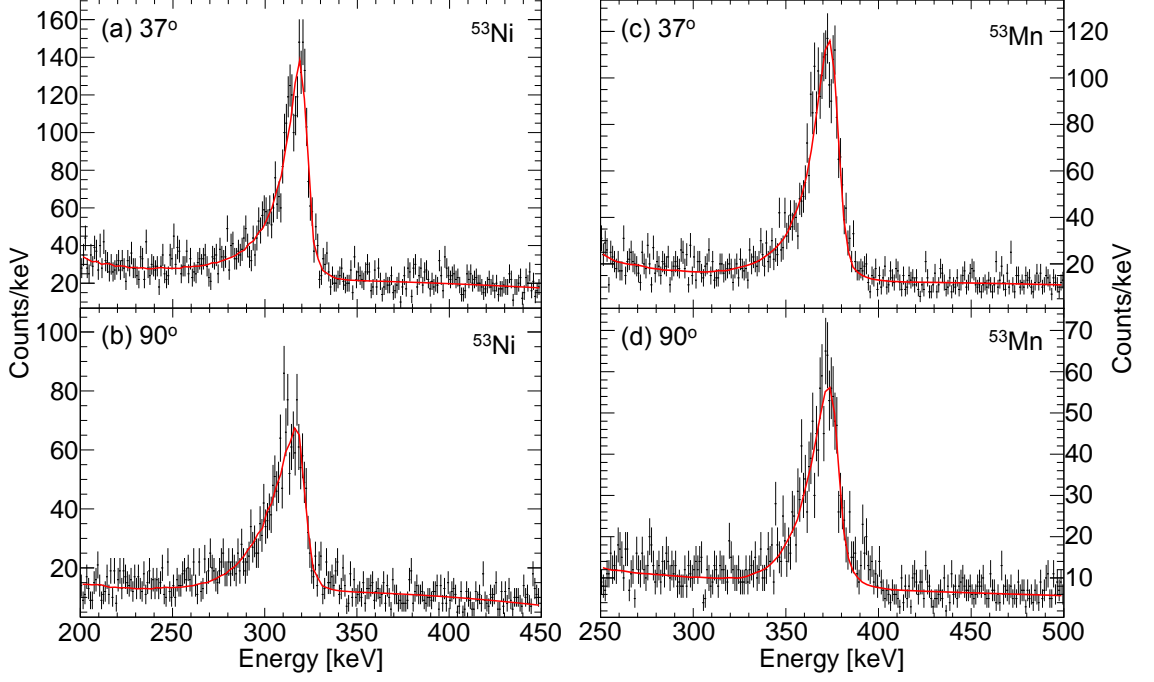


Figure 4.11: The best-fit simulated line-shapes (red line) to the experimental data (black points), as determined using a reduced χ^2 , for (a,c) the 37° SeGA ring data and (b,d) the 90° SeGA ring data for the $J^\pi: \frac{5}{2}_1^- \rightarrow \frac{7}{2}_{g.s.}^-$ transition in ^{53}Ni (320 keV) and ^{53}Mn (377.9 keV).

the $J^\pi = \frac{5}{2}_1^-$ state in both ^{53}Mn and ^{53}Ni . The agreement between the relative γ -ray intensities of the isobaric analogue transitions in the mirror pair appears to be poor, though this is mainly due to the much stronger observed intensity of the 377.9 keV transition in ^{53}Mn , where possible reasons for this are discussed in more detail in Section 4.4. Despite this discrepancy however, the overall agreement between the observed γ -ray intensities in the mirror pair is good, as can also be seen in Fig. 4.6. In addition, it was also possible to measure the branching ratios of the two decay paths from the $\frac{3}{2}_1^-$ state in both ^{53}Ni and ^{53}Mn . In ^{53}Ni , branching ratios of 47(4)% and 53(4)% were measured for the 972(2) and 1292(2) keV transitions, respectively, while in ^{53}Mn , branching ratios of 46(5)% and 54(5)% were measured for the 912.0 and 1289.8 keV transitions, respectively, where the latter measurements are also in very good agreement with previous studies, where branching ratios of 46% and 54% were also obtained for these transitions in ^{53}Mn [64]. Furthermore, the agreement between the observed branching ratios of the $\frac{3}{2}_1^-$ state in both nuclei is also very good.

Table 4.3: Details of the new excited states observed in ^{53}Ni and the relevant isobaric analogue states observed in ^{53}Mn . Ground state and excited state half-lives for ^{53}Ni and ^{53}Mn , with the exception of the measured half-life for the $\frac{5}{2}^-$ state in ^{53}Ni and the upper limit set for the $(\frac{5}{2})_1^+$ state in ^{53}Mn , are taken from Ref. [64]. State and transition energies for ^{53}Mn are taken from more accurate previous measurements [64].

		Initial State			Final State	
E_x (keV)	J^π	$t_{1/2}$	E_γ	$I_{\gamma(rel)}$	E_x (keV)	J^π
^{53}Ni						
0	$(\frac{7}{2}^-)$	45(15) ms				
320(3)	$(\frac{5}{2}^-)$	198(12) ps	320(3)	100.0(36)	0	$(\frac{7}{2}^-)$
1292(2)	$(\frac{3}{2}^-)$		972(2)	49.5(32)	320(3)	$(\frac{5}{2}^-)$
			1292(2)	55.3(41)	0	$(\frac{7}{2}^-)$
1456(4)	$(\frac{11}{2}^-)$		1456(4)	9.5(27)	0	$(\frac{7}{2}^-)$
2391(4)	$(\frac{3}{2}_2^-)$		1099(3)	11.2(23)	1292(2)	$(\frac{3}{2}^-)$
2842(3)	$(\frac{1}{2}^+)$		1550(2)	53.9(49)	1292(2)	$(\frac{3}{2}^-)$
3010(4)	$(\frac{5}{2}^+)$		1718(3)	21.6(32)	1292(2)	$(\frac{3}{2}^-)$
^{53}Mn						
0	$\frac{7}{2}^-$	$3.74(4) \times 10^6$ y				
377.89(7)	$\frac{5}{2}^-$	117(6) ps	377.88(9)	100.0(35)	0	$\frac{7}{2}^-$
1289.83(11)	$\frac{3}{2}^-$	0.55(4) ps	912.0(3)	29.2(25)	377.89(7)	$\frac{5}{2}^-$
			1289.8(4)	33.7(29)	0	$\frac{7}{2}^-$
1441.15(10)	$\frac{11}{2}^-$	0.60(8) ps	1441.2(1)	26.3(30)	0	$\frac{7}{2}^-$
2407.03(14)	$\frac{3}{2}_2^-$	0.11(4) ps	1117.5	16.3(23) ¹	1289.83(11)	$\frac{3}{2}^-$
2706.92(22)	$\frac{1}{2}^+$	0.8(3) ps	1416.8	29.1(32)	1289.83(11)	$\frac{3}{2}^-$
3007.13(18)	$(\frac{5}{2})^+$	<4 ps	1717.5	9.5(18)	1289.83(11)	$\frac{3}{2}^-$

¹Proposed in this work to correspond to a 1117.5/1121.7 keV doublet, but has been fitted as a single peak here, with the intensity assigned to the 1117.5 keV transition.

4.2 Population of States in ^{52}Co ($T_z = -1$)

States in the exotic proton-rich ^{52}Co were populated via two different reactions in the experiment performed at MSU. Firstly, and more importantly for the majority of the analysis discussed in this section, states were populated via direct one-neutron knockout from a ^{53}Co secondary beam, while in a second reaction, states were populated via the indirect $1n1p$ removal from a ^{54}Ni secondary beam. In this section it will be discussed how a range of spin-parity states were populated in ^{52}Co , including several high-spin states with angular momentum $J > 7$, which could only be populated through these reactions in the presence of high-spin isomeric state(s) in the secondary beams.

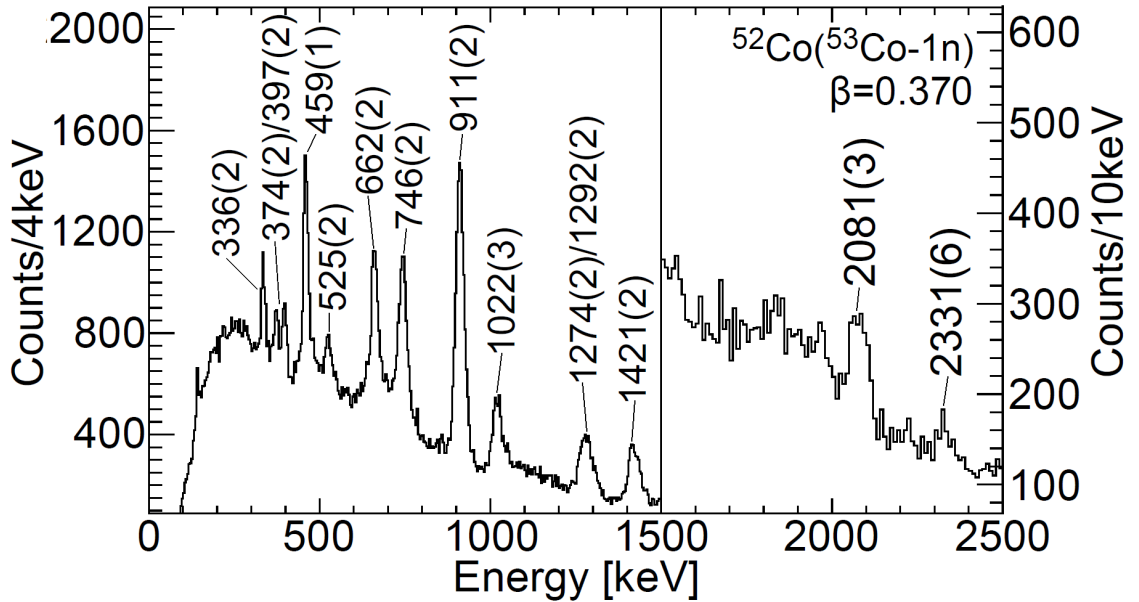


Figure 4.12: The Doppler corrected γ -ray spectra for γ rays in coincidence with ^{52}Co fragments populated via one-neutron knockout from ^{53}Co . The spectrum has been produced using an average $\beta = \frac{v}{c}$ value of 0.370.

4.2.1 Spectroscopy of ^{52}Co

The Doppler corrected γ -ray spectra for ^{52}Co , populated either via direct one-neutron knockout from ^{53}Co or indirect $1n1p$ removal from ^{54}Ni , are presented in Fig. 4.12 and 4.13, respectively. In ^{52}Co , only two γ -ray transitions have been previously observed, at energies of 2407(1) keV and 141(1) keV, as reported in Ref. [99], whereby these transitions were additionally detected to be in coincidence with each other, as reported in Ref. [100].

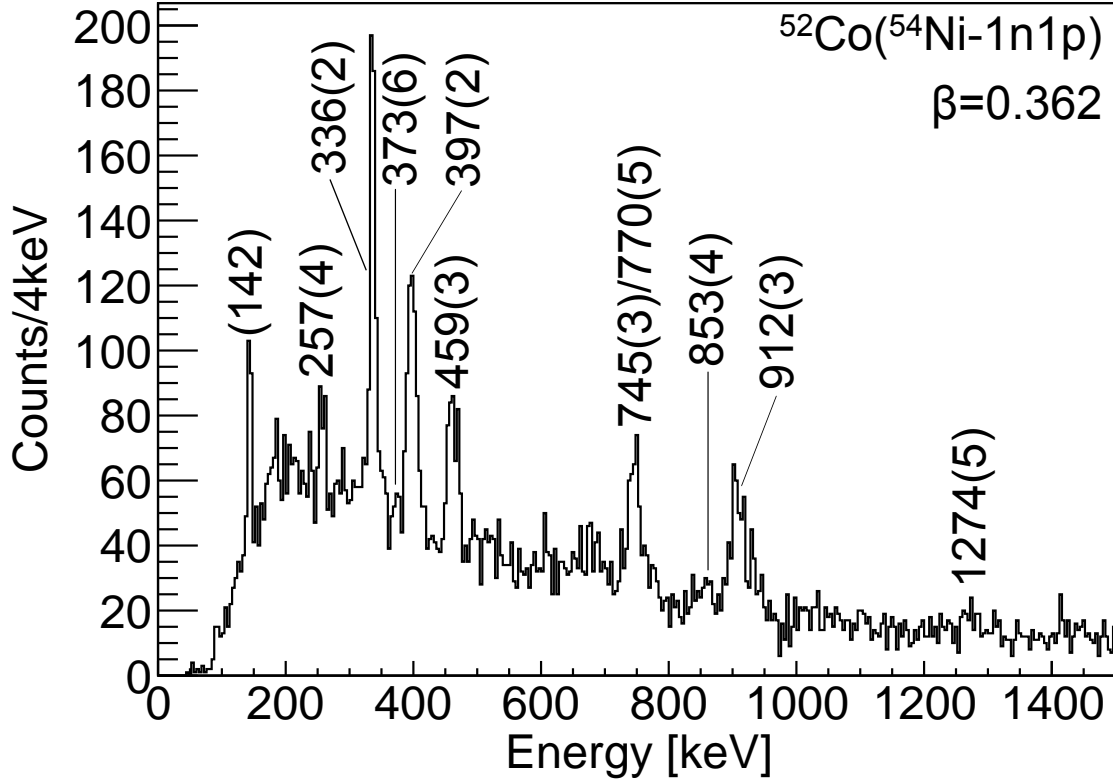


Figure 4.13: The Doppler corrected γ -ray spectra for γ rays in coincidence with ^{52}Co fragments populated either via $1n1p$ removal from ^{54}Ni . The spectrum has been produced using an average $\beta=\frac{v}{c}$ value of 0.362.

Through the use of mirror symmetry arguments, i.e. comparing with well-known transitions in the mirror nucleus ^{52}Mn , these transitions were (tentatively) proposed to correspond to the $J^\pi:(0_1^+) \rightarrow (1_1^+)$ and $J^\pi:(1_1^+) \rightarrow (2_1^+)$ transitions, respectively [99,100]. However, excitation energies for the (0^+) , (1_1^+) and (2_1^+) states in ^{52}Co could not be established, due to the non-observation of γ decays from the (2_1^+) state to the (6^+) ground state. This is because, as very recently reported in Ref. [101], this state is known to be both isomeric, with a measured half-life of 102(6) ms, and decay only via β^+ decay to ^{52}Fe . In contrast, the proposed 2_1^+ IAS in ^{52}Mn , with a measured half-life of 21.1(2) minutes and state energy of 377.89(7) keV [65,102], has been observed to decay via two decay branches, either via β^+ decay (98.22(5)%) to ^{52}Cr or an internal transition (1.78(5)%) to the 6^+ ground state [65,103]. This is due to the Fermi β decay of this state in ^{52}Mn being forbidden, which, coupled with the smaller Q_β -value, makes the decay of this state much slower, and therefore results in competition with the slow E4 transition [101]. The work presented in this section therefore, represents the first detailed study of excited states in ^{52}Co , and also

greatly extends upon the work previously performed for this nucleus.

In both population methods of ^{52}Co , many new γ -ray transitions were observed, as shown in Figs. 4.12 and 4.13, though with significantly greater statistics in the one-neutron knockout reaction. It was therefore due to the greater statistics, the strong presence of an isomer in the ^{53}Co secondary beam and the direct nature of the one-neutron knockout reaction, for which a theoretical framework could be established, why the majority of the analysis conducted in the following sections is based upon this reaction. In Section 4.2.2 it will be discussed how, through the use of γ - γ coincidence analysis, a new level scheme of high-spin states in ^{52}Co was established, indicating the presence of an isomeric state in the ^{53}Co secondary beam. While in Section 4.2.3, it will be discussed how the remaining strong transitions were identified using a range of different methods in order to help establish a level scheme for the low-spin states in ^{52}Co .

4.2.2 Population of High-spin States in ^{52}Co

The lack of an isospin symmetric reaction to one-neutron knockout from ^{53}Co , i.e. one-proton knockout from ^{53}Fe , meant it was especially important to perform a thorough spectroscopic analysis in order to understand the γ -ray spectrum observed in Fig. 4.12 and therefore establish a new level scheme for ^{52}Co . In particular, this analysis involved the use of γ - γ coincidence analysis, γ -ray intensity arguments, comparisons with branching ratios in the mirror nucleus ^{52}Mn and finally a Doppler correction/Lifetime analysis.

The use of background subtracted γ - γ coincidence analysis for the one-neutron knockout reaction, as shown in Fig. 4.14, proved to be particularly crucial in the construction of a new level scheme for ^{52}Co . For example, in Fig. 4.14(a), it is shown how several transitions were detected in coincidence with the 911(2) keV transition, including the 662(2), 1022(3), 1292(2), 1421(2) and 2081(3) keV transitions. While in Fig. 4.14(b), only the 662(2), 911(2), 1421(2) and 2081(3) keV transitions were detected in coincidence with the 1022(3) keV transition, but not the 1292(2) keV transition. Whilst finally, in Fig. 4.14(c), only the 662(2), 911(2), 1022(3) and 1292(2) transitions were detected in coincidence with the 1421(2) keV transition, but not the 2081(3) keV transition. Therefore, using both this analysis, as well as γ -ray intensity arguments, a new level scheme for ^{52}Co was established, as shown in Fig. 4.15, where the spins and parities were tentatively assigned on the basis of mirror symmetry arguments, comparing with well-known states in ^{52}Mn . Furthermore, upon comparing with these known states in ^{52}Mn , it was additionally noticed that a sec-

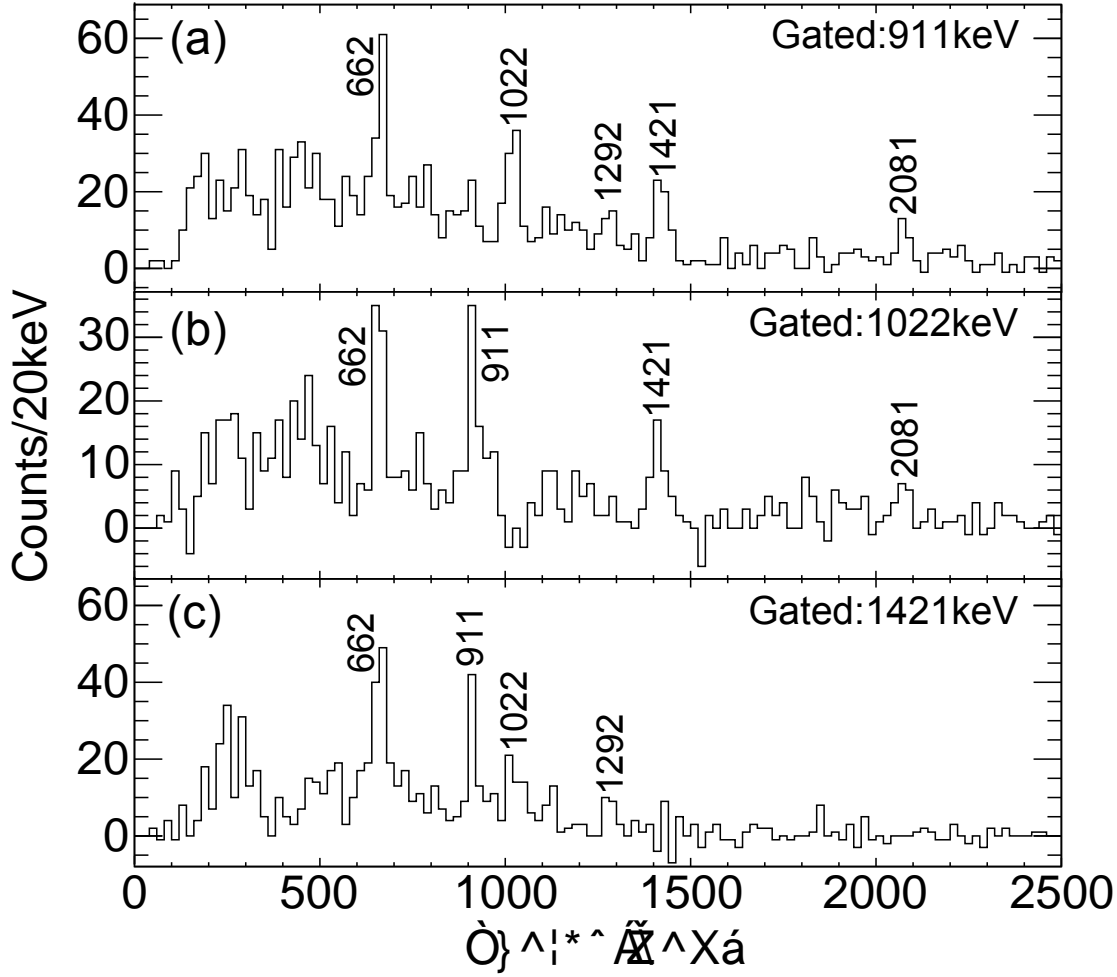


Figure 4.14: The Doppler corrected γ - γ coincidence spectra for γ rays in coincidence with the (a) 911(2) keV, (b) 1022(3) keV and (c) 1421(2) keV transitions observed in ^{52}Co , populated via one-neutron knockout from ^{53}Co . All spectra have been produced using an average $\beta = \frac{v}{c}$ value of 0.370.

ond, weak ($I_\gamma=9.4(20)$), γ -ray transition from the 8_1^+ state (to the 6^+ ground state) had been previously observed, with a transition energy of 2285.9(4) keV [104]. Further investigation of the ^{52}Co spectrum shown in Fig. 4.12, led to the discovery of a similarly weak transition, with a transition energy of 2331(6) keV and a branching ratio of $I_\gamma=10(2)$, which also corresponded within error with the energy of the (8_1^+) state. Therefore it was decided, based upon this analysis, that this transition should be assigned as the analogue of the 2285.9(4) keV transition observed in ^{52}Mn .

Only two transitions shown in the high-spin cascade of ^{52}Mn , see Fig. 4.15, were not observed in ^{52}Co . This included the 325 keV ($J^\pi:10_1^+ \rightarrow 11_1^+$) and 1876 keV ($J^\pi:10_1^+ \rightarrow 8_1^+$)

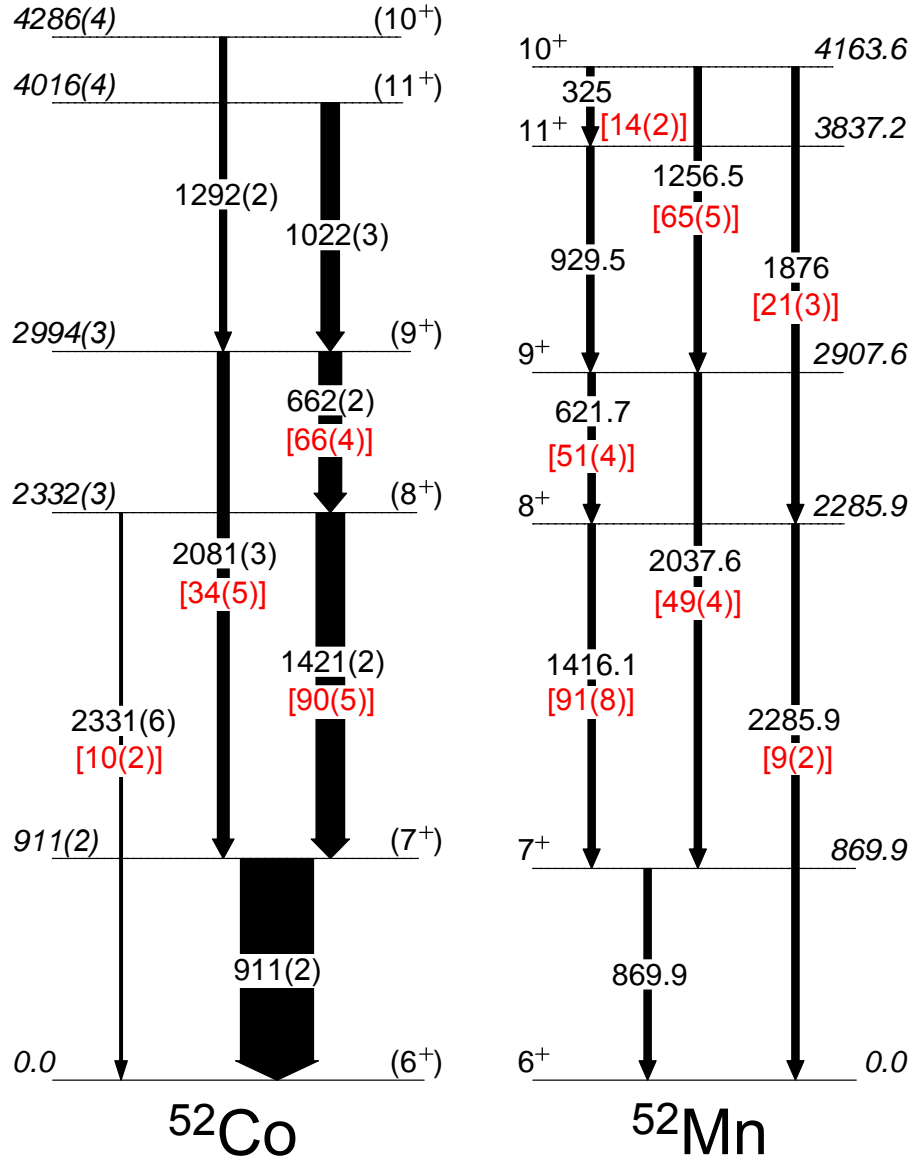


Figure 4.15: The deduced energy-level scheme for the high-spin states ($J \geq 7$) in ^{52}Co , as observed in this work, shown next to a partial level scheme of ^{52}Mn , using information from Ref. [65]. The spins and parities for ^{52}Co are shown in parentheses as the assignments are made on the basis of mirror symmetry arguments. The widths of the arrows (for the ^{52}Co level scheme) are proportional to the observed relative γ -ray intensities. Branching ratios are shown in red with square brackets.

transitions, each with measured branching ratio of 14(2) and 21(3), respectively, as reported in Ref. [105]. In ^{52}Co , this should correspond to γ -ray transitions of ~ 270 keV and ~ 1954 keV, however the expected peaks at these energies were too weak to be observed.

4.2.2.1 The Longer-lived (11_1^+) State

Additional support for both the ordering and observation of this high-spin cascade in ^{52}Co came from investigating the β -value required for the Doppler correction performed in this analysis, i.e. the β -value required to align a γ -ray transition in both the 37° and 90° SeGA ring spectra. Since (directly populated) states with a very short half-life (i.e. ≤ 0.5 ps) have an average decay point at the centre of the reaction target, the β -value required to align transitions from such states gives us an insight into the ion velocity at the centre of the target, as discussed in Section 3.4.5. In ^{52}Co , the transitions which required the highest β -values for the Doppler correction, and which are also believed to correspond to transitions from short-lived states based on mirror symmetry, were the 525(2), 1274(2) and 1292(2) KeV transitions, which each required a β -value of 0.382(2), 0.381(2) and 0.381(2), respectively. This gives an approximate β -value of 0.381(1) at the centre of the reaction target, which, through the use of energy loss calculations using LISE [73], roughly corresponds to a β -spread of 0.381(1) to 0.358(1) from the centre to the back of the reaction target. Since it takes ~ 8 -9 ps for the beam to traverse the reaction target ($188\text{mg}/\text{cm}^2$ ^9Be), any state with a half-life of ~ 4.5 ps or greater will have an average decay point downstream of the reaction target. The reason why this analysis is particularly important in the case of ^{52}Co is because the IAS of the proposed (11_1^+) state in ^{52}Co has a measured half-life of 15.1(10) ps [65], which would be sufficiently long-lived for the majority of the decays to take place downstream of the reaction target. Assuming mirror symmetry, we would expect the (11_1^+) state in ^{52}Co to have a similarly long half-life, which would result in a much lower β -value for the Doppler correction of the 1022(3) keV transition (compared to a typical fast transition). Indeed, this appears to be the case, since a β -value of 0.359(1) was required for the Doppler correction of this transition, suggesting the state has a half-life of at least 9 ps or greater. Furthermore, due to the longer half-life of this state, any transitions which form a cascade which the 1022(3) keV transition feeds into will be given an ‘effective’ half-life. Therefore, using the measured branching ratios observed in this work, it is possible to estimate what portion of the measured intensity of each state in the high-spin cascade resulted from feeding (direct or indirect) from the (11_1^+) state. This analysis showed that 54(4)%, 40(4)% and 24(5)% of the (9_1^+), (8_1^+) and (7_1^+) states population, respectively, resulted from feeding from the (11_1^+) state. Furthermore, by using this information, it is possible to perform a quick calculation to estimate (approximately) the β -values required for the Doppler correction of

transitions from each of these states by taking the sum of (a) the portion of state populated by the (11_1^+) multiplied by the β -value required to align the 1022(3) keV transition (0.359) and (b) multiplying the remaining portion by the average β -value required to align fast transitions (0.381). This resulted in estimated β -values of 0.369(1), 0.372(1), and 0.376(1) to align transitions from the (9_1^+) , (8_1^+) and (7_1^+) states, respectively. In fact, these rough estimates are in very good agreement with the β -values required for the Doppler correction of transitions originating from these states, where β -values of 0.369(2), 0.370(2), 0.375(2) and 0.376(1) were required for the 662(2), 2081(3), 1421(2) and 911(2) keV transitions, respectively.

4.2.2.2 Summary of the Observation High-spin States in ^{52}Co

In summary, strong evidence, using a range of analytical techniques, has been presented for the observation of a high-spin cascade in ^{52}Co . It was clear from an early stage in this analysis, due to the unexpected observation of these high-spin states in ^{52}Co , that a high-spin isomeric state must have been present in the ^{53}Co secondary beam. This is due to $J = 7$ being the maximum angular momentum which can be reached in one-neutron knockout from ^{53}Co , with a ground state of $(\frac{7}{2}^-)$, though states up to, and including, the band terminating (11^+) state were observed. In ^{53}Co , only one high-spin isomeric state has been previously observed with a spin-parity of $19/2^-$ and a half-life of 247(12)ms [106], which is sufficiently long-lived to still be strongly populated at the secondary target position, after its initial population at the primary target. One-neutron knockout from this isomer could in theory populate a large range of high-spin states ranging from 6^+ to 13^+ in ^{52}Co , and, as will be discussed later in Section 4.5, cross section calculation predicted, in particular, the strong population of the 8^+ , 9^+ , 10^+ and 11^+ states, as observed in this analysis.

4.2.3 Population of Low-spin States in ^{52}Co

However, establishing the level scheme for the lower spin states was much more difficult, particularly due to the lack of γ - γ coincidences for the transitions in question, as can be seen in Fig. 4.16b. A comparison between the γ -ray spectrum, shown in Fig. 4.16(a), and the γ - γ total projection over all γ rays, shown in Fig. 4.16(b), demonstrates a significant reduction in the relative intensities of the 459 keV, 746 keV and 1274 keV transitions. This suggests that the transitions in coincidence must be particularly weak. Attempts

to perform a background subtracted γ - γ analysis for these transitions did not yield any clear transitions in coincidence and thus it was not possible to use this method in order to establish the location of these transitions in the level scheme. However, what could be deduced from this analysis is that the states from which these transitions decay are most likely populated directly and that they directly feed either the ground state or some long-lived isomeric state.

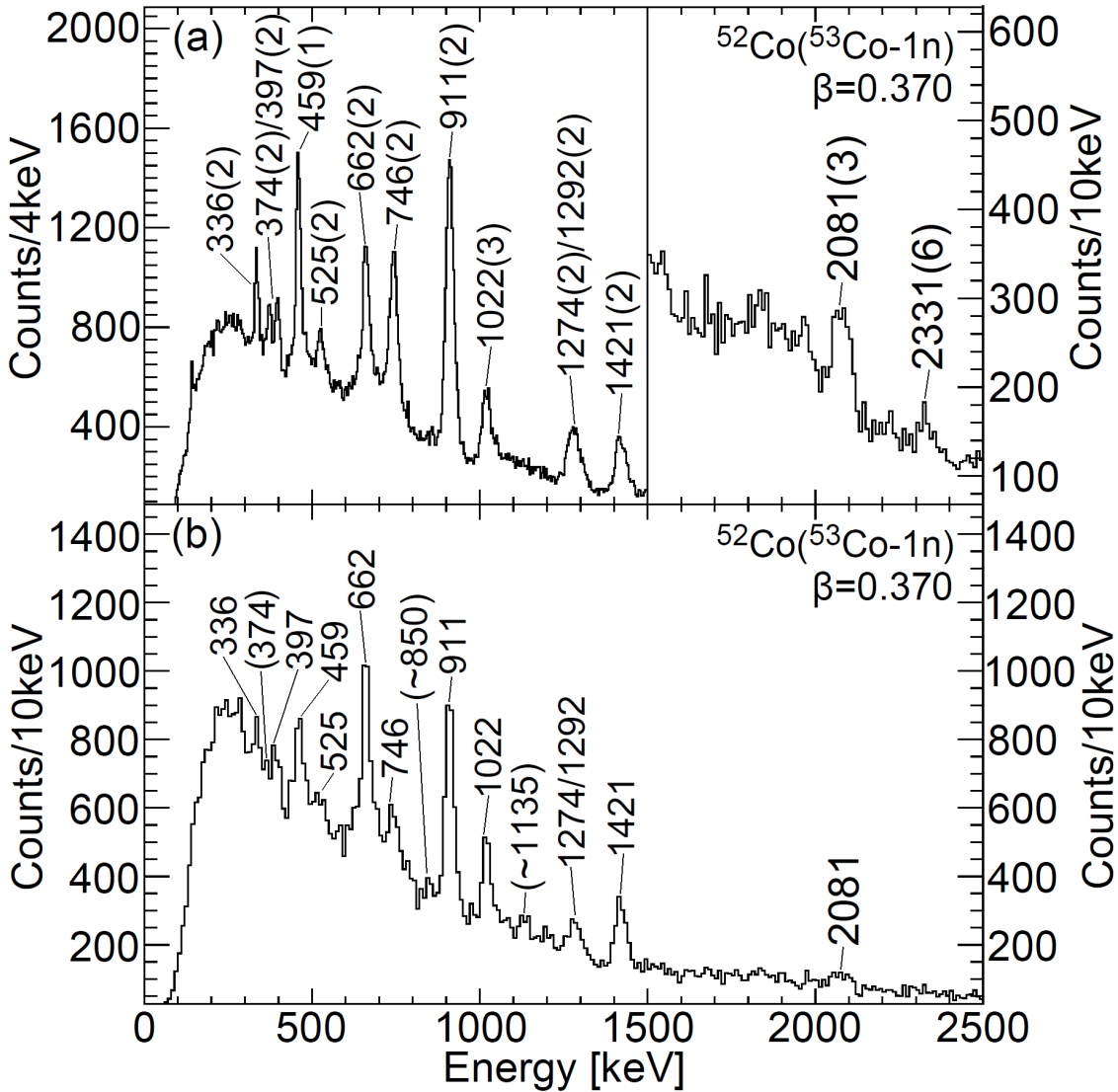


Figure 4.16: A comparison between the ^{52}Co Doppler corrected (a) γ -ray spectrum and (b) γ - γ total projection spectrum. The $\beta = \frac{v}{c}$ value used was chosen in order to optimise the γ -ray spectra to give the best resolution for the observed transitions.

In order to establish a level scheme for the remaining unassigned, strongly observed transitions in ^{52}Co , a comparison with known transitions in the mirror nucleus ^{52}Mn was

performed. As previously discussed, the 459(1) keV, 746(2) keV and 1274(2) keV transitions most likely feed either the ground state or a long-lived isomeric state. Therefore, it was important to identify such transitions in ^{52}Mn , with a similar transition energy, which could correspond to the analogues of these unassigned transitions.

4.2.3.1 Establishing the (5^+) State

In ^{52}Mn , only one previously observed transition could be identified with a similar transition energy to that of the 1274(2) keV transition observed in ^{52}Co , which also decayed to either the ground state or an isomeric state. This was the 1253.7(5) keV transition, which was observed from the decay of the 5_1^+ to the 6^+ ground state [65] with a branching ratio of 81%. Furthermore, this 5_1^+ state was also observed to decay via an alternative decay branch, feeding the 4_1^+ state, with a transition energy of 521.8(5) keV and a branching ratio of 19%. Comparing these two transitions observed in ^{52}Mn with the two unassigned transitions observed in ^{52}Co (1274(2) and 525(2) keV) was very favorable, both in terms of the transition energies and the branching ratios, where branching ratios of 82(6)% and 18(2)% were measured for the 1274(2) and 525(2) keV transitions, respectively. Therefore, based upon this analysis, these transitions were assigned as analogues.

4.2.3.2 Establishing the (4^+) State

The 4_1^+ state in ^{52}Mn has been observed to γ -ray decay via two branches, feeding either the 6^+ ground state via a 731.5(5) keV transition, or the isomeric 2_1^+ state via a 353.7(5) keV transition [65]. The majority of the intensity (92%) for the γ decay of this 4_1^+ state proceeds directly to the 6^+ ground state, whilst only a small portion (8%) proceeds to the 2_1^+ isomeric state [65]. In ^{52}Co , only one transition, with an energy of 746(2) keV, was observed with a similar transition energy to that of the 731.5(5) keV transition in ^{52}Mn and was therefore assigned as the analogue of this transition. Additional support for both this assignment as well as the previous assignments made in this section includes, (a) the 746(2) keV and 525(2) keV transitions, within error, sum to the correct energy of the alternative 1274(2) keV decay branch from the (5_1^+) state and (b) the 746(2) keV transition feeds the ground state and only has a very weak transition in coincidence, as previously predicted from the γ - γ coincidence analysis.

In regards to the 353.7(5) keV, $J^\pi:4_1^+ \rightarrow 2_1^+$ transition in ^{52}Mn , three potential candidate transitions were observed in ^{52}Co with energies of 336(2) keV, 374(2) keV and

397(2) keV, each with a relative γ -ray intensity of 17(1)%, 10(2)% and 15(2)% compared to the 746(2) keV transition, respectively. In addition, these three transitions were also observed in an alternative population method of ^{52}Co via $1n1p$ removal from ^{54}Ni , as shown in Fig. 4.13. It can be concluded from comparing the γ -ray spectra for both population methods of ^{52}Co that the 336(2) keV and 397(2) keV transitions can be definitively ruled out, since their respective relative γ -ray intensities, when compared to the 746(2) keV transition, differ significantly in both spectra. However, the 374(2) keV transition, whilst especially weak/tentative in Fig. 4.13, as well as possibly partially hidden under the tails of the much stronger 336(2) and 397(2) keV transitions, still corresponds (within error) with the same relative γ -ray intensity (6(4)%) to the 746(2) keV transition, as measured in the $^{52}\text{Co}(^{53}\text{Co}-1n)$ reaction. Furthermore, a different approach was also considered in this analysis, which involved investigating the β -value required to align the γ -ray transitions in both the 37° and 90° SeGA ring spectra, since a transition decaying from the same state (i.e. same half-life) should require the same β -value for the Doppler correction. Interestingly, β -values of 0.364(2) and 0.362(2) were required to align the 374(2) keV and the 746(2) keV transitions, respectively, in the $^{52}\text{Co}(^{53}\text{Co}-1n)$ reaction, which are both (a) consistent with each other and (b) indicative of an average decay point downstream of the secondary target. This is due to, as discussed previously in Section 4.2.2, there being a β spread of around 0.381(1) to 0.358(1) from the centre to the back of the secondary target for this reaction. Therefore, using this information, an average β value of 0.363(1) and Equation 3.18 as discussed in Section 3.4.5, this gives a half-life of 12(6) ps for this (4^+) state, which compares reasonably with the 3.6(14) ps half-life previously measured for the IAS in ^{52}Mn [65]. The final, but much more tentative, analysis technique to be considered when trying to identify the analogue of the 353.7(5) keV transition in ^{52}Co involved making a comparison between the γ ray and γ - γ coincidence spectra shown in Fig. 4.16. What can be observed from this is the significant relative reduction in the intensity of the 336(2) keV transition in the γ - γ total projection spectrum, as shown in Fig. 4.16(b), especially when compared to most other γ -ray transitions, mirroring what we observe for the 746(2) keV transition. In summary, whilst the analysis performed in this section does not definitively prove the 374(2) keV transition observed in ^{52}Co to be the analogue of the 353.7(5) keV, $J^\pi:4_1^+ \rightarrow 2_1^+$ transition in ^{52}Mn , in the absence of any other likely candidates, present in both population methods of ^{52}Co , it was decided in this analysis to tentatively assign these as analogue transitions.

4.2.3.3 Establishing the (3^+ , 4^+) State

The last strong transition in ^{52}Co to be assigned was the 459(1) keV transition, which was strongly observed in both population methods of ^{52}Co , see Figs. 4.12 and 4.13, which suggests it most likely originates from a low-spin state with an angular momentum $J \leq 7$ (the maximum angular momentum which can be reached in both reactions, from the ground state of the parent nuclei). This presumption is based upon the fact that in the case of the ^{54}Ni secondary beam, the population of the 10^+ isomeric state was deduced to be small, based on the analysis in section 4.1.2, which may also explain the very weak/tentative observation of transitions from high-spin states with $J > 7$ in this population method of ^{52}Co . Therefore, using the same approach as discussed previously, where only similar transitions in ^{52}Mn , which also fed the ground state (or an isomeric state) were considered, this left three candidate analogue transitions, as shown in Table 4.4.

Table 4.4: Three candidate analogue transitions in ^{52}Mn to the 459(1) keV transition observed in ^{52}Co , using information from Ref. [65].

^{52}Mn	Transition A	Transition B	Transition C
Initial State	3_1^+	$1_2^+, 2_2^+$	$3_2, 4_2^+$
Final State	2_1^+	2_1^+	2_1^+
Transition Energy [keV]	447.4(5)	508.8(5)	506.6(5)
Half-life [ps]	$0.17^{+0.04}_{-0.03}$	$0.06^{+0.03}_{-0.04}$	1.4

Firstly, by considering alternative decay branches from the initial state of these three candidate analogue transitions, it was possible to tentatively rule out transition B. This is because in ^{52}Mn , the $1_2^+, 2_2^+$ state is also observed to decay to the 1_1^+ isomeric state via a 340.4(5) keV transition ($I_\gamma=10\%$), which, in the case of ^{52}Co , should correspond to a transition with an energy of ~ 318 keV, whereby this transition was not observed in either population method of ^{52}Co , see Figs. 4.12 and 4.13.

Secondly, considering the results of the shell-model calculations discussed later in Section 4.5, a 3_2^+ state is predicted to be strongly populated. In this case, this may correspond to the initial state of either transition A or C, since the energy difference between these two states is very small (< 60 keV) and thus the order of these states may swap in ^{52}Co . Furthermore, the order of these states may also swap in the calculations.

Finally, the last consideration to be made relates to the half-life of the state from which the 459(1) keV transition decays. By using the Doppler correction β value of 0.378(1) for this transition, the β spread of 0.381(1) to 0.358(1) from the centre to the back of the target (as discussed previously), and Equation 3.18, a half-life of 1.5(3) ps was obtained. This compares most favourably with transition C, though this proof is not definitive.

In conclusion, since it was not possible to definitively rule out either transition (a) or (c), and only possible to tentatively rule out transition (b), the state from which the 459(1) keV transition decays was assigned a spin-parity of $(3^+, 4^+)$.

4.2.3.4 Summary of the Observed States in ^{52}Co

In summary, a new level scheme has been deduced for ^{52}Co , as shown in Fig. 4.17, using a wide range of analytical techniques including γ - γ coincidence analysis, γ -ray intensity arguments, transition energy sums, a Doppler correction/lifetime analysis and finally mirror symmetry arguments, all of which provide a compelling argument for the assignments made.

4.2.3.5 Mass Measurement of ^{52}Co

In a recent publication, see Ref. [99], they report upon the observation of a $T = 2, 0_2^+$ state in ^{52}Co , as shown in Fig. 4.17, which was populated via Fermi β^+ decay from the ground state of ^{52}Ni . Since this state lies above the proton separation energy in ^{52}Co , it was additionally observed to decay via proton emission, populating the ground state of ^{51}Fe with a decay branch of 13.7(2)% [99]. Therefore, by using the previously measured mass excess of ^{51}Fe (40.202(9) MeV [108]), in addition to the measured proton energy, E_p , of 1352(10) keV, the authors calculated a mass excess of 31.561(14) MeV for the $T = 2, 0_2^+$ state in ^{52}Co [99]. However, in order to measure the mass excess of the ground state, the excitation energy of the $T = 2, 0^+$ state needs to first be measured. The tentative establishment of the (2^+) state energy in the work performed here however, i.e. from the energy difference between the observed 746(2) and 374(2) keV transitions (see Fig. 4.17), fixes, again tentatively, the 1_1^+ and 0_2^+ state excitation energies. Hence, the mass excess of ^{52}Co could be measured for the first time, yielding a value of -34.481(14) MeV. Furthermore, since the excitation energy of states which decay via proton emission is given by $E_X = E_p + S_p$, the proton separation energy, S_p , could also be measured for ^{52}Co , which gave a value of 1568(10) keV.

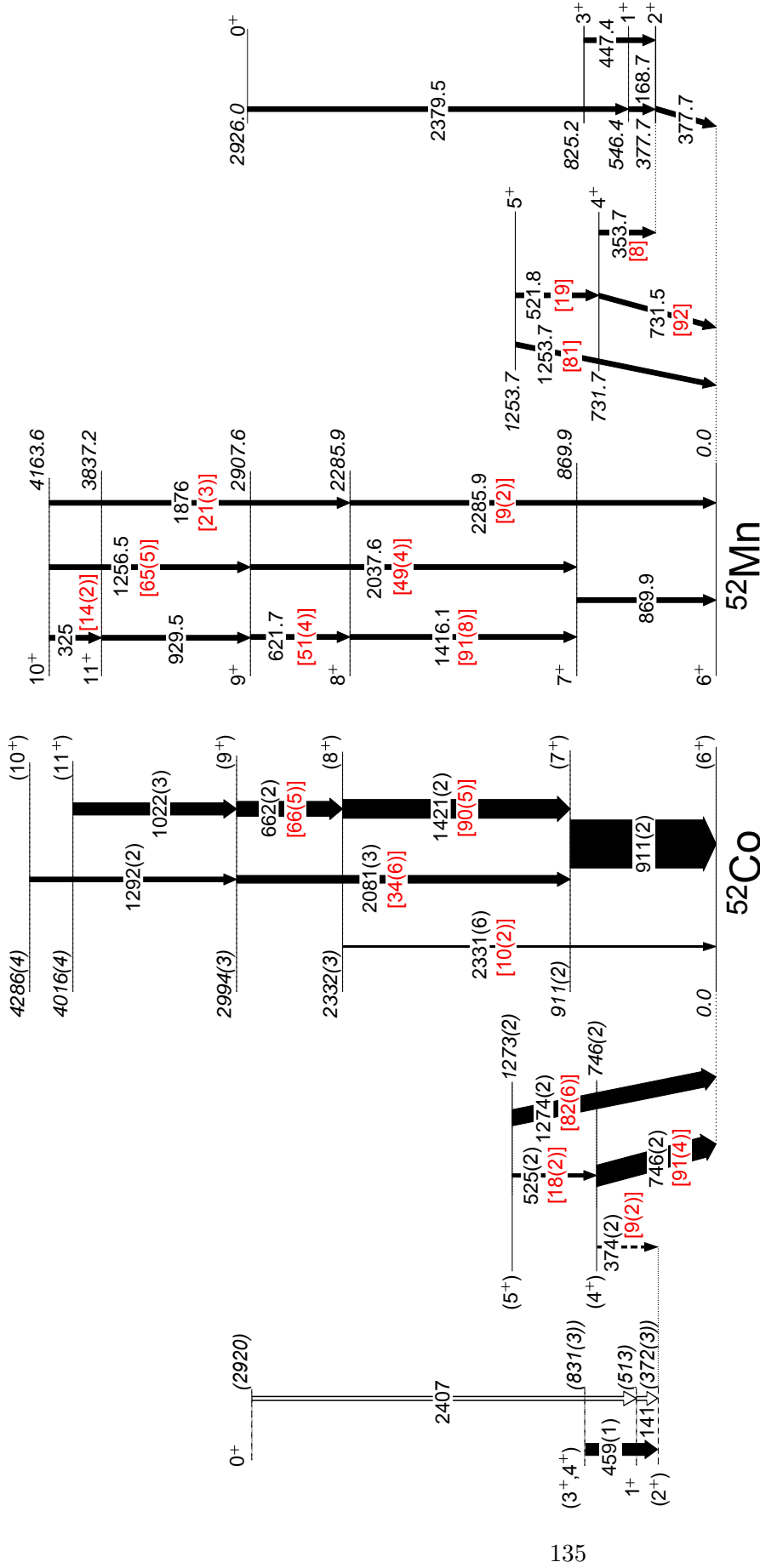


Figure 4.17: The deduced energy-level scheme for ^{52}Co , as observed in this work, shown beside a partial level scheme of ^{52}Mn , using information from Ref. [65]. The spins and parities for ^{52}Co are in parentheses as the assignments are made on the basis of mirror-symmetry arguments. Tentatively assigned transitions are indicated by dashed lines. A number of state energies are tentative as indicated by dashed lines with energies in parentheses due to the uncertainty in the energy of the (2^+) state, see text for more details. The widths of the arrows (for the ^{52}Co level scheme) are proportional to the relative γ -ray intensities observed. State branching ratios for both ^{52}Co and ^{52}Mn are shown in red with square brackets. Two previously observed transitions in ^{52}Co , as reported in Ref. [99], are also included for comparison purposes and shown as hollow arrows.

A summary of all the assigned excited states and transitions observed in ^{52}Co (in addition to the two previously observed γ -ray transitions reported in Ref. [99]) are tabulated in Table 4.5 and can be compared with the relevant IAS in ^{52}Mn , shown in Table 4.6.

Table 4.5: Details of the new excited states and transitions observed in ^{52}Co . Two previously observed transitions in ^{52}Co , as reported in Ref. [99], have also been included for completeness (with $I_{\gamma(\text{rel})}$ of X). Excited state half-lives in ^{52}Co have been estimated using a Doppler correction analysis in conjunction with energy loss calculations performed using LISE [73], see text for more details. Tentative state energies and assigned transitions are shown in parentheses, see text for more details. The ground state half-life for ^{52}Co is taken from Ref. [65].

Initial State					Final State	
E_x (keV)	J^π	$t_{1/2}$	E_γ	$I_{\gamma(\text{rel})}$	E_x (keV)	J^π
^{52}Co						
0.0	(6 ⁺)	112(3) ms				
(372(3))	(2 ⁺)	102(6) ms				
(513(3))	1 ⁺		141(1)	X	(372(3))	(2 ⁺)
746(2)	(4 ⁺)	12(6) ps	(374(2))	4.3(8)	(372(3))	(2 ⁺)
			746(2)	43.8(15)	0.0	(6 ⁺)
(831(3))	(3 ⁺ , 4 ⁺)	1.5(3) ps	459(1)	25.1(8)	(372(3))	(2 ⁺)
911(2)	(7 ⁺)		911(2)	100.0(21)	0.0	(6 ⁺)
1273(2)	(5 ⁺)		525(2)	7.2(7)	746(2)	(4 ⁺)
			1274(2)	33.1(18)	0.0	(6 ⁺)
2332(3)	(8 ⁺)		1421(2)	39.4(16)	911(2)	(7 ⁺)
			2331(6)	4.1(9)	0.0	(6 ⁺)
(2920(3))	0 ₂ ⁺		2407(1)	X	(513(3))	(1 ⁺)
2994(3)	(9 ⁺)		662(2)	31.9(14)	2332(3)	(8 ⁺)
			2081(3)	16.4(22)	911(2)	(7 ⁺)
4016(4)	(11 ⁺)	> 9 ps	1022(3)	26.1(14)	2994(3)	(9 ⁺)
4286(4)	(10 ⁺)		1292(2)	9.4(7)	2994(3)	(9 ⁺)

Table 4.6: Details of the proposed IAS and mirror transitions in ^{52}Mn to those observed in ^{52}Co , using data from Ref. [65].

Initial State					Final State	
E_x (keV)	J^π	$t_{1/2}$	E_γ	$I_{\gamma(rel)}$	E_x (keV)	J^π
^{52}Mn						
0.0	6^+	5.591(3) d				
377.749(5)	2^+	21.1(2) m	377.748(5)		0.0	6^+
546.438(6)	1^+	1.85(7) ns	168.688(2)		377.749(5)	2^+
731.66(25)	4^+	3.6(14) ps	353.7(5)		377.749(5)	2^+
			731.5(5)		0.0	6^+
825.2(4)	3^+	0.17_{-3}^{+4} ps	447.4(5)		377.749(5)	2^+
869.89(18)	7^+	0.12_{-8}^{+6} ps	869.9(2)		0.0	6^+
884.2(3)	$3, 4^+$	1.4 ps	506.6(5)		377.749(5)	2^+
1253.7(4)	5^+	0.018(55) ps	521.8(5)		731.66(25)	4^+
			1253.7(5)		0.0	6^+
2285.94(22)	8^+	<0.069 ps	1416.1(2)		869.89(18)	7^+
			2285.9(4)		0.0	6^+
2907.6(3)	9^+	0.08(6) ps	621.7(2)		2285.94(22)	8^+
			2037.6(4)		869.89(18)	7^+
2926.0(5)	0_2^+		2379.5(5)		546.438(6)	1^+
3837.2(4)	11^+	15.1(10) ps	929.5(2)		2907.6(3)	9^+
4163.6(4)	10^+	0.12(4) ps	325		3837.2(4)	11^+
			1256.5(3)		2907.6(3)	9^+
			1876		2285.94(22)	8^+

4.3 Shell Model and Cross Section Calculations

Following the establishment of new energy-level schemes for both the $A = 53$, $T_z = \pm\frac{3}{2}$ and $A = 52$, $T_z = \pm 1$ mirror pairs, $^{53}\text{Ni}/^{53}\text{Mn}$ and $^{52}\text{Co}/^{52}\text{Mn}$, respectively, it was then possible to extract experimental Mirror Energy Differences (MED). In order to interpret this data, large-scale shell-model calculations, using the ANTOINE code [24], were performed for both mirror pairs, in the full fp valence space using the KB3G interaction [25], whereby no restrictions were placed upon the movement of particles between the fp orbitals. For the analysis discussed in the following sections, these calculations were performed by Professor Mike Bentley [109], using the shell model prescription described in Refs. [9, 10], see Section 2.3.2 for more details.

The use of one-nucleon knockout reactions, to populate the nuclei of interest in this experiment, also presented the opportunity to perform a detailed cross section analysis for the observed states populated in these nuclei. The cross sections calculations for this analysis were performed by Dr Ed Simpson [67], whereby spectroscopic factors for the knockout process were calculated using the shell-model code ANTOINE [24], in the full fp space, using the KB3G interaction [25]. Following this, one-nucleon knockout cross sections were then calculated under the spectator-core approximation assuming eikonal reaction dynamics [46, 47], using shell-model structure input, as discussed previously in Section 2.4.

In the following sections, experimental data will be compared with the theoretically calculated MED and cross section results for both the $A = 53$, $T_z = \pm\frac{3}{2}$ and $A = 52$, $T_z = \pm 1$ mirror pairs.

4.4 The $A = 53$, $T_z = \pm\frac{3}{2}$ mirror pair

4.4.1 Relative Cross Sections Analysis

In order to measure the relative cross section of states in a particular recoil, both the population of the ground state and excited states needed to be calculated. This was achieved by firstly measuring the population of the excited states by taking the sum of the intensity of the efficiency corrected γ -rays exiting a state, then subtracting the sum of the efficiency corrected intensity of γ -rays feeding the state. It should be noted however, that effects relating to the momentum acceptance of the S800 were not considered in this analysis, when calculating the relative intensity of γ -ray transitions. Such restrictions

on the accepted momentum can bias the measured relative intensity of γ rays due to the different resulting momentum distributions of nuclei, depending on which orbital a nucleon is removed from, as shown in Fig. 4.18, for the removal of either an $f_{\frac{7}{2}}$, $d_{\frac{5}{2}}$ or an $s_{\frac{1}{2}}$ proton from ^{54}Fe .

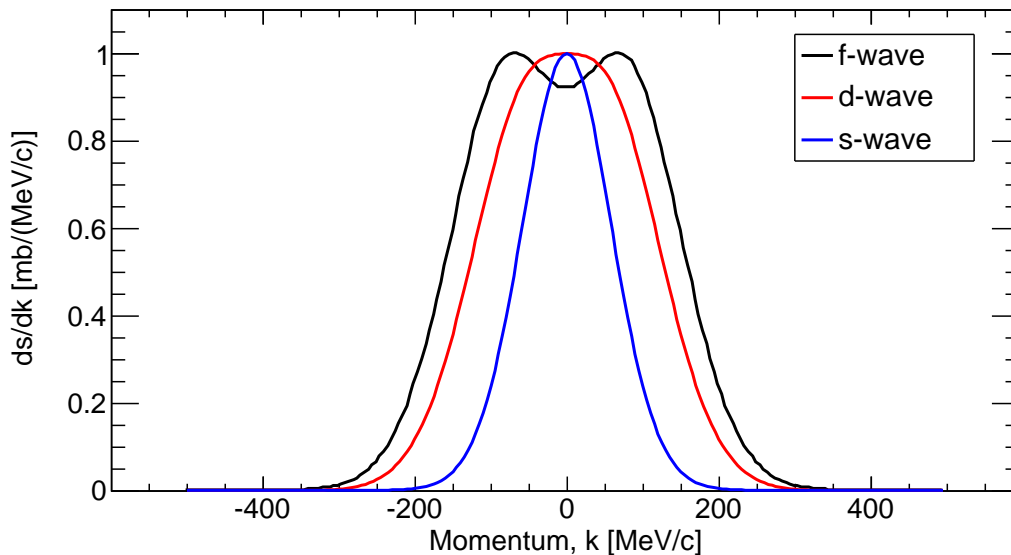


Figure 4.18: Calculated momentum distributions for the removal of either an $f_{\frac{7}{2}}$ (black), $d_{\frac{5}{2}}$ (red) or an $s_{\frac{1}{2}}$ (blue) proton from ^{54}Fe [67].

In this analysis, momentum cut off points are observed towards the tail of one side of the inclusive momentum distributions. This will have the effect of slightly negatively biasing the measured relative intensity of states populated via the removal of either an $f_{\frac{7}{2}}$ or $d_{\frac{5}{2}}$ nucleon, with respect to states populated via the removal of an $s_{\frac{1}{2}}$ nucleon. In addition to this, effects relating to the anisotropic γ -ray angular distributions for different multipolarity transitions, due to the alignment of magnetic substates induced by the knockout reaction process, were also not considered in this analysis [68]. The severity of this effect however, depends on both the type of alignment, prolate or oblate, and the degree of alignment [68]. Moreover, as detailed in Ref. [68], the γ -ray angular distributions for dipole, quadrupole and octupole transitions are predicted to overlap at around 40° and 100° , for the beam velocities concerned here. Therefore, due to the SeGA detectors being positioned in two rings at 37° and 90° during this experiment, the effect on the measured relative intensity of different multipolarity γ -ray transitions is likely to be small. After calculating the population of the excited states, the population of the ground state was

then found by calculating the total number of recoil ions created, then subtracting the sum of the intensity of the excited states populated in the recoil. In order to determine the total number of recoil ions created, the total number of recorded single events (i.e. the detection of an ion only) and the total number of recorded coincidence events (i.e. the detection of an ion and a γ -ray) need to be summed, but only after firstly applying some additional corrections. The first correction to be made relates to the use of a ‘downscaler factor’, whereby, in order to reduce pile up in the Data Acquisition (DAQ) system during high rate experiments, an S800 downscaler factor is applied to the single events data. In the case of the experiment performed for this analysis, a downscaler factor of 4 was used, which meant that only every 1 in 4 detected single events was recorded. This was simply corrected for in the analysis by scaling up the recorded single events by a factor of 4. The second correction to be made relates to the dead time of the DAQ system, whereby this dead time needs to be calculated for both the single and coincidence events separately. This is due to it being slightly less likely for the DAQ to be busy for an S800 singles trigger than for a coincidence trigger, as the former is evenly distributed in time while the latter is random in time. Following the application of these corrections for both the S800 downscaler and DAQ dead time, the total corrected number of recoil ions produced could then be calculated and therefore the population of the ground state also.

The calculated relative cross sections for ^{53}Ni and ^{53}Mn , using the approach described in Section 2.4.2, are shown in Figs. 4.19(a) and (c), respectively. Due to the lack of an available shell model interaction encompassing both the *sd* and *fp* shell regions, it meant that shell model calculations could only be performed in the *fp* valence space, and therefore could not be used to calculate the spectroscopic factors for one-nucleon removal from the *sd* shell. Therefore, in order to estimate the population of positive-parity states, resulting from one-nucleon knockout from the *sd*-shell, previously extracted spectroscopic factors from transfer reactions onto ^{53}Mn [110] were used, whereby it was assumed that these were the same for ^{53}Ni . However, it is worth noting that in the case of ^{53}Ni , a number of these positive-parity states may also decay through proton emission since they lie above the proton separation energy ($S_p = 2930$ keV [111]). Furthermore, it should additionally be noted that measured inclusive knockout cross sections are found to be systematically smaller, by around a factor of 2 (for the separation energies concerned here), than cross sections calculated using theoretical spectroscopic factors from the shell model, in line with systematics for other systems [47, 112]. Therefore, the comparison of the relative cross

sections derived here, using a combination of theoretically and experimentally deduced spectroscopic factors, can only be used as a guide.

Since the calculated spectroscopic factors for each member of the mirror pair are also identical within the shell-model approach, the theoretical cross sections in Figs. 4.19(a) and (c) are virtually identical. Including positive parity states in the calculations in the way described previously, the majority of the intensity ($\sim 50\%$) proceeds directly to the ground state, with $\sim 20\%$ going to high-lying positive-parity states.

In order to perform a detailed comparison between the calculated cross sections and the experimental data, the presence of isomeric state(s) in the ^{54}Fe or ^{54}Ni secondary beams must first be considered, as this will lead to noticeable discrepancies between the two. As discussed previously in Section 4.1.3, the most likely explanation for the observation of high-spin states in the daughter nuclei, with spin much greater than $\frac{7}{2}$, was the presence of the known 10^+ spin-trap isomeric state in both the ^{54}Fe and ^{54}Ni secondary beams. Since one-nucleon knockout from these isomers can only directly populate high-spin states between $\frac{13}{2}^-$ to $\frac{27}{2}^-$ in the daughter nuclei, this will lead to a stronger observed population of excited states in these nuclei but also a weaker population of the ground state.

A comparison between the theoretical and measured cross sections for ^{53}Ni , as shown in Figs. 4.19(a) and (b), shows a reasonable level of agreement, with the exception of a few differences. In particular, the $(\frac{5}{2}^+)$ state is observed to have a lower than predicted relative intensity by about a factor of two. However, the analogue state in ^{53}Mn is known to decay via two alternative decay branches, which account for about half the decay strength, but which were not observed here due to their high decay energies, where the SeGA efficiency is much lower, as discussed in Section 3.4.1. The non-observation of these transitions in ^{53}Mn however, has been accounted for, as can be seen in Fig. 4.19(d), by using the previously measured branching ratios for this state. If a similar decay pattern exists in ^{53}Ni , then the measured $(\frac{5}{2})^+$ cross section in Fig. 4.19(b) is in reality a factor of two larger and would therefore have a similar population intensity to that predicted in Fig. 4.19(a). The second noticeable discrepancy between Figs. 4.19(a) and (b) is the much higher observed relative cross section of low-lying states in ^{53}Ni , in particular, the $(\frac{5}{2}_1^-)$, $(\frac{3}{2}_1^-)$ and $(\frac{3}{2}_2^-)$ states. However, a possible explanation for this is that these states were populated via fast E1 transitions from a number of low-spin, high-energy, positive-parity states, which are predicted to be populated, as shown in Fig. 4.19(a), with a combined total relative cross section of $\sim 20\%$. Indeed, several such decay paths are known to

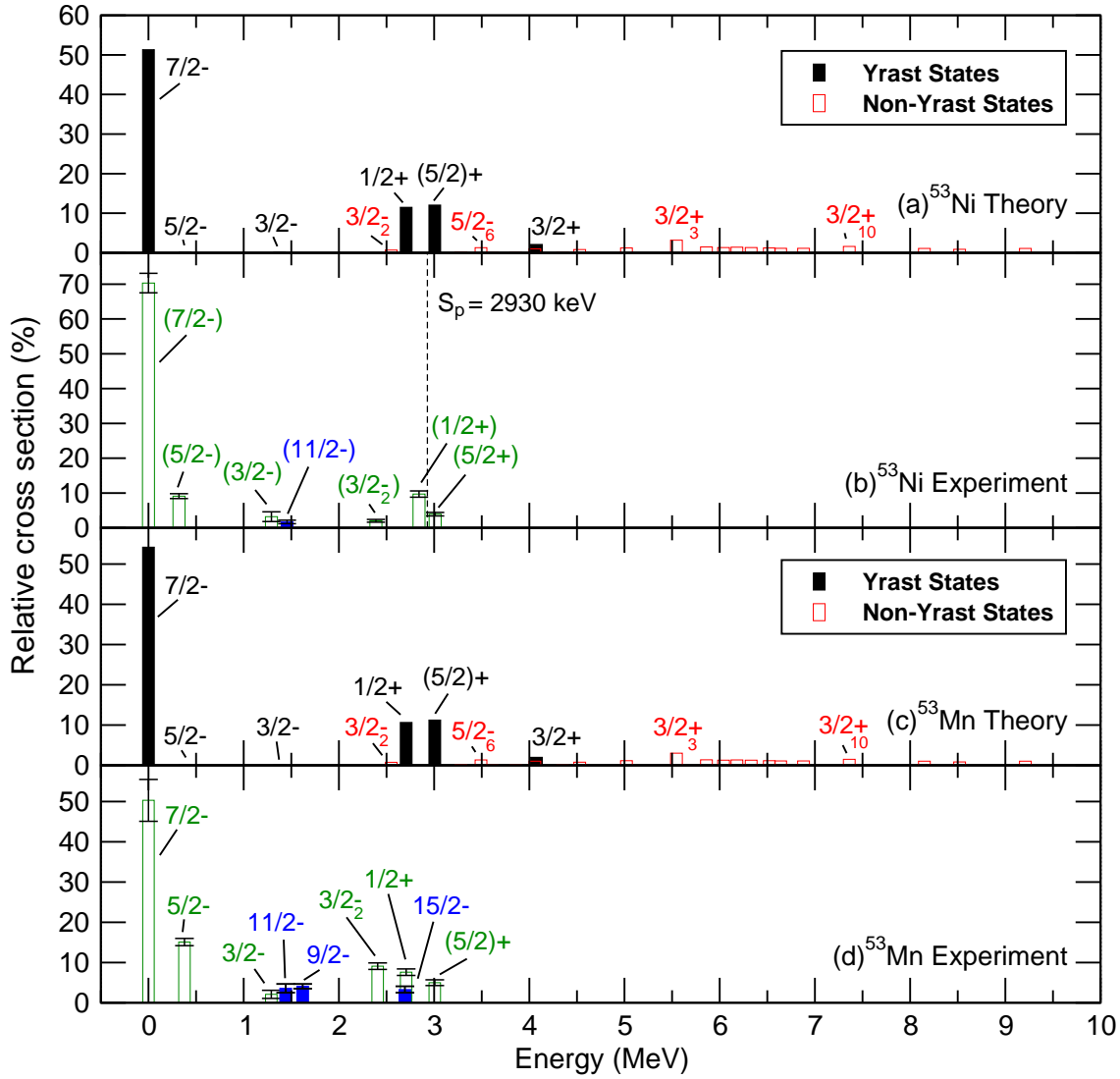


Figure 4.19: Calculated and experimental relative cross sections for states in ^{53}Ni and ^{53}Mn , populated via one-neutron and one-proton knockout, respectively. The calculations for ^{53}Ni and ^{53}Mn (panels (a) and (c)) were obtained using spectroscopic factors calculated in the shell-model, while spectroscopic factors for the positive parity states were taken from experimental data for ^{53}Mn and assumed to be the same for ^{53}Ni . The predicted relative cross sections and energies of both yrast states (black filled) and non-yrast states (red unfilled) are shown. Panels (b) and (d) show the measured relative cross sections to states in ^{53}Ni and ^{53}Mn , respectively, where statistical errors are also shown. States coloured in green (unfilled) can be compared with the calculated cross sections, while states coloured in blue (filled) can not be populated in direct knockout reactions from the ground state of the projectiles.

exist in ^{53}Mn . Furthermore, decays from other high-lying negative parity states will also contribute to the observed intensity for the low-lying negative parity states. In general, having considered the discrepancies discussed here, mainly due to the non-observation of high-energy γ -ray transitions due to low high-energy detector efficiency of SeGA, the agreement between the theoretical and measured cross sections for ^{53}Ni is fairly good.

Considering the direct mirrored reactions used to populate these mirror nuclei, one would expect that the observed experimental relative cross section distributions should be near identical. However, as can be seen in Fig. 4.19(b) and (d), a number of differences are apparent, particularly regarding the observed strengths of the $\frac{5}{2}_1^-$ and $\frac{3}{2}_2^-$ states in both nuclei. Furthermore, as discussed previously in Section 4.1.3, there is strong evidence for the presence of the 10^+ isomer in the secondary beams used in this experiment, with a much stronger residual population of this isomer, at the reaction target position, in the ^{54}Fe beam. This is due to the much stronger observed population of high spin states ($\frac{9}{2}^-$, $\frac{11}{2}^-$ and $\frac{15}{2}^-$) in ^{53}Mn than in ^{53}Ni , whereby, as mentioned previously, the stronger population of this isomer in the secondary beam should also result in a lower observed population of the ground state, as is observed in ^{53}Mn . However, this does not explain the much stronger observed population of the $\frac{5}{2}_1^-$ and $\frac{3}{2}_2^-$ states in ^{53}Mn . As can be seen in Figs. 4.19(a) and (c), a number of high-energy low-spin states are predicted to be populated in both nuclei, which could cascade through the low-lying states, such as the $\frac{3}{2}_2^-$ and $\frac{5}{2}_1^-$ states. However, in ^{53}Ni some of these low-spin high-energy states will be proton unbound and therefore this will lead to both a higher population of the ground state and a lower population of low-lying negative-parity states in this nuclide. Finally, the last observation to be made, regarding the $\frac{3}{2}_2^-$ state in ^{53}Mn , is that the large observed intensity of this transition compared to the analogue in ^{53}Ni , supports a previous hypothesis that the transition observed in the energy spectrum, from this state, is in fact a doublet. Therefore, the total intensity measured here may in fact correspond to a combination of the population of the $\frac{3}{2}_2^-$ and $\frac{13}{2}_2^-$ state, whereby the latter is additionally predicted to be strongly populated in one-proton knockout from the 10^+ isomer in the ^{54}Fe secondary beam. In this analysis, it should also be noted that any high-lying states populated, which directly feed the ground state, will also lead to an overestimation of the relative cross section to the ground state, and such effects may be slightly different between the mirror nuclei.

In conclusion, the relative population of the states in both nuclei can be understood well in terms of the direct knockout process, assuming symmetry between the spectroscopic

factors of the mirror pair and having accounted for the presence of isomeric states in the beams. This again gives further confidence in the assignments made for the newly identified states in ^{53}Ni .

4.4.2 MED Analysis

The results of the shell-model calculations performed for the $^{53}\text{Ni}/^{53}\text{Mn}$ mirror pair, in addition to the experimentally deduced MEDs, are shown in Fig. 4.20(a). As can be seen, the agreement is quite poor between the experimental data and the standard shell model calculation (dashed line), which only accounts for the isospin-breaking terms arising due to the EM interaction. However, the inclusion of the isospin non-conserving (V_B) term, as shown by the dotted line, results in an improvement in the fit to the experimental data, which is consistent with other recent findings in this region, i.e. see Refs. [9, 86, 87], which have indicated that inclusion of this V_B term for just $J = 2$, $f_{\frac{7}{2}}$ matrix elements, in general, provides a much better description of experimental MED. A recent study [10] however, has suggested that better agreement with the experimental MED data can be achieved by instead including a full set of effective isovector ($V_{pp} - V_{nn}$) matrix elements in the $f_{\frac{7}{2}}$ shell, whereby values for these matrix elements were extracted by fitting the shell model to all experimental MED data so far obtained in the shell. This yielded matrix elements of $V_B = -72, +32, +8, -12$ keV for $J = 0, 2, 4, 6$ couplings of the $f_{\frac{7}{2}}$ orbital, respectively. The results of a shell-model calculation, performed by including these four matrix elements, added to the two-body interaction for protons in the $f_{\frac{7}{2}}$ shell, is shown by a solid line in Fig. 4.20(a), where the four individual isospin non-conserving components of this solid line are additionally shown in Fig. 4.20(b). This results in a very noticeable further improvement in the agreement with the experimental data, where the agreement is now excellent. It should be noted however, that the three MEDs concerned here for the $^{53}\text{Ni}/^{53}\text{Mn}$ mirror pair, i.e. for the $\frac{3}{2}_1^-$, $\frac{5}{2}_1^-$ and $\frac{11}{2}_1^-$ states, are also included in the fit, which is made up from 93 pairs of excited states in 17 mirror nuclei between $A = 42$ and 54. However, the exclusion of these states from the fit only changes the result by less than 1 keV.

While the agreement with shell model (including a full set of effective isovector matrix elements) and experimental data is very good for the yrast states, a large discrepancy is still observed for the $\frac{3}{2}_2^-$ state, as can be seen in Fig. 4.20(a). By inspecting the individual isospin-breaking components of this fit, see Fig. 4.20(b), it can be seen that this discrepancy

arises due to the V_{Cr} term. This term is used to track changes in radii along the yrast band, and determine the resulting MED contribution due to the difference in proton number [39]. In order to determine the size of the effect, the $p_{\frac{3}{2}}$ occupancy of excited states is tracked in the shell model calculations [39]. However, this method for calculating the V_{Cr} term appears to not be appropriate when pure single-particle excitations to the $p_{\frac{3}{2}}$ orbital are present, such as for this $\frac{3}{2}^-$ state, which contains a significant fraction of a pure $p_{\frac{3}{2}}$ single-particle configuration in its wavefunction.

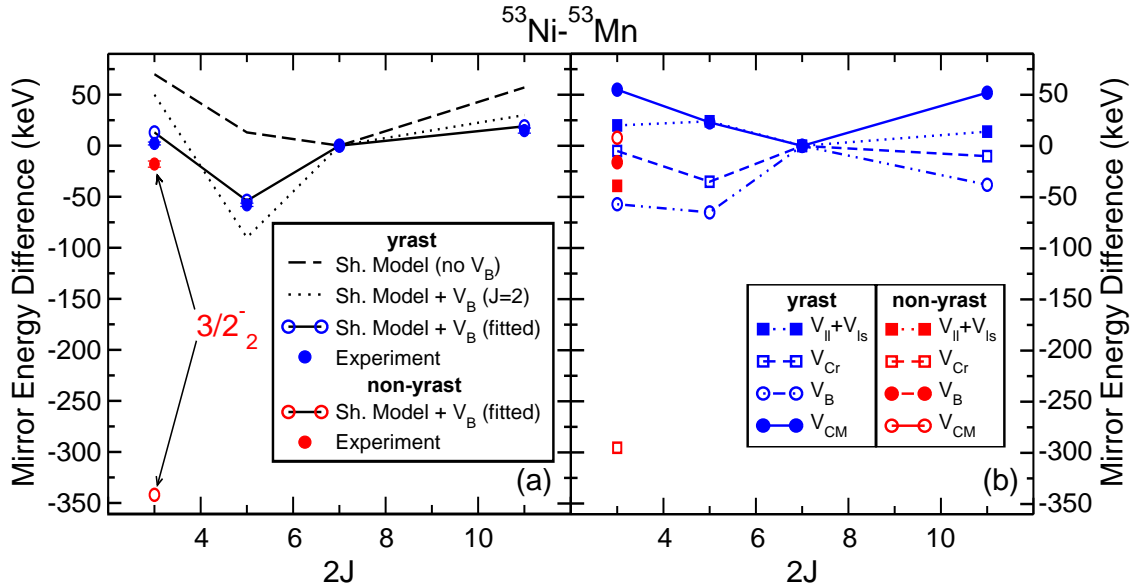


Figure 4.20: (a) A comparison between the experimental MED and the shell-model calculations. The dotted line shows the shell-model calculations including the V_B term for $J = 2$ only, the solid line shows inclusion of the fitted parameters for V_B , and the dashed line shows the calculations with no V_B term included, see text for more details. (b) The four isospin-breaking components of the shell-model calculations (described in Section 2.3.2), the sum of which yields the solid line in (a). For the V_B term, the fitted parameters have been used, see text for details. In (a) and (b) theoretical and experimental data points for yrast states and non-yrast states are coloured blue and red, respectively, where the lines only connect the yrast states.

4.5 The $A = 52$, $T_z = \pm 1$ mirror pair

4.5.1 Relative Cross Section Analysis

The calculated relative cross sections for ^{52}Co , using the approach described in Section 2.4.2, are shown in Fig. 4.21(a). These knockout cross section calculations were performed separately, for one-neutron knockout from either the ground state or the $J^\pi = \frac{19}{2}^-$ isomer, after which they were then combined to produce this plot, by assuming an isomeric ratio, as will be discussed later. In the shell-model calculations performed, spectroscopic factors were calculated for the four lowest energy states of each spin which could be populated in both of these reactions. These calculations showed that the vast majority ($\sim 98\%$) of the intensity proceeded directly to the 12 states shown in Fig. 4.21(a), while all other states were predicted to be populated with $< 0.25\%$ and therefore are not shown in this plot. In Fig. 4.21, three sets of states are shown, i.e. those which can be directly populated through one-neutron knockout reactions from (i) the $J^\pi = \frac{7}{2}^-$ ground state (no fill), (ii) the $J^\pi = \frac{19}{2}^-$ isomer (blue filled) or (iii) both (red/white diagonal lines).

The experimentally deduced relative cross sections for ^{52}Co , using the same method as described in Section 4.4, are shown in Fig. 4.21(b). Through the direct comparison between the measured experimental values and the calculated relative cross sections, an isomeric ratio of 22% was deduced, which gave the best level of agreement between the theory and the experimental values. In the knockout calculations, the majority of the intensity is predicted to go to the yrast states, with the exception of the 3^+ state, where the majority of the intensity is predicted to go to the 3_2^+ state. The shell-model calculations performed for this spin predicted the first two 3^+ states to be very close in energy. However, upon inspection of the wavefunction of both of these states, it was observed that the 3_1^+ state wavefunction contained a significant portion of a pure $p_{\frac{3}{2}}$ single-particle configuration and hence had a small overlap with the predominantly $f_{\frac{7}{2}}$ configuration of the ground state in ^{53}Co . Instead, the majority of the overlap was found between the 3_2^+ state and the ground state. As was discussed earlier in this analysis, see Section 4.2.3, the spin-parity of the currently labelled $(3^+, 4^+)$ state in ^{52}Co is uncertain, though with some analysis indicating this may be the analogue of the $3, 4^+$ state (possibly the 3_2^+ state) in ^{52}Mn . The cross section analysis performed here, also appears to support this, where a similar relative cross section branch is predicted to that observed for the $(3^+, 4^+)$ state in ^{52}Co .

Only a few minor differences are observed between the experimentally observed and

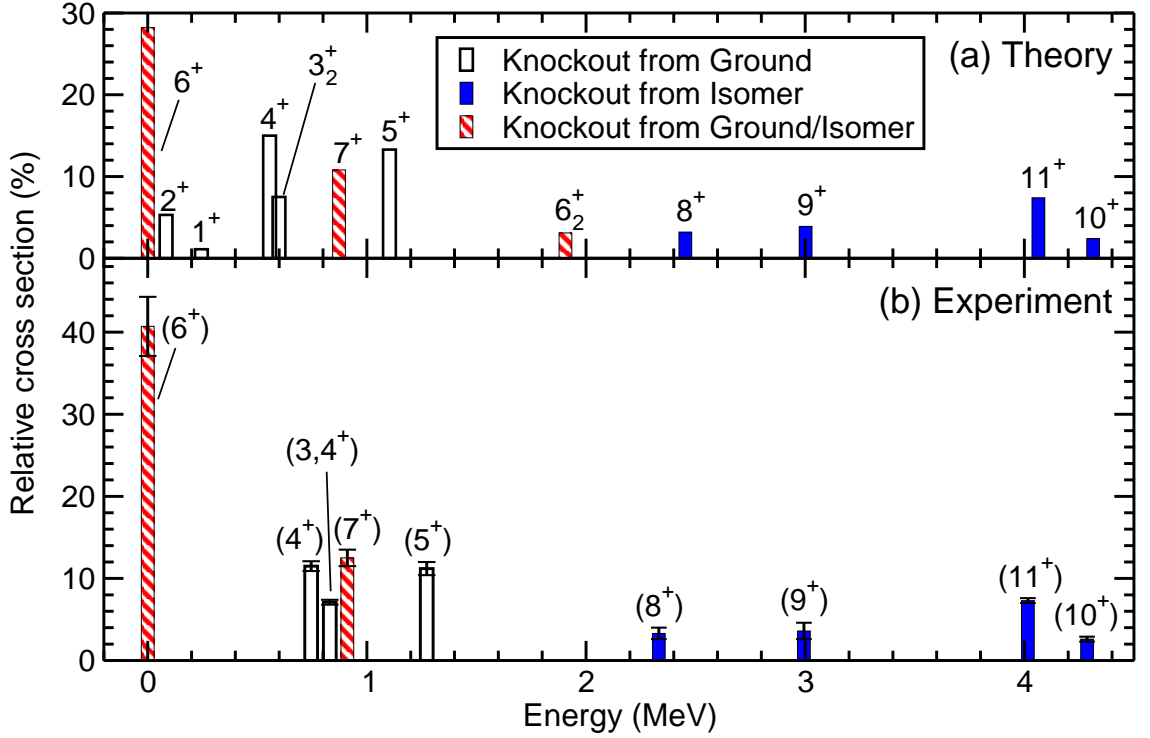


Figure 4.21: (a) Calculated relative cross sections for states in ^{52}Co populated either via one-neutron knock-out from the ^{53}Co ground state ($J^\pi = \frac{7}{2}^-$) [no fill], the high-spin isomeric state ($J^\pi = \frac{19}{2}^-$) [blue filled] or both [red/white diagonal lines]. A fractional population of the isomer of 22% has been assumed, see text for more details. The cross sections were calculated using a knockout reaction model using spectroscopic factor inputs from a shell-model calculation performed in the full fp valence space. (b) The experimentally measured relative cross sections for states in ^{52}Co .

the calculated cross sections, in particular, the non-observation of the weakly predicted 1^+ , 2^+ and 6_2^+ states. However, the non-observation of the former two states is simply due to the isomeric nature of these states, whereby, in addition, the 2^+ state is only observed to decay via β^+ decay to ^{52}Fe , as reported in Ref. [101]. In regards to the 6_2^+ state however, no such state has been firmly established in ^{52}Mn , though one possible candidate for this state has been previously observed, i.e. the $5^+, 6^+, 7^+$ state, which decays via a 1956(2) keV transition to the 6^+ ground state [65]. Upon inspection of the ^{52}Co γ -ray spectrum, previously shown in Fig. 4.12, one such unidentified weak transition with a similar transition energy is observed, at an energy of ~ 1960 keV. Another noticeable discrepancy between the experimentally observed and the calculated cross sections is the stronger observed population of the ground state. This discrepancy however, is mostly

likely due to the population of the three aforementioned states not being accounted for experimentally, which, in combination, are predicted to account for $\sim 10\%$ of the total intensity of states populated in ^{52}Co .

In summary, despite the fact that the isomeric ratio has been favourably adjusted in Fig. 4.21(b), excellent agreement is observed between Figs. 4.21(a) and (b), with a clear correspondence between experiment and theory on a state-by-state basis. Furthermore, the work performed here represents the first measurement and analysis of one-nucleon knockout from a high-spin isomer, whereby the agreement between the experimental and theoretical relative cross sections, amongst the high-spin states, is excellent.

4.5.2 MED Analysis

The results of the shell-model calculations performed for the $^{52}\text{Co}/^{52}\text{Mn}$ mirror pair, in addition to the experimentally deduced MEDs, are shown in Fig. 4.20(a). As can be seen, the agreement is quite poor between the experimental data and the shell model calculation including the usual INC V_B term (dashed line), calculated using a single $+100$ keV INC matrix element for $J = 2$ $f_{\frac{7}{2}}$ proton couplings, which is unusual for this mass region. However, calculating the V_B component for these states through the inclusion of a full set of effective isovector ($V_{pp} - V_{nn}$) matrix elements for $J = 0, 2, 4, 6$ proton couplings in the $f_{\frac{7}{2}}$ shell [10], as discussed previously in Section 4.4, resulted in the solid black line in Fig. 4.20(a). Here, the agreement with the experimental data is significantly improved, whereby this analysis also provides a compelling case for the inclusion of a full set of isospin-breaking matrix elements for all J -couplings for MED calculations performed in this region. The four isospin-breaking terms for the MED calculation of the solid line are shown in Fig. 4.20(b), where the fitted values of V_B have been used. It should be noted however, that the four matrix elements used here, in the calculation of the $V_B(J)$ terms, were extracted by fitting the shell model to all experimental MED data so far obtained in the shell, which also included the seven experimental data points discussed here [10]. Therefore, a new set of matrix elements were extracted, excluding these 7 data points, following which a new set of $V_B(J)$ terms were extracted, resulting in the fit shown by the dotted line in Fig. 4.20(a). As can be seen, the agreements is still very good and the conclusions of this analysis remain unchanged.

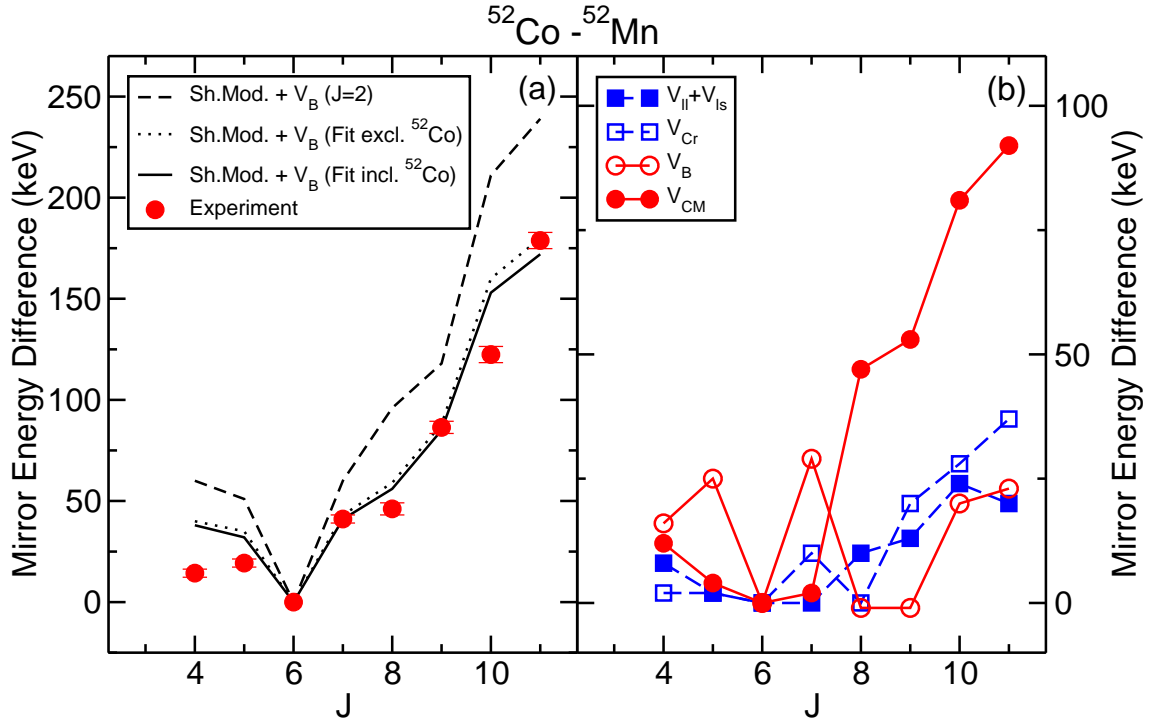


Figure 4.22: (a) A comparison between the experimental MED and the shell-model calculations. The three lines correspond to three different methods for determining the INC term, V_B . The dashed line determines V_B using a single +100 keV INC matrix element for $f_{7/2}$ protons coupled to $J = 2$, as in previous work (i.e. see Ref. [9]). The solid line uses four INC matrix elements ($-72, +32, +8, -12$ keV for $J = 0, 2, 4, 6$ extracted from a fit across the $f_{7/2}$ shell) to calculate the V_B term. The dotted line also uses four fitted matrix elements, but where the data for ^{52}Co has been excluded from the fit. (b) The four isospin-breaking components of the shell-model calculations (described in Section 2.3.2), the sum of which yields the solid line.

4.6 Discussion

In the following sections, some of the key findings and results from both the mirrored one-nucleon knockout and isomer knockout analyses will be discussed.

4.6.1 Mirrored Knockout Process

As has been demonstrated in a number of previous studies [86–88], the use of mirrored reactions can be a highly effective tool in the study of IAS in mirror nuclei. This is due to mirrored reactions leading to significant similarities in the resulting γ -ray spectra, allowing for mirror transitions to be readily identified and assigned, providing they are well known

in the neutron-rich mirror partner. This can be particularly useful when studying exotic proton-rich nuclei, far from stability, where γ -ray intensities can often be too small to either perform $\gamma - \gamma$ analysis or to measure state spins and parities.

Much of this previous work however, does not involve the use of **direct** mirrored reactions, as presented in this thesis, which can therefore lead to some discrepancies in the resulting spectra. Since in the shell model the wavefunctions of mirror nuclei are seen to be nearly identical, the use of mirrored one-nucleon knockout reactions should, in theory, result in an almost identical population of IAS in the mirror pair. Thus, the use of this mirrored reaction process can also be seen as a probe of the symmetry of the wavefunctions of mirror nuclei. In the work presented here, for the $^{53}\text{Ni}/^{53}\text{Mn}$ mirror pair, after accounting for discrepancies in the population of states due to differences in the isomeric populations of the beams and binding-energy effects, a high degree of symmetry was observed.

Previous work by Gade *et al.* [47,112], investigating one-neutron and one-proton knockout in a wide range of nuclei showed that for the removal of strongly bound neutrons, the experimental spectroscopic factors were highly suppressed compared to their theoretical equivalents, while the experimental spectroscopic factors for the removal of weakly bound protons were only slightly reduced. The use of mirrored one-nucleon knockout should therefore represent an ideal way to test these previous findings and expand this to the study of spectroscopic factors of excited states populated in these nuclei. For the work performed here however, it was not possible to make such a detailed comparison of experimental and theoretical spectroscopic factor for a number of reasons, the most important of which being the unknown population of the isomers in the secondary beams. Furthermore, a number of low-lying states were observed to be populated much more strongly than predicted, most likely due to unaccounted feeding from higher-lying states. This therefore suggests that any future work performed using mirrored one-nucleon knockout, particularly for the study of the mirror symmetry of wavefunctions, should be careful to either choose beams in which isomeric states are not expected to be populated, or alternatively, make sure the isomeric ratios are measured during the experiment. Furthermore, the work presented here also demonstrates the need for the use of a γ -ray detector system which can measure higher energy transitions with a reasonable efficiency, in order to ensure the feeding of low-lying states is more properly accounted for.

In summary, the mirrored knockout process is a tool which can be used to study

mirror symmetry, both in terms of MEDs and the study of the symmetry of wavefunctions in mirror nuclei, however the latter requires additional experimental considerations to be made.

4.6.2 One-nucleon Knockout from Isomeric States

One of the more interesting findings in this work was the discovery of a new technique to populate high-spin states in exotic nuclei, through the use of one-nucleon knockout from isomeric states. The work presented in this thesis represents the first analysis of this new technique, where it has been shown that the states populated can be predicted with a high level of accuracy providing the isomer is correctly identified in the shell-model calculations.

In general, particularly towards the proton drip line, nuclear physicists are limited to the study of low-spin states. The use of one-nucleon knockout from high-spin isomeric states however allows for these studies to be extended to higher-spin states through a direct process which can also be accurately modelled. Thus, this technique could play an important role in future nuclear structure studies, particularly using the planned new generation of fragmentation-based radioactive beam facilities.

4.6.3 Significance of the MED Results

It has been shown now in numerous studies, performed right across the $f_{7/2}$ shell, that the inclusion of the INC interactions due to the electromagnetic interaction alone, are not sufficient to explain the observed MED in nuclei [86–88]. Since the inclusion of the Charge Symmetry Breaking (CSB) V_B term for $J = 2$ $f_{7/2}$ proton couplings, the agreement with the experimental data has been significantly improved [86–88]. The origins of this CSB effect however remain unknown. Therefore, it was interesting in this work for the $^{52}\text{Co}/^{52}\text{Mn}$ mirror pair to observe, for the first time, a worsening in the fit to the experimental data following the inclusion of this CSB V_B term. This therefore suggests that the current shell-model prescription, outlined in Ref. [9], is not sufficient to explain all nuclei in the shell and therefore needs further development. This was performed by Bentley *et al.* in Ref. [10], where a full set of effective isovector ($V_{pp} - V_{nn}$) matrix elements for $J = 0, 2, 4, 6$ proton couplings in the $f_{7/2}$ shell were determined. The inclusion of these matrix elements in the calculations, particularly for the $^{52}\text{Co}/^{52}\text{Mn}$ mirror pair, resulted in a significant improvement in the fit to the experimental data, compared to using only the single CSB V_B term for $J = 2$ couplings. This work therefore strongly supports the use of these new

matrix elements in future calculations. In the mean time, more data needs to be collected across the shell in order to further test the inclusion of these new matrix elements.

4.7 Summary

In conclusion, many new states and γ -rays have been identified in the proton-rich nuclei ^{53}Ni ($T_z = -\frac{3}{2}$) and ^{52}Co ($T_z = -1$), from which new energy-level schemes have been constructed using a wide range of analytical techniques.

In the first work, concerning the $^{53}\text{Ni}/^{53}\text{Mn}$ mirror pair, the direct mirrored process used to populate these nuclei has allowed for a detailed understanding of the observed states populated in these nuclei, where the use of spectral comparison, γ - γ analysis and mirror symmetry arguments has allowed for the confident assignment of mirror transitions in addition to the assignment of state spins and parities. Furthermore, the asymmetrical line shape of the transitions observed from the long-lived $\frac{5}{2}^-$ state, in both ^{53}Ni and ^{53}Mn , has allowed for a comparison of mirrored lifetimes, where half-life measurements of 198(12) ps and 120(14) ps, respectively, were obtained, through the performance of a detailed line shape analysis. In addition, the observation of mirrored hole states, based on excitation from the $d_{\frac{5}{2}}$ -orbital (though possibly the $d_{\frac{3}{2}}$ -orbital) and the $s_{\frac{1}{2}}$ -orbital have been presented in this work. Finally, detailed comparisons have been made between experimental and theoretical relative cross sections for the mirrored one-nucleon knockout reactions populating the mirror pair. A high degree of symmetry is observed in the knockout process, where differences are attributed to binding-energy effects and the presence of isomers in the secondary beams. Accounting for these differences, a good agreement with the theoretical cross sections is obtained.

In the work performed for ^{52}Co , where no mirrored reaction was present in the data, a thorough analysis was performed involving the use of γ - γ coincidence analysis, a Doppler correction/lifetime analysis and mirror symmetry arguments in order to construct a new energy-level scheme and confidently assign state spins and parities. Compelling evidence has been presented for the observation of high-spin states, which could have only been populated through one-neutron knockout reactions from a high-spin isomeric state. This work therefore presents a new method to access high-spin states in exotic nuclei. Furthermore, it has additionally been shown in this work that a reaction model, coupled to spectroscopic factors determined in a full pf shell-model analysis, can be used to predict the distribution of cross section amongst high-spin states with excellent accuracy. Through the use of data

from a previous study of ^{52}Co [99], it was additionally possible to measure, for the first time, the mass excess (-34.481(14) MeV) and proton separation energy (1568(10) keV) of this nucleus.

Finally, experimental MEDs between IAS in the $A = 53 T_z = \pm\frac{3}{2}$ and the $A = 52 T_z = \pm 1$ mirror pairs have been computed, compared to large-scale shell-model calculations and interpreted in terms of INC interactions. The results, particularly in regards to the $^{52}\text{Co}/^{52}\text{Mn}$ mirror pair, show strong evidence for the need to include a full set of J -dependent INC terms in the analysis of mirror nuclei.

Chapter 5

Lifetime and Coulex

Measurements Across the $T = 1$

$A = 46$ Triplet of Nuclei

A topic of considerable interest in nuclear structure physics is the degree of purity of the isospin quantum number, where a great number of studies have attempted to investigate the phenomenon of isospin mixing in nuclei [2, 113–117], i.e. the mixing between states with a different isospin, T . Such mixing is expected to grow rapidly with increasing Z , due to the increasing strength of the long-range (and additive) Coulomb interaction, which acts to violate the underlying charge invariance and thus breaks isospin symmetry [119]. Moreover, isospin mixing is expected to be greatest along the $N \approx Z$ line, since here, proton and neutrons occupy the same orbitals and therefore have the maximum spatial overlap. Isospin mixing in nuclei can be studied in a number of ways, such as through the measurement of Fermi β decays to isospin-forbidden states [118] or through the study of isospin-forbidden transitions in nuclear charge exchange reactions [114]. Another way in which isospin mixing can be investigated is through the study of reduced EM matrix elements of analogue transitions, across a $T = 1$ isobaric triplet of nuclei [113]. In this case, providing isospin is a good quantum number, one would expect to observe a linear dependence between the EM matrix elements and T_z . This is due to the total EM matrix element, M_{tot} , for decays between analogue states of isospin, T , in an isobaric multiplet, being given by

$$M_{tot} = M_0 + \frac{T_z}{\sqrt{(2T+1)(T+1)T}} M_1, \quad (5.1)$$

where M_0 and M_1 are the isoscalar and isovector matrix elements, respectively [119]. Therefore, in order to perform a stringent test of this theoretical relationship, precise $B(E2 : 2_1^+ \rightarrow 0_{g.s.}^+)$ measurements need to be performed, across a $T=1$ isobaric triplet of nuclei. Direct information on these reduced transition strengths however, can only be obtained through the performance of lifetime, Coulex cross section or Nuclear Resonance Fluorescence (NRF) measurements.

In the present investigation, a combination of lifetime and Coulex cross section measurements were performed for the analogue $2_{T=1}^+ \rightarrow 0_{T=1}^+$ transition, across the $T = 1$, $A = 46$ triplet of nuclei, ^{46}Cr , ^{46}V and ^{46}Ti . Due to the large uncertainties associated with the previously measured reduced E2 matrix elements, particularly in the case of ^{46}Cr and ^{46}V (as will be discussed in Section. 5.1), an opportunity was presented to improve on these measurements, in order to investigate isospin mixing in ^{46}V . Furthermore, following the development of our new target device for high-precision lifetime measurements (in states populated via Coulomb excitation), an opportunity was also presented to test, for the first time, the use of this new technique for the nuclei studied here.

The following Chapter is divided into several sections. In the first section (Section 5.1), details on previous studies performed for the $T = 1$ $A = 46$ triplet are given. In the following section, the experimental considerations (Section 5.1) are presented, including details of the simulations performed for the new ‘‘Stretched Gold Target’’ (SGT) device. Following this, details on the experimental set up are given (Section 5.3), followed by details on the calibrations procedures which were followed in order to be able to identify incoming particles (Section 5.4) and outgoing particles (Section 5.5). Finally, in Section 5.6, details on the optimisation of γ -ray spectra are presented.

5.1 Previous Information

The $T = 1 \rightarrow 1$, $J^\pi : 2_1^+ \rightarrow 0_{g.s.}^+$ transitions, in each of the three nuclei studied here, have been observed in a number of previous studies [120–123] and therefore their respective transition energies are well established, as shown in Fig. 5.1(a). However, the $B(E2)$ transition strengths and therefore transition matrix elements, M_p , are not precisely known for all of these transitions [120–122], as demonstrated in Fig. 5.1(b). This therefore presented an opportunity to try and improve on these previous measurements, in order to investigate isospin mixing in ^{46}V , where, in this case in particular, mixing between the $2_{T=1}^+$ and $2_{T=0}^+$ states is of particular interest. Based upon both a previous

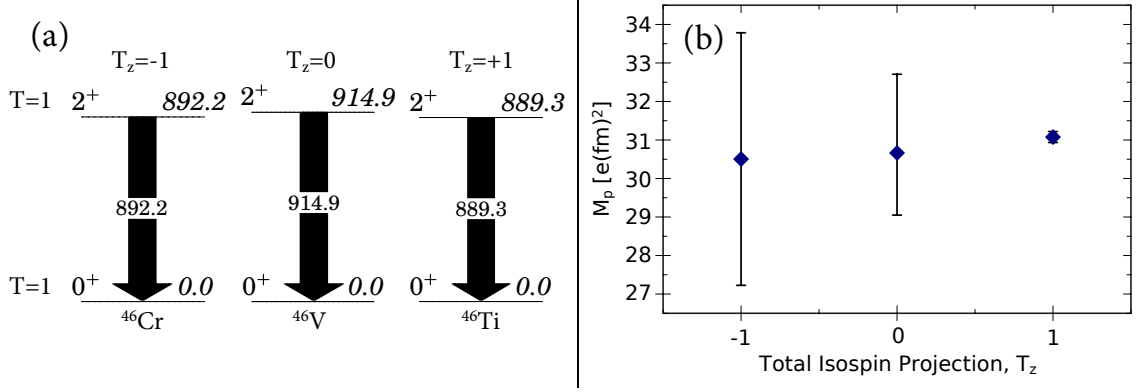


Figure 5.1: (a) The first excited $2_{T=1}^+$ states in the $T = 1$ $A = 46$ triplet of nuclei. (b) Matrix elements for the $T = 1 \rightarrow 1$, $J^\pi : 2^+ \rightarrow 0^+$ transitions in the $T = 1$ $A = 46$ triplet of nuclei. Data for both plots is taken from Refs. [120–123].

study, see Fig. 5.2, and a later shell-model calculation, the currently unobserved $2_{T=0}^+$ state is expected to occur within 100-200 keV of the $2_{T=1}^+$ state. Therefore, given their predicted close proximity in energy, the isospin mixing between these two states could be sizeable and therefore may result in a small modification in the M_p value for the $T = 1 \rightarrow 1$, $J^\pi : 2^+ \rightarrow 0^+$ transition in ^{46}V . As previously discussed, in the absence of isospin mixing, plots of M_p vs T_z , for $T = 1 \rightarrow 1$, $J^\pi : 2_1^+ \rightarrow 0_{g.s.}^+$ transitions in $T = 1$ triplet systems, should result in the observation of a linear trend. Therefore, by testing this linear relationship for the $T = 1$ $A = 46$ triplet system, information on isospin mixing in ^{46}V can be obtained. In order to investigate this however, the uncertainties in the measured transition matrix elements must first be significantly reduced, particularly in the case of ^{46}Cr and ^{46}V .

5.2 Experimental Considerations

The original aim of this investigation was to be able to measure the E2 matrix elements for each $T = 1 \rightarrow 1$, $J^\pi : 2_1^+ \rightarrow 0_{g.s.}^+$ transition across the $T = 1$ $A = 46$ triplet of nuclei, in a model independent way, i.e. through high-precision lifetime measurements. This was to be achieved through the use of a new technique for lifetime measurements, as will be discussed in detail in Section. 5.2.1, using a new device known as the Stretched Gold Target (SGT). However, in the lead up to the experiment, a number of issues regarding both the achievable intensity and the inhomogeneous structure of the beam, meant contingency plans had to be made for the experiment. Furthermore, the situation was made worse

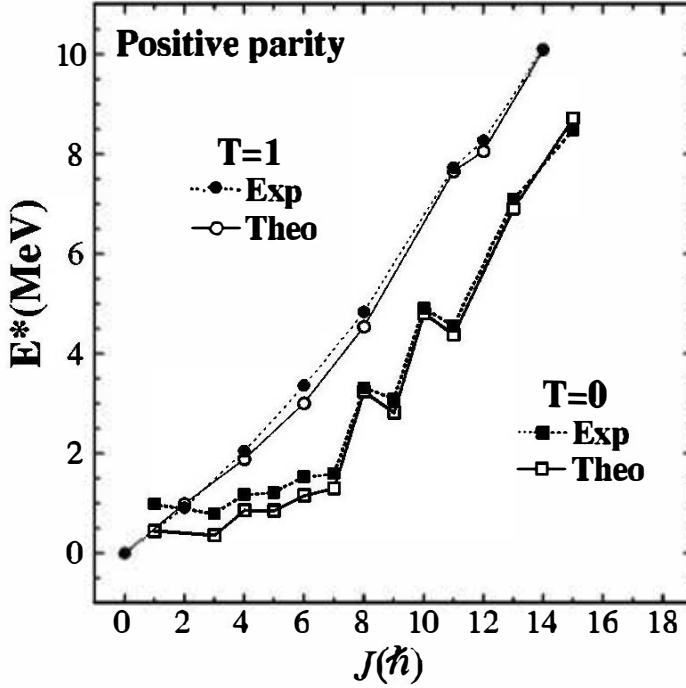


Figure 5.2: Comparison of shell model predicted and experimentally observed energies for $T = 0$ and $T = 1$ states in ^{46}V , taken from Ref. [124]

when updates to the production cross sections for one of the nuclei of interest, ^{46}Cr , were discovered, showing a reduction from 1.59×10^{-2} mb [125] to 5.16×10^{-3} mb [126], i.e. a factor of 3 lower than the original experimental proposal. As a result, the achievable ^{46}Cr beam rate was predicted to be too small to be able to perform lifetime measurements for the $2_{T=1}^+$ state in this nucleus, and therefore the experiment was instead proposed to be split into two sub experiments. In the first of these sub experiments, Coulex cross section measurements would be performed for both ^{46}Cr and ^{46}Ti , while in the second sub experiment, lifetime measurements would be performed for both ^{46}V and ^{46}Ti , where in both cases the well-studied ^{46}Ti would be used to test the reliability of the measurements and to serve as a calibration point. This therefore would allow for $2_{T=1}^+ \rightarrow 0_{T=1}^+$ matrix elements to be extracted for ^{46}Cr , but without the need for very high statistics. However, this also meant that the matrix elements could not be obtained in a model independent way. Furthermore, this also meant that any feeding/population of this $2_{T=1}^+$ state via alternative mechanisms than direct Coulomb excitation would also need to be accounted for.

The experimental requirements for this investigation therefore included the ability to uniquely identify incoming particles on an event-by-event basis (particularly for the Coulex

cross section analysis) and the ability to be able to at least identify outgoing particles by their atomic number, Z . Furthermore, due to the technique used to measure lifetimes during this experiment, it was particularly important to be able to measure particles velocities on an event-by-event basis at the reaction target position. Finally, the last requirement for the experiment included the need for a γ -ray detector system with both a high energy resolution and a high efficiency, as this would be particularly crucial for both the lifetime and Coulex measurements. All of these experimental requirements were met in the experimental set-up described in Section. 5.3.

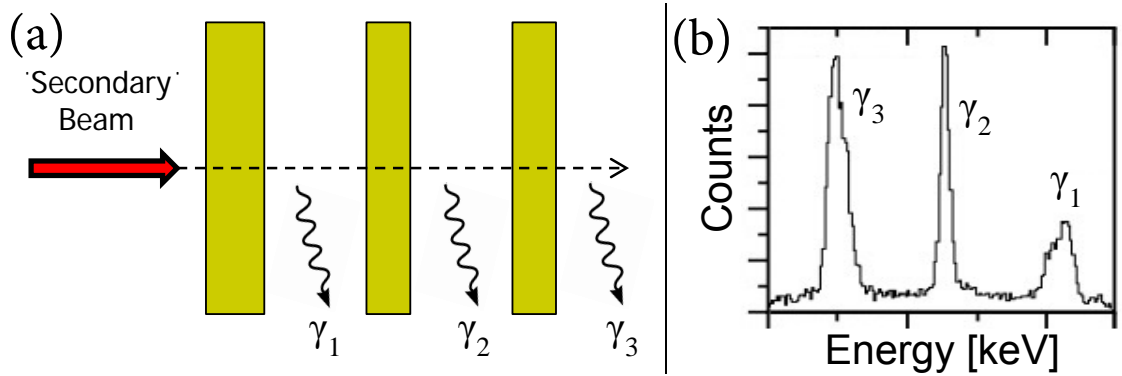


Figure 5.3: (a) Illustration of the Stretched Gold Target (SGT), where each gold foil acts as both a Coulex target and as a degrader, resulting in the observation of a triple peak distribution, due to differences in the ion emitter velocity after each target. (b) Simulated triple peak distribution for the stretched target device, where the Doppler correction has been optimised for the second peak.

5.2.1 Stretched Gold Target (SGT) Lifetime Simulations

Prior to the experiment, a new technique for high-precision in-beam lifetime measurements of short-lived states was developed at the University of York. This technique, similar to that of the Recoil Distance Doppler-Shift (RD DS) technique [127], involves the use of a device known as the Stretched Gold Target (SGT), which consists of three gold target, each separated by a predetermined distance, depending upon the half-life of the nuclear state of interest. Unlike the standard RD DS technique however [127, 128], which usually involves the use of a single target foil, to populate the nuclear states of interest, followed by a degrader foil, to either slow or stop the beam, each gold target in the SGT acts both as a Coulex target and as a degrader. Moreover, this use of three gold target foils, as opposed to one target foil followed by two degrader foils, also distinguishes this new device from other

similar devices such as the TRIPLE PLunger for EXotic beams (TRIPLEX) [129]. Due to this, this new device can more accurately be categorised as a stretched target, rather than a plunger, where the small gaps between each target results in the observation of a triple peak distribution, due to the different ion emitter velocity after each subsequent target, as demonstrated in Fig. 5.3. The distribution of counts in the three peaks therefore, is highly correlated with the half-life of the state, which in turn can either be extracted from a detailed lineshape analysis of the resulting distributions or, if both the separation and statistics of the three peaks is sufficient, by comparing simulated and experimental ratios of counts in the observed peaks.

In order to be able to utilise this new technique, to perform high-precision lifetime measurements in the nuclei of interest, a number of experimental considerations, both regarding the beam and the SGT, had to first be made. These included considerations regarding:

- The thickness of the gold targets - As this will affect the production of 2^+ states, the energy loss of the beam and the number of decays occurring between the peaks.
- The beam energy - As this will affect the separation of the peaks.
- The separation of the targets - As this will affect the sensitivity of this technique to the half-life of the state.

Firstly, when deciding upon the thickness of the three targets to be used for this experiment, three main factors were considered. These included, the production yield of $2^+_{T=1}$ states, the portion of decays expected to occur inside the target (relative to outside the target), and finally, the energy loss of the ions after each target. As a result, the targets needed to be sufficiently thick, to ensure a good level of statistics, but not too thick such that a large portion of the decays occurred inside the targets (with a varying ion velocity), as this would increase the number of counts occurring between the peaks, thereby reducing the resolvability of the triple peak structure. Furthermore, the targets also needed to be thick enough in order to sufficiently degrade the beam, such that the separation between the triplet distribution was not too small, though this effect also depended upon the beam energy, as will be discussed later. Therefore, a number of simulations were performed to try and estimate a suitable target thickness, initially for the first target. These simulations involved a beam of ^{46}Ti impinging upon a single gold Coulex target with a variable thickness. A total beam rate of 1×10^8 ions was used, in addition to a

Coulex cross section of 100 mb and a half-life of 5.3 ps, all of which approximately match the experimentally measured values for this nucleus [122]. From these simulations, the total number of excited ions produced for each gold target thickness was determined and the portion of these ions which either decayed inside the target, or further downstream. The results of this simulation are shown in Fig. 5.4(a), where it can be clearly observed at a thickness of ~ 0.1 mm that an increasing portion of the number of excited ions produced (for any further increase in thickness) results in more decays occurring inside the target. However, this only starts to become more significant after around ~ 0.4 mm, where for example, an increase of 100 mg/cm^2 results in an increase of ~ 3000 total excited ions produced, however 25% of this total increase arises from more ions decaying inside the target. In Fig. 5.4(b), the energy loss of the beam, for different gold target thicknesses, is shown, where an initial beam energy of around 170 MeV/u was used. In order to see any significant separation/shift in the centroid energy of each peak, at these beam energies, would require a reduction in beam energy of around $15\text{-}20 \text{ MeV/u}$ (or a change in β of $\sim 0.02\text{-}0.03$). Therefore, based upon both this analysis and the previous simulation, gold target thicknesses of $0.375/0.25/0.25$ mm were chosen. The thicker first target allows for a large initial population of ions, which is particularly necessary for the third peak in the distribution, while the second two targets serve to further degrade the beam, to separate the peaks, and also increase the statistics through further Coulomb excitation reactions.

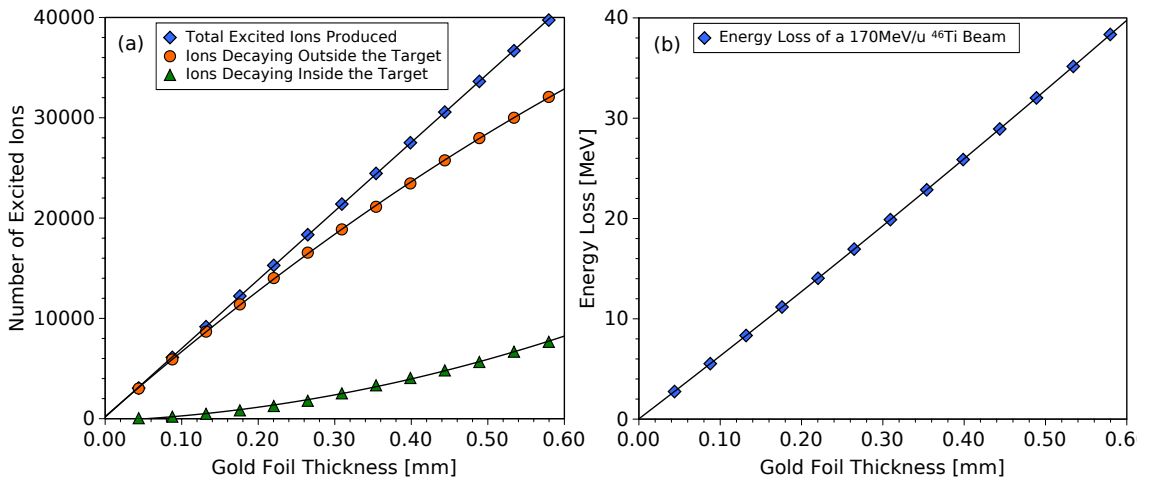


Figure 5.4: (a) Simulated number of total excited ions produced through Coulomb excitation reactions with a gold target of different thicknesses, where the number of ions decaying both inside and outside the target is calculated, see text for more details. (b) Calculated energy loss for a $170 \text{ MeV/u } ^{46}\text{Ti}$ ion beam passing through a gold foil.

Secondly, regarding the beam energy, the most important consideration made here relates to the result of a shell model calculation, which predicted the $2_{T=0}^+$ and $2_{T=1}^+$ states in ^{46}V to be very close in energy (within 100 keV). In addition, there were also concerns that the 1^+ might also be populated, which is within 80 keV of the $2_{T=1}^+$ state. Due to this, the beam energy was chosen such that the spread of the triple peak distribution was large enough to be able to resolve the triple peak structure, but small enough to ensure that if the $2_{T=0}^+$ state was populated during the experiment that it would not overlap with the triple peak structure. This was achieved by performing energy loss calculations, for different secondary beam energies, to calculate the approximate energy (and therefore velocity) of ions after each target, and therefore determine the approximate separation of the peaks in the resulting energy spectrum. In this case, it was decided to limit the spread of the triplet peak distribution to around 50 keV, which, for nuclei studied here, corresponded to a secondary beam energy of around 170 MeV/u, before the SGT.

The final experimental consideration to be made relates to the optimisation of the separation between the gold targets, such that the highest sensitivity to changes in half-life, in the region of interest (~ 5 ps), could be achieved. This firstly involved optimising the separation between the first two gold foils, whereby simulations were performed for different target separations, over a range of half-lives, with a suitable total number of counts in the two peaks (5000). Following this, by comparing the ratio of counts in the two peaks against half-life, for different target separations, the optimal distance could be found. This was achieved by firstly considering a linear fit to the simulated data of ratio vs half-life, then taking a data point, X , along this line and its respective error in ratio (derived from the \sqrt{n} errors of the two peaks added in quadrature), then determining the resulting $\pm 1\sigma$ in the half-life. Following this, by considering two data points, X_- and X_+ , with half-lives $\pm 5\%$ of this value, the equivalent $\pm 1\sigma$ half-life values for both of these data points could also be found. Finally, to optimise the target separation, the difference between $X_- + 1\sigma$ and $X - 1\sigma$ was plotted against target separation, where the larger the difference, the more precise the measurement. For completeness the same procedure was followed for the difference between $X^+ - 1\sigma$ and $X + 1\sigma$. This method yielded an optimal separation of 1.0 mm, which is approximately the same distance travelled in one lifetime at these beam velocities. Following this, a similar approach was also taken to determine the optimal separation between the second and third target, while keeping the separation between the first two targets constant at 1.0 mm. Since in this case there were three

peaks, a larger number of different ratios could also be considered, where one of the more favourable ratios, in terms of lifetime sensitivity, was Peak 1/(Peak 2 + Peak 3). For this ratio, an optimal separation of 0.7 mm was obtained, which also allowed for a lifetime precision better than 4%, which was also slightly better than the experimental aim of 5%. However, for simplicity of design, and since the precision was still simulated to be better than 4%, a second separation of 1.0 mm was also used. The final schematic design of the SGT is shown in Fig. 5.5, where due to slight concerns regarding the flatness of the gold foils, thick aluminium frames and thin (1.0 mm) aluminium frame dividers were produced to both surround and clamp the entire outer edge of each gold foil. Furthermore, in order to allow air to be removed from between the targets during the experiment, four small insertions, to each aluminium frame divider, were made, as shown in the side view of the target in Fig. 5.6(a), where for completeness, the front view of the target is also shown in Fig. 5.6(b).

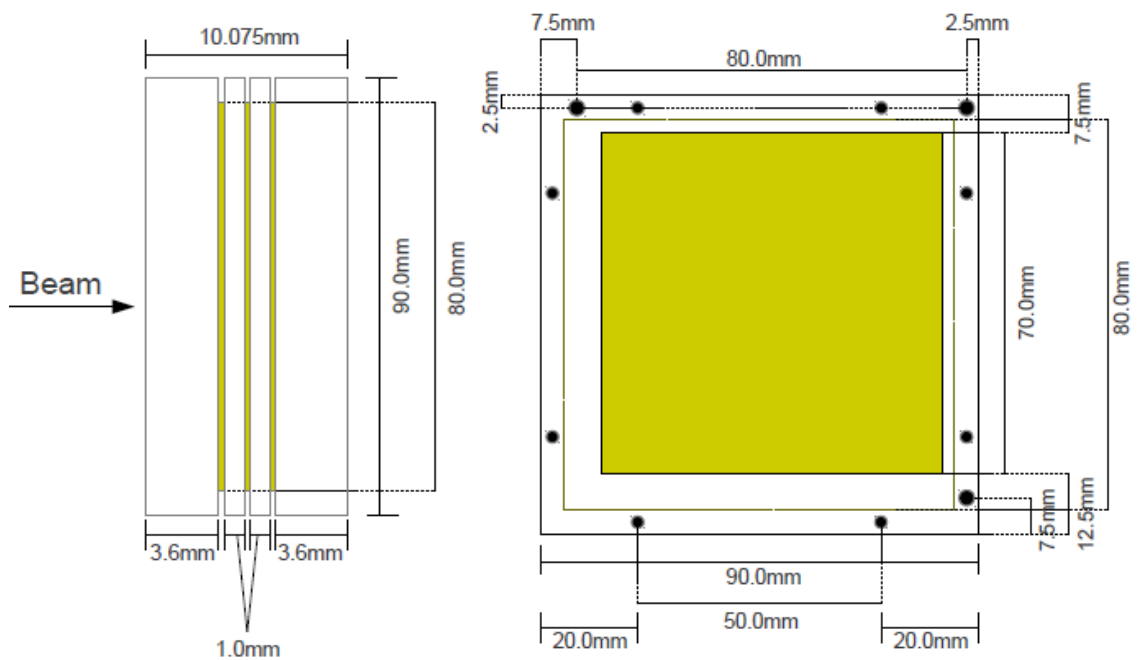


Figure 5.5: Schematic diagram of the Stretched Gold Target (SGT) target, showing the target measurements from both the side and front.

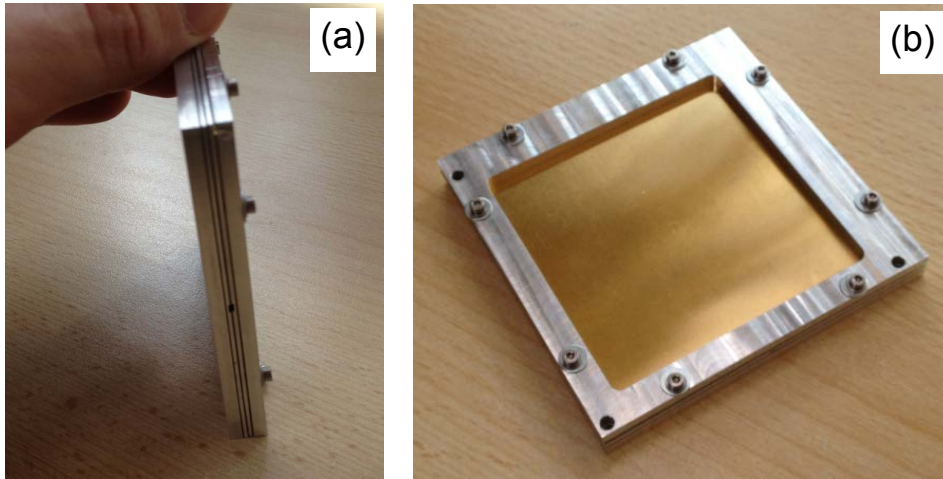


Figure 5.6: Photographs of the Stretched Gold Target (SGT), showing the target from both (a) the side and (b) the front. The target consists of three gold foils, each with a thickness of 0.375, 0.25 and 0.25 mm from front to back, where each gold foil is separated by a distance of 1.0 mm.

5.3 Experimental Set-up

The experiment for this investigation was performed at the Gesellschaft für SchwerIonenforschung (GSI) facility near Darmstadt, Germany, where secondary beams of the nuclei of interest were produced through the use of primary beam acceleration (Section 5.3.1) and in-flight projectile fragmentation (Section 5.3.2) techniques. These secondary beams were impinged upon a reaction target consisting of either a single gold foil, for Coulex measurements, or a triple stack of gold foils, for lifetime measurements. The resulting reaction products were identified downstream using the LYCCA calorimeter (Section 5.3.4) while γ rays emitted in-flight from excited nuclei inside the target chamber were detected using AGATA (Section 5.3.4). A schematic of the experimental set-up for this investigation is shown in Fig. 5.7.

5.3.1 Primary Beam Production

The process of primary beam production at GSI firstly begins with the acceleration of ions, provided from an Electron Cyclotron Resonance (ECR) ion source, using the UNiversal LINear ACcelerator (UNILAC), where beam energies up to 20 MeV/u can be achieved [130]. Following this, the pre-accelerated beam is injected into the the SchwerI-

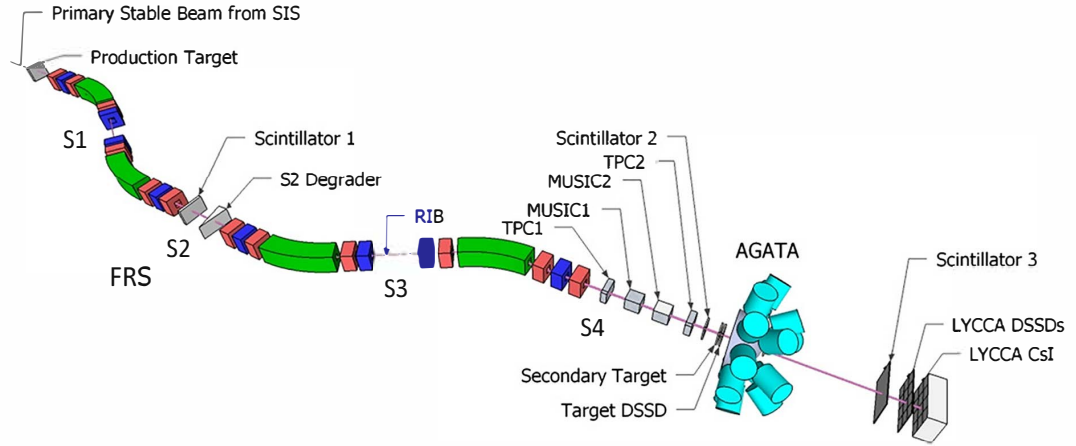


Figure 5.7: Schematic of the experimental set-up used at GSI during the 2014 AGATA-PreSPEC campaign, showing from left to right, the SIS, the FRS, AGATA and LYCCA. Taken from Ref. [131].

onensynchrotron (SIS-18), where ions are further accelerated up to energies of 2 GeV/u. The extraction process of ion beams from the SIS-18, typically involves a one second extraction time (spill length) and two second ramping time, yielding a total spill duration (period) of three seconds, where beam intensities up to around 3×10^9 ions/spill can currently be achieved, particularly for lighter ion beams.

5.3.2 Secondary Beam Production and the GSI Fragment Separator

To produce the secondary beams of interest, a 600 MeV/u ^{58}Ni primary beam, provided by the SIS-18, was impinged upon a thick 2.5g/cm^2 ^9Be production target, positioned at the entrance of the FRagment Separator (FRS) [132]. At these beam energies, the dominant reaction channel was fragmentation, resulting in the production of many $A < 58$ fragments. These beam fragments, in addition to any unreacted primary beam, were then separated using the FRS, a high-resolution forward spectrometer, located immediately after the production target [132]. This separation was achieved, in the FRS, through the use of four 30° bend superconducting dipole magnets (with a maximum magnetic rigidity of 18.5 Tm), where each dipole magnet was also equipped with a set of quadrupole and sextupole magnets both before and after the dipole. Here, the quadrupole magnets were used to focus the beam, while the sextupole magnets were used to perform higher-order aberration corrections and the 30° bend dipole magnets were used to provide an A/Z

dispersion of the beam in accordance with equation Equation 5.2,

$$B\rho = \frac{Mc}{Ze}\beta\gamma \approx \frac{Am_u c}{Ze}\beta\gamma. \quad (5.2)$$

In this expression, B is the strength of the magnetic field, ρ is the bending radius of the dipole magnet (or alternatively the bending radius of the particle trajectory), $M(\approx Am_u)$ and Z are the mass and charge of the particle, e is the elementary charge, and $\beta = v/c$ and $\gamma = (1/\beta^2)^{-1/2}$ are the relativistic factors.

Four focal planes are defined in the FRS (one after each dipole magnet), labelled S1 to S4 in Fig. 5.7, where a set of slits can be inserted at each in order to reduce the number of contaminants in the beam. In addition, at S2, a wedge degrader is used to introduce a momentum spread into the beam, for nuclei with a different atomic number, Z , in accordance with the Bethe-Bloch formula (Equation 5.3), which describes the energy loss of a charged particle travelling through matter.

$$-\left\langle \frac{dE}{dx} \right\rangle = \frac{4\pi n Z^2}{m_e c^2 \beta^2} \left(\frac{e^2}{4\pi\epsilon_o} \right)^2 \left[\ln \left(\frac{2m_e c^2 \beta^2}{I(1-\beta^2)} \right) - \beta^2 \right] \quad (5.3)$$

In this expression, n is the electron density of the material, m_e and e are electron mass and charge, respectively, c , is the speed of light in a vacuum, ϵ_o , is the vacuum permittivity, $\beta = \frac{v}{c}$ is the velocity of the particle, and I is the average excitation potential of the material. By adjusting either the angle or the shape of the wedge at S2, the FRS can be chosen to be run in either achromatic mode or mono-energetic mode. In achromatic mode, the spatial distribution of a given nuclide at the final focal plane is reduced, therefore allowing for contaminants arriving at different positions to be removed through the use of slits at S3 and S4. In mono-energetic mode, the position dependence of momentum at S2 is corrected for, such that all centred ions after the wedge degrader have the same momentum, though this also results in a much broader spatial distribution at the final focal plane.

Therefore, the beam fragments of interest can be selected by the FRS utilising a $B\rho - \Delta E - B\rho$ method, where the magnetic rigidity of the first pair of dipole magnets are set to select beam fragments of a single magnetic rigidity (i.e. nuclei with a similar A/Q), after which a wedge acts to disperse nuclei with a similar A/Q but different atomic number, Z . Finally, the beam fragments of interest are separated from the remaining contaminants through the use of a second pair of dipole magnets and slits.

In the experiment performed, three different FRS settings were used in order to produce secondary beams of ^{46}Cr , ^{46}V and ^{46}Ti , as tabulated in Table. 5.1. Since the aim was to

Table 5.1: Summary of the different degrader material used during each FRS setting.

FRS Setting	^{46}Ti	^{46}V	^{46}Cr
Primary Beam	^{58}Ni	^{58}Ni	^{58}Ni
Primary Beam Energy [MeV/u]	599.65	599.65	599.65
Production Target	2.5 g/cm ² ^9Be	2.5 g/cm ² ^9Be	2.5g/cm ² ^9Be
S1 Degrader	2.0 g/cm ² ^{13}Al	2.0 g/cm ² ^{13}Al	2.0 g/cm ² ^{13}Al
S2 Degrader/Wedge	8.0 g/cm ² ^{13}Al	6.8 g/cm ² ^{13}Al	5.7 g/cm ² ^{13}Al

produce each of these secondary beams with a beam energy of ~ 170 MeV/u at the reaction target position, additional degrader material was also used at the S1 and S2 position. Due to the different atomic number, Z , of the nuclei of interest, different thickness degrader material was used at S2 during each setting, as detailed in Table. 5.1. For all three settings the FRS was run in achromatic mode, due to the higher rates predicted by the LISE calculations [73] in this mode, compared to using mono-energetic mode, where only a small improvement in the energy spread was also predicted. Following the production of these secondary beams, they were then delivered to the experimental area and impinged upon a reaction target, placed at the centre of the reaction chamber.

5.3.3 FRS Auxiliary Detectors

In order to uniquely identify ions reaching the final focal plane of the FRS, their positions, velocities and charge must first be measured. This is achieved through the use of a selection of FRS detector systems, where position, time-of-flight (ToF) and energy loss information is provided by the Time Projection Chambers (TPCs), the scintillator detectors (SC_{21} and SC_{41}) and the Multiple Sampling Ionisation Chamber (MUSIC) detectors, respectively. In the following sections, a brief description will be given of each detector system.

5.3.3.1 Time Projection Chambers

Time Projection Chambers (TPCs) are position-sensitive detectors, used to measure the XY-positions of charged particles which traverse them [133]. At both the S2 and S4 focal plane positions of the FRS, a pair of TPCs are installed for this purpose, whereby the position information provided by these detectors is used to track particle trajectories through the separator. Each TPC detector has an active area of 240 mm (in the dispersive plane) \times

60/80/100/120 mm (in the non-dispersive plane), depending upon the experimental needs, and an active thickness of 70 mm. The volume of each chamber is filled with a gas mixture of 90% Ar and 10% CH₄, at atmospheric pressure. Incident charged beam particles ionise the gas mixture, which results in the production of electron-ion pairs. In the presence of a uniform electric field, generated by applying a high voltage to the cathode and Mylar strips surrounding the chamber (see Fig. 5.8), these electrons drift towards four anode wires located at the bottom of the TPC. Each anode wire sits inside a C-pad formed cathode, whereby the charge collected on the anode wires induces a positive charge on these C-pads. In addition, each C-pad is connected to one of two delay lines, which provides a 15 ns delay between neighbouring pads. The dispersive position of a particle is determined by measuring the time difference between the induced signals on the left and right side of each delay line, while the non-dispersive position is measured by the drift time of electrons to the anode wires. Each TPC therefore, provides two independent measurements in the dispersive plane and four independent measurements in the non-dispersive plane. A commissioning experiment for the TPCs, using ⁴⁰Ar and ⁸⁰Kr primary beams, obtained external resolutions (including scattering in materials between TPCs) of $\sigma_x \approx 160\mu\text{m}$ and $\sigma_y \approx 200\mu\text{m}$, and internal resolutions of $\sigma_x \approx 88\mu\text{m}$ and $\sigma_x \approx 38\mu\text{m}$ [133]. Furthermore, using a 1 GeV/u ²³⁸U beam, tracking efficiencies of >99% and >90% were obtained for beam intensities of 40 and 250 kHz, respectively [133].

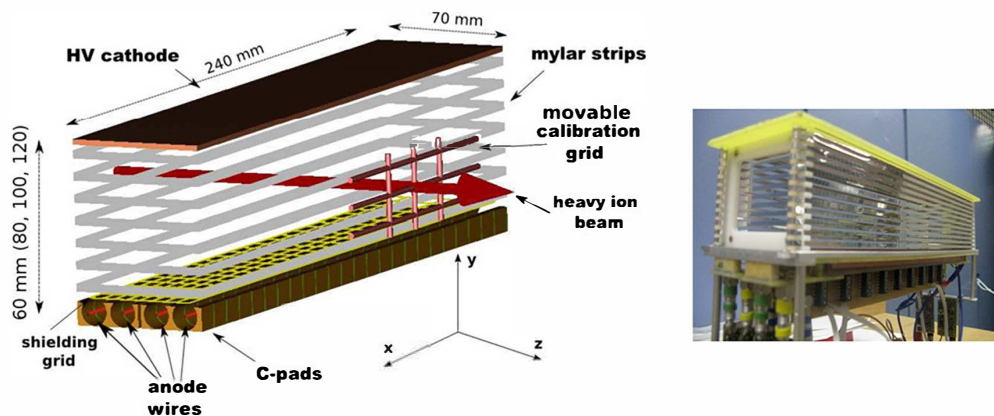


Figure 5.8: Schematic diagram of the TPC detectors used to track particle positions through the FRS, shown beside a picture of the mounted detector [133].

5.3.3.2 FRS Scintillator Detectors

Ion velocities in the FRS are obtained by measuring their Time-of-Flight (ToF) between two plastic scintillators, SC_{21} and SC_{41} , located at the S2 and S4 focal planes, respectively. Each scintillator has an active area of 200 mm (in the dispersive plane) \times 80 mm (in the non-dispersive plane) and an active thickness of either 3 mm or 5 mm, for the SC_{21} and SC_{41} scintillators, respectively [134]. Incident charged beam particles generate light within the plastic scintillator material, through the process of scintillation, whereby the resulting photons are collected by two PhotoMultiplier Tubes (PMTs) connected to both the left and right side of each scintillator. The ToF of a particle is then determined, independent of its position, by

$$ToF = \frac{ToF_{LL} + ToF_{RR}}{2}, \quad (5.4)$$

where ToF_{LL} and ToF_{RR} are the ToF measurements made using timing information from either the left PMT of both scintillators or the right PMT of both scintillators. Therefore, the ion velocities can be determined, using the known distance, x , between the two scintillators,

$$\beta = \frac{x}{ToF} \cdot \frac{1}{c}. \quad (5.5)$$

In addition to measuring the ToF, the scintillator detectors can also be used to measure particle positions, which is particularly useful for experiments with very high beam rates, where the tracking efficiencies of the TPCs are much lower [133]. However, the position resolution of the scintillators is much worse, where a spatial resolution as large as a few mm has been previously observed for the mass region of interest in this study [134].

5.3.3.3 Multiple Sampling Ionisation Chambers

In order to obtain the charge of ions at the final focal plane of the FRS, energy loss measurements are performed using two Multiple Sampling Ionisation Chamber (MUSIC) detectors [135], situated at the S4 focal plane between two TPC detectors, see Fig. 5.7. Each detector has an active area of 200 mm (in the dispersive plane) \times 200 mm (in the non-dispersive plane) and an active thickness of 400 mm, where the anode plate of each chamber is divided into eight identical sections along the beam direction. The gas fill of each chamber is a mixture of 90% Ar and 10% CH₄, at atmospheric pressure. The principle of operation is similar to that of the TPCs, whereby incident charged particles ionise the gas molecules, resulting in the production of electron-ion pairs. The electrons

then drift toward the positively biased anode strips, generating a pulse, the height of which is directly proportional to the energy loss of the charged particle traversing the chamber. The energy loss for a given event is then found by taking the average of the energy-loss signals of all eight anode sections. Since the energy loss of the ion is proportional to Z^2 , in accordance with the Bethe-Bloch formula (Equation 5.3), the atomic number, Z , of a charged particle can be determined, following a correction for its dependence on β .

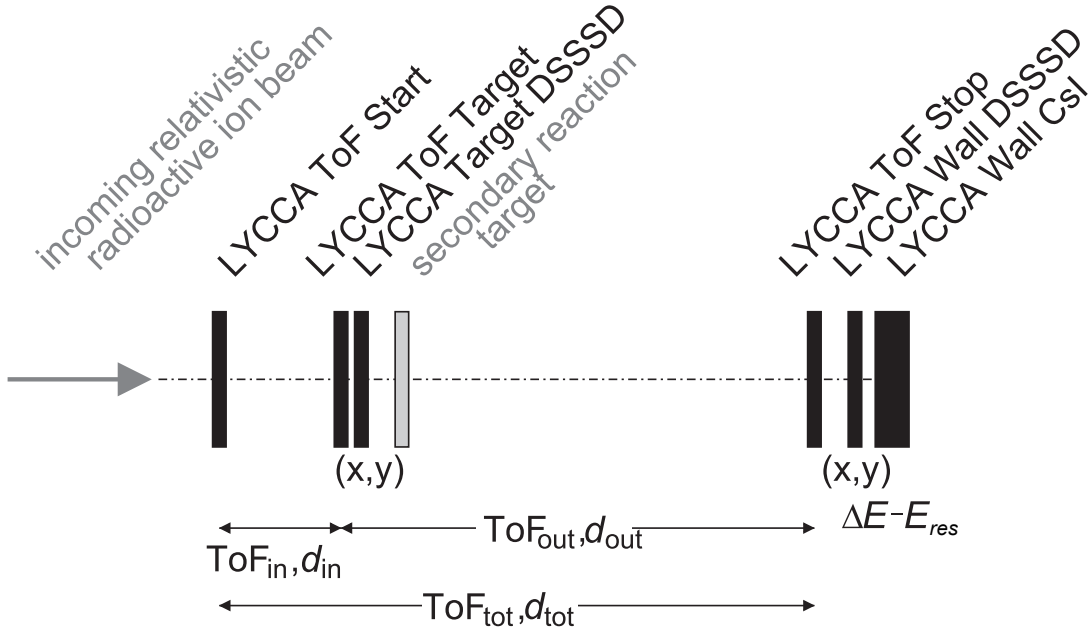


Figure 5.9: Schematic layout of the various LYCCA detectors (shown in black) used at GSI [136]. The LYCCA ToF target detector was not available during the experiment, see text for more details.

5.3.4 The LYCCA Detector Array

The Lund-York-Cologne CALorimeter (LYCCA) [136] is used for the identification and tracking of ions after the reaction target. As shown in Fig. 5.9, LYCCA is comprised of a number of detector systems, whereby position, ToF, energy loss (ΔE) and residual energy (E_{res}) measurements are performed through the use of Double-Sided Strip Silicon Detectors (DSSSDs), fast plastic scintillators, wall DSSSD modules and Caesium Iodide (CsI(Tl)) crystals, respectively. Ions after the secondary target are identified by their atomic number (Z), through $\Delta E - E_{res}$ measurements in the LYCCA wall, while different isotopes can additionally be identified by combining this information with ion velocity measurements obtained using ToF and position information. In addition, this ion velocity,

also commonly referred to as the event-by-event LYCCA β , can also be used for the Doppler correction of γ -ray spectra. In the following sections, a brief description will be given of the various detector systems used in LYCCA.

5.3.4.1 Double-Sided Silicon Strip Detectors (DSSSDs)

Double-Sided Silicon Strip Detectors (DSSSDs) are commonly used detectors in physics experiments due to their ability to measure both the energy loss (ΔE) and position of charged particles passing through the silicon material [136]. Each DSSSD module used in LYCCA has an active area of $58.5 \times 58.5 \text{ mm}^2$ and a nominal thickness of $300\text{-}320\mu\text{m}$. The active area on both the front (p-side) and back (n-side) of each DSSSD is subdivided into 32 horizontal strips, running in orthogonal directions for both sides, which results in the creation of 1024, $1.83 \times 1.83 \text{ mm}^2$ pixels. For the Target DSSSD, each strip is read-out individually, while for the 16 Wall DSSSD modules (see Fig. 5.10), the strips are read-out two by two, i.e. resulting in 256, $3.66 \times 3.66 \text{ mm}^2$ pixels for each module.

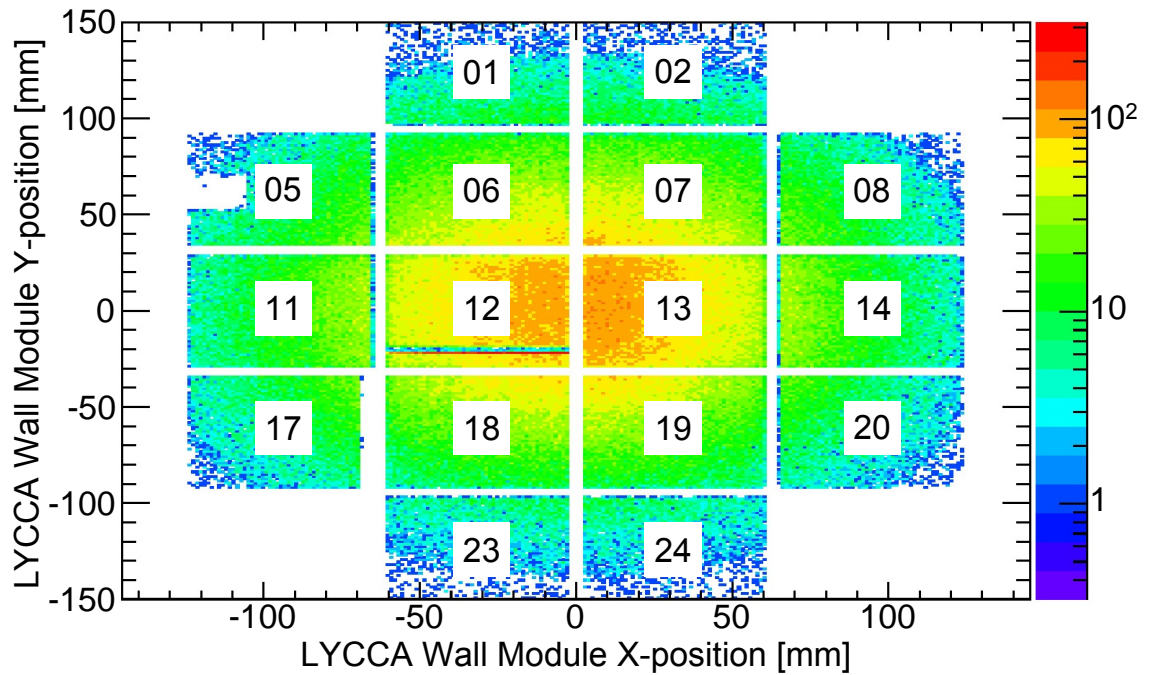


Figure 5.10: Hit pattern of the LYCCA wall DSSSD modules used at GSI, where the standard labelling convention for the LYCCA modules used in this experiment is also shown. The white lines observed in this plot represent either the gaps between the modules, or in some cases, faulty strips in the DSSSD detector modules.

Particle positions are found by the strips with the largest energy deposition on both

sides of the DSSSD. Positions measured in both the Target DSSSD, located just before the target, and the wall DSSSD, located ~ 3.7 m downstream, are used to track the trajectories of ions after the reaction target. Combining this with position information provided by the TPCs at S4 allows for the incoming trajectories of ions to also be tracked and therefore for the scattering angle of ions at the reaction target to be measured on an event-by-event basis.

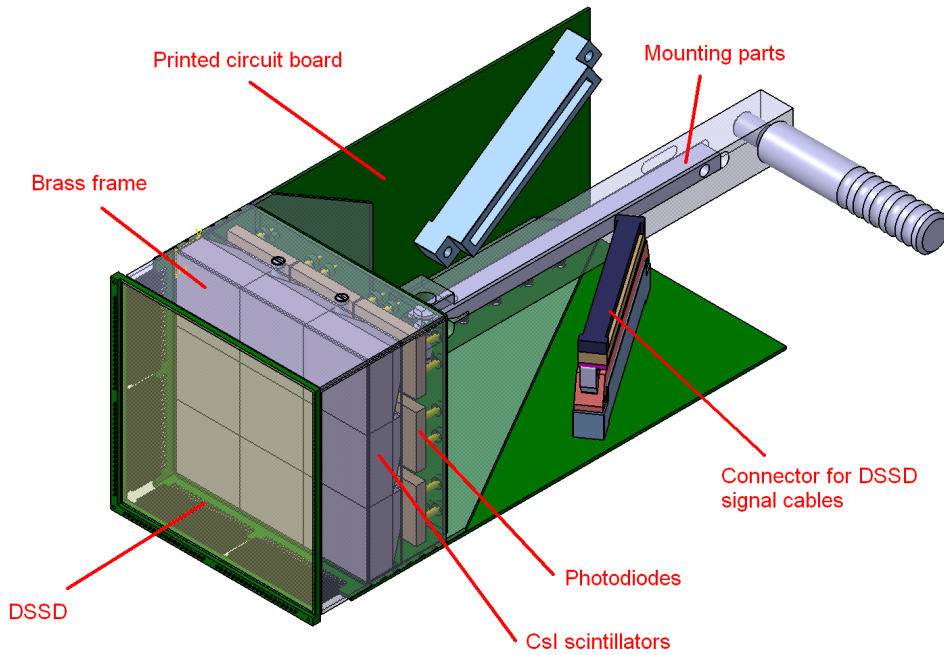


Figure 5.11: Schematic drawing of a LYCCA wall module, taken from Ref. [137].

5.3.4.2 Caesium Iodide (CsI) Scintillators

Situated 10 mm behind each wall DSSSD module is an array of 9 CsI(Tl) crystals, as shown in Fig. 5.11, which are used to measure the residual energy (E_{res}) of implanted ions. Each crystal, with the exception of those at module positions 1, 2, 23 and 24 (see Fig. 5.10), has an area of 19.4×19.4 mm² and a depth of 33 mm, followed by a 7 mm deep pyramidal light guide, which tapers to a surface area of 10.4×10.4 mm², matching that of the PhotoDiode (PD) located at the back of the detector [136]. The other crystals however, at the aforementioned module positions, have a depth of 10 mm and a pyramidal light guide depth of 5 mm. Each CsI crystal is doped with Thallium (Tl), with a typical concentration of 0.08-0.10% per mol, whereby this CsI(Tl) scintillator material was chosen due to its high stopping power and high light output, with a peak intensity at 550 nm, at

which the PDs have a high quantum efficiency of 82-86% [136]. The detectors function by incident charged beam particles being stopped in the CsI(Tl) material, generating photons through the process of scintillation, which are then guided by the pyramidal light guides to the PDs at the back of the detector, where they are collected.

5.3.4.3 LYCCA Plastic Scintillator Detectors

Timing information of ions is provided on an event-by-event basis by two plastic scintillator detectors, labelled LYCCA ToF Start and LYCCA ToF Stop in Fig. 5.9, whereby the time difference between the time signals registered in both of these detectors gives the total time-of-flight, ToF_{tot} [136]. The design of each detector is that of a large-area circular membrane with a 27 cm diameter, as shown in Fig. 5.12(a). Light generated by charged particles traversing the plastic scintillator material is collected by 32 PhotoMultiplier Tubes (PMTs), thus allowing for 32 independent measurements, from which an average is taken, therefore increasing the intrinsic time resolution of the detector by a factor of $1/\sqrt{32}$ [136]. As detailed in a previous commissioning experiment, see Ref. [138], a timing resolution below 10 ps RMS was observed using this detector design.

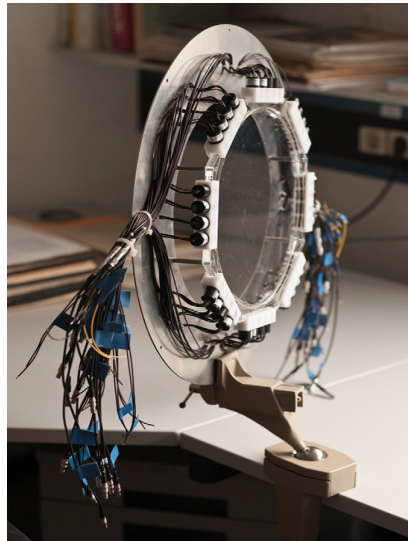


Figure 5.12: Photograph of the LYCCA ToF Start/Stop scintillator, see text for details, photos taken from Ref. [138].

In addition to measuring the ToF, the plastic scintillators can also be used to determine the position of incident particles, as detailed in Ref. [139], by making use of differences in light collection times by the 32 PMTs, for a given event. This can be particularly useful

when the secondary beam rate is very high, particularly in regards to the TPCs at S4, since the tracking efficiency of these detectors is known to decrease at higher rates [133]. However, the use of these plastic scintillators to measure positions also leads to worse position resolution, where a comparison between both the interpolated positions (using the tracking detectors) and the scintillator detected positions yielded position resolutions of 6.7 mm and 5.1 mm FWHM in the x and y-direction, respectively [139].

5.3.5 Stretched Gold Target (SGT) and Coulex Target

During the experiment at GSI, two types of target were used, depending upon the measurement being performed. For Coulex cross section measurements, a single gold target, with a thickness of 0.25 mm was used, while for lifetime measurements, the SGT was used (see Section 5.2.1). Both targets during the experiment were mounted upon a target ladder, separately, which was positioned at the centre of the reaction target chamber, see Fig. 5.13. Surrounding this were the AGATA and HECTOR+ arrays, used for the detection of γ rays, emitted in flight, from the nuclei of interest.

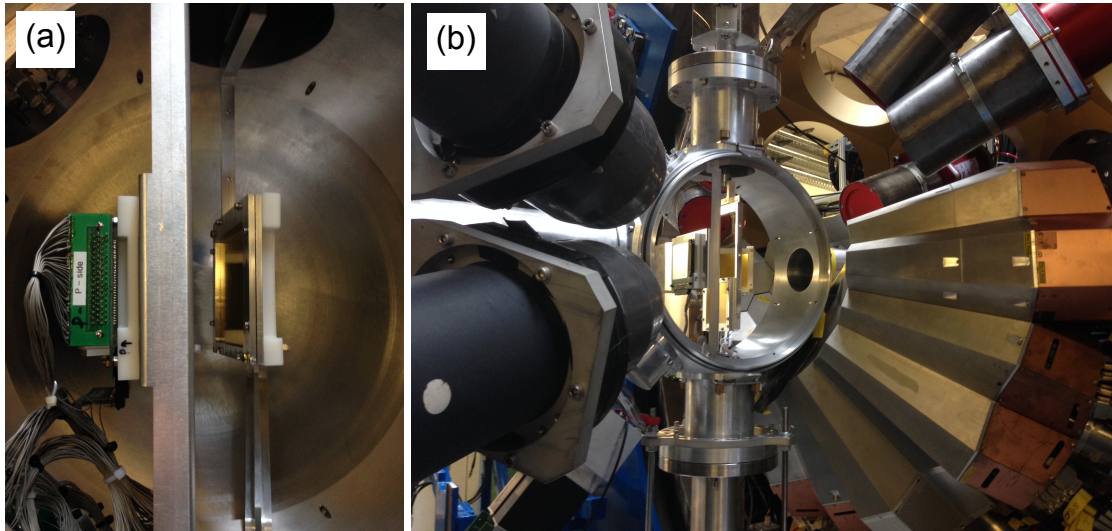


Figure 5.13: Photographs of (a) the mounted 0.25 mm thick gold Coulex target and (b) the mounted SGT (Section 5.2.1), at the centre of the reaction target chamber.

5.3.6 AGATA

The experiment presented in this Chapter was performed using the Advanced GAMMA Tracking Array (AGATA) [140], as part of the 2014 PreSPEC-AGATA campaign at GSI.

This state-of-the-art γ -ray spectrometer, represents part of the new generation of γ -ray tracking arrays, consisting of highly segmented High-Purity Germanium (HPGe) detectors. Once fully constructed, AGATA will consist of 180 HPGe detectors, with an angular coverage of 4π , which will be capable of accurately tracking the interactions of γ rays detected within, with a far greater efficiency than its predecessors. As a result, the study of even the most exotic of reaction channels will become possible with this γ -ray spectrometer, allowing for a greater understanding of nuclear structure, even at the very limits of nuclear stability.

In Section 5.3.6.1, a description of both the AGATA detectors and the set up of the AGATA array used during this experimental campaign are given. Following this, in Section 5.3.6.2, details on how γ -ray interaction positions in the AGATA crystals are determined through the use of Pulse Shape Analysis (PSA) techniques are presented. Finally, in Section 5.3.6.3, the basic principles of γ -ray tracking are discussed.

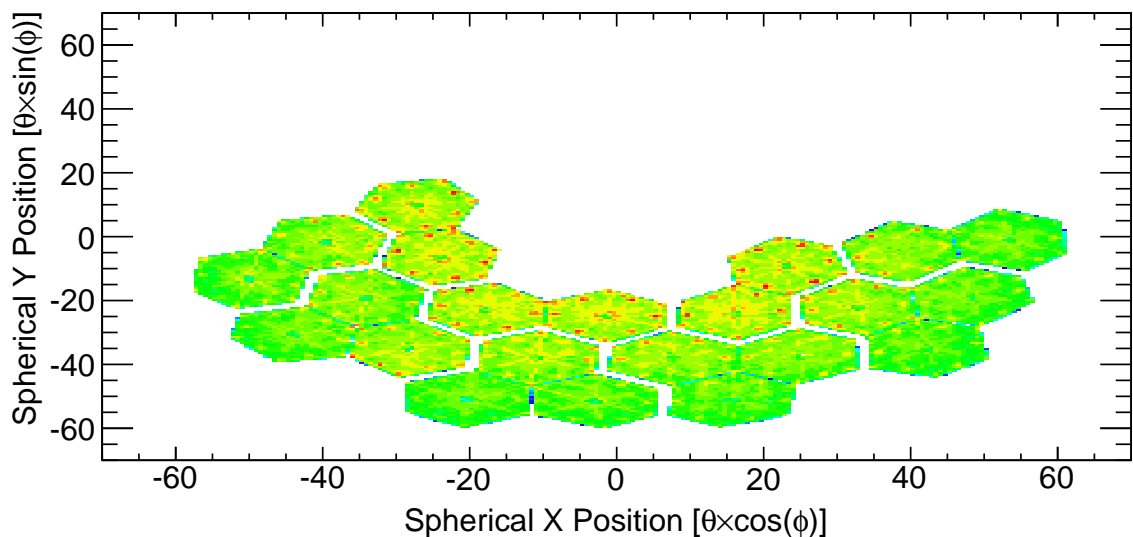


Figure 5.14: Configuration (hit pattern) of AGATA during the 2014 PreSPEC-AGATA campaign at GSI, showing the six triple cryostats (with two missing outer crystals) and three double cryostats.

5.3.6.1 The AGATA Array

During the 2014 PreSPEC-AGATA campaign at GSI, the AGATA array consisted of 22 electronically segmented (36-fold) HPGe detectors, arranged into six triple cryostats (with two missing outer crystal) and three double cryostats, as shown in Fig. 5.14, where each

detector was positioned at a nominal distance of 23.5 cm from the centre of the reaction target chamber. Normally, the standard arrangement of AGATA would see all detectors arranged into cryostats containing three detectors [140], however, due to the size of the beam spot (typically 3-5 cm) and therefore the beam pipe at GSI, the cryostats closest to the beam line had to instead be modified to include only two detectors.

Each detector in AGATA is comprised of an encapsulated n-type HPGe crystal, which is electronically segmented into six section longitudinally, and 6 sections radially, giving each detector a total 36-fold segmentation as shown in Fig. 5.15(a). Furthermore, since the total energy deposited in each crystal is also collected by the central contact (core), this results in a total of 37 signals generated per crystal [140]. The geometry of each crystal is that of a slightly asymmetric tapered hexagon, where in order to fit the geometry of the intended full 4π AGATA array, containing 180 detectors (60 cryostats), the shape of each crystal in a triple cryostat is slightly different, as shown in Fig. 5.15(b). Each crystal within a triple cryostat is therefore labelled either A, B or C according to their shape, where individual crystals in the AGATA array can be easily identified by the their cryostat position number and crystal type. Furthermore, the individual segments of each crystal can also be identified by using the standard labelling scheme shown in Fig. 5.15(a).

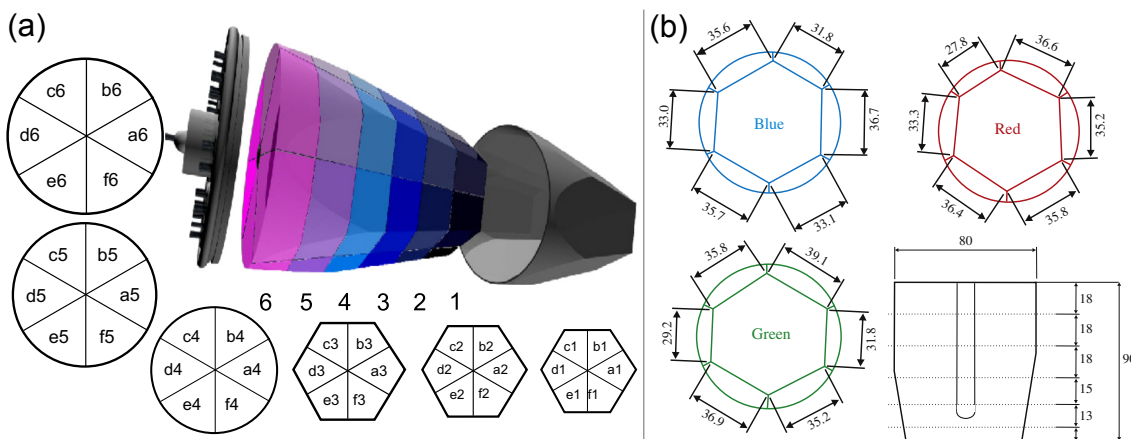


Figure 5.15: (a) The standard labelling scheme for a 36-fold segmented HPGe AGATA crystal, where the six ring along the longitudinal axis, labelled 1-6, are each subdivided into six segments labelled a-f. (b) Schematic drawing of the three different shaped crystal in a standard AGATA triple cryostat, where the dimensions of each crystal are displayed in mm. Adapted from Ref. [140].

5.3.6.2 Determination of the γ -ray Interaction Position

In electronically segmented γ -ray detectors, the position of a γ -ray interaction can be determined to a sub-segment resolution. This is achieved by utilising the measured charge signals recorded in each segment, where, in addition to charge being deposited in the segment in which the interaction occurred, charges are also induced on the neighbouring segments due to the drift of charge carriers inside the crystal. The size of these induced charge signals, also referred to as transient signals, depends upon the position of the primary interaction, relative to the neighbouring segment. This effect is illustrated in Fig. 5.16, for a 6-fold segmented detector, where an interaction occurring in segment 4 results in a sharp rise in the charge collected in this segment, while also inducing a charge on the nearby segments 3 and 5. Due to the interactions closer proximity to segment 3, the amplitude of the signal recorded here is slightly larger. In the case of AGATA however, transient signals observed in neighbouring segments, both above and below the segment in which the interaction occurred, are also considered. Therefore, the use of transient charge information, in electronically segmented γ -ray detectors, allows for a much better position resolution to be achieved, compared to simply using the central position of the segment in which the net charge signal is registered.

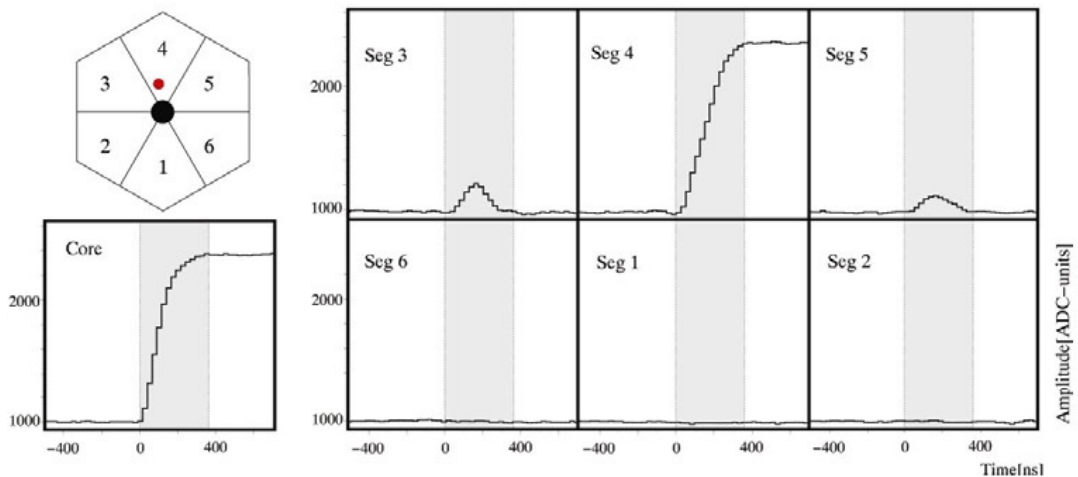


Figure 5.16: An example of the signals produced in both the core and six segments of a 6-fold segmented detector following the full absorption of a γ ray in segment 4. Due to the interactions closer proximity to segment 3, the amplitude of the signal recorded here is slightly larger than in segment 5. Taken from Ref [141].

In order to obtain the interaction positions of γ rays in AGATA, experimentally digitised pulse shapes, for both the segment with a net charge and its neighbouring segments, are compared to a basis data set, through the use of a Pulse Shape Analysis (PSA) algorithm [144]. These basis data sets of net and transient charge signals, for different interaction positions, are built through the use of both experimental data from scanning tables, such as the Liverpool and Orsay scanning tables [145, 146], and theoretical data, extracted from simulations. However, the use of scanning tables to obtain such data can be a very lengthy procedure. For example, the full characterisation of a single crystal with a 1 mm grid, using the Liverpool scanning table, can take up to 3 months [140, 145]. Therefore, in general, only the the most important positions in each crystal are scanned, while the remainder are simulated through the use of electric field simulation codes, such as the Multi Geometry Simulation (MGS) [147] or the AGATA Data Library (ADL) [148, 149] (used in this analysis), which, in combination allows for the realisation of on-line PSA. Furthermore, the employment of such PSA techniques has allowed for a position resolution of around 5 mm (FWHM) to be achieved [150].

5.3.6.3 Principles of γ -ray Tracking

In a Compton scattering event, i.e. where a photon inelastically scatters off a loosely bound or free electron, the energy of the scattered γ ray, E_f , is related to both the initial energy of the γ ray, E_i , and the scattering angle between their trajectories, θ , by the following Compton scattering formula,

$$E_f = \frac{E_i}{1 + (1 - \cos\theta)E/(m_e c^2)}, \quad (5.6)$$

where m_e is the mass of the electron and c is the speed of light. If the scattered photon then subsequently deposits its remaining energy in the detector, the total energy of the initial photon can be found from the sum of the energy deposited during the Compton scattering event and the final energy deposited. However, given the finite volume of a Ge detector, γ rays may also escape the detector volume before depositing their remaining energy. This effect is greatly reduced in the case of AGATA however, due to its closely packed Ge crystals, where the initial energy of a γ ray which deposits its energy into multiple crystals can be determined through an add-back procedure. However, the process of reconstructing a γ -ray event can become significantly more complex, especially for higher

energy γ rays which may undergo multiple Compton scattering events before depositing their entire energy. In this case, in order to measure the full energy of the initial γ ray, its path through the detector must be accurately tracked. Furthermore, since the Doppler correction of a γ ray emitted in flight also depends upon the measured angle between the ion trajectory and the emitted γ ray, the first interaction point within the detector must also be determined. As it is not possible to resolve multiple Compton scattering events of a single γ ray in time, the only available information provided by AGATA is the position (following PSA) and the energy deposited, during each γ -ray interaction. Therefore, γ -ray interaction points, within a close proximity, are grouped into clusters, as shown in Fig. 5.17. Providing the cluster only includes the interaction points of a single Compton-scattered γ ray, the correct initial energy of the γ ray can be established. From this, the path of the γ ray through the detector can be reconstructed through the use of a forward tracking algorithm, which evaluates all the different possible sequences in accordance with the Compton scattering formula (Equation 5.6) and assigns it with a Figure of Merit (FoM). If the FoM for a particular sequence of Compton scattering events within a cluster is above a certain value, the cluster is accepted, while those below this value are rejected and alternative clustering is then considered. This therefore allows for Compton scattered γ rays, which escape the detector volume, to be rejected and therefore remove their contribution to the background of the γ -ray spectrum. For the analysis discussed in this thesis, the Mars Gamma Tracking (MGT) code was used [151], which uses the “forward tracking method” described within this section.

One of the key assumptions of Compton scattering however, is that the photon scatters off a free or loosely-bound electron. In reality, a photon will usually scatter off a bound electron within the detector volume, where both the binding energy and pre-collision momentum of the electron will have an impact on the energy-angle relationship of the scattered photon [142, 143]. In particular, this has the effect of Doppler broadening the scattered photons energy distribution, as a function of scattering angle [142], which has clear implications for the tracking and reconstruction of γ -ray events in AGATA. For example, this can result in γ -ray events being tracked incorrectly, or, potentially disregarded, due to the FoM criteria. In the former case, if the initial interaction point is not correctly determined, this will result in a worsening of the energy resolution of the detector, due to an incorrect angle between the ion and γ -ray trajectories being calculated for the Doppler correction. Furthermore, in the case where a photon elastically scatters off a bound elec-

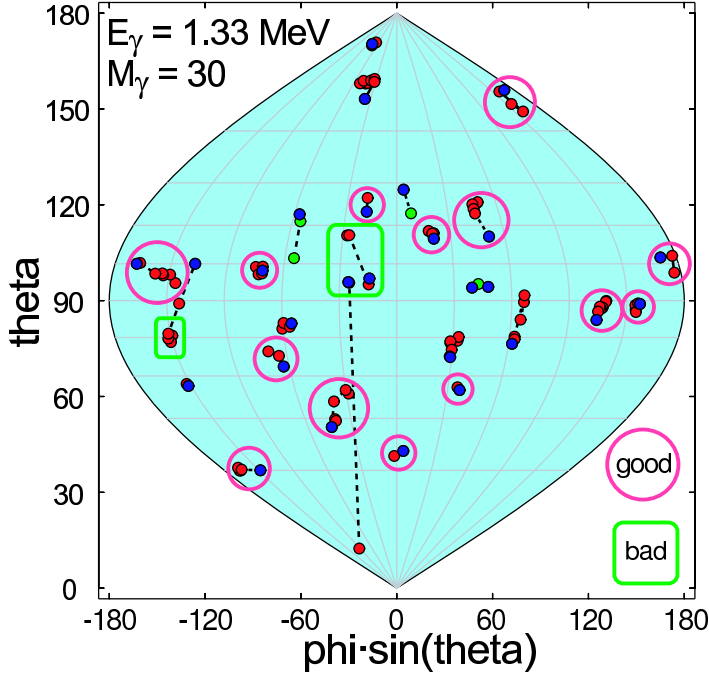


Figure 5.17: Simulation of a 1.33 MeV, multiplicity=30 γ -rays interaction positions in a 4π Ge shell, where γ -ray events have been reconstructed using a cluster tracking algorithm. Correctly and incorrectly identified clusters are shown inside pink circles or green rectangles, respectively. Taken from Ref. [141].

tron, also known as Rayleigh Scattering, the trajectory of the photon can also be modified, but without any corresponding transfer in energy. This also has implications for the tracking and energy resolution of the detector, though the effects of Rayleigh Scattering are only more significant at lower γ -ray energies (although many orders of magnitude less important than the photoelectric effect), while at higher energies, the effects of Rayleigh Scattering can be considered as negligible.

5.4 FRS Calibrations/Corrections and Incoming Particle Identification

Prior to the experiment, LISE simulations [73] were performed to calculate a set of $B\rho$ values for the four dipole magnets to be used to select the nuclei of interest. However, since the exact amount of matter in the beam line is not known in these simulations, this often results in the actual experimental $B\rho$ values differing slightly to the simulated ones. Therefore, to better understand the material in the beam line, particularly regarding

the different S2 degrader material used during the experiment, a number of unreacted (effective matter) beam runs were performed using a 599.65 MeV/u ^{58}Ni primary beam, with different amounts of degrader material in the beam line, as detailed in Table 5.2. Due to this difference in degrader material, the energy (and therefore velocity) of the ^{58}Ni beam during each run was also different, allowing for a number of FRS detector calibrations to be performed.

Table 5.2: Summary of the four ^{58}Ni FRS calibration (effective matter) runs performed during the experiment at GSI. The FRS ToF and $\beta = \frac{v}{c}$, between the SC₂₁ and SC₄₁ scintillators, were extracted from LISE simulations [73].

FRS Setting	^{58}Ni - Cal 1	^{58}Ni - Cal 2	^{58}Ni - Cal 3	^{58}Ni - Cal 4
Primary Beam				
Energy [MeV/u]	599.65	599.65	599.65	599.65
S2 Degrader/Wedge [^{13}Al]	-	5.7 g/cm ²	6.8 g/cm ²	8.0 g/cm ²
FRS ToF [ns]	159.675	175.116	180.227	187.478
FRS β	0.78505	0.71583	0.69553	0.66863

Since the nuclei of interest for this investigation, ^{46}Cr , ^{46}V and ^{46}Ti , were quite far from the primary beam, to ensure the correct nuclei were selected by the FRS, an “isomer tagging” technique was used. This technique consisted of the FRS scanning the region of interest, with an approximately correct set of $B\rho$ values, to find a nuclide with a well-known isomeric state. Ideally, this state needed to have a half-life longer than 200 ns, i.e. the approximate ToF between the production target and reaction chamber. All nuclei produced in the setting were then implanted into a thick plastic target at the centre of the target chamber, where the excited nuclide could then be identified via γ -ray transitions emitted from the decaying isomer, detected using the AGATA array. Following the identification of the corresponding nuclide, the FRS settings were then simply adjusted to centre the nuclide of interest. The use of this technique allowed for the correct FRS settings to be found in just a few hours of beam time, which was certainly preferable to the much more lengthy procedure of manually scanning down from ^{58}Ni . In the experiment performed, the $J^\pi = (19/2^-)$, $T_{1/2} = 556(6)$ ns isomer in ^{43}Ti [152, 153] was used for this procedure.

In the following sections, a brief summary will be given of the calibrations performed for the different FRS detectors, after which, the resulting FRS Particle IDentification (PID) plots will be presented in Section 5.4.5.

5.4.1 Central Beam Trajectory Correction

To correct the central trajectory of the beam through the FRS, theoretical $B\rho$ values (extracted using LISE [73]) were compared with experimentally measured magnetic field strengths for each dipole magnet using Hall probes. From this, corrected experimental ρ_0 values were obtained for the central beam trajectory through each dipole.

5.4.2 TPC Calibrations

Prior to the experimental beam runs, a number of “fibre mask” runs were performed in which an *active scintillator grid* was placed in front of each TPC detector [133]. This scintillator grid consisted of three vertical scintillator fibres, separated by a distance of 12 mm, and three horizontal fibres, separated by a distance of 6 mm, where all scintillator fibres were 1 mm thick. By setting a trigger condition such that only events in coincidence with signals from the PMTs of the grid were considered, resulted in the observation of hit patterns in the TPC spectra, corresponding to the positions of the scintillator fibres. The raw signal positions of each TPC were then plotted against the known scintillator grid positions, from which, gains and offsets relating the two were extracted from linear fits. This allowed for the raw signals from each TPC to be converted to real spatial XY-positions. The results of this calibration are shown in Fig. 5.18.

5.4.3 FRS Scintillator Calibrations

A number of a calibrations were performed for the FRS scintillators during this analysis, both to achieve a calibrated ToF (and therefore β) between the SC_{21} and SC_{41} scintillators and to obtain calibrated x-positions, both of which are required for calculating the A/Q of a nuclei, see Section 5.4.5. These calibration procedures, in addition to the issues encountered, are summarised in the following sections.

5.4.3.1 ToF Calibrations

To calibrate the ToF of nuclei through the FRS, the difference between the raw time signals of both left PMTs, ToF_{LL} , and both right PMTs, ToF_{RR} , are compared to the

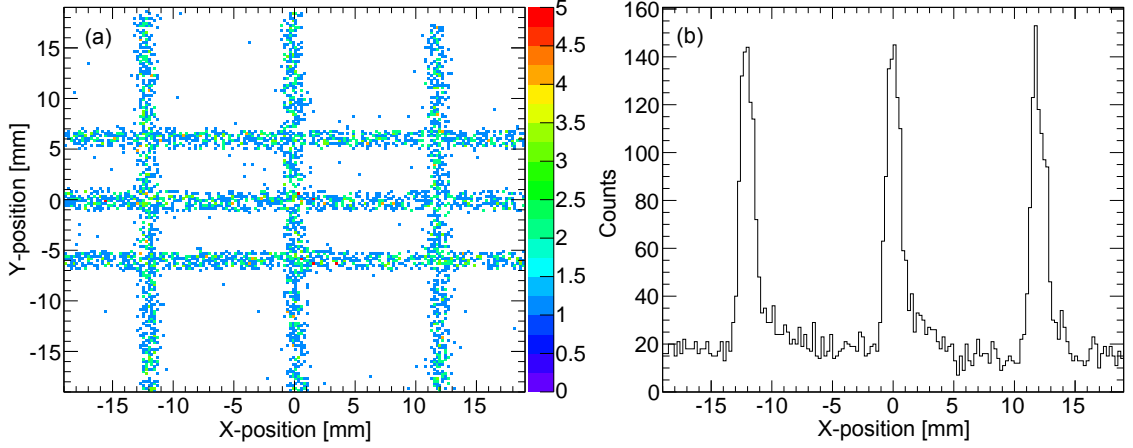


Figure 5.18: (a) Calibrated position spectrum of TPC₂₁ using an active scintillator grid and (b) the corresponding x-position spectrum.

theoretical ToF value of a particular nuclide between the two FRS scintillators (SC_{21} and SC_{41}), calculated using LISE [73]. In this analysis, the four unreacted ^{58}Ni beams runs (with different degrader material in the beam line) were used to perform this calibration, due to their negligible contamination and smaller velocity spreads, allowing for a more accurate ToF calibration. The calibration was performed by plotting the calculated LISE ToF values for each run against the corresponding measured raw ToF_{LL} and ToF_{RR} values, where gains and offsets were extracted from linear fits. The ToF and β value of particles travelling between these scintillators was then found by using Equations 5.7 and 5.5, respectively.

Upon investigating the calibrated ToF spectrum for the experimental beam runs however, a sharp cut of point was noticed at 210 ns, where all events with a greater ToF were instead added to the last bin before this cut off point. This was due to the ToF of these events occurring outside of the range of the Time-to-Digital Converter (TDC). In principle, this was not such an issue, since the nuclei of interest were still within the range of the TDC, however in order to produce a cleaner PID, and observe events outside of the range of the TDC, the signals from the Multi-hit TDC (MhTDC) were used instead. This involved repeating the ToF calibration procedure discussed previously, however this calibration had to be performed using the experimental beam runs. This was due to changes in either the cabling or delay times of the MhTDC (between the effective matter beam runs and the experimental beam runs), which meant that calibrations using the effective matter beam runs were not compatible. Following this calibration, further issues were

also noticed regarding the signals from the left PMT of both scintillators, resulting in an additional structure in the ToF_{LL} spectrum, which was not present in the ToF_{RR} spectrum. Upon further investigation, it was found that the events in the separate structures in ToF_{LL} also corresponded to the nuclei produced in the FRS setting, but at the wrong ToF value, therefore leading to a duplicated PID at a slightly shifted location. Furthermore, this problem was only observed during some, but not all experimental beam runs and only during some of the ^{46}Ti and ^{46}Cr Coulex experimental beam runs. Therefore, the origins of this anomaly are unclear, but one way in which the effects of this anomaly could be removed from the analysis was by simply using only the calibrated ToF_{RR} (and therefore β_{RR}) between SC_{21} and SC_{41} , to produce the PID.

5.4.3.2 Position Calibrations

Due to the very high secondary beam rates during the experiment, particularly at S2 during the ^{46}Ti and ^{46}V experimental beam runs (where rates as high as 3-4 MHz/spill were observed), the tracking efficiencies of the TPCs were very low, where only $\sim 20\%$ of particles positions were tracked. This was not unexpected however, as in a previous commissioning experiment for the TPCs it was found that while tracking efficiencies $>90\%$ are achievable for sub 250 kHz rates, this efficiency decreases quite quickly at higher rates [133]. Since it is not possible to measure a particle's A/Q without this position information, the nuclei of interest could therefore not be distinguished from the contaminants. Therefore, in order to account for this, position measurements were instead performed using the scintillators, by using the the time difference for light to be collected in the left and right PMT, dt_{LR} , of each scintillator. However, in order to correlate this information with actual positional information in the scintillators, it was compared with the interpolated x-positions of nuclei at the scintillator positions, using calibrated positions of nuclei in the TPCs. By plotting one against the other, for both scintillators, a linear relationship was found, therefore allowing for dt_{LR} measurements in each scintillator to be directly converted into corresponding x-position measurements. Therefore, the $B\rho$ of a particle can be determined from the x-position measurements at S2 (x_{S2}) and S4 (x_{S4}) by,

$$B\rho = B\rho_0 \left(1 - \frac{x_{S2} - M \cdot x_{S4}}{D} \right) \quad (5.7)$$

where $B\rho_0$ is the magnetic rigidity of the central beam trajectory, M is the magnification between S2 and S4, and D is the dispersion between S2 and S4. Therefore, the A/Q of a

particle can be found by Equation 5.2.

5.4.4 MUSIC Calibrations and Corrections

The energy loss of a particle travelling through matter (dE/dx) is dependent on both its atomic number (Z) and its velocity (β), in accordance with the Bethe-Bloch formula (Equation 5.3), which can also be summarised as

$$-\left\langle \frac{dE}{dx} \right\rangle = Z^2 \cdot f(\beta), \quad (5.8)$$

where $f(\beta)$ is a function of β . Therefore, for this analysis, both the energy loss and charge identification calibrations for the MUSIC detectors were performed using the unreacted ^{58}Ni beam runs, as the only variable in these runs was the beam velocity. The first calibration involved a simple gain-matching procedure, where the energy loss (dE/dx) recorded in each of the 8 anode segments (in both MUSIC detectors) was aligned to an arbitrary value, using a single beam run. Following this, the calibrated energy loss (dE/dx) for each beam run was plotted against the corresponding LISE FRS β value, for both MUSIC detectors, from which a quadratic relationship was observed, thus allowing for a measured FRS β value for the corresponding energy loss (dE/dx) of a Ni ion ($Z = 28$) in MUSIC1 or MUSIC2 to be found. Since $f(\beta)$ only depends upon β , the atomic number of an ion, Z , can be found by scaling the energy loss of the ion in MUSIC (following a small correction for position dependence), $\langle \frac{dE}{dx} \rangle_{ion}$, to that of a Ni ion, $\langle \frac{dE}{dx} \rangle_{Ni}$, for the same FRS β value, by,

$$Z = Z_{Ni} \sqrt{\frac{\langle \frac{dE}{dx} \rangle_{ion}}{\langle \frac{dE}{dx} \rangle_{Ni}}} \quad (5.9)$$

where Z_{Ni} is the atomic number of Ni ($Z = 28$). The final Z value of an ion is then found by the modulus of the two Z values calculated by the MUSIC detectors.

5.4.5 Incoming Particle Identification

The calibrated FRS PIDs for the ^{46}Ti and ^{46}Cr FRS beam setting are presented in Fig. 5.19 and 5.20, respectively. In Fig. 5.19(a) and 5.20(a), the PID are shown using more accurate position information from the TPCs (to find the A/Q), while in Fig. 5.19(b) and 5.20(b), the PID are shown using position information from the scintillators. The low tracking efficiencies of the TPCs at higher rates, particularly during the ^{46}Ti beam setting, resulted in a large number of ions with no A/Q information (>84%). As for a comparison, using positions calculated with the FRS scintillators resulted in a four-fold

increase in the number of events in the ^{46}Ti ‘blob’. For the ^{46}Cr beam setting, where the total rate at S2 was lower, the difference was smaller, where an improvement of ~ 1.8 in the number of statistics was observed. However, due to the much smaller intensity of ^{46}Cr , the more exotic of the three nuclei studied here, it was especially important to try and minimise the loss of statistics in the FRS PID where possible.

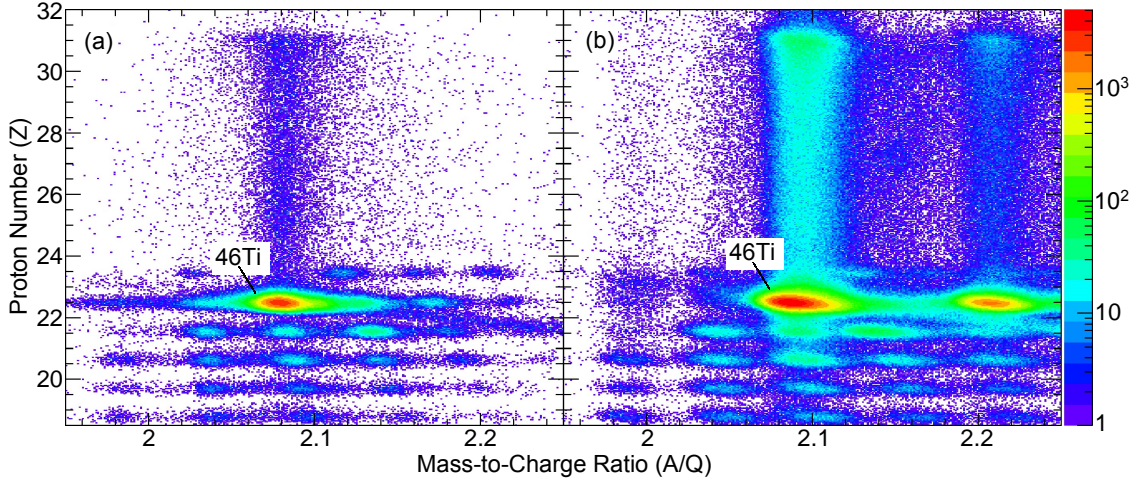


Figure 5.19: Calibrated FRS PID for the ^{46}Ti FRS beam setting (Coulex data), using x-positions measured either by (a) the TPCs or (b) the scintillators. Due to issues regarding the recorded signals from the left FRS scintillator PMTs a repeated ID is also observed, while the high beam rate also resulted in pile up in the MUSIC detectors, see text for more details. The nuclide of interest, ^{46}Ti , has been labelled in both PID.

A few issues are still apparent in these calibrated PID however. For example, in Fig. 5.19(b), a (laterally) repeated PID is observed, suggesting an issue in the calculation of A/Q (but not β since this would also affect the charge determination). This problem was in fact due to the scintillator x-positions being determined using the time difference between the left and right PMTs of both scintillators, whereby, as discussed in Section 5.4.3.2, for a small number of runs, data from the left PMTs of both scintillators was corrupted. Fortunately, because this anomalous behaviour occurred over fixed periods of time during the experimental beam runs rather than randomly throughout, events with the correct and incorrect position measurements could be mostly grouped and analysed separately, as shown in Fig. 5.21. This was particularly important for the Coulex analysis, where the number of incoming ions needed to be accurately measured in order to determine the Coulex cross section. A second issue which can also be seen in Fig. 5.19(b) is the large number of events located above ^{46}Ti ($\sim 1.3\%$ of events in the PID), resulting from pile-

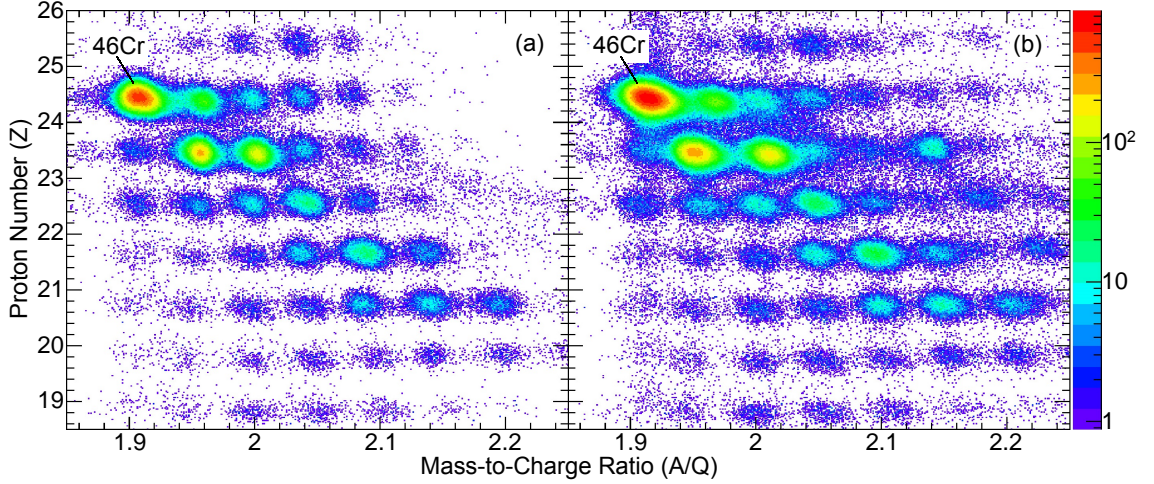


Figure 5.20: Calibrated FRS PID for the ^{46}Cr FRS beam setting, using x-positions measured either by (a) the TPCs or (b) the scintillators. The nuclide of interest, ^{46}Cr , has been labelled in both PID.

up effects in the MUSIC detectors, which were induced by the large beam rates. Since ^{46}Ti accounts for approximately 82% of all events, while the nuclei below only account for $\sim 0.3\%$, it is safe to assume the large majority of these events are from ^{46}Ti . A final but very minor issue is that the nuclei are identified with a slightly incorrect value of Z . This may be due to the separation between the nuclei used for the FRS calibration (^{58}Ni) and the nuclei of interest. However, the main objective of the FRS PID was to be able to identify and apply software gates on the nuclei of interest, which could be achieved from these calibrations.

5.5 LYCCA Calibrations/Corrections and Outgoing Particle Identification

The unique identification of particles after the reaction target was achieved by using the LYCCA array of tracking and energy loss detectors. In the following sections a brief description will be given of the detector calibrations performed, after which, calibrated LYCCA PID spectra will be presented.

5.5.1 DSSSD Calibrations and Corrections

Position measurements (x,y) in the DSSSD detectors depend upon the measured energy losses (dE) in the strips, both on the p-side and n-side of the detector. Therefore, to

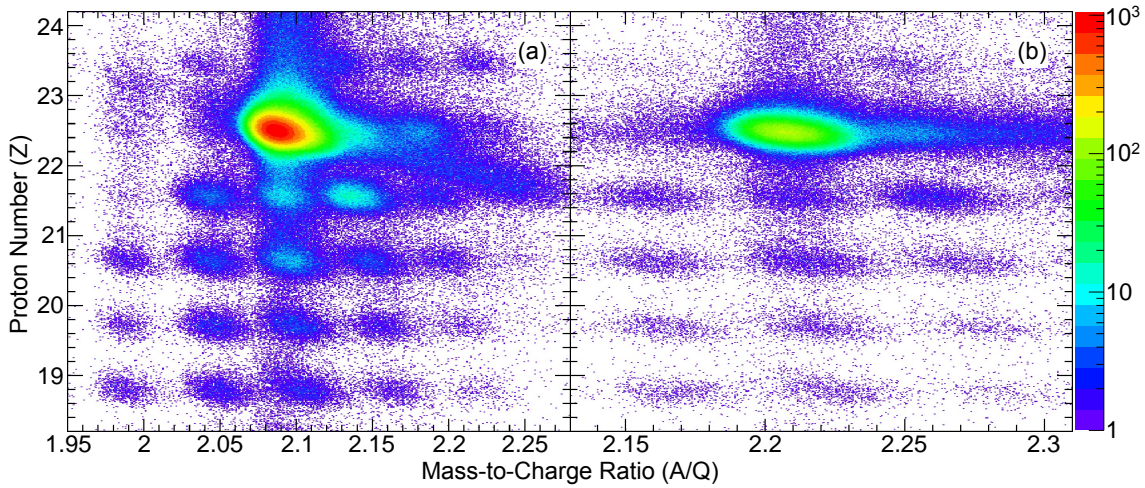


Figure 5.21: Calibrated FRS PID for the ^{46}Ti FRS beam setting (Coulex data), where x-positions were measured using the scintillators. The PID are shown with (a) correctly determined positions and (b) incorrectly determined positions, where differences in position measurements arose due to issues regarding the signals from the left PMTs of the FRS scintillators, SC_{21} and SC_{41} , see text for more details.

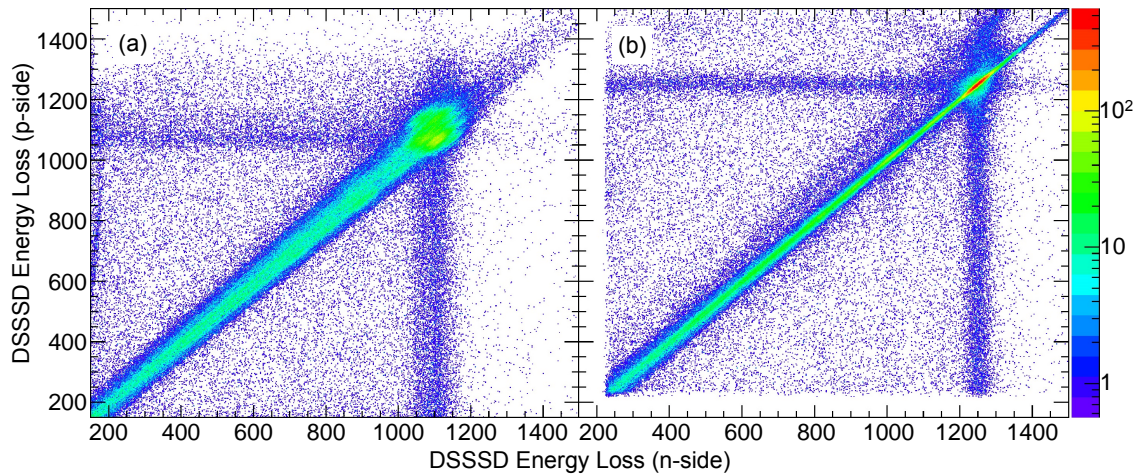


Figure 5.22: Recorded energy loss in the LYCCA wall DSSSD module 13, both (a) before and (b) after calibrating the energy loss recorded in the strips on both the n-side and p-side of the detector.

calibrate both the position and energy loss measurements of each DSSSD module, only the energy loss in each strip needed to be calibrated. This was achieved in the analysis by performing a gain-matching procedure for each strip, using data from an unreacted experimental beam run, where the energy loss recorded in each strip, gated on a particular nuclide, was aligned to an arbitrary value. Following this, the XY-positions of a particle

could be deduced from the strip, both front and back, with the largest energy loss recorded, while the total energy loss (ΔE) of a particle could be found from the average of the energy loss recorded in each strip. An example of such a calibrated LYCCA wall DSSSD module is presented in Fig. 5.22. To correct the total energy loss of particles measured in both the target DSSSD and wall DSSSDs, calculated energy losses for different nuclides, using LISE [73], were plotted against experimentally measured energy losses, where gains and offsets relating the two were extracted from linear fits.

5.5.2 CsI Scintillator Calibrations

The residual energy (E_{res}) measured by the CsI(Tl) scintillator detectors was calibrated using a gain-matching procedure, where the energy recorded in each detector for a particular nuclide was aligned to an arbitrary value. Residual energy (E_{res}) measurements were then corrected by plotting the calculated residual energies for different nuclei, using LISE [73], against the experimentally measured equivalents, where gains and offsets relating the two were extracted from linear fits.

5.5.3 Plastic Scintillator Corrections

In the standard set up, the incoming angle of particles is determined using positions measured in the TPCs at S4 and the target DSSSD, placed just before the reaction target. However, due to the low TPC tracking efficiencies in this experiment, caused by the high beam rates, the positions of particles which were not tracked using the TPCs were instead determined using the ToF start scintillator. In order to calibrate both the ToF and position measurements performed by the ToF start and ToF stop scintillators, the 32 PMTs of both detectors had to be calibrated separately. This was achieved by using interpolated particle positions at the scintillator detectors, using position information from the TPCs at S4, the target DSSSD and the wall DSSSDs, then plotting the time delay between a particle hit and the PMT signal, dt , against the distance between the particle hit position and the PMT, dx . Following this, gains and offsets were extracted from linear fits to each plot, allowing for distance corrections to be determined for each PMT. Following the calibration of the PMTs, the scintillators could then be used to also determine particle positions. This was achieved by utilising a minimisation routine where scintillator XY-positions were scanned to find the minimum variance in the position-corrected time signal. The event-by-event LYCCA β was then finally found by using the LYCCA ToF, determined from the difference

between time signals recorded in the ToF start and ToF stop scintillators, and the path length, determined using the deduced particle trajectories from the measured particle positions.

5.5.4 Outgoing Particle Identification

Following the calibration of the LYCCA detectors, a number of different outgoing PIDs could be produced to identify fragments after the reaction target through the use of different combinations of the measured particle information. For example, by using the calibrated $\Delta E - E_{res}$ information provided by the LYCCA wall DSSSDs and CsI(Tl) scintillators, the atomic number (Z) of outgoing nuclei could be identified, as shown in Fig. 5.23. While using $E_{res} - \beta_{LYCCA}$ information, the outgoing nuclei could also be identified by their mass. In the analysis presented here however, an outgoing gate on the atomic number was sufficient, as the reaction mechanism of interest studied here was Coulomb excitation, where no transitions from other isotopes were expected to occur in the energy region of interest. Furthermore, for the Coulex analysis, the use of an incoming gate also assured that only reactions from the nuclide of interest were considered.

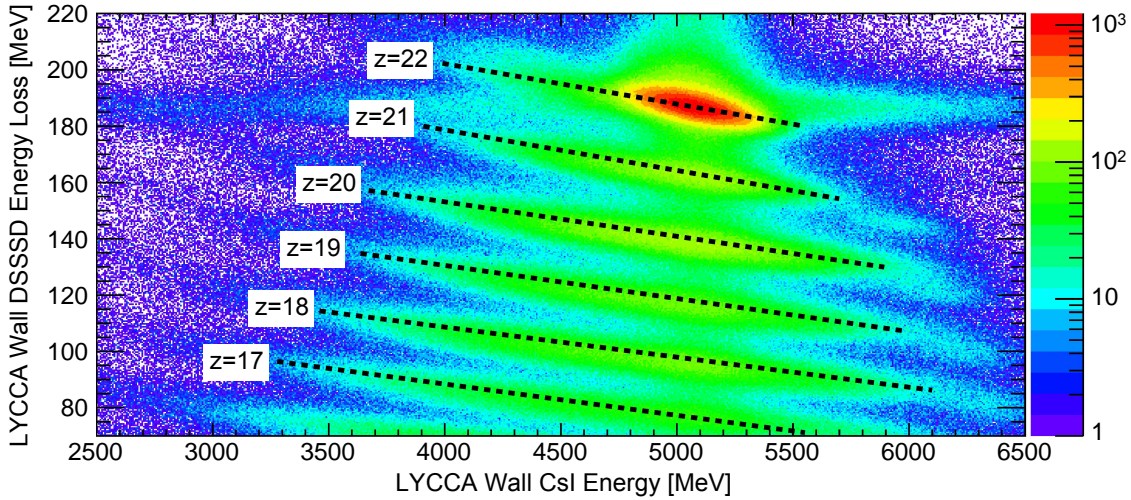


Figure 5.23: Calibrated LYCCA PID for outgoing fragments after the reaction target, produced in the ^{46}Ti FRS setting. The unique identification of different isobars of nuclei can be observed by the horizontal stripes.

5.6 AGATA and γ -ray Calibrations

During the experiment performed at GSI, the interaction positions of γ rays in the AGATA detectors were determined on-line, through the use of Pulse Shape Analysis (PSA), as discussed in Section 5.3.6.2, using the adaptive grid search algorithm [154]. Following this, the data was then analysed offline, using the Mars Gamma Tracking (MGT) code [151] for γ -ray tracking. While the “traces”, i.e. the electrical signals measured in the core and segments of each AGATA crystal, were written to disk during the experiment, this data was not further examined during the offline analysis and therefore the quality of the on-line PSA was not further optimised during this work. However, as will be shown in Chapter 6, the PSA was sufficiently optimised for the preliminary analysis discussed in this thesis. A more detailed discussion on these calibrations and optimisations can be found in Refs. [155].

The application of software gates in this analysis, both to an incoming FRS PID and outgoing LYCCA PID, allowed for γ -ray spectra to be produced for the reaction channels of interest, with negligible contamination from other reaction channels. However, other sources of background still remained in these spectra, which needed to be addressed.

In Section 5.6.1, both the Doppler reconstruction and procedure to determine the target position will be discussed. Following this, in Sections 5.6.2 and 5.6.3 it will be discussed how the background was reduced in these spectra through the application of particle-time and γ -ray multiplicity gates. Finally, in Section 5.6.4 it will be discussed how the resolution of the observed transitions was significantly improved.

5.6.1 Doppler reconstruction of γ rays

During the experiment performed at GSI, high secondary beam energies of 170-180 MeV/u were used, which, for the nuclei studied here, corresponded to an average ion velocity of 0.50-0.55c. As a result, the γ rays emitted from these nuclei were heavily Doppler shifted in the lab frame, in which they were detected. Therefore, in order to obtain the correct γ -ray energy for these transitions, in the nuclear rest frame, $E_{\gamma(res)}$, the observed γ -ray energies in the lab frame, $E_{\gamma(lab)}$, needed to be reconstructed by

$$E_{\gamma(res)} = \frac{E_{\gamma(lab)}(1 - \beta \cos\theta)}{\sqrt{1 - \beta^2}}, \quad (5.10)$$

where $\beta = \frac{v}{c}$ is the velocity of the recoil and θ is the angle between the γ ray and the ion trajectory. In this case, the ion trajectory was determined using the positions measured in the target DSSSD and the wall DSSSDs, while the γ -ray trajectory was determined using the target position and first interaction position in AGATA. Since the positions measured in the target DSSSD, wall DSSSDs and AGATA had already been calibrated, this left only an uncertainty in the target position, Z . Therefore, in order to determine the correct target position, an iterative peak fitting procedure was followed, where both β and Z were modified. In this case, the analysis was conducted by fitting a strongly observed transition with a known energy, where for each value of Z , β was modified until the sharpest peak was obtained. By repeating this procedure for a range of Z values, it was possible to find the Z value at which the measured centroid energy of the peak agreed with the literature value [122]. For this analysis, the procedure was performed for the $J^\pi : 2^+ \rightarrow 0^+$ transition in ^{46}Ti , which yielded a Coulex target position of -2.75 mm, with respect to the centre of AGATA. As a result, this target position was subsequently used for all analyses involving the Coulex target, while slightly modified positions, accounting for the respective geometry of the SGT, were used for the lifetime analysis.

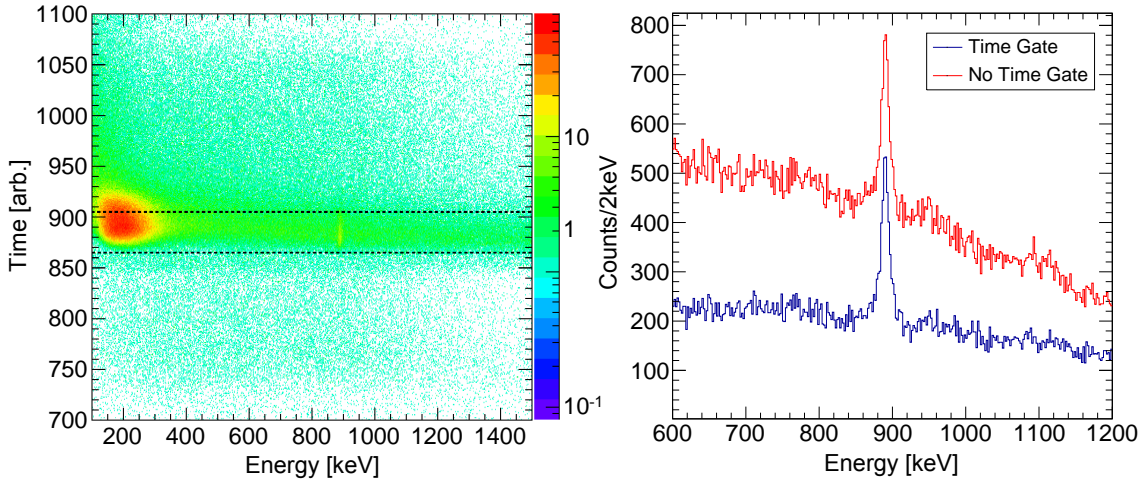


Figure 5.24: (a) Time-Energy histogram for ^{46}Ti , showing the applied time gate (45 ns wide). (b) Doppler corrected energy spectrum for ^{46}Ti , with (black) and without (red) an applied time gate.

5.6.2 AGATA Timing Condition

The most significant source of background radiation observed in the γ -ray spectra produced in this analysis was from Bremsstrahlung radiation, resulting from the deceleration of charged beam particles in the nuclear electric field of the reaction target. One way in which this and other sources of background radiation could be reduced was through the application of a particle-time gate, using timing information from AGATA and the last scintillator of the FRS (SC_{41}), both of which were measured relative to the trigger of the data acquisition. Since the nuclei under investigation have a particular spread of velocities, the time difference between a particular nuclide being detected at SC_{41} and a γ ray from this nuclide being detected by AGATA is expected to fall within a well-defined distribution in time. Therefore, uncorrelated background events, not associated with the reaction channel of interest, can be easily removed by excluding all events outside of a reasonable time window, typically 30-50 ns wide, depending upon the momentum spread of the beam. In Fig. 5.24, an example of such a time gate applied to the ^{46}Ti Coulex data is shown.

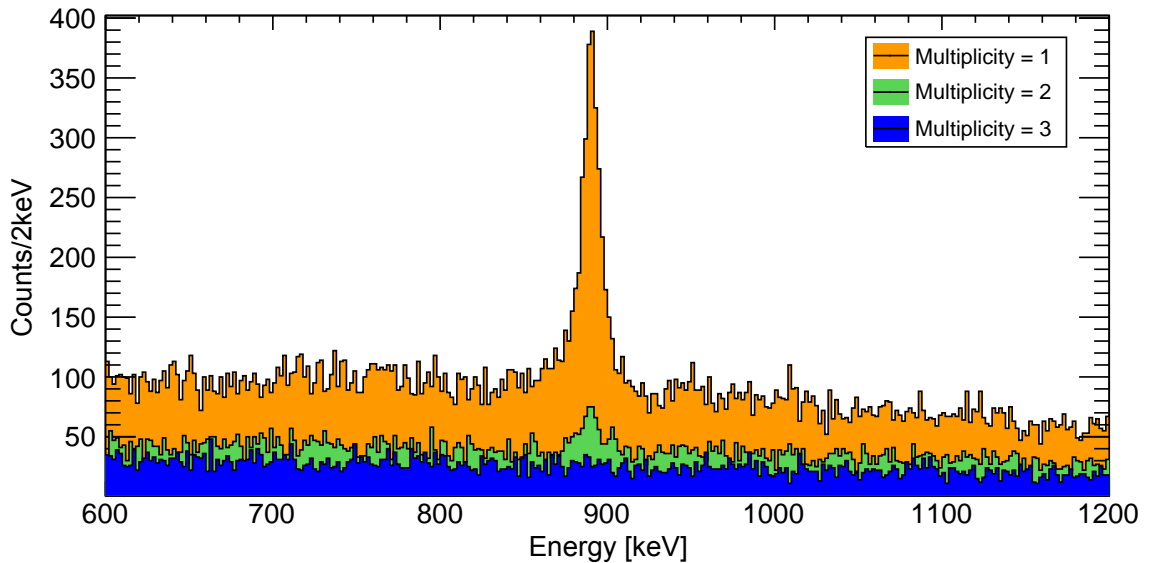


Figure 5.25: Doppler corrected energy spectrum for ^{46}Ti , showing the effects of different multiplicity gates on the Coulex peak.

5.6.3 Multiplicity Gate

An additional way in which background radiation can be reduced in γ -ray spectroscopy is through the application of a multiplicity gate, where in this case, multiplicity defines

the number of reconstructed γ -ray events (or photons) detected within a particular event, i.e. within a particular coincidence time window in AGATA. For the Coulomb excitation experiment performed here, the γ rays associated with the decay of the 2^+ state should predominantly be composed of multiplicity one events. Two possible exceptions to this are (a) if a γ ray from this state is detected in coincidence with a random uncorrelated background event (including Bremsstrahlung radiation) and (b) if a higher-lying state is populated, which subsequently feeds the 2^+ state. In Fig. 5.25, the effects of different multiplicity gates to the ^{46}Ti Coulex peak are shown. From this analysis it is clear that the majority of events in the peak occur from multiplicity one events, as expected, with a small portion of events occurring from multiplicity two events and negligible amounts occurring from higher multiplicities, which therefore only contribute to the background. Therefore, in order to improve the Peak-to-Total (P/T) ratio, only γ rays with multiplicity <3 were considered.

5.6.4 Optimising Peak Resolution

Obtaining the highest possible γ -ray energy resolution was of particular importance during this analysis, especially for the triple peak lineshape analysis. In order to improve this energy resolution, a number of additional corrections had to be performed, including, corrections applied to the event-by-event LYCCA β and to the XY-positions of particles measured in the target DSSSD. The corrections performed are summarised in the following sections.

5.6.4.1 LYCCA β Corrections

During the experiment, the lack of an available ToF target scintillator, normally positioned just before the reaction target, meant that the full LYCCA ToF, measured between the ToF start and ToF stop scintillators, had to be used instead. Since the ToF start scintillator is located approximately 140 cm upstream of the reaction target, the ToF (and therefore β) measured using this method is slightly biased. However, due to the small amount of material between the ToF start scintillator and the reaction target, i.e. only the target DSSSD, the measured ToF distribution should in principle be very similar to that between the ToF target and ToF stop scintillators, except with a slight shift, i.e. the ToF between the ToF start and ToF target. Therefore, by applying an offset to the full LYCCA ToF on an event-by-event basis, a corrected event-by-event LYCCA β can be found, for the

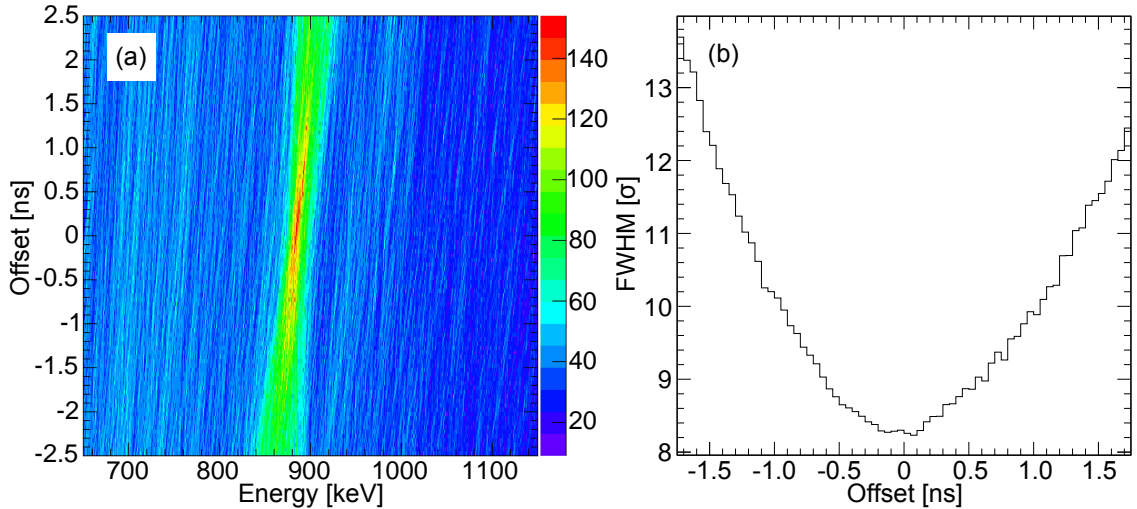


Figure 5.26: (a) LYCCA ToF offset scanner for γ rays in coincidence with ^{46}Ti . Each energy spectrum is Doppler corrected using the LYCCA β , derived from the modified event-by-event average LYCCA ToF, between the ToF start and ToF stop scintillators. (b) Plot of FWHM for the ^{46}Ti Coulex peak against ToF offset, where the minimum represents the optimal offset.

Doppler correction of γ -ray spectra. In order to optimise this offset however, a ToF offset scanner was produced, as shown in Fig. 5.26(a), where each energy spectrum was Doppler corrected using a slightly modified LYCCA β , derived using the modified ToF. Furthermore, by fitting a strongly observed transition in the resulting spectra with an automated fitting program, the optimal offset could be found by minimising on the FWHM, as shown in Fig. 5.26(b).

5.6.4.2 LYCCA Target DSSSD XY-Corrections

The positions of the LYCCA wall DSSSD modules are both fixed and well-defined in the experimental set up. However, the target DSSSD, located a few cm upstream of the reaction target, is often not positioned exactly central relative to the wall DSSSD modules. Unless this is accounted for in the analysis, it can lead to a significant worsening of the Doppler correction, which requires accurate information regarding the outgoing trajectory of ions, in order to calculate the angle of emission of a γ ray. One way in which this can be corrected for in the analysis is by taking the same approach as used to find the optimal ToF offset, except instead, scanning over X and Y positional offsets, added to the measured event-by-event positions in the target DSSSD. Furthermore, in addition to

correcting for the central position of the Target DSSSD, the optimised XY-offsets also include a small correction for the true XY-positions of ions at the reaction target. The reason for this is because the target DSSSD is actually positioned ~ 6 cm upstream of the reaction target, meaning the XY-positions measured here will be slightly incorrect. The severity of this effect however, will depend upon the magnitude of the scattering angle. As a result, this analysis had to be repeated for each experimental beam setting. The effects of this correction, for the ^{46}Ti Coulex peak, are shown in Fig.5.27, where an improvement of $\sim 0.7\%$ in the FWHM was observed, resulting in a final FWHM of $\leq 1.6\%$. While this improvement was not particularly important for the Coulex analysis, as will be seen later, it was essential for resolving the triple peak structure observed in the lifetime analysis (see Section 6.3).

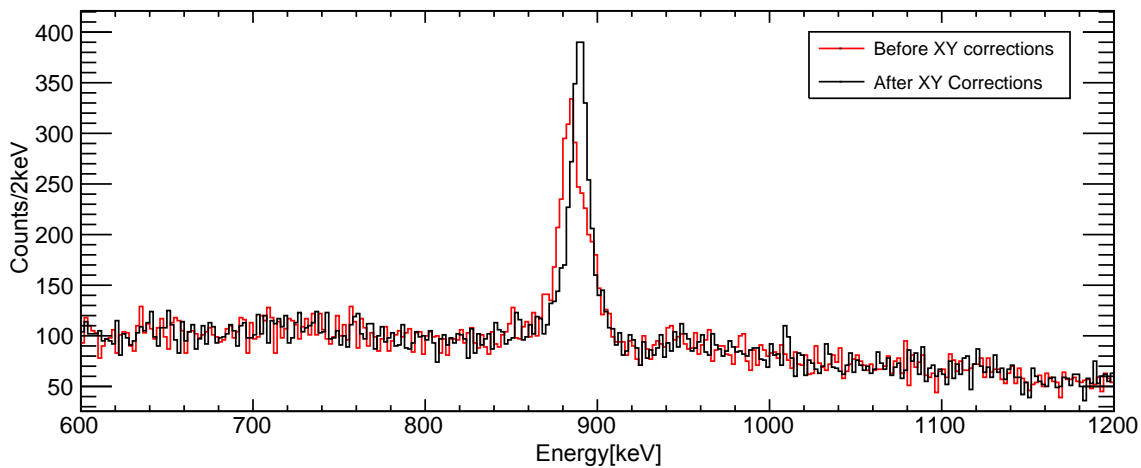


Figure 5.27: Doppler corrected energy spectrum for ^{46}Ti , showing the effects of the peak resolution both before (red) and after (black) XY-position corrections have been applied to the target DSSSD.

Chapter 6

Results for Lifetime and Coulex

Measurements across the $T = 1$

$A = 46$ Triplet of Nuclei

The results for the analysis of the experiment performed at GSI are divided into two sections. Firstly, in Section 6.2, the analysis for the Coulex experiments, performed for ^{46}Ti and ^{46}Cr , is presented. Secondly, in Section 6.3, the analysis of the lifetime experiments, performed for ^{46}Ti and ^{46}V , is presented. Due to differences in secondary beam intensities and concerns regarding the population of the 3^+ isomeric state in ^{46}V , each sub experiment was run for a different length of time, where there was a particular emphasis on maximising the beam time for the very low intensity ^{46}Cr setting. Details regarding each of the sub experiments performed at GSI, in addition to the main beam constituents in each FRS setting, are tabulated in Table 6.1. In both the Coulex and the Lifetime experiments, the well-studied ^{46}Ti was used to test the reliability of the method employed to measure the B(E2) transition strengths as well as to serve as a calibration point.

6.1 Scope of this Thesis

It is important to note that the experiment performed at GSI occurred during the latter stages of my PhD, which, coupled with the complexity of the analysis, meant it was decided that my focus should predominantly be on performing a “proof-of-principle” test for the new lifetime method. A full simulated spectral analysis is out of the scope of this thesis and will instead be performed at a later date by Marc Labiche at Daresbury.

Table 6.1: Summary of the FRS settings and experimental details for the four sub experiments performed during the experiment at GSI. The S2 and S4 Beam rates are extracted from the average scalar rates, per spill length, during each FRS setting. Secondary beam energies, before the reaction target, were calculated for the nuclei of interest through the use of LISE [73].

FRS Setting	^{46}Ti	^{46}Cr	^{46}Ti	^{46}V
Measurement	Coulex Cross Section	Coulex Cross Section	Lifetime	Lifetime
Beam Time [h]	19.1	65.5	8.2	40.9
Primary Beam	^{58}Ni	^{58}Ni	^{58}Ni	^{58}Ni
Primary Beam Energy [MeV/u]	599.65	599.65	599.65	599.65
Primary Beam Rate	$\sim 5.0 \times 10^8$	$\sim 2.0 \times 10^9$	$\sim 1.4 \times 10^9$	$\sim 2.5 \times 10^9$
Spill Length [s]	10	1	5	3
Spill Period [s]	12	3	7	5
S2 Rate [s^{-1}]	$\sim 3.0 \times 10^5$	$\sim 1.1 \times 10^5$	$\sim 7.6 \times 10^5$	$\sim 8.0 \times 10^5$
S4 Rate [s^{-1}]	$\sim 1.4 \times 10^4$	$\sim 1.2 \times 10^3$	$\sim 4.1 \times 10^4$	$\sim 2.5 \times 10^4$
Main Beam Constituent	^{46}Ti ($\sim 82\%$)	^{46}Cr ($\sim 53\%$)	^{46}Ti ($\sim 82\%$)	^{46}V ($\sim 69\%$)
Main Beam Contaminants	^{47}Ti ($\sim 2\%$) ^{45}Sc ($\sim 1\%$) ^{42}Ca ($\sim 1\%$)	^{45}V ($\sim 16\%$) ^{46}V ($\sim 11\%$) ^{47}Cr ($\sim 4\%$)	^{47}Ti ($\sim 2\%$) ^{45}Sc ($\sim 1\%$) ^{42}Ca ($\sim 1\%$)	^{45}Ti ($\sim 9\%$) ^{47}V ($\sim 4\%$) ^{46}Ti ($\sim 2\%$)
Secondary Beam Energy [MeV/u]	^{46}Ti - 178(2)	^{46}Cr - 180(3)	^{46}Ti - 178(2)	^{46}V - 176(3)
Reaction Target [^{197}Au]	0.25 mm	0.25 mm	0.375 mm 0.25 mm 0.25 mm	0.375 mm 0.25 mm 0.25 mm

In addition, it should also be noted that the analysis discussed here was performed in collaboration with Alberto Boso, from the Univerità Degli Studi di Padova, where his focus was predominantly on the Coulex analysis. This analysis is still ongoing and will be completed at a later date by A. Boso. All of the work presented in this thesis however,

both for the Lifetime and Coulex analysis, was performed independently, where the latter was confirmed/verified with the parallel analysis of A. Boso [156].

6.2 Results for the $^{46}\text{Ti}/^{46}\text{Cr}$ Coulex Analysis

The analysis performed for the Coulex beam runs firstly involved the careful application of an incoming FRS gate, in order to both reduce contamination in the final γ -ray spectra from other reaction channels, and, more importantly, to ensure that the number of incoming ions impinging upon the reaction target could be accurately calculated. However, since the FRS PID were produced using positions measured with the FRS scintillators, where the position resolution is worse compared to using the TPCs, some small overlap with surrounding ions in the FRS PID was observed. Therefore, the gates applied to the nuclei of interest, ^{46}Ti and ^{46}Cr , needed to be fairly stringent, particularly on their right sides, as shown in Fig. 6.1, due to slight overlaps with ^{47}Ti and ^{47}Cr ions, respectively. Furthermore, it should additionally be noted that these FRS PID were produced with a condition on trigger 10, i.e. the reduced (downscaled) particle FRS trigger, the reasons for which will be discussed later.

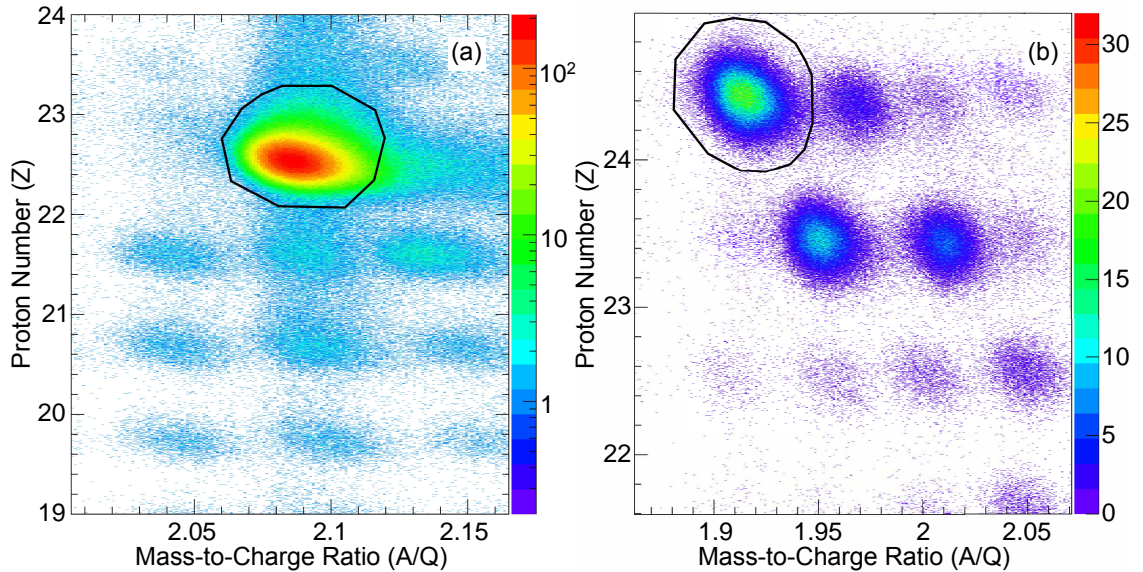


Figure 6.1: Incoming gates applied to the FRS PID for (a) the ^{46}Ti beam setting and (b) the ^{46}Cr beam setting. Both PID were produced with a condition on trigger 10, see text for more details.

Following the application of an incoming gate, an outgoing gate was applied in LY-CCA, gating upon the atomic number (Z) of the nuclei of interest. Since in principle the

main purpose of the outgoing gate was to produce a cleaner γ -ray spectra and remove contamination from other reaction channels resulting from $^{46}\text{Ti}/^{46}\text{Cr}$, the gates applied here were slightly less stringent. This was also to ensure that no “good events” were neglected, as this would negatively bias the measured cross section. The gates applied in LYCCA, for both ^{46}Ti and ^{46}Cr , are shown in Fig. 6.2.

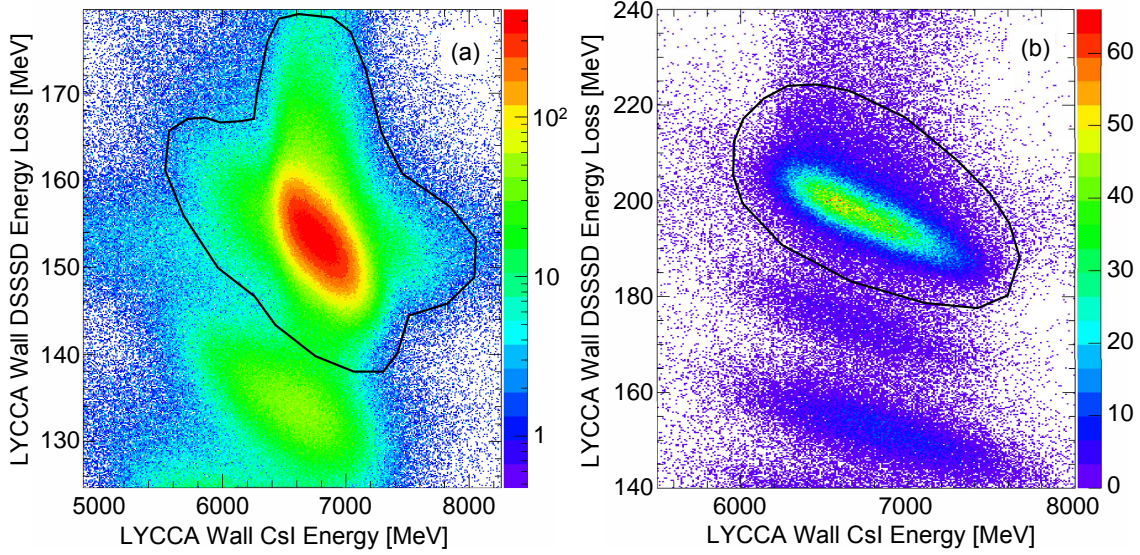


Figure 6.2: Outgoing gates applied to the LYCCA PID for (a) the ^{46}Ti beam setting and (b) the ^{46}Cr beam setting. Both PID were produced with an incoming FRS gate on the nuclei of interest.

The final gates to be applied for the nuclei of interest included a particle-time gate (45 ns wide in both cases), in order to reduce background resulting primarily from Bremsstrahlung radiation, and a gate on γ -ray multiplicity events lower than 3, in order to remove uncorrelated background events not associated with the reaction channel of interest. The resulting γ -ray spectra, following the application of these gates and the optimisation of the LYCCA β and target DSSSD XY-positions, as discussed in Section 5.6.4.1, are presented in Fig. 6.3.

In both spectra, a sharp peak on top of a relatively small and flat background can be observed. By fitting each peak with a Gaussian function plus a linear background, the total number of counts in each peak could be extracted. For the well-studied and stable nuclide ^{46}Ti , the total number of counts measured was 2610 ± 69 , while for the more exotic ^{46}Cr , 210 ± 19 counts were measured. Due to the high beam energies (~ 175 MeV/u) used to study Coulomb excitation in these nuclei however, a further correction had to be

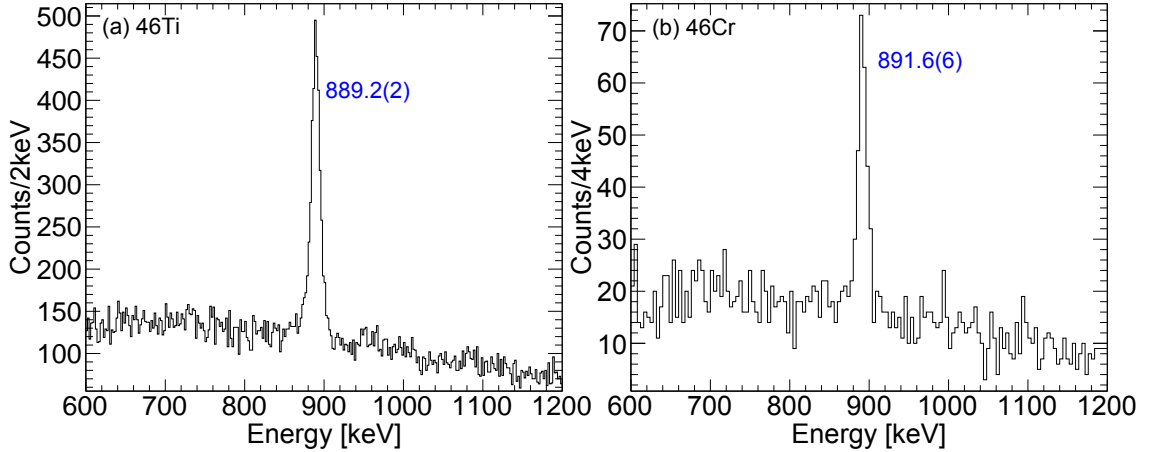


Figure 6.3: Doppler corrected γ -ray spectra for (a) ^{46}Ti and (b) ^{46}Cr , using the optimised event-by-event LYCCA β .

applied to the data in order to ensure that only genuine Coulex events were considered. This is because at these beam energies, the contribution to the reaction process from the strong nuclear force cannot be considered as negligible and must therefore be accounted for. Therefore, following the use of Equations 2.31 and 2.30, in addition to the calculated beam energies prior to the secondary targets using LISE [73], “safe” CoM scattering angles of 0.0228 rads and 0.0246 rads were determined for ^{46}Ti and ^{46}Cr , respectively. These corresponded to “safe” scattering angles of 0.0185 rads and 0.0199 rads in the laboratory frame.

In this analysis, the scattering angles of nuclei were determined using positions measured in the TPCs at S4, the target DSSSD and the wall DSSSD modules, each with their own associated errors, which resulted in scattering angle distributions like the one shown in Fig. 6.4(a). This meant that the previously calculated “safe” scattering angles could not, in principle, be simply applied to these spectra, since in reality the number of events occurring at around 0 mrad, should not go to zero. As a result, the scattering angles needed to be simulated. This was achieved through the use of a simple scattering angle simulation, where experimentally measured XY-positions in the first two position-sensitive detectors (gated on the nuclei of interest) were replicated in the simulation. Meanwhile, the XY-positions in the LYCCA wall DSSSDs were allowed to vary, as these positions instead depended upon the simulated scattering angles. In addition to this, previously measured position resolutions for the three tracking detectors, as well as the measured distances between the three detectors, were also included in the simulation. The results

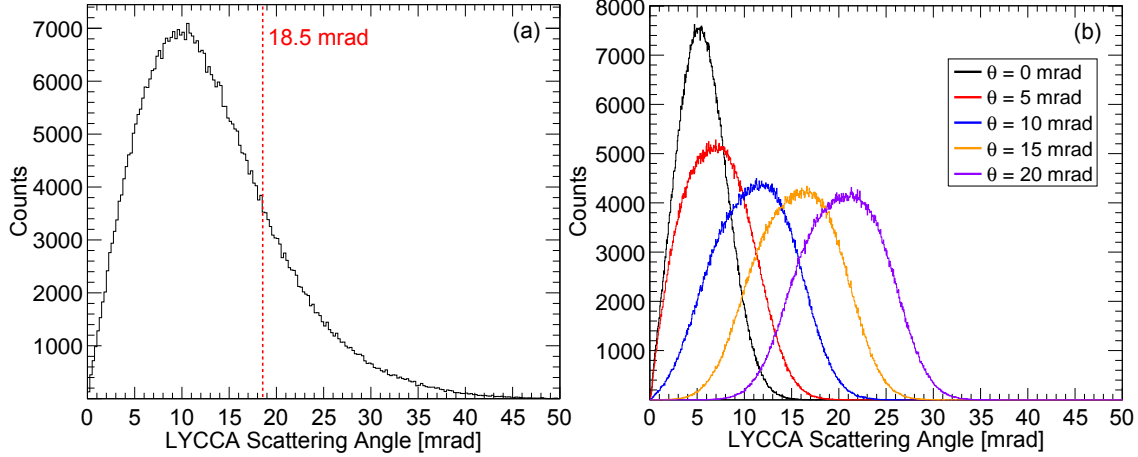


Figure 6.4: (a) Measured scattering angle for ^{46}Ti ions, using positions measured in the TPCs at S4, the target DSSSD and the wall DSSSDs. (b) Simulated scattering angle distributions for ^{46}Ti ions, using a number of experimentally extracted parameters such as XY-positions and the resolutions of the various position-sensitive detectors, see text for details.

for these simulations are presented in Fig. 6.4(b), where it can be seen that the distributions for the different simulated scattering angles in fact occur and peak at larger angles. Furthermore, it can also be seen that the various distributions of greatly different angles also overlap with each other. This therefore suggests that while some events from smaller angles will be lost by applying such a “safe” scattering angle cut to the experimental scattering angle distributions, other events from larger angles will also be included. In order to better understand this effect and to determine the correct scattering angle cut to use, a more refined simulation needs to be performed including the true, experimentally measured, position resolutions of the detectors using unreacted beam runs.

In order to perform a preliminary analysis for the Coulex cross sections however, the previously calculated “safe” scattering angles of 0.0185 rads and 0.0199 rads for ^{46}Ti and ^{46}Cr , respectively, were used instead, while acknowledging that these values may result in a slightly underestimated cross section. In Fig. 6.5, the resulting γ -ray spectra for ^{46}Ti and ^{46}Cr , following the application of a “safe” scattering angle condition, are shown. This resulted in a 40-50% reduction in the total number of observed counts in the Coulex peaks, where 1165(51) and 108(12) counts were measured in the ^{46}Ti and ^{46}Cr Coulex peaks, respectively.

The number of incoming ions during this experiment was determined from the number

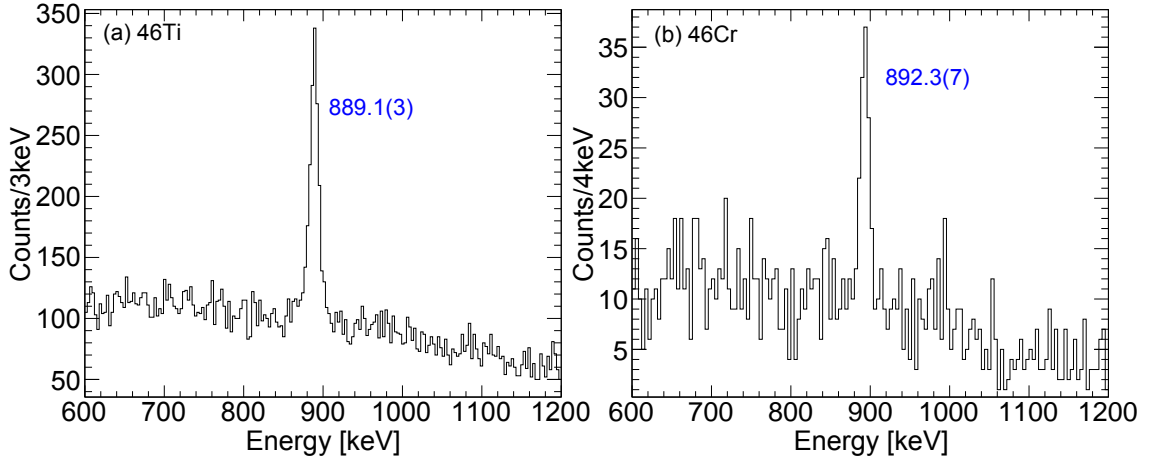


Figure 6.5: Doppler corrected γ -ray spectra for (a) ^{46}Ti and (b) ^{46}Cr , using the optimised event-by-event LYCCA β . A cut on the LYCCA scattering angle has been applied to the data to ensure only “safe” Coulex events are considered, see text for more details.

of ions detected inside the incoming gate applied to the FRS PID, with a condition on trigger 10 (the reduced particle trigger). Since this trigger was additionally downscaled by a factor of 2^8 during the experiment, i.e. only 1 in 256 events in the FRS was recorded by the Multi-Branch System (MBS) based Data AcQuisition (DAQ), the correct number of ions was therefore found by scaling up the measured number of ions by a factor of 256. Following this, the number of incoming ions also needed to be corrected for the average dead time of the FRS. This was achieved by comparing two signals, the 10kHz and the 10kHz-veto-dT, which were recorded online during the experimental beam runs. These signals came from a pulser fed into a scalar module, which was read out every 0.1s. Here, the 10kHz signal was scaled continually during the experimental beam runs, while the 10kHz-veto-dT was only scaled when the MBS DAQ was not busy. As a result, the average dead time of the FRS could be found by comparing changes in the two signals between different events, during the experimental beam runs which, for this analysis, was performed separately for both FRS settings, due to differences in the beam rates. In addition, since the MBS DAQ was also used to record data from LYCCA, the dead time measured here can also be considered as the combined dead time for both the FRS and LYCCA sub systems. In Fig. 6.6(a), the MBS dead time, as a function of time is shown for ^{46}Ti , where a clear structure can be observed, resulting from the beam spills. Lastly, the number of incoming ions was corrected for the number of ions involved in the Coulex process, by applying the same scattering angle cut as applied to the γ -ray spectrum.

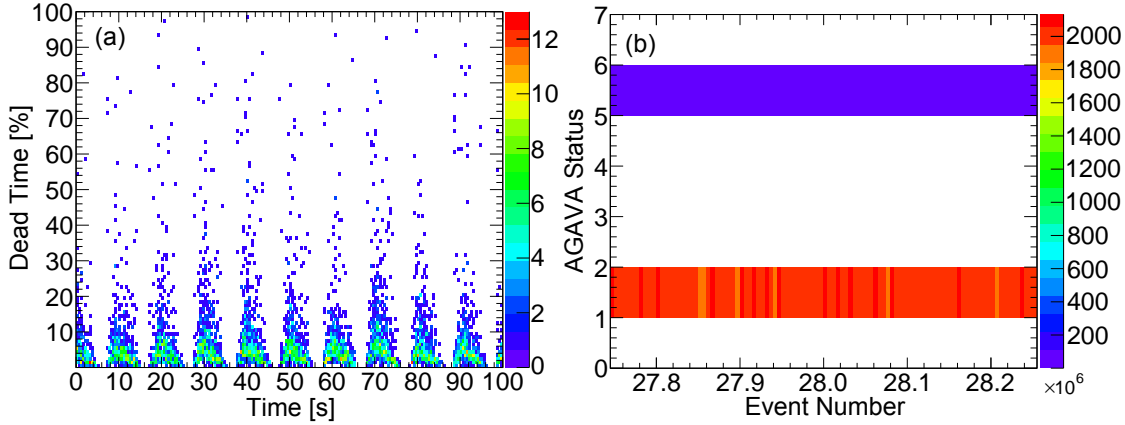


Figure 6.6: (a) MBS dead time as a function of time, during a ^{46}Ti beam run, where the dead time was calculated by comparing two scaler signals, 10kHz and 10kHz-veto-dT, see text for more details. (b) AGAVA status as a function of event number, for trigger 9 events (FRS+AGATA+LYCCA), shown during a ^{46}Ti beam run. Events in y-bin 1 refer to validated (accepted) events and events in y-bin 5 refer to rejected events.

Since data from AGATA was recorded by the “Nouvelle Acquisition temps Rel Version 1.2 Avec Linux” (NARVAL) based DAQ instead, the dead time of AGATA had to be determined separately. In principle, this could be achieved by comparing the rejected and validated AGAVA scaler signals where, in this case, a validated AGAVA signal refers to an event in which it was possible to read out an AGATA signal, following an external trigger request from the ancillary detector. However, under this condition, the rejected AGAVA scaler is also scaled even when there is no γ ray at all, such as during a trigger 10 event, leading to an overestimation of the dead time. Instead, an alternative way to estimate the dead time is to view the AGAVA status with a trigger 9 condition (FRS+AGATA+LYCCA), whereby if it is not possible to record an AGATA signal due to the NARVAL DAQ being busy, the flag is set to rejected. In Fig. 6.6(b), a plot of AGAVA status as a function of event number, during a ^{46}Ti beam run, is shown, where events in y-bin 1 refer to validated (accepted) events and events in y-bin 5 refer to rejected events. The NARVAL dead time could therefore be calculated by the sum of the rejected events divided by the sum of the accepted and rejected events.

Lastly, to determine the efficiency corrected number of γ rays, the previously measured AGATA (tracked) efficiency during the 2014 experimental campaign, as taken from Ref. [157], was used, after accounting for the Lorentz boost.

The results for this analysis are summarised in Table. 6.2, where the measured Coulex

cross sections, σ , for both nuclei are also shown, as calculated using the following expression,

$$\sigma = \frac{N_\gamma}{N_i \cdot N_t} \quad (6.1)$$

where, N_γ is the corrected number of γ rays, N_i is the corrected number of incoming ions of the nuclei of interest and N_t is the number of target ions per unit area. In order to obtain these cross sections into the more conventional units of barns, b, they were additionally multiplied by a factor of 10^{28} .

Table 6.2: Summary of the experimental data and the resulting Coulex cross section, for both ^{46}Ti and ^{46}Cr , obtained using Equation. 6.1. The dead time for the MBS DAQ was calculated by comparing two scaler signals, 10kHz and 10kHz-veto-dT, while the dead time for NARVAL DAQ was calculated by comparing the validated and rejected AGAVA status events, with a trigger 9 condition (FRS+AGATA+LYCCA), see text for more details. The AGATA efficiency used here (after accounting for the Lorentz boost) was taken from Ref. [157].

Nuclei of Interest	^{46}Ti	^{46}Cr
Number of Detected γ rays	1165(51)	108(12)
Number of Detected Incoming Ions	173.89M	14.59M
MBS DAQ Dead Time	4.0%	0.8%
NARVAL Dead Time	0.8%	0.3%
AGATA γ -ray Efficiency	5.3%	5.3%
Corrected Number of γ rays	22.07k	2.04k
Corrected Number of Incoming Ions	181.13M	14.71M
Coulex cross Section [mb]	79.8(35)	91(10)

Firstly, it is important to note that the dead times obtained in this analysis appear to be particularly low, during both the ^{46}Ti and ^{46}Cr beam runs. In regards to the MBS dead time, this is most likely due to the beams rates being comfortably below the maximum allowable rates at S2 and S4 of $\sim 1\text{MHz}$ and $\sim 50\text{kHz}$, respectively. For example, during the ^{46}Cr beam setting, as previously shown in Table. 6.1, the average S2 and S4 rates were only 0.11MHz and 1.2kHz , respectively. In regards to the low dead time for AGATA, this is most likely due to the very low counting rates of the AGATA crystals during the experimental beam runs, resulting from (a) the relatively low beam rates (particularly in the case of ^{46}Cr) and (b) the low multiplicity reaction mechanism under investigation

(Coulomb excitation). For example, during the ^{46}Ti and ^{46}Cr beam runs, the counting rates were approximately $\sim 1\text{kHz}$ and $\sim 0.1\text{kHz}$ per crystal, respectively, which are both significantly below the maximum allowable rates of $\sim 50\text{kHz}$ per crystal.

In conclusion, this analysis yielded preliminary Coulex cross section values of $79.8(35)$ mb and $91(10)$ mb for ^{46}Ti and ^{46}Cr , respectively, where the result obtained for ^{46}Ti compares favourably with the predicted Coulex cross section of 83.2 mb obtained from a DWEIKO calculation [59, 156], using both experimental information and the previously measured $B(E2)$ transition strength for this transition [122]. It is important to note however that these cross section values are still only preliminary.

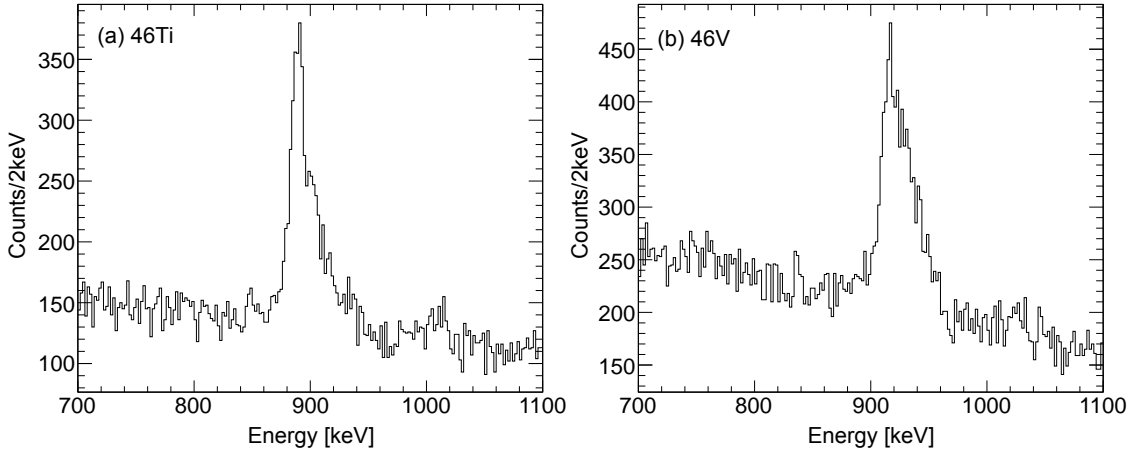


Figure 6.7: Doppler corrected γ -ray spectra for (a) ^{46}Ti and (b) ^{46}V , using the event-by-event LYCCA β . The Doppler correction is only approximately optimised for the first peak in the triplet distributions.

6.3 Results for the $^{46}\text{Ti}/^{46}\text{V}$ Lifetime Analysis

The analysis for the lifetime experiments was performed by taking a similar approach as used to analyse the Coulex data. However, since the aim here was to maximise the number of γ rays observed in triple peak distributions, no incoming FRS gate was applied. This was in order to avoid statistics being lost due to missing particle information in the FRS detectors, often caused by high FRS beam rates. In Fig. 6.7, the Doppler corrected triple peak distributions observed in ^{46}Ti and ^{46}V , following the application of an outgoing LYCCA gate, a particle-time gate and a multiplicity < 3 gate, are shown. In both of these spectra some other weak transitions can be tentatively observed, both before and after the triplet distribution, which appear to be mirrored in both reactions. By investigating

transitions with a similar energy in both Ti and V isotopes, no clear corresponding transitions could be identified. However, since these transitions appear to be both sufficiently weak and well separated from the triplet distributions of interest, they were simply ignored during this analysis.

While the general lineshape of the triple peak distributions in both nuclei can be observed in Fig. 6.7, the individual peaks can not be clearly resolved. This was in part due to the small separation energy between the peaks, but more importantly due to differences in the emitter ion velocity after each gold target, such that only one peak could be Doppler corrected at a time, resulting in the other two (non-Doppler corrected) peaks becoming much broader. This effect can additionally be observed by performing a simple simulation for the Doppler correction of a γ -ray transition, emitted at three different ion velocities, while only Doppler correcting the resulting three transitions for one of these velocities. As shown in Fig. 6.8, by plotting the Doppler corrected γ -ray Energy, as a function of the angle of the emitted γ ray, the two non-Doppler corrected transitions in fact occur over a large range of energies, thereby reducing the separation between the individual peaks. Furthermore, when other factors such as the energy resolution of the detector, the energy spread of the beam and the quality of the event-by-event Doppler correction employed, are also accounted for, the overlaps become even more significant.

In order to be able to better resolve the peaks in this analysis, strict angle cuts were applied to the γ -ray angle of emission. In Fig. 6.9(a), the distribution of events at different angles in ^{46}Ti is shown, where it can be clearly seen that an angle cut at around 40° would yield the most statistics. However, as previously shown in Fig 6.8, the separation between the peaks is expected to quickly reduce at higher angles, especially towards 60° . Therefore, due to a compromise between statistics and peak separation for the initial test of this new method, the following analysis was performed with an angle cut at $30 \pm 5^\circ$, an example for which is shown in Fig. 6.9(b), where a clear triple peak structure can now be observed. In this case, a separation of approximately 18-19 keV between the centroids of each peaks centroids was observed, similar to that predicted in Fig 6.8.

Following this, through the guidance of LISE simulations [73], the approximate velocity after each target, for both the ^{46}Ti and ^{46}V runs could be found, while the Z position of each target could be determined from the experimentally deduced Z position for the Coulex target, and the known respective geometry of the SGT device. Through the use of a ToF offset scanner, as discussed in Section 5.6.4.1, with an additional cut on γ -ray angle, the

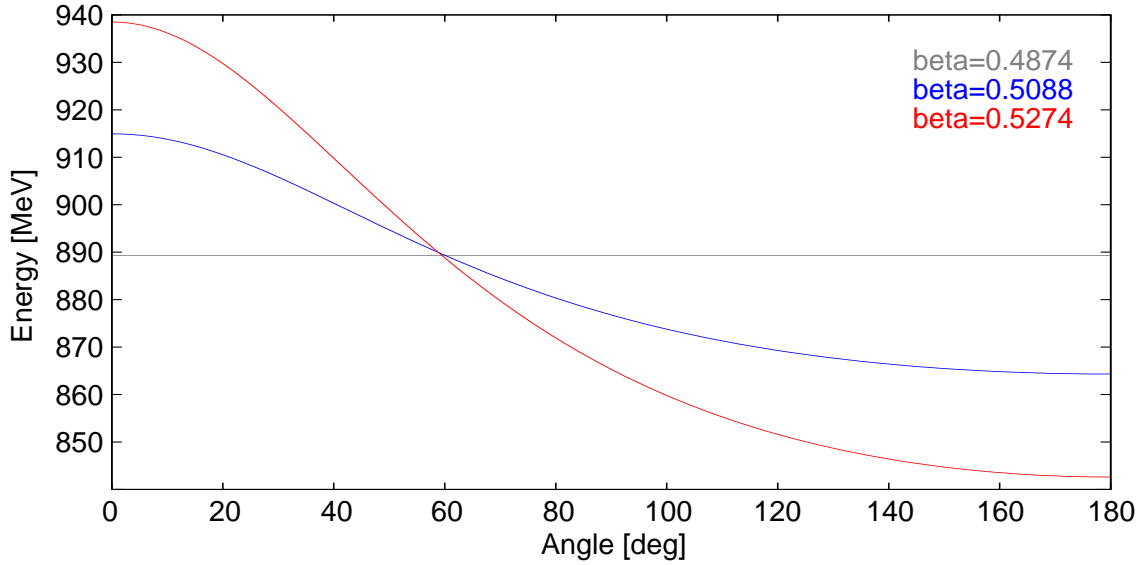


Figure 6.8: Simulated Doppler corrected energy, as a function of γ -ray angle, for the same energy transition emitted at three different velocities, where the Doppler correction was performed for only one of these velocities. In this case, the predicted velocities of ^{46}Ti after each gold target, using LISE [73] calculations, have been used.

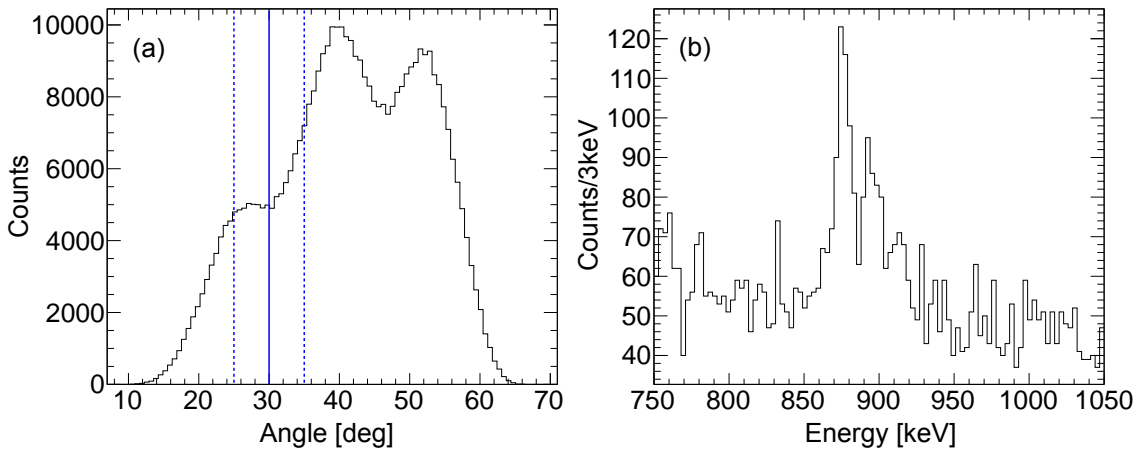


Figure 6.9: (a) Distribution of γ -ray events observed at different γ -ray angles of emission, where the angle cut of $30 \pm 5^\circ$ used during this analysis is also shown. (b) The observed Doppler corrected ^{46}Ti triple peak spectrum following the application of an angle cut at $30 \pm 5^\circ$.

Doppler correction could then be “fine tuned” from the initial LISE estimates, to try and find the sharpest peak possible at the correct energy. While this type of analysis could be readily performed for the ^{46}Ti lifetime analysis, where the optimal XY-position offsets of the target DSSSD (see Section 5.6.4.2) had already been determined during the

^{46}Ti Coulex analysis, this was not the case for ^{46}V . Instead, due to the lack of a single Coulex peak from which these parameters could be simply optimised, a slightly different approach needed to be taken. This involved using the already optimised XY-offsets for the ^{46}Ti Coulex setting, approximately optimising the LYCCA β for lowest energy peak in the triplet distribution, then investigating X and Y offset scans to try find the optimal settings to sharpen this peak. Despite this method not being quite as clean as that used to optimise the Coulex peaks, it still resulted in comparable improvements in the peak resolution, which was essential for resolving the peaks observed in the ^{46}V triplet distribution. The resulting spectra, following the optimisation of the Doppler correction for each peak in the triplet distribution of ^{46}Ti and ^{46}V , are presented in Fig. 6.10.

In the spectra shown in Fig. 6.10, clear triplet distributions, for both ^{46}Ti and ^{46}V , can be observed, where each peak also appears to sharpen and align at the correct energy, following the optimisation of the Doppler correction using the event-by-event LYCCA β . As a result, this analysis therefore demonstrates, for the first time, the principle technique of the SGT device, where any differences in the distribution of counts amongst the three peaks, in both nuclei, should almost entirely depend upon the half-life of the state investigated. This is because other experimental parameters, such as the beam energy, were kept approximately the same, for both nuclei. Therefore, by comparing the distribution of counts in the three peaks, in particular the intensity of latter two peaks relative to the first peak, for both ^{46}Ti and ^{46}V , it can be tentatively inferred that the $2_{T=1}^+$ state in ^{46}V has a slightly shorter half-life. This is due to the slightly greater relative intensity of the latter two peaks in ^{46}V , suggesting that more decays (relative to ^{46}Ti) occurred after the first and second targets, than further downstream after the third target.

In order to obtain a first-order approximation of the half-life given by this technique, simulations for the SGT device, as discussed in Section 5.2.1, were used. In this case, half-lives were extracted by comparing theoretically deduced ratios (from the simulated distribution of counts in the three peaks), with those observed experimentally. From analysis conducted before this experiment, it was found that one of the more sensitive ratio to changes in half-life (out of those investigated), was the ratio of counts in the first peak, divided by the sum of the counts in the second two peaks. In Fig 6.11(a), the simulated ratio, Peak 1/(Peak 2+Peak 3), as a function of half-life, is shown, while in Fig 6.11(b), the best separated triple peak distribution observed in ^{46}Ti during this

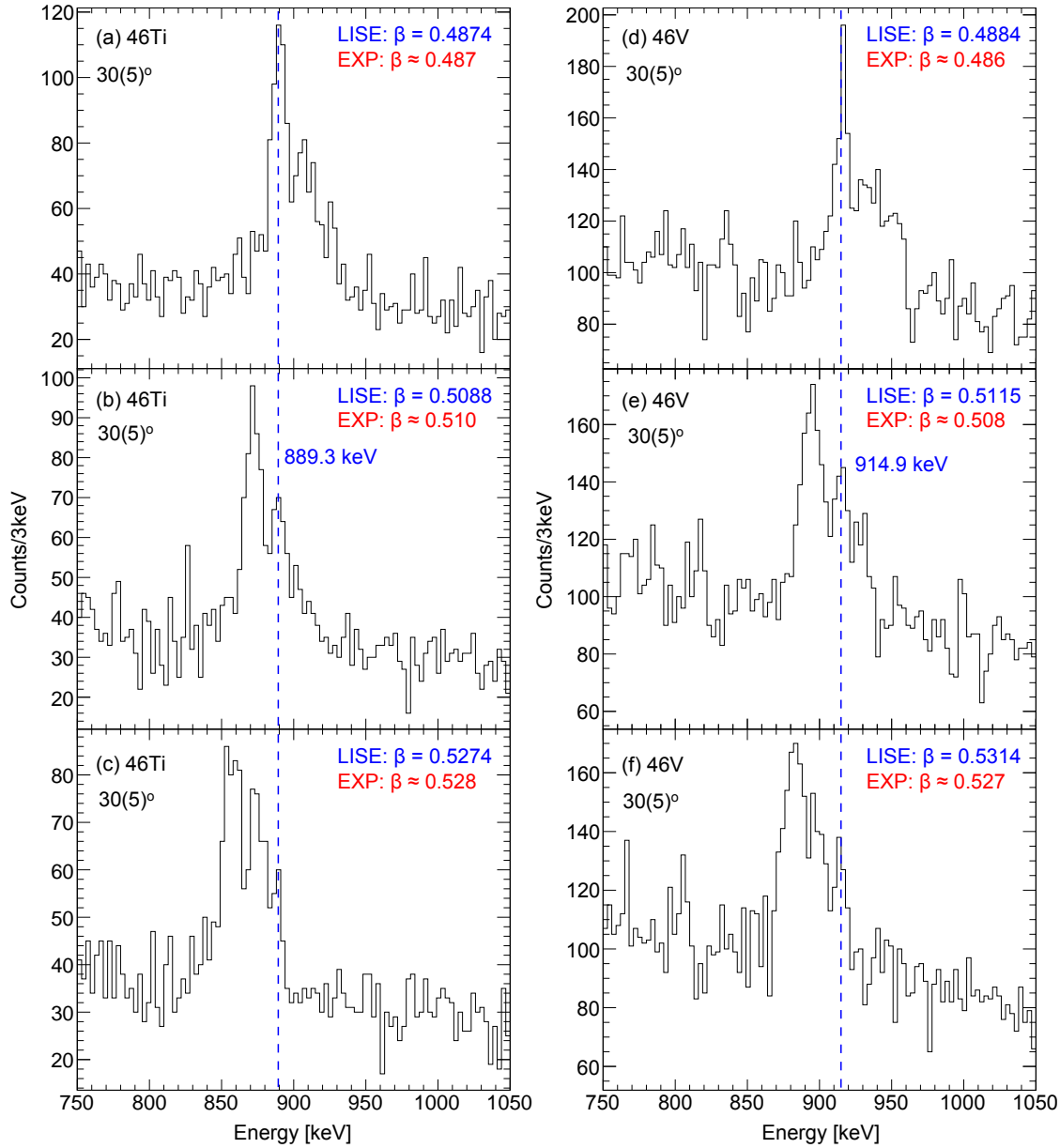


Figure 6.10: Doppler corrected γ -ray spectra, with Doppler correction optimised for (a-c) each peak of the triplet distribution in ^{46}Ti and (d-f) each peak of the triplet distribution in ^{46}V , using the event-by-event LYCCA β . The Doppler correction of each peak was guided by simulations performed using LISE, where both the LISE β and optimised LYCCA β for each peak are shown.

analysis is shown. By fitting this triplet distribution with a triple Gaussian function plus a linear background, the number of counts in each peak could be obtained, resulting in 276(17), 184(14) and 83(9) counts in peaks 1, 2 and 3, respectively, where errors were derived from \sqrt{n} . This therefore corresponded to a ratio of 1.03(15) and a half-life of

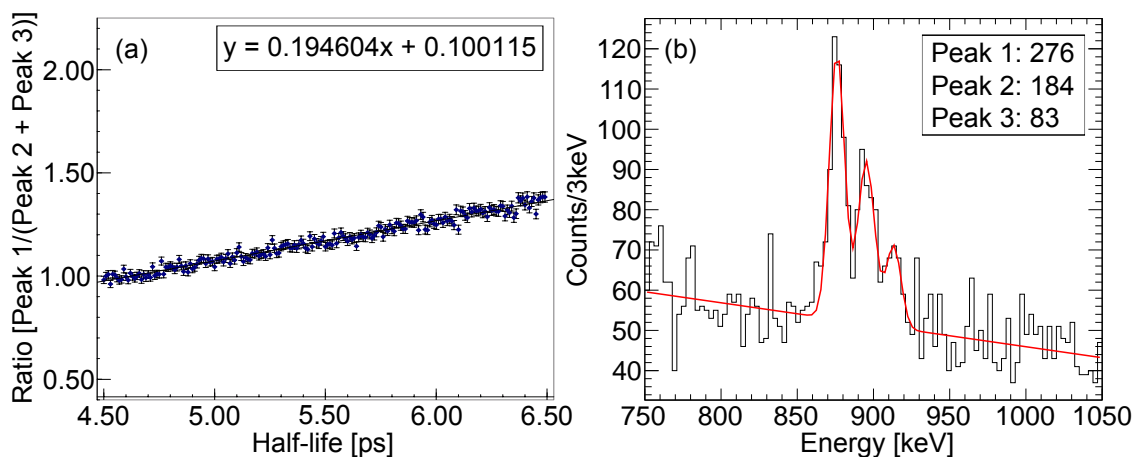


Figure 6.11: (a) Simulated ratio of counts in peak1/(peak2+peak3), as a function of half-life. See Section 5.2.1 for more details. (b) Doppler corrected γ -ray spectrum for ^{46}Ti , fitted with a triple Gaussian function plus linear background to extract the number of counts in each peak.

4.8(8) ps, which also compares favourably with the literature value of 5.29(5) ps [122] for the $2^+_{1,T=1}$ state in ^{46}Ti . However, this simplistic approach does not fully account for a number of additional higher-order effects, such as decays occurring inside the three targets with a varying emitter velocity (i.e. counts added to the tails of the peaks, which may have been included in the fits but not in the simulated ratios), or issues regarding the flatness of the targets. Therefore, the value obtained here may vary slightly by accounting for these additional issues in the simulations, but the result should still represent a good first-order approximation. The error in this half-life however, represents a very large uncertainty of $\sim 17\%$, which is much greater than the $<5\%$ aimed for in the proposal of this experiment, despite not considering any additional systematic errors. However, the final analysis of these lifetimes will most likely involve a detailed lineshape analysis, with much less of a restriction on the γ -ray angle, or possibly none at all. Furthermore, by utilising the full statistics available in these distributions (2-3k), in addition to using a more sensitive method for measuring half-lives, more accurate lifetime results (with a higher precision), should be able to be extracted from this data.

For completeness, a brief investigation of the effect of different angles cuts was also performed for this analysis. In general, it was found that an angle cut at around $39(5)^\circ$ yielded a significant improvement in the statistics (55-60%), while also maintaining a reasonable separation between the three peaks. In Fig. 6.12, the resulting spectra for both

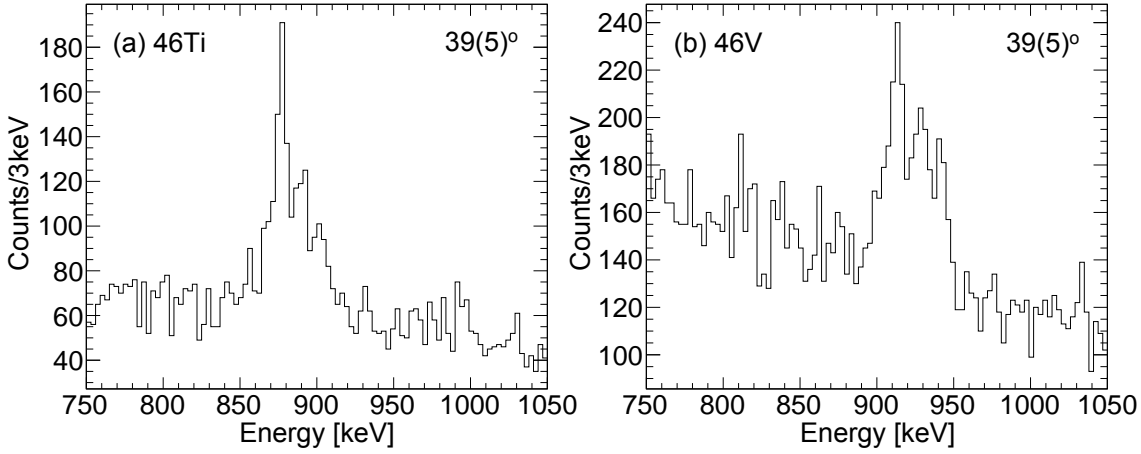


Figure 6.12: Doppler corrected γ -ray spectra for (a) ^{46}Ti and (b) ^{46}V , using the event-by-event LYCCA β . Both spectra have been produced with a γ -ray angle cut of $39(5)^\circ$.

^{46}Ti and ^{46}V , following the application of this angle cut, are shown, where a clear difference in the distribution of counts in the three peaks can be observed. This observation further supports the previous (tentative) inference that the $2_{1,T=1}^+$ state in ^{46}V must be shorter lived than the IAS in ^{46}Ti . Indeed, this is also supported by the current literature, where half-life measurements of 5.29(5) and 4.7(6) ps have previously been performed for ^{46}Ti and ^{46}V , respectively [122].

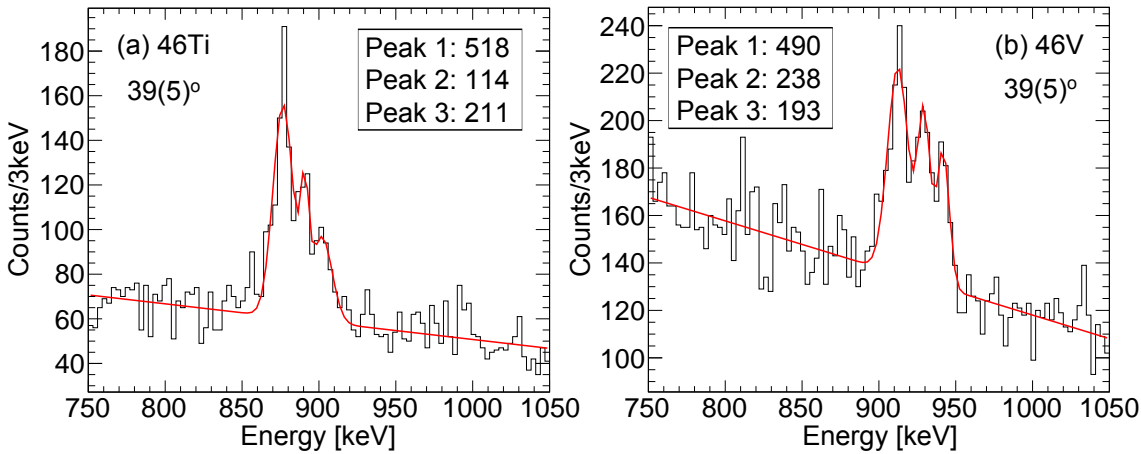


Figure 6.13: Doppler corrected γ -ray spectrum for (a) ^{46}Ti and (b) ^{46}V , using the event-by-event LYCCA β , fitted with a triple Gaussian function plus linear background to extract the number of counts in each peak. Both spectra have been produced with a γ -ray angle cut of $39(5)^\circ$.

To test this observation here however, the ^{46}Ti and ^{46}V triplet distributions in Fig. 6.12

were both fit with a triple Gaussian function plus a linear background, to extract the number of counts in each peak, as shown in Figs. 6.13(a) and 6.13(b). By performing a similar analysis to that discussed previously, i.e. extracting a transitions half-life by comparing the observed ratio of counts in the three peaks to simulated ratios, half-lives of 7.7(5) ps and 5.3(4) ps were obtained for ^{46}Ti and ^{46}V , respectively. However, as can be seen in Fig. 6.13, due to the reduction in the separation of the peaks, the fits performed here are not quite as good. For example, in the fit performed to the triplet distribution in ^{46}Ti , see Fig. 6.13(a), the width of the second peak is much smaller than the other two peaks, resulting in an unrealistic lower number of counts in this peak. This issue can be tentatively resolved by fixing the FWHM of this peak to a similar width of the other two peaks, as shown in Fig. 6.14, which gives a more realistic number of counts in each peak and a half-life of 6.0(4) ps. Therefore, the preliminary analysis performed here appears to support the current findings in the literature, i.e. that the $2_{1,T=1}^+$ state in ^{46}V is slightly shorter lived than the IAS in ^{46}Ti , however the half-life values obtained here are slightly higher, in both cases.

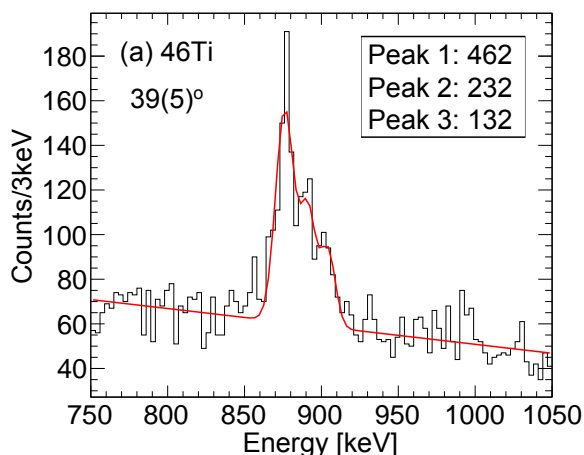


Figure 6.14: Doppler corrected γ -ray spectrum for ^{46}Ti , using the event-by-event LYCCA β , fitted with a triple Gaussian function plus linear background to extract the number of counts in each peak. The spectrum has been produced with a γ -ray angle cut of $39(5)^\circ$. The FWHM of the Gaussian fit to the second peak has been fixed to a similar width as the other two peaks ($\sim 1.4\%$), see text for more details.

In conclusion, the preliminary results obtained using this new technique are quite positive. The fits performed to these triplet distributions however, also show the need for a more detailed lineshape analysis to be performed in order to extract more accurate and

precise lifetimes.

6.4 Summary

In summary, preliminary Coulex cross section results of 79.8(35) mb and 91(10) mb have been obtained for ^{46}Ti and ^{46}Cr , respectively. The cross section obtained for ^{46}Ti compares favourably with the predicted Coulex cross section of 83.2 mb obtained from a DWEIKO calculation [59, 156], using both experimental information and the previously measured B(E2) transition strength for this transition [122]. In addition, the Coulex cross section values obtained for both ^{46}Ti and ^{46}Cr also compare quite favourably, which, due to isospin symmetry and the near identical experimental conditions in which these analogue $2_{T=1}^+$ states were populated, is expected. It is important to note however that these cross section values are still only preliminary.

In regards to the lifetime analysis, the first demonstration of the new SGT technique has been presented with promising results. Clear triple peak distributions in both ^{46}Ti and ^{46}V have been observed following the application of strict cuts on the angle of the emitted γ ray, where differences in the distribution of counts amongst the peaks in both nuclei are tentatively attributed to small differences in the half-lives of the $2_{T=1}^+$ states in ^{46}Ti and ^{46}V . Through the use of a simple simulation program, the distribution of counts in the 3 peaks, for different half-lives has been computed and compared with those observed experimentally in ^{46}Ti and ^{46}V . This analysis was performed for two different γ -ray angle cuts applied to the experimental data. Firstly, for an angle cut of $30(5)^\circ$, where the best separation in the triple peak distributions was observed, this analysis yielded a very preliminary half-life of 4.8(8) ps for the $2_{T=1}^+$ state in ^{46}Ti , which also compares quite favourably with the literature value of 5.32(15) ps [122]. Meanwhile, for an angle cut of $39(5)^\circ$, where the peak separation was reduced but the statistics were greater, this analysis yielded very preliminary half-lives of 6.0(4) ps and 5.3(4) ps for ^{46}Ti and ^{46}V , respectively. This preliminary analysis also supports the current findings in the literature, i.e. that the $2_{T=1}^+$ state in ^{46}V is slightly shorter lived than the IAS in ^{46}Ti , however the half-life values obtained here are slightly higher, in both cases. This is most likely due to the slight reduction in the quality of the fits however, due to the reduced separation of the peaks. Therefore, the preliminary results presented in this Chapter, in principle, demonstrate the first application of this new technique to measure half-lives of relatively short-lived states. A more refined analytical approach however, involving the use of simulations and

a lineshape analysis may yield a more accurate and precise result.

6.5 Future Work

As discussed in the previous sections of this chapter, the analysis performed here is now at a particularly advanced stage. However, in order to reach a conclusion in regards to the investigation of isospin mixing between the $2_{T=1}^+$ and $2_{T=0}^+$ states in ^{46}V , $B(E2 : 2_{T=1}^+ \rightarrow 0_{T=1}^+)$ transition strengths need to be measured for each nuclide across the $T = 1, A = 46$ triplet. In order to achieve this, a thorough investigation of both the scattering angle cut and the dead time of the various detector systems used during this experiment needs to be performed, to ensure that reliable Coulex cross section results are obtained for both ^{46}Ti and ^{46}Cr . Moreover, effects relating to the anisotropy of the γ -ray angular distributions for this quadrupole transition, due to the alignment of magnetic substates induced in the Coulex reaction, also need to be considered [68]. Following this, $B(E2)$ transition strengths can then be obtained through the use of the DWEIKO code [59]. In regards to the lifetime analysis, a detailed lineshape analysis needs to be performed for both ^{46}Ti and ^{46}V , most likely with a reduced restriction on the angle of the emitted γ ray, in order to reduce the statistical error in the final result. $B(E2)$ values for the decay of the $2_{T=1}^+$ state in both ^{46}Ti and ^{46}V can then be obtained by using the measured half-lives from the lineshape analysis in conjunction with Equation. 2.35. In both methods employed to measure $B(E2)$ transition strengths, the results from the well-studied ^{46}Ti should be used to test their reliability. Following the completion of this analysis, isospin mixing between the $2_{T=1}^+$ and $2_{T=0}^+$ states in ^{46}V can finally be investigated by testing the linearity of M_p vs T_z . Early indications from this analysis suggest that the errors in the measured values, particularly in the case of ^{46}Cr , may be too large to investigate this relationship fully. However, this will also depend upon both the absolute measured $\sqrt{B(E2)}$ values as well as the level of precision which can be achieved from the lifetime analysis.

Chapter 7

Summary

In summary, an investigation of isospin symmetry breaking and isospin purity has been performed for nuclei in the $f_{7/2}$ region, from which a number of new results have been obtained.

For the analysis concerning the experiment performed at MSU, many new γ rays have been identified in the proton-rich nuclei ^{53}Ni ($T_z = -\frac{3}{2}$) and ^{52}Co ($T_z = -1$), from which new level schemes have been constructed, using a wide range of analytical techniques. The presence of high-spin isomeric states in the secondary beams used during the experiment, particularly in the case of the ^{53}Co beam, facilitated the study of high-spin states up to and including the 11^+ band termination state in ^{52}Co . Furthermore, it was also shown that a reaction model, coupled to spectroscopic factors determined in a full pf shell-model analysis, could be used to predict the distribution of cross section amongst high-spin states with excellent accuracy. In addition to this, detailed comparisons between experimental and theoretical relative cross sections were also made for the mirrored one-nucleon knockout reactions populating the $^{53}\text{Ni}/^{53}\text{Mn}$ mirror pair. A high degree of symmetry is observed in the knockout process, where differences are attributed to binding-energy effects and the presence of isomers in the secondary beams. Accounting for these differences, a good agreement with the theoretical cross sections is obtained.

Experimental MEDs between IAS in the $A = 53$ $T_z = \pm\frac{3}{2}$ and the $A = 52$ $T_z = \pm 1$ mirror pairs have been computed, compared to large-scale shell-model calculations and interpreted in terms of INC interactions. The results, particularly in regards to the $^{52}\text{Co}/^{52}\text{Mn}$ mirror pair, show the strongest evidence to date for the inclusion of a full set of J -dependent INC terms in the analysis of mirror nuclei. Lastly, lifetimes for the long-lived $J^\pi = 5/2^-$ analogue states in both ^{53}Mn and ^{53}Ni have been extracted through a

lineshape analysis, giving half-lives of $T_{\frac{1}{2}} = 120(14)$ ps and $T_{\frac{1}{2}} = 198(12)$ ps, respectively.

For the experiment performed at GSI, a preliminary analysis of the data has been performed, where Coulex cross sections of 79.8(35) mb and 91(10) mb have been obtained for ^{46}Ti and ^{46}Cr , respectively. The preliminary value obtained for ^{46}Ti compares favourably with the predicted Coulex cross section of 83.2 mb obtained using the DWEIKO code [59, 156]. Furthermore, the first demonstration of the new SGT technique has been presented in this thesis with promising results, where clear triple peak structures can be observed for both ^{46}Ti and ^{46}V following the application of strict γ -ray angle cuts. Differences in the observed distribution of counts in the triple peak structures for ^{46}Ti and ^{46}V are attributed to small differences in the half-lives of the $2_{T=1}^+$ analogue states in both nuclei. This observation is additionally supported by very preliminary half-life measurements, performed by comparing experimental and simulated ratios of counts in the three peaks, where half-lives of 6.0(4) ps and 5.3(4) ps were obtained for the $2_{T=1}^+$ state in ^{46}Ti and ^{46}V , respectively. These preliminary values also compare quite favourably with the literature values of 5.29(5) and 4.7(6) ps for ^{46}Ti and ^{46}V , respectively [122]. The final half-life values extracted from this data however, will most likely involve the performance of a detailed lineshape analysis, which should, in theory, yield much more accurate and precise results.

Abbreviations

NSCL - National Superconducting Cyclotron Laboratory

MSU - Michigan State University

GSI - Gesellschaft für SchwerIonenforschung

MED - Mirror energy differences

IAS - Isobaric Analogue States

CSB - Charge Symmetry Breaking

MDE - Mirror Displacement Energies

INC - Isospin-Non-Conserving

CME - Coulomb Matrix Elements

HO - Harmonic Oscillator

PEP - Pauli Exclusion Principle

TBME - Two-Body Matrix Elements

EMSO - ElectroMagnetic Spin-Orbit

RIBs - Radioactive Ion Beams

CCF - Coupled Cyclotron Facility

ECR - Electron Cyclotron Resonance

SuSI - Superconducting Source for Ions

ToF - Time-of-Flight

CRDCs - Cathode-Readout-Drift-Counters

PMTs - PhotoMultiplier Tubes

SeGA - Segmented Germanium Array

HPGe - High-Purity Germanium

PID - Particle Identification

DAQ - Data AcQuisition

NRF - Nuclear Resonance Fluorescence

SGT - Stretched Gold Target

RDDS - Recoil Distance Doppler-Shift
UNILAC - UNiversal LINear ACcelerator
SIS - SchwerIonenSynchrotron
FRS - FRagment Separator
TPCs - Time Projection Chambers
MUSIC - MUltiple Sampling Ionisation Chamber
LYCCA - Lund-York-Cologne CALorimeter
DSSSDs - Double-Sided Strip Silicon Detectors
PD - PhotoDiode
AGATA - Advanced GAMMA Tracking Array
PSA - Pulse Shape Analysis
MGS - Multi Geometry Simulation
ADL - AGATA Data Library
FoM - Figure of Merit
MGT - Mars Gamma Tracking
TDC - Time-to-Digital Converter
MhTDC - Multi-hit Time-to-Digital Converter
P/T - Peak-to-Total

Bibliography

- [1] R. Machleidt and I. Slaus, J. Phys. G: Nucl. Part. Phys. **27**, R69 (2001).
- [2] N.S. Pappabiraman *et al.* Phys. Rev. C **78**, 024301 (2008).
- [3] J. A. Nolen and J. P. Schiffer, Ann. Rev. Nucl. Sci. **19**, 471 (1969).
- [4] J. A. Cameron *et al.*, Phys. Lett. B **235**, 239 (1990).
- [5] J. Ekman, “Mirror Nuclei Isospin Symmetry Breaking in the Mass A=35 and A=51 Mirror Nuclei”, PhD thesis, Lund University, (2004).
- [6] S. J. Williams *et al.*, Phys. Rev. C **68**, 011301(R) (2003).
- [7] A. P. Zuker, S. M. Lenzi, G. Martínez-Pinedo, and A. Poves, Phys. Rev. Lett. **89**, 142502, (2002).
- [8] A. Gadea *et al.*, Phys. Rev. Lett. **97**, 152501 (2006).
- [9] M. A. Bentley and S. M. Lenzi, Prog. Part. Nucl. Phys. **59**, 497 (2007).
- [10] M.A. Bentley, S.M. Lenzi, S.A. Simpson and C.Aa. Diget, Phys. Rev. C **92** 024310 (2015).
- [11] S. A. Milne, M. A. Bentley *et al.* Phys. Rev. C **93**, 024318 (2016).
- [12] S. A. Milne, M. A. Bentley *et al.* Phys. Rev. Lett. **117**, 082502 (2016).
- [13] E. Wigner, Phys. Rev. **51**, **106** (1937).
- [14] B. Cederwall *et al.*, Nature **469**, 68 (2011).
- [15] M. Bentley, Private Communications, (2012).
- [16] D. J. Dean *et al.*, Phys. Lett. B **399**, 1 (1997).

Bibliography

- [17] A. Chodos, American Physical Society News, **17**, 8 (2008).
- [18] H. Grawe, Springer Lect. Notes in Phys. **651**, 33-75 (2004).
- [19] T. S. Brock, “Isomer and β -decay Studies of Very Neutron-deficient ^{94}Pd and ^{97}Cd ”, PhD thesis, University of York (2011).
- [20] R. F. Casten, “Nuclear Structure from a Simple Perspective”, Oxford University Press, 2nd edition, (2000).
- [21] S. S. M. Wong, “Introductory Nuclear Physics”, Wiley-VCH, 2nd edition, pp. 235-238 (2008).
- [22] P. Navratil and B.R. Barrett, Phys. Rev. C **57**, 3119 (1998).
- [23] B.R. Barrett, P. Navratil and J.P. Vary, Nucl. Phys. A **704**, 254c (2002).
- [24] E. Caurier and F. Nowacki, Acta Phys. Pol. B **30** 705 (1999).
- [25] A. Poves, J. Sanchez-Solano, E. Caurier and F. Nowacki, Nucl. Phys. A **694**, 157 (2001).
- [26] B. Cohen, D. Kurath, Nucl. Phys. A **101**, 1 (1967).
- [27] W. Kutschera, B. A. Brown, K. Ogawa, Riv. Nuovo Cim. **1**, No. 12 (1978).
- [28] T. R. H. Skyrme, Nucl. Phys. **9**, 615 and 635 (1959).
- [29] D. Gogny, Nucl. Phys. A **237**, 399 (1975).
- [30] R. Machleidt, Adv. Nucl. Phys. **19**, 189 (1989).
- [31] M. Lacombe *et al.*, Phys. Rev. C **21**, 861 (1980).
- [32] M. Honma *et al.*, Eur. Phys. J. A **25**, 499 (2005).
- [33] G. E. Brown and T. T. S. Kuo, Nucl. Phys. A **92**, 481 (1967).
- [34] T. T. S. Kuo and G. E. Brown, Nucl. Phys. A **114**, 241 (1968).
- [35] T. Hamada and I. D. Johnston, Nucl. Phys. **34**, 382 (1962).
- [36] A. Poves and A. Zuker, Phys. Rep. **70**, 235 (1981).
- [37] M. Hjorth-Jensen, T. T. S. Kuo, and E. Osnes, Phys. Rep. **261**, 125 (1995).

- [38] D. D. Warner, M. A. Bentley, and P. Van Isacker, *Nature Phys.* **2**, 311 (2006).
- [39] A. P. Zuker, S.M. Lenzi, G. Martínez-Pinedo, and A.Poves, *Phys. Rev. Lett.* **89**, 142502 (2002).
- [40] T. W. Henry, “Mirror and Triplet spectroscopy in the *fp* shell with SeGA and GREYINA”, PhD thesis, University of York (2015).
- [41] J.A. Nolen and J.P. Schiffer, *Annu. Rev. Nucl. Sci.* **19**, 471 (1969).
- [42] J. Duo and A. P. Zuker, *Phys. Rev. C*, **66**, 051304, (2002).
- [43] S. J. Williams, *et al.*, *Phys. Rev. C*, **68**, 011301, (2003).
- [44] D. Cortina-Gil, *Springer Lect. Notes in Phys.* **879**, 183-232 (2014).
- [45] T. Lesinski *et al.*, *Phys. Rev. C* **74**, 044315 (2006).
- [46] P.G. Hansen and J.A. Tostevin, *Ann. Rev. Nucl. Part. Sci.* **53**, 219 (2003).
- [47] A. Gade *et al.*, *Phys. Rev. C* **77**, 044306 (2008).
- [48] J.A. Tostevin, *J. Phys. G* **25**, 735 (1999).
- [49] V. Maddalena *et al.*, *Phys. Rev. C* **63**, 024613 (2001).
- [50] A. E. L. Dieperink and T. de Forest, *Phys. Rev. C* **10**, 543 (1974).
- [51] B.A. Brown, *Phys. Rev. C* **58**, 220 (1998).
- [52] J.S. Al-Khalili and J.A. Tostevin, *Phys. Rev. Lett.* **76**, 3903 (1996).
- [53] E. Fermi, *Z. Phys.* **29**, 315 (1924).
- [54] T. Glasmacher, *Nucl. Phys. A* **693** 90 (2001)
- [55] T. Glasmacher, *Springer Lect. Notes in Phys.* **764**, 27-55 (2009).
- [56] D. Cline, *Annu. Rev. Nucl. Part. Sci.* **36**, 683 (1986).
- [57] A. Winther, K. Alder, *Nucl. Phys. A* **319** 518 (1979).
- [58] T. Czosnyka, D. Cline, C.Y. Wu, *Bull. Am. Phys. Soc.* **28**, 745 (1983).
- [59] C. A. Bertulani, C. M. Campbell, and T. Glasmacher, *Comput. Phys. Commun.* **152**, 317 (2003).

Bibliography

- [60] E. Padilla-Rodal *et al.*, Phys. Rev. Lett. **94**, 122501 (2005).
- [61] R. W. Ibbotson *et al.*, Phys. Rev. Lett. **80**, 2081 (1998).
- [62] D. C. Dinca *et al.*, Phys. Rev. C **71**, 041302(R) (2005).
- [63] K. S. Krane, “Introductory Nuclear Physics”, John Wiley & Sons, pp. 327-333 (1987).
- [64] H. Junde, Nucl. Data Sheets **110**, 11 (2009).
- [65] Y. Dong, H. Junde, Nucl. Data Sheets **128**, 185 (2015).
- [66] Y. Dong and H. Junde, Nucl. Data Sheets **121**, 1 (2014).
- [67] E. Simpson, Private Communications (2013-14).
- [68] H. Olliver, *et al.*, Phys. Rev. C **68**, 044312 (2003).
- [69] D. J. Morrissey, Nucl. Phys. A **616**, 1-2 (1997).
- [70] P. A. Zavodszky *et al.*, Nucl. Instrum. Methods Phys. Res., Sect. B **241**, 1-4 (2005).
- [71] D. J. Morrissey *et al.*, Nucl. Instrum. Methods Phys. Res., Sect. B **204**, 90 (2003).
- [72] D.J. Morrissey, Nucl. Instrum. Methods Phys. Res., Sect. B **126**, 316 (1997).
- [73] O.B. Tarasov and D. Bazin, Nucl. Instrum. Methods Phys. Res., Sect. B, **266**, 19-20 (2008).
- [74] D. Bazin, J.A. Caggiano, B.M. Sherrill, J. Yurkon, and A. Zeller, Nucl. Instrum. Methods Phys. Res., Sect. B **204**, 629 (2003).
- [75] J. Yurkon, D. Bazin, W. Benenson, D.J. Morrissey, B.M. Sherrill, D. Swan, and R. Swanson, Nucl. Instrum. Methods Phys. Res., Sect. A **422**, 291 (1999).
- [76] K. Makino and M. Berz, Nucl. Instrum. and Methods A, **427**, 338-343 (2007).
- [77] M. Berz, K. Joh, J. A. Nolen, B. M. Sherrill, and A. F. Zeller, Phys. Rev. C, **47**, 537-544 (1993).
- [78] W.F. Mueller, J.A. Church, T. Glasmacher, D. Gutknecht, G. Hackman, P.G. Hansen, Z.Hu, K.L. Miller, and P. Quirin, Nucl. Instrum. Methods Phys. Res., Sect. A **466**, 492 (2001).

- [79] R. R. C. Clement, *A New Method for the Nuclear Structure Measurement of Neutron Deficient Nuclei*, PhD thesis, Michigan State University, (2003).
- [80] Yasukazu Yoshizawa, Yosei Iwata and Yasuo Inuma, Nucl. Instrum. and Methods, **174**, 1-2 (1980).
- [81] M. Hautala, A. Anttila and J. Keinonen, Nucl. Instrum. and Methods, **150**, 3 (1978).
- [82] Dale G. Olson, Nucl. Instrum. and Methods in Physics, **206**, 1-2 (1983).
- [83] A. Lemasson, *et al.*, Phys. Rev. C **85**, 041303 (2012).
- [84] S. Agostinelli, *et al.*, Nucl. Instrum. Methods Phys. Res. Sect. A **598**, 250303 (2003).
- [85] Zoltan Elekes and Janos Timar, Nucl. Data Sheets **112**, 1 (2011).
- [86] P. J. Davies *et al.* Phys Rev Lett. **111**, 072501 (2013).
- [87] J. R. Brown *et al.*, Phys. Rev. C **80**, 011306 (2009).
- [88] M.A. Bentley *et al.*, Modern Physics Letters A, **25**, 21-23 (2010).
- [89] N.G. Puttaswamy *et al.* Nuclear Physics A **401**, 2 (1983).
- [90] E. Dafni *et al.*, Phys. Lett. B **76**, 1, 50-53 (1978).
- [91] D. Rudolph *et al.*, Phys. Rev. C **78**, 021301 (2008).
- [92] E. Newman and J.C. Hiebert, Nuclear Physics A **110** 366 (1968)
- [93] P.D. Georgopoulos, E.J. Hoffman and D.M. Van Patter. Nuclear Physics **226**, 1 (1974).
- [94] R.L. Schulte, J.D. King, H.W. Taylor, Nuclear Physics A **243**, 2 (1975).
- [95] P.M. Endt, Atomic Data and Nuclear Data Tables, **23**, 6 (1979).
- [96] S. Gorodetzky *et al.*, Nuclear Physics **85**, 3 (1966).
- [97] A. Lemasson, *et al.*, Phys. Rev. C **85**, 041303 (2012).
- [98] S. Agostinelli, *et al.*, Nucl. Instrum. Methods Phys. Res. Sect. A **598**, 250303 (2003).
- [99] S. E. A. Orrigo, *et al.*, Phys. Rev. C **93**, 044336 (2016).
- [100] C. Dossat *et al.*, Nucl. Phys. A **792**, 18 (2007).

Bibliography

- [101] arXiv:1605.08769v1 (2016).
- [102] J. O. Juliano, C. W. Kocher, T. D. Nainan, and Allan C. G. Mitchell, *Phys. Rev.* **113**, 602 (1959).
- [103] R. P. Yaffe and R. A. Meyer, *Phys. Rev. C* **16**, 1581 (1977).
- [104] D. F. Geesaman, R. L. McGrath, J. W. No, and R. E. Malmin, *Phys. Rev. C* **19**, 1938 (1979).
- [105] M. Axiotis, *et al.*, *Phys. Rev. C* **76**, 014303 (2007).
- [106] J. Cerny, R.A. Gough, R.G. Sextro and John E. Esterl, *Nucl. Phys. A* **188**, 3 (1972).
- [107] J. P. Downing, *Diss. Abst. Int.* 39B, 1361 (1978).
- [108] G. Audi, F. Kondev, M. Wang, B. Pfeiffer, X. Sun, J. Blachot, and M. MacCormick, *Chin. Phys. C* **36**, 1157 (2012).
- [109] M. A. Bentley, Private Communications (2015-16).
- [110] N.G. Puttaswamy *et al.* *Nuclear Physics A* **401**, 2 (1983).
- [111] M. Wang, G. Audi, A.H. Wapstra, F.G. Kondev, M. MacCormick, X. Xu and B. Pfeiffer, *Chin.Phys.C* **36**, 1603 (2012).
- [112] J. A. Tostevin and A. Gade, *Phys. Rev. C* **90**, 057602 (2014).
- [113] F.M. Prados Estévez *et al.* *Phys. Rev. C* **75**, 014309 (2007).
- [114] H. Fujita *et al.*, *Phys. Rev. C* **88**, 054329 (2013).
- [115] P.D. Cottle *et al.* *Phys. Rev. C* **60**, 031301(R) (1999).
- [116] R. Orlandi *et al.* *Phys. Rev. Lett.* **103**, 052501 (2009).
- [117] E. Farnea *et al.* *Phys. Lett. B* **551**, 5662 (2003).
- [118] C. D. Hoyle *et al.*, *Phys. Rev. C* **27**, 1244 (1983).
- [119] D. H. Wilkinson, *Isospin in Nuclear Physics*, p. 173, (1970).
- [120] K. Yamada *et al.*, *Eur. Phys. J. A* **25**, 409 (2005).
- [121] O. Moller *et al.*, *Phys.Rev. C* **67**, 011301 (2003).

- [122] F. Brandolini *et al.*, Phys. Rev. C **70**, 034302 (2004).
- [123] S. C. Wu, Nuclear Data Sheet **91**, 1 (2000).
- [124] S. M. Lenzi *et al.*, Phys. Rev. C **60**, 021303 (1999).
- [125] K. Summerer *et al.*, Phys. Rev. C **61**, 034607 (2000).
- [126] K. Summerer *et al.*, Phys. Rev. C **86**, 014601 (2012).
- [127] A. Dewald *et al.*, Prog. Part. Nucl. Phys. **67**, 786-839 (2012).
- [128] R. Krücken, J. Res. Natl. Inst. Stand. Technol. **105**, 53 (2000).
- [129] H. Iwasaki, *et al.*, Nucl. Instrum. Methods Phys. Res., Sect. A **806**, 123-131 (2016).
- [130] W. Henning, Nucl. Phys. A, 538, 637 (1992).
- [131] C. Domingo-Pardo *et al.*, Nucl. Instrum. Methods Phys. Res., Sect. A **694**, 297 (2012).
- [132] H. Geissel *et al.*, Nucl. Instrum. Methods Phys. Res., Sect. B **70**, 286 (1992).
- [133] R. Janik *et al.*, Nucl. Instrum. Methods Phys. Res., Sect. A **640**, 54 (2011).
- [134] R. Janik *et al.*, Nucl. Instrum. Methods Phys. Res., Sect. A **364**, 150 (1995).
- [135] M. Pfützner *et al.*, Nucl. Instrum. Methods Phys. Res., Sect. B **86**, 213 (1994).
- [136] P. Golubev *et al.*, Nucl. Instrum. Methods Phys. Res., Sect. A **723**, 55 (2013).
- [137] A. Wendt, “Isospin symmetry in the sd shell. Coulomb excitation of ^{33}Ar at relativistic energies and the new Lund-York-Cologne-Calorimeter”. PhD thesis, Kln University (2013).
- [138] R. Hoischena *et al.*, Nucl. Instrum. Methods Phys. Res., Sect. A **654**, 354 (2011).
- [139] M. Reese, N. Pietralla, P. Golubev and D. Rudolph, GSI Scientific Report, **2013-1**, 185 (2013).
- [140] S. Akkoyun *et al.*, Nucl. Instrum. Methods Phys. Res., Sect. A **668**, 26 (2012).
- [141] F. Recchia, “In-beam test and imaging capabilities of the AGATA prototype detector”. PhD thesis, Univerità Degli Studi di Padova (2008).

- [142] J.M.C. Brown *et al.*, Nucl. Instrum. Methods Phys. Res., Sect. B **338**, 77-88 (2014).
- [143] R. Ribberfors, Phys. Rev. B **12**, 2067 (1975).
- [144] R. Venturelli, D. Bazzacco, LNL Annual Report 2004, INFN-LNL, Legnaro, Italy, 220 (2005).
- [145] M. Descovich, et al., Nucl. Instrum. Methods Phys. Res., Sect. A **553**, 535 (2005).
- [146] F. C. L. Crespi, F. Camera, B. Million, M. Sassi, O. Wieland, A. Bracco, Nucl. Instrum. Methods A **593**, 440 (2007).
- [147] P. Médina, C. Santos, D. Villaume, Proceedings of the Twenty-first IEEE Instrumentation and Measurement Technology Conference, **3**, 1828 (2004).
- [148] B. Bruyneel, P. Reiter, G. Pascovici, Nucl. Instrum. Methods Phys. Res., Sect. A **569**, 764 (2006).
- [149] Bruyneel, B., Birkenbach, B. Reiter, P. Eur. Phys. J. A **52**, 70 (2016).
- [150] P. A. Söderström *et al.*, Nucl. Instrum. Methods Phys. Res., Sect. A **638**, 96 (2011).
- [151] D. Bazzacco, Nucl. Phys. A **746** 248 (2004).
- [152] O. Häusser *et al.*, Phys. Lett. B **73** 127 (1978).
- [153] B. Singh, J. Chen, Nuclear Data Sheets, **126**, 1 (2015).
- [154] A. Venturelli, D. Bazacco, LNL Annual Report 2004, 220 (2004).
- [155] C. Michelagnoli, “The lifetime of the 6.79 MeV state in ^{15}O as a challenge for nuclear astrophysics and γ -ray spectroscopy: a new DSAM measurement with the AGATA Demonstrator array”, PhD thesis, Univerità Degli Studi di Padova (2013)
- [156] A. Boso, Private Communications (2016).
- [157] N. Lalović *et al.*, Nucl. Instrum. Methods Phys. Res., Sect. A **806**, 258 (2016).